

**DEPOSITION AND APPLICATION OF ELECTROLESS
NI-W-P UNDER BUMP METALLISATION FOR HIGH
TEMPERATURE LEAD-FREE SOLDER
INTERCONNECTS**

By
Li Liu

A DOCTORAL THESIS
SUBMITTED IN PARTIAL FULFILMENT OF THE REQUIREMENTS
FOR THE AWARD OF
DOCTOR OF PHILOSOPHY OF LOUGHBOROUGH UNIVERSITY

November 2016

© Li Liu (2016)

ABSTRACT

A reliable and robust diffusion barrier, commonly known as under bump metallisation (UBM), is indispensable in solder interconnects in order to retard the interfacial reaction rate, hence the growth of intermetallic compounds (IMCs). However, electroless Ni-P coatings are not adequate to inhibit interfacial reactions effectively since the formation of columnar structure and voids in the crystalline Ni_3P layer in hybrid automotive devices (operating temperature above 300 °C) can significantly deteriorate the mechanical integrity of solder joints. In this thesis, electroless Ni-W-P coatings, as an effective UBM capable to serving under high temperature (up to 450 °C), are developed, characterised and subsequently applied onto the high temperature lead-free solder interconnects.

An electroless Ni-W-P coating has exhibited an excellent thermal stability and delay of crystallisation process under elevated temperature (up to 750 °C) subject to their W and P contents. In particular, it is found that W content can significantly elevate crystallisation temperatures of Ni_3P and Ni phases from 347 °C (Ni-10P) to 390 °C (Ni-5.5W-9P). When reflowing with the lead-free solders below crystallisation temperature (e.g. 400 °C), an amorphous layer formed between unreacted Ni-W-P coating and solders is able to effectively resist the interfacial IMCs growth. More interestingly, a resultant compact and voids free interlayer from reflow above the crystallisation temperature is also proven to be as effective as the unreacted Ni-W-P coating itself in terms of their property as a diffusion barrier.

Without Ni-W-P UBM, excessive growth of $\varepsilon\text{-CuZn}_4$ layer, $\gamma\text{-Cu}_5\text{Zn}_8$ layer and $\beta'\text{-CuZn}$ layer as well as some Kirkendall voids were found at the Cu/Zn-Al solder interface formed through a reflow process with the aid of a self-prepared flux. By applying Ni-W-P coatings as a diffusion barrier, formation and growth of Cu-Zn IMCs have been significantly prevented and reduced owing to a thin interlayer of Al_3Ni_2 after certain time of reflowing at 450 °C.

As an insertion UBM, Ni-W-P coatings in sandwich-structured Au-Ge and BiAgX solder joints have been further verified their validity as a diffusion barrier layer, which has reduced greatly the interfacial reactions of these solder joints on the basis of analysis and characterisation results. In Au-Ge solder joints, Ni_5Ge_3 is formed at Ni-W-

P/Au-Ge interface taking various morphologies, such as dendrite, scallop and granular according to TEM observations. In BiAgX joints, large Ag_3Sn particles ($> 100\text{ nm}$) are observed to be scattered along grain boundaries, the smaller particles ($< 100\text{ nm}$) inside of grains. At Ni-W-P/BiAgX interfaces, Ni_3Sn_4 of columnar-like with a thickness ranging from $100 - 700\text{ nm}$ is also formed. Shear strength tests showed the fracture of Au-Ge solder joints inside of the solder taking a ductile failure mode. The mean value of shear strength of these Au-Ge solder joints was 138.4 MPa , proving a robust interfacial adhesion. However, BiAgX solder joints mainly fractured at the metallisation of die side, giving average shear strength of approximately 32.0 MPa , which is also four times higher than the required strength of IEC standard (6.25 MPa).

Key words: Electroless Ni-W-P deposition, crystallisation characteristics, lead-free high temperature solders, diffusion barrier characteristics, power electronics, interfacial reactions, IMCs.

ACKNOWLEDGEMENTS

The work is financially supported by the 7th European Community Framework Programme (M6 project, No. PIRSES-GA-2010-269113) and the EPSRC project via CPE at University of Nottingham. Besides, special thanks to the financial support of Loughborough University studentship for my PhD study.

I would like to take this opportunity to express my sincere gratitude and deep appreciation to my supervisor, Prof. Changqing Liu for his invaluable guidance, support and encouragement throughout my PhD study. I would also like to thank Dr. David A Hutt for his helpful advice along this course.

I am deeply grateful to Prof. Fengshun Wu, Dr. Longzao Zhou, and Prof. Xianglin Zhang in Huazhong University of Science and Technology (HUST) for their support and supervision during my stay in HUST. Many thanks to my friends in HUST, Dr. Zhiwen Chen, Dr. Zhijun Shi, and Mr. Guang Chen for their help and knowledge.

This PhD work would have been unsuccessful without the support of our collaborators. Firstly, I would like to thank our collaborators, Miss Jinzi Cui and Prof. Wayne Johnson in Auburn University and University of Tennessee, for the shear tests of Au-Ge and BiAgX solder joints. Thanks also go to Dr. Keming Chen and Dr. Trevor Pearson in MacDermid for their training and suggestion in electroless plating. The training and support of gas dynamic cold spray experiments from Prof. Changjiu Li in Xi'an Jiaotong University is also appreciated. Thanks are also extended for Dr. Simin Li and Mr. Mayao Wang for their assistance in nanoindentation tests as well as Dr. Wenbo Zhu for his help in self-propagation experiments in Loughborough University.

My thanks are also due to Dr. Zhaoxia Zhou, Mr. Scott Doak, Dr. Keith Yendall, Dr. Sabrina Yang, and Mr. Shaun Fowler in Loughborough Materials Characterisation Centre for their assistance and discussion on materials characterisations.

Thanks are also extended to all my colleagues in the Interconnection Group and technicians in Wolfson School for their help and knowledge, particularly for Dr. Weiwei Zhao, Dr. Xu Zha, Mr. Long Sun, Mr. Bob Temple, and Mr. Mike Porter.

Finally, I would like to express my deepest gratitude to my parents and my fiancé for their unconditional love and support during all the years of this education.

Table of Contents

ABSTRACT	I
ACKNOWLEDGEMENTS	III
Table of Contents.....	IV
List of Figures	VIII
List of Tables.....	XV
Glossary of Symbols	XVII
Chapter 1 Introduction	1
1.1 Background and motivations	1
1.2 Research aim and objectives	3
1.3 Contributions to the body of knowledge	4
1.4 Structure of the thesis	5
References	7
Chapter 2.....	9
2.1 High temperature electronics packaging	9
2.1.1 High temperature electronics.....	9
2.1.2 High temperature electronics packaging	9
2.1.3 First-level packaging	11
2.2 High temperature solders.....	13
2.2.1 High lead solders	14
2.2.2 Global legislations	14
2.2.3 High temperature lead-free solder	15
2.3 Under bump metallisation	21
2.3.1 Various electroless Ni-based coatings.....	21
2.3.2 Thermal stability of electroless Ni-based plating.....	23
2.3.3 Diffusion barrier properties of Ni-based metallisation.....	25
2.3.4 Electroless Ni-W-P plating.....	27
2.4 Joining process	31
2.4.1 Soldering.....	32
2.4.2 Sintering	33

2.4.3 Transient liquid phase bonding/sintering	34
2.4.4 Other novel joining approaches	35
2.5 Interfacial reactions between high temperature solders and metallisation	36
2.5.1 Interfacial reactions in Zn-Al-based solder joints	37
2.5.2 Interfacial reactions in Au-Ge solder joints.....	38
2.5.3 Interfacial reactions in Bi-Ag-based solder joints	40
2.6 Mechanical properties of high temperature solder joints	42
2.6.1 Shear strength and of high temperature solder joints	43
2.6.2 Fractographic analysis of high temperature solder joints.....	45
2.6.3 Mechanical properties of interfacial IMCs in solder joints	46
2.7 Summary.....	49
References	50
Chapter 3.....	62
3.1 Introduction	62
3.2 Development of electroless Ni-W-P plating.....	64
3.2.1 Experimental details	64
3.2.2 Results and discussions	68
3.3 Effects of plating parameters on electroless Ni-W-P deposits	71
3.3.1 Experimental details	72
3.3.2 Results	73
3.3.3 Discussions	81
3.4 Summary.....	84
References	85
Chapter 4.....	88
4.1 Introduction	88
4.2 Experimental details	89
4.2.1 Electroless Ni-W-P and Ni-P coatings	89
4.2.2 Electroplate Ni-W coating	93
4.3 Results and discussions	94
4.3.1 Composition and phase analysis.....	94
4.3.2 Phase transformation behaviours of Ni-based coatings.....	96
4.3.3 Surface morphology of Ni-W-P alloys after thermal treatments.....	100
4.3.4 Cross-section morphology of Ni-based coatings during <i>in-situ</i> heating	102
4.4 Summary.....	105

References	106
Chapter 5	109
5.1 Introduction	109
5.2 Soldering process with a self-developed flux.....	110
5.2.1 Experimental details	110
5.2.2 Solderability of Zn-Al/Cu and Zn-Al/UBM Solder	114
5.2.3 Interfacial microstructure at Cu/Zn-Al and Ni-W-P/Zn-Al interfaces	115
5.3 Gas Dynamic Cold Spray	117
5.3.1 Experimental details	118
5.3.2 Characteristics of Zn-Al solder particles	120
5.3.3 Microstructure of the as-deposited samples	121
5.3.4 Microstructure of as-reflowed Zn-Al solder interconnects	122
5.4 Self-propagation method	126
5.4.1 Experimental details	126
5.4.2 Interfacial microstructure of Zn-Al solder joints.....	128
5.5 Discussions	132
5.6 Conclusions	134
References	135
Chapter 6	138
6.1 Introduction	138
6.2 Experimental details	140
6.2.1 Preparations of Ni-W-P/Zn-Al solder joints.....	140
6.2.2 Morphological and Microstructural Observations.....	140
6.2.4 Nanoindentation tests	142
6.3 Results & Discussions	143
6.3.1 As-deposit Ni-W-P UBM	143
6.3.2 Interfacial microstructure of Zn-Al solder interconnects	144
6.3.3 Growth mechanisms of IMC layers during reaction	149
6.3.4 Crystallisation characteristics of Ni-W-P UBM during reactions	151
6.3.5 Nanoindentation characterisations.....	154
6.5 Summary.....	157
References	158
Chapter 7	162
7.1 Introduction	162

7.2 Experimental details	163
7.2.1 Electroless Ni-W-P plating.....	163
7.2.2 Formation of solder joints	164
7.2.3 Morphological and microstructural observations	165
7.2.4 Shear tests and fracture analysis.....	166
7.3 Interfacial microstructure and shear strength of as-built Au-Ge solder joints ..	166
7.3.1 As-deposited Ni-W-P coatings	167
7.3.2 Interfacial reactions of Au-Ge solder joints	167
7.3.3 Shear strength and fracture analysis of Au-Ge solder joints	171
7.4 Interfacial microstructure and fracture analysis of as-built BiAgX solder joints	176
7.4.1 As-deposited Ni-W-P coatings	176
7.4.2 Interfacial microstructure analysis of BiAgX solder joints	177
7.4.3 Shear strength and fracture analysis of BiAgX solder joints	181
7.5 Summary.....	184
References	185
Chapter 8.....	187
8.1 Main conclusions.....	187
8.1.1 Development of electroless Ni-W-P plating process.....	187
8.1.2 Thermal stability and phase transformation of electroless Ni-W-P coatings	188
8.1.3 Formation of Zn-Al solder interconnects	189
8.1.4 Crystallisation characteristics of Ni-W-P coatings in lead-free solder joints	190
8.1.5 Interfacial reactions between electroless Ni-W-P coatings and high temperature lead-free solders	191
8.2 Future work	194
8.2.1 Electroless deposition of Ni-W-P coatings.....	194
8.2.2 Phase transformation of electroless Ni-W-P coatings	194
8.2.3 Applications of Ni-W-P UBM with low-cost high temperature solder.....	195
8.2.4 Interfacial reactions in high temperature lead-free solder joints	196
8.2.5 Reliability tests of high temperature lead-free solders joints	197
Publications	198

List of Figures

Figure 1-1 Schematic illustration showing the cross section of: a) a power module (with the associated heatsink); b) a die attachment (the size portion is not according to the actual product).....	2
Figure 1-2 Schematic diagram of the thesis structure.....	7
Figure 2-1 Electronic packaging hierarchy with first-, second-, third-level packages.	10
Figure 2-2 A schematic diagram revealing the cross section of a typical power modules.	11
Figure 2-3 A schematic diagram revealing the cross section of a typical solder die attachment.	13
Figure 2-4 Backscattered SEM image showing voids in the Ni ₃ P layer at Sn-Ag-Cu/Ni(P) interface.	22
Figure 2-5 Amorphous-crystalline transition temperature in electroless Ni-based coatings.	24
Figure 2-6 Solder joint microstructures of Sn-3.5Ag/Ni-W-P after 1 (1 st , 3 rd column) and 5 minutes reflow (2 nd , 4 th column).	25
Figure 2-7 The IMCs in the a) Ni-W-P/Sn-Bi solder joint after reflowing for 28h at 200 °C, and b) Ni-W-P/Sn-3.5Ag solder joints aging for 625h at 200 °C.	26
Figure 2-8 Cross-section SEM and TEM micrographs and diffraction patterns from regions A and B.....	27
Figure 2-9 The reaction pathways for the oxidation process of DMAB via intermediates on Cu.	29
Figure 2-10 Schematic diagrams of the nickel and tungstate reduction and hypophosphite oxidation process.	30
Figure 2-12 Schematic diagram of soldering process.....	32
Figure 2-12 Illustration of contact angles formed by liquid drops on a smooth solid surface.	33
Figure 2-13 Schematic diagram of Ag sintering process.	33
Figure 2-15 Schematic diagrams of a) transient liquid phase sintering, b) transient liquid phase soldering.	35
Figure 2-15 Microstructures of (a) Cu/molten Zn-4Al at 460 °C for 5 minutes, and Cu/IMCs/ Zn-4Al aged at (b) 120 °C for 10 days, (c) 200 °C for 5 days, and (d) 300 °C for 5 days.....	37
Figure 2-16 Back scattered electron (BSE) images of microstructure of (a) Ni/molten Zn-4Al soldered at 420 °C for 5 minutes; (b) enlarged image of (a); (c) Ni/molten Zn-4Al soldered at 450 °C for 5 minutes; and (d) enlarged image of (c) at the interfaces among Al ₃ Ni ₂ , hcp-Zn, γ and Ni.	38

Figure 2-17 Cross-section and formation of reaction layer in the vicinity of the: (a) Cu/Au-Ge solder interface; (b) Ni/Au-Ge solder interface.....	39
Figure 2-18 The SEM micrograph of the Au-12Ge/Ni interface reacted at 400 °C for 4 hours.....	40
Figure 2-19 Mechanism of the microstructural evolution of the joint during high temperature aging: (a) as-reflowed; (b) initial aging stage; (c) break-up of the IMC layer; and (d) oxidation of the interface and Cu diffusion to the solder.	40
Figure 2-20 Structural feature of the Bi-2.5Ag/Ni interface after reaction at 350 °C for: (a) 1 minute; (b) magnified structure of (a) showing that only NiBi ₃ was found; for (c) 5 minutes; (d) magnified structure of (c) illustrating that NiBi and intercellular cracks of NiBi ₃ appeared.....	41
Figure 2-21 Improved wetting of the mixed solder paste comparing to Bi-11Ag paste on Cu and Alloy 42.	42
Figure 2-22 Solder joints subjected to shear strain during thermal cycling due to CTE mismatch between the Die, the solder and the substrate.....	43
Figure 2-23 Images of: a) Universal Bond tester for measuring the shear strength of die attachment; b) schematic shear test.....	43
Figure 2-24 Modified fracture modes of die attachments in power electronic packaging.	46
Figure 2-25 Nanoindentation depth-load curve shows the parameters for analysis of the result.....	47
Figure 3-1 Experimental setup of the electroless Ni-W-P plating system.	64
Figure 3-2 Procedures of making up the electroless Ni-W-P plating solution.	65
Figure 3-3 The schematic diagram of the tape test on adhesion strength of the Ni-W-P coatings.	67
Figure 3-4 An example of the tape test results on Ni-W-P coatings (~10 µm thickness).	69
Figure 3-5 Procedures of pre-treatment process of electroless Ni-W-P plating on Cu substrates.....	70
Figure 3-6 The surface morphologies of the Ni-W-P coatings with a) no additives; b) SLS addition (concentration: 0.3 mg/L).	70
Figure 3-7 Effects of SLS concentration on composition and deposition rate of the Ni-W-P deposits.	71
Figure 3-8 The surface morphologies of the Ni-W-P deposits using different concentrations of NiSO ₄ 6H ₂ O: a) 7 g/L. b) 20 g/L, c) 30 g/L, d) 40 g/L.....	74
Figure 3-9 Effects of NiSO ₄ 6H ₂ O concentration on composition and deposition rate of the Ni-W-P deposits.	74
Figure 3-10 The surface morphologies of the Ni-W-P deposits using different concentrations of Na ₂ WO ₄ 2H ₂ O: a) 35 g/L, b) 55 g/L, c) 75 g/L.	75
Figure 3-11 Effects of Na ₂ WO ₄ 2H ₂ O concentration on composition and deposition rate of the Ni-W-P deposits.....	76

Figure 3-12 The surface morphologies of the Ni-W-P coatings using different concentrations of $\text{NaH}_2\text{PO}_2 \cdot \text{H}_2\text{O}$: a) 10 g/L, b) 18 g/L, c) 25 g/L, d) 30 g/L.	76
Figure 3-13 Effects of $\text{NaH}_2\text{PO}_2 \cdot \text{H}_2\text{O}$ concentrations on composition and deposition rate of the Ni-W-P deposits.....	77
Figure 3-14 The surface morphologies of the Ni-W-P coatings using different concentrations of $\text{Na}_3\text{C}_6\text{H}_5\text{O}_7 \cdot 2\text{H}_2\text{O}$: a) 40 g/L, b) 75 g/L, c) 100 g/L.	78
Figure 3-15 Effects of $\text{Na}_3\text{C}_6\text{H}_5\text{O}_7 \cdot 2\text{H}_2\text{O}$ concentrations on chemical composition and deposition rate of the Ni-W-P deposits.	78
Figure 3-16 The surface morphologies of the Ni-W-P coatings with different plating temperature: a) 70 °C; b) 80 °C; c) 90 °C.	79
Figure 3-17 Effects of plating temperature on composition and deposition rate of the Ni-W-P deposits.	80
Figure 3-18 The surface morphologies of the Ni-W-P coatings with different pH: a) 7; b) 8; c) 9.	81
Figure 3-19 Effects of pH values on composition and deposition rate of the Ni-W-P deposits.....	81
Figure 4-1 The electroless Ni-based deposits with different W contents in ceramic boat for subsequent thermal treatments.	91
Figure 4-2 Temperature profile of annealing treatments at the peak temperature of 400, 450 and 750 °C.....	92
Figure 4-3 The temperature profile for the Ni-W-P coatings in high temperature optical microscopy.	93
Figure 4-4 DSC thermograms obtained for the electroless Ni-based metallisation with various W contents (0, 5.5, 15.2, and 25.3 wt.%)	95
Figure 4-5 XRD diffraction patterns of the Ni-10P coating annealed for 2 hours at various temperature.....	96
Figure 4-6 XRD diffraction patterns of the Ni-15W-10P coating annealed for 2 hours at various temperature.....	97
Figure 4-7 XRD diffraction patterns of various Ni-based coatings annealed at 400 °C for 2 hours.	99
Figure 4-8 SEM and AFM images of electroless Ni-15W-10P coatings after 2 hours annealing at: a) room temperature (20 °C); b) 400 °C; c) 750 °C.	101
Figure 4-9 The cross-section images of microstructure of electroless Ni-25W-9P coating during <i>in-situ</i> thermal treatments.	103
Figure 4-10 The cross-sectional microscopy of crystallised Ni-25W-9P coating on Cu substrates after observations in high temperature optical microscopy.....	103
Figure 4-11 The <i>in-situ</i> cross-section images of microstructure of electroplated Ni-29W coating during thermal treatments.....	104
Figure 4-12 The cross-section microscopy of the Ni-W coating on Cu substrates: a) As-deposit; b) After <i>in-situ</i> observation in high temperature optical microscopy (In back-scattered mode).	105
Figure 5-1 Surface structure of solid metal.....	111

Figure 5-2 The binary phase diagram of LiCl-KCl system.	112
Figure 5-3 The triangulation of ZnCl ₂ -LiCl-KCl ternary system.	112
Figure 5-4 Pseudo-binary diagrams of: a) LiCl-(2ZnCl ₂ -KCl) system; b) LiCl-(ZnCl ₂ -2KCl) system.....	113
Figure 5-5 Wetting angles of Zn-Al solder on (a) Cu substrate after 5 minutes soldering; (b) Cu substrate after 30 minutes; (c) Ni-W-P/Cu substrate after 5 minutes soldering; (d) Ni-W-P/Cu substrate after 30 minutes soldering.	115
Figure 5-6 Back-scattered SEM image showing Cu-Zn IMCs formed at the as-soldered Cu/Zn-Al interface with line-scanned EDX results.	116
Figure 5-7 Back-scattered SEM image showing the IMCs formed at the as reflowed Ni-W-P/Zn-5Al interface with line-scanned EDX results.	116
Figure 5-8 A schematic diagram of gas dynamic cold spray system.....	117
Figure 5-9 The reflow profile for the cold sprayed samples.....	119
Figure 5-10 Back-scattered images of the morphology of Zn-Al solder particles with elemental results: a) overview image; b) typical Zn-Al particles (enlarged view of the highlight region in figure 5-10 a)); EDX spectrum on dispersive Al particles; d) EDX spectrum on Zn-Al particles.....	120
Figure 5-11 The particle size distribution of Zn-5Al solder particles.....	121
Figure 5-12 Cross-sectional image of as-deposited Zn-Al coatings: a) on Cu substrate; b) on Ni-W-P plated Cu substrate; c) with distinct voids and boundaries of Zn-Al solder particles.	121
Figure 5-13 Surface morphology of cold-sprayed Zn-Al coating in N ₂ atmosphere at a temperature of 190 °C: a) Overview image; b) Enlarged view of the region highlighted in figure 5-13 a).....	122
Figure 5-14 Interfacial microstructures of as-soldered Zn-Al coatings. a) Overview image showing the Zn-Al particle grains; b) The unmelt Al particle embedded in Zn-Al coating matrix.	123
Figure 5-15 As-soldered Ni-W-P/Zn-Al solder interconnects with elemental mapping results.	123
Figure 5-16 The interfacial microstructure at Ni-W-P/Zn-Al interface with elemental line results.	124
Figure 5-17 Fracture at Cu/Zn-Al solder interconnects: a) massive cracks and voids formed within the solder joint; b) penetrating cracks near the Cu-Zn IMCs.....	125
Figure 5-18 SAM images of the Cu/Zn-Al solder interconnects: a) As-deposited specimen; b) After soldering process.....	125
Figure 5-19 Schematic microstructure of the Al-Ni Nanofoil used for reactive bonding.	127
Figure 5-20 Schematic diagram of self-propagation test.	128
Figure 5-21 SEM images of the Zn-Al solder joints: a) entire solder joint; b) enlarged image at the Si/Zn-Al/AlNi interface highlighted in figure 5-21 a); c) The original microstructure of the original (unreacted) Zn-Al solder film.	129
Figure 5-22 TEM image of the morphology at the SiC/ZnAl/AlNi interfaces.....	129

Figure 5-23 The TEM elemental mapping results at the Si/Zn-Al solder interface....	130
Figure 5-24 The TEM elemental mapping results at the AlNi Nanofoil/Zn-Al solder interface.....	131
Figure 6-1 Cross section of the Cu/Zn-5Al solder interconnect with a crack.....	138
Figure 6-2 Reflow profiles of the Zn-Al solder interconnects.....	140
Figure 6-3 Micro-machining process by Dual FIB for TEM sample preparation. a) Pt layer deposited on top of the region of interest; b) two rectangular trenches fabricated on both sides of the Pt layer for preparation of the TEM sample; c) “U” cut of the TEM sample to be lifted up; d) Foil attached to the omniprobe and lifted up; e) TEM sample attached to the Mo grid holder by Pt deposition; f) TEM sample further thinning to electron transparency.	141
Figure 6-4 Micrographs of as-deposit Ni-W-P coatings: a) surface morphology; b) cross-section morphology.	143
Figure 6-5 Phase diagram of Cu-Zn binary system	144
Figure 6-6 Phase diagram of a) Ni-Zn binary system, b) Ni-Al binary system.....	144
Figure 6-7 Back-scattered SEM images showing IMCs at Zn-Al/Cu interfaces after liquid-solid reaction for: a) 1 minute; b) 5 minutes; c) 15 minutes; d) 30 minutes. ...	145
Figure 6-8 Kirkendall voids formed around the CuZn interlayer at the Cu/Zn-Al interface after 30 minutes reaction at 450 °C.	146
Figure 6-9 Schematic diagram illustrating the interfacial microstructure and IMC evolutions after liquid-solid reactions at 450 °C for: a) 1 minute; b) 30 minutes.....	146
Figure 6-10 SEM images showing the morphology and size of the Al ₃ Ni ₂ particles observed at the Ni-W-P/Zn-Al interfaces from cross-section view after liquid-solid reactions at 450 °C for: a) 1 minute; b) 5 minutes; c) 15 minutes; d) 30 minutes, and from top view: e) 1 minute; f) 5 minutes; g) 15 minutes, h) 30 minutes.	147
Figure 6-11 Elemental mapping and pointing analysis of the Ni-W-P/Zn-Al interface after 30 minutes liquid-solid reactions at 450 °C.....	149
Figure 6-12 Thickness of the Zn-Cu IMCs formed after liquid-solid reactions at 450 °C for 1, 5, 15 and 30 minutes at: a) Cu/Zn-5Al interfaces; b) Ni-W-P/Zn-5Al interfaces.	150
Figure 6-13 Interfacial microstructure and SADP at Ni-W-P/Zn-Al interfaces: a), b): after 1 minute liquid-solid reaction; c), d): after 30 minutes liquid-solid reaction.	152
Figure 6-14 Schematic diagram illustrating the IMC evolutions and Ni-W-P crystallisations after reaction at 450 °C for: a) 1 minute; b) 15 minutes; c) 30 minutes.	154
Figure 6-15 Indents on the IMC layers at the Cu/Zn-Al and Ni-W-P/Zn-Al interfaces after 30 minutes reaction at 450 °C: a) indents near Zn-Al solder; b) indents near Cu substrate; c) indent on CuZn ₄ ; d) indent on Cu ₅ Zn ₈ ; e) indent on CuZn; f) indents on Al ₃ Ni ₂	155
Figure 6-16 Representative load-displacement curves of nanoindentation tests on the constituent phases at the Cu/Zn-Al and Ni-W-P/Zn-Al interfaces after reactions at 450 °C for 30 minutes.	156
Figure 7-1 Direct bond copper ceramic substrate.	164

Figure 7-2 The schematic diagrams of SiC dies with the metallisation for: a) Au-Ge solders, b) BiAgX solders.	165
Figure 7-3 Reflow profile of BiAgX solder joints.	165
Figure 7-4 Schematic diagram of shear tests.	166
Figure 7-5 Micrographs of the as-deposited Ni-W-P coating: a) surface morphology; b) cross-section morphology.	167
Figure 7-6 Cross-section SEM images of as-built Au-Ge solder joints: a) Overview of entire joints, b) enlarge view of Region b (back-scattered electron mode).	168
Figure 7-7 EDX element mapping analysis of the Au-Ge solder joints: a) back-scattered SEM image, b) mapping for Si, c) mapping for Au, d) mapping for Ni, e) mapping for Ge, f) mapping for Cu.	168
Figure 7-8 Calculated Ni-Ge phase diagram.	169
Figure 7-9 Micrographs of prepared FIB sample selected at as-built Ni-W-P/Au-Ge interface from: a) cross-sectional view (tilted at 52 °); b) top view (tilted at 7 °).	169
Figure 7-10 TEM bright-field image at the Ni-W-P/Au-Ge interface with SAED pattern.	171
Figure 7-11 Shear strength of as-built Au-Ge solder joints.	172
Figure 7-12 SEM and EDX mapping of the fracture surface of Au-Ge solder joints from the DBC substrate side: a) SEM micrograph of overview image; b) mapping for Au; c) mapping for Ni; d) mapping for Ge.	172
Figure 7-13 Typical fracture surface of the Au-Ge solder joints on substrate side: a) typical fracture surface; b) enlarged view of the dimples; c) NiGe grains; d) EDX spectrum of NiGe in c).	173
Figure 7-14 SEM images of: a) fracture surface on SiC die; b) enlarge image of Region b; c) enlarge image of Region c; d) Elemental mapping results of Region b.	175
Figure 7-15 Schematic diagram of the fracture mode for as-built SiC/Au-Ge/Ni-W-P solder joints.	176
Figure 7-16 Micrographs of as-deposited Ni-W-P coatings: a) surface morphology, b) cross-section morphology.	177
Figure 7-17 Cross-sectional SEM images of as-built BiAgX solder joints: a) Overview microscopy of entire joint, b) enlarge view of region B (back-scattered mode).	177
Figure 7-18 Phase diagram of Ag-Sn system.	178
Figure 7-19 EDX element mapping analysis of the BiAgX solder joint: a) SEM-backscattered image; b) mapping for Si; c) mapping for Bi; d) mapping for Ag; e) mapping for Sn; f) mapping for Ni; g) mapping for Cu; h) mapping for W.	179
Figure 7-20 TEM results of a) TEM bright-field image at the Ni-W-P/BiAgX solder interconnect with a selected-area diffraction pattern (SADP) taken from Ni-W-P coating; b) high-resolution image of the area highlighted in Region b in figure 7-20 a); c) elemental mapping results of figure 7-20.	180
Figure 7-21 Shear strength of BiAgX solder joints.	181

Figure 7-22 SEM and EDX mapping images of the fracture surface on DBC substrate side: a) SEM micrograph; b) mapping for Sn; c) mapping for Ni; d) mapping for Bi.	182
Figure 7-23 The fracture surface of BiAgX solder joints on SiC die side: a) overview image; b) enlarged image of Region b; c) enlarged image of Region c; d) enlarged image of Region d.	182
Figure 7-24 Schematic diagram of the failure characteristics of as-built BiAgX solder joints.	184

List of Tables

Table 2-1 A summary of typical packaging hierarchy for electronics assemblies.....	10
Table 2-2 An overview of typical high temperature solders.	20
Table 2-3 The possible alloys that can be co-deposited with Ni in electroless plating...	22
Table 2-4 Advantages and corresponding salts for the third alloys in ternary Ni-based metallisation.	23
Table 2-5 The functions and related materials of plating components/parameters.....	30
Table 2-6 A summary of shear strength of current high temperature solder joints.....	44
Table 2-7 A summary of elastic moduli and hardness of interfacial IMCs at solder joints.	48
Table 3-1 Formulations and plating conditions of electroless Ni-W-P plating with various pre-treatments.	66
Table 3-2 Classification of adhesion test results.	67
Table 3-3 Formulations and plating conditions of electroless Ni-W-P plating with different SLS concentrations.	68
Table 3-4 Comparisons of the different pre-treatment approaches.	69
Table 3-5 Formulations and plating conditions of electroless Ni-W-P plating solution (unit: g/L).	72
Table 3-8 Summary of coating parameters on the proportion of W in Ni-W-P deposits.	83
Table 3-9 Summary of coating parameters on the proportion of P in Ni-W-P deposits.	84
Table 4-1 Procedures of pre-treatment process for aluminium substrate prior to electroless plating.	90
Table 4-2 Formulations and plating conditions of three electroless Ni-W-P baths (wt. %).	90
Table 4-3 Formulations and plating conditions of the electroless Ni-P bath (wt.%).	91
Table 4-4 Formulations and plating conditions of the electroplate Ni-W bath.....	93
Table 4-5 Chemical composition of as-plated Ni-W-P coatings (wt.%).	94
Table 4-6 Crystallisation temperatures of the Ni-based metallisation obtained in DSC results.....	96
Table 4-7 The surface roughness of the Ni-15W-10P coatings after thermal treatments.	102
Table 5-1 The physical properties of main chemicals in the flux.	111
Table 5-2 The formulations and plating conditions of the electroless Ni-W-P plating.	114
Table 5-3 Dimensions of the nozzle.....	118
Table 5-4 The process parameters for GDSCS pre-tests.....	119

Table 5-5 The composition of spectrums indicated in figure 5-23 (at.%).....	130
Table 5-6 The composition of spectrums indicated in figure 5-24 (at.%).....	131
Table 5-7 The characteristics of these joining approaches.....	133
Table 6-1 Major parameters of nanoindentation.	143
Table 6-2 Comparisons of the formation and growth of IMCs at Ni-W-P/Zn-Al and Cu/Zn-Al interconnects during liquid-solid reactions.	151
Table 6-3 Elastic moduli and hardness of phases in Zn-Al solder interconnects.....	156
Table 7-1 Composition of the electroless Ni-W-P plating bath.	164
Table 7-2 Composition of as-deposited Ni-W-P coatings through EDX analysis.	167
Table 7-3 Compositions of the spectrums at the Ni-W-P/Au-Ge interface (at.%).....	171
Table 7-4 Composition of the spectrums on the fracture surface at substrate part (at.%).	174
Table 7-5 Composition of the spectrums on the fracture surface at die side (at.%).....	175
Table 7-6 Compositions of as-deposited Ni-W-P coatings through EDX analysis.	176

Glossary of Symbols

2D	Two-Dimension
3D	Three-Dimension
AFM	Atomic Force Microscope
at. %	Atomic Percentage
BGA	Ball Grid Array
BSE	Back-Scattered Electron
CALPHAD	Calculation of Phase Diagram
CSP	Chip-scale Package
CTE	Coefficient of Thermal Expansion
DBC	Direct Bond Copper
DMAB	Dimethylamine Borane
DSC	Differential Scanning Calorimetry
EDX	Energy Dispersive X-Ray Spectroscopy
ELV	End of Life Vehicle
ENIG	Electroless Nickel Immersion Gold

FIB	Focused Ion Beam
GDCS	Gas Dynamic Cold Spray
HRTEM	High Resolution Transmission Electron Microscope
HTE	High Temperature Electronics
HTOM	High Temperature Optical Microscopy
IC	Integrated Circuit
IEC	International Electrotechnical Commission
IPC	Interconnecting and Packaging Electronic Circuits
IMC	Intermetallic Compound
JEITA	Japan Electronics and Information Technology Industries Association
MCM	Multi-chip Module
PCB	Printed Circuit Board
PVD	Physical Vapour Deposition
RoHS	Restriction of Hazardous Substance
RT	Room Temperature
SADP	Selected Area Diffraction Pattern

SAM	Scanning Acoustic Microscope
SEM	Scanning Electron Microscope
SLID	Solid-Liquid Interface Diffusion
SLS	Sodium Lauryl Sulphate
TEM	Transmission Electron Microscopy
TGA	Thermal Gravimetric Analyser
TLP	Transient Liquid Phase
XRD	X-Ray Diffraction
UBM	Under Bump Metallisation
WEEE	Waste Electrical and Electronic Equipment
wt. %	Weight Percentage

Chapter 1

Introduction

This chapter firstly introduces the background of this PhD project and then identifies the general issues related to high temperature power electronic applications. Based on these challenges, the research aim and objectives are defined, followed by the main contributions and an overview structure of this thesis.

1.1 Background and motivations

The demand for high temperature power electronics that are capable of operating under high power density and high temperature continues to grow, particularly in the applications of aerospace, automotive and drilling devices. However, due to the harsh operation environments, such as elevated temperature, impact and vibration, the interconnection integrity of power modules is a major concern in high temperature packaging technology [1.1-3].

Figure 1-1 schematically illustrates the cross-section structure of a typical power module. In this power module, a high temperature solder is in direct contact with the metallisation on the chip (normally consists of several thin layers of refractory metal in nano-scale) and the metallisation (e.g. copper) on ceramic substrate. This is known as a die attachment. During reflow process, intermetallic compounds (IMCs) can be produced through the reactions between solder and the metallisation to form a solder joint. It can provide not only electrical and mechanical interconnections between the chip and substrate, but also heat dissipation paths within the package. Consequently, the die attachment (highlighted with the dash box in figure 1-1 a)) is the key element in the assembly of such power devices.

Although the formation of IMCs can establish a good metallurgical bond between high temperature solder and substrate, excessive growth of IMCs would deteriorate the

interfacial integrity, due to the differences of physical properties (e.g. elastic modulus and coefficient of thermal expansion) of solders involved (Figure 1-1 b)) [1.4, 1.5]. This is particularly true in high temperature power electronics, because the devices normally operate at elevated temperature that can significantly accelerate the growth of IMCs. Hence, in high temperature power electronics, suppressing the growth of the interfacial IMCs in die attachments is essential to the reliability of the entire module, which normally requires a reliable diffusion barrier to retard the interfacial reaction rate.

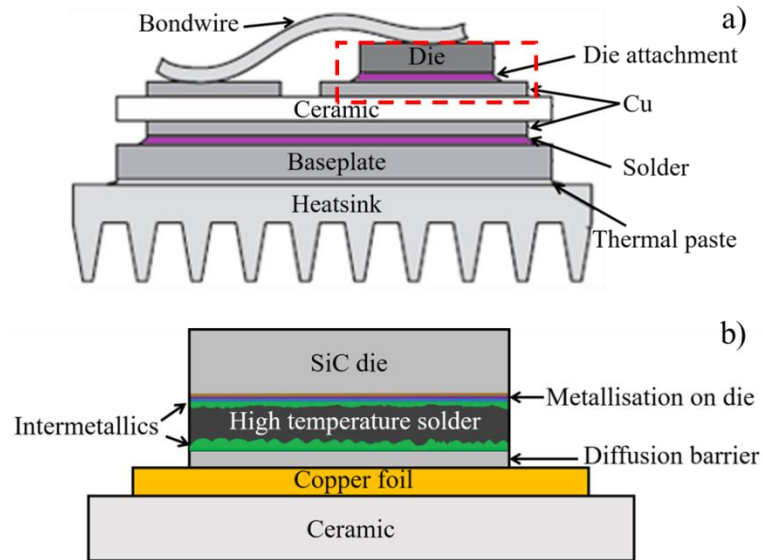


Figure 1-1 Schematic illustration showing the cross section of: a) a power module (with the associated heatsink); b) a die attachment (the size portion is not according to the actual product).

In past decades, the Ni-P coating produced by electroless plating has been widely used as a diffusion barrier to inhibit the Cu-Sn interaction in commercial electronics (reflow temperature: 240 °C approximately) for their low cost, low residual intrinsic stress and excellent uniformity. However, the reactions between solders and Ni atoms in Ni-P coatings activate the transformation of the Ni-P coatings from amorphous into crystalline layers of Ni_3P , which has fine columnar structure containing numerous grain boundaries. These columnar grain boundaries can serve as fast paths for Ni or even Cu diffusion, leading to an accelerated interfacial reaction and formation of micro-sized voids [1.6]. Especially in hybrid automotive electronics, at an operating temperature up to 300 °C, the electroless Ni-P coating can be disintegrated completely due to Cu diffusion and complete transformation into IMCs.

Therefore, in the applications of high temperature packaging, an alternative diffusion barrier is required to retard the interfacial reactions and to prevent the presence of the fast diffusion paths at elevated temperature (e.g. 400 °C) in a long-term usage.

Incorporation of a refractory metal element W into electroless Ni-P coatings can greatly enhance the thermal stability of Ni-P alloy, which can be acting as an effective under bump metallisation (UBM).

Though high lead alloys (solders with 85 - 97 wt.% of Pb) are widely used as die-attach solders in high temperature electronic packaging, Pb is a hazardous material thus restricted to be applied in consumer electronics products by RoHS (Restriction of Hazardous Substances in Electrical and Electronic Equipment) and WEEE (Waste Electrical and Electronic Equipment) directives. Presently, some potential lead-free alternatives have been proposed to replace high lead solders, including Zn-based, Au-based, and Bi-based solder alloys. In this thesis, electroless Ni-W-P metallisation have been deposited and employed subsequently in Zn-5Al, Au-12Ge, and Bi-Ag-based (BiAgX solder paste in Indium Corporation) solder joints [1.7] to characterise their performance and effectiveness as a diffusion barrier. In particular, for hybrid automotive applications, Zn-Al solders exhibit enormous advantages including low cost, excellent mechanical properties, good thermal and electrical properties, attracting growing interests in industry field.

1.2 Research aim and objectives

In this thesis, electroless Ni-W-P coatings, as an effective UBM capable to serving under high temperature (up to 450 °C), are developed, characterised and subsequently applied onto the high temperature lead-free solder interconnects. To achieve this aim, the following detailed objectives are identified:

1. Establish and optimise plating bath chemistry, chemical formulas and process procedures to allow precise control of composition and microstructure of electroless Ni-W-P coatings. As such, the Ni-W-P coatings with required compositions can be prepared by electroless plating for further investigations.
2. Investigate the phase transformation between amorphous and crystalline structure of the deposited Ni-W-P ternary alloys to detect the crystallisation temperature and to elaborate the crystallisation mechanism of the coatings.

3. Characterise the microstructure and crystallisation behaviours of the Ni-W-P coatings as a diffusion barrier in the interfacial reactions with Zn-Al, Au-Ge and BiAgX high temperature lead-free solders.
4. Develop joining/interconnect processes for formation of reliable Zn-Al solder joints by improving the wettability of Zn-5Al solders onto metallic substrates.
5. Examine the mechanical integrity and interfacial IMCs characteristics of the high temperature solders joints with Ni-W-P coatings.
6. Elaborate the interfacial reactions and microstructure between electroless Ni-W-P coatings and Zn-Al, Au-Ge and BiAgX solders during soldering process.

1.3 Contributions to the body of knowledge

This thesis focuses on the depositions and applications of electroless Ni-W-P coatings in high temperature lead-free solder interconnects. It contributes to the current body of knowledge on the following aspects:

1. An electroless Ni-W-P plating process has been developed and optimised through a stable plating bath under a high plating temperature and pH value (95 °C, 9.5); critical plating parameters of the Ni-W-P deposition process have been systematically investigated as to their effects on microstructure, composition and deposition rate of Ni-W-P coatings.
2. The crystallisation transformation characteristics of Ni-W-P coatings due to annealing at elevated temperature (up to 750 °C) and reacting with lead-free high temperature solders (Zn-5Al, Au-12Ge, and BiAgX alloys) have been examined, leading to a comprehensive understanding of crystallisation mechanisms and thermal characteristics of Ni-W-P UBM.
3. A self-prepared flux has been used in the trail to enhance the wettability of Zn-Al solders for reflow process to successfully form Zn-Al solder interconnects. In addition, novel interconnection processes without flux have been developed in the preparations of Zn-Al solder interconnects at a relative low temperature (below 250 °C).

4. The growth, evolutions and mechanical properties (elastic moduli and hardness) of interfacial IMCs formed at Cu/Zn-5Al and Ni-W-P/Zn-5Al interfaces after varying liquid-solid reaction durations have been characterised, assisting a fundamental understanding of the reaction mechanisms of Zn-Al solder interconnects during reflowing.
5. The interfacial reaction, mechanical strength and fracture characteristics of SiC/Au-Ge/Ni-W-P and SiC/BiAgX/Ni-W-P solder joints with a “sandwich” structure have been investigated, evaluated and compared.

1.4 Structure of the thesis

To properly address the objectives set out in Section 1.2, this thesis is divided into eight chapters and organised in five cohesive sections (Figure 1-2): 1) introduction (Chapter 1), 2) literature review (Chapter 2), 3) preparation and analysis of electroless Ni-W-P UBM (Chapter 3 and 4), 4) interfacial reaction between Ni-W-P metallisation with high temperature lead-free solders (Zn-Al, Au-Ge, and BiAgX) (Chapter 5, 6, and 7), and 5) conclusions (Chapter 8).

Chapter 1 provides an overview of the research background and motivations identified to understand the research problems and existing knowledge gaps. The aim and objectives of this thesis are also described in this chapter.

Chapter 2 summarises the relevant researches in aspects of high temperature electronics packaging, high temperature solder, under bump metallisation, joining process, interfacial reactions between Ni-based UBM and high temperature lead-free solders, and mechanical properties of high temperature solder joints. The research gaps pertaining to this thesis are given in this chapter.

Chapter 3 and 4 focus on the plating process and thermal stability of electroless Ni-W-P coatings. In Chapter 3, the procedures of electroless Ni-W-P plating were developed and the effects of varying plating parameters on characteristics of Ni-W-P coatings were investigated. Chapter 4 aims at elaborating the crystallisation mechanisms and thermal stabilities of various electroless Ni-W-P coatings. In addition, the effects of W contents on crystallisation characteristics of ternary Ni-W-P coatings were examined in order to further improve their diffusion barrier properties.

Chapter 5 describes the formation and characterisation of Zn-Al solder interconnects through the joining processes including soldering process, gas dynamic cold spray, and self-propagation methods to overcome the issues of wettability and oxidation of Zn-Al high temperature solders. The advantages and disadvantages of these methods can then be summarised in this chapter.

Chapter 6 investigates the diffusion barrier ability of electroless Ni-W-P UBM with molten Zn-5Al solder under harsh conditions. The reaction mechanisms and mechanical characteristics of interfacial IMCs at Cu/Zn-Al and Ni-W-P/Zn-Al interfaces under liquid-solid reactions are proposed in this chapter.

After achieving a comprehensive understanding of electroless Ni-W-P coatings, Chapter 7 presents the interfacial reactions between Ni-W-P UBM with Au-Ge and BiAgX high temperature solders. The shear strength and failure modes of these solder joints in a sandwich structure are evaluated in connection with their interfacial IMCs.

Finally, Chapter 8 summarises the major contributions of this entire thesis based on the current work and main results. Suggestions for future work are thus provided.

The overall thesis structure is summarised in figure 1-2.

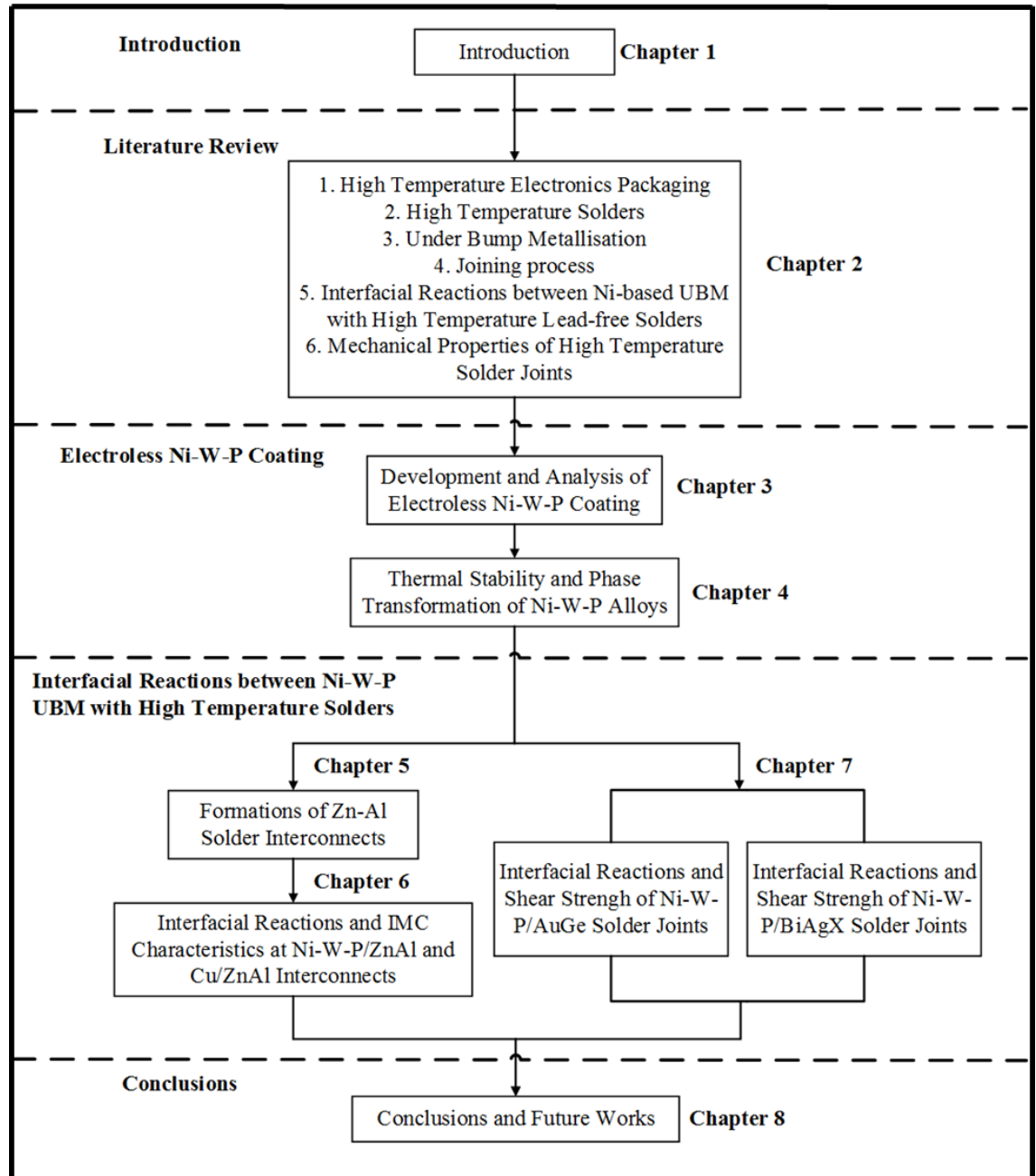


Figure 1-2 Schematic diagram of the thesis structure.

References

- [1.1] S.W. Yoon, M.D. Glover, H.A. Mantooth, and K. Shiozaki, "Reliable and repeatable bonding technology for high temperature automotive power modules for electrified vehicles", *Journal of Micromechanics and Microengineering*, vol. 23, pp. 015017, 2013.
- [1.2] R. Khazaka, L. Mendizabal, D. Henry, and R. Hanna, "Survey of High-Temperature Reliability of Power Electronics Packaging Components", *IEEE Transactions on Power Electronics*, vol. 30, No. 5, pp. 2456-2464, 2015.

- [1.3] C. Buttay, D. Planson, B. Allard, D. Bergogne, P. Bevilacqua, and etc., “State of the art of high temperature power electronics”, *Materials Science and Engineering: B*, vol. 176, No. 4, pp. 283-288, 2011.
- [1.4] H.B. Qin, W.Y. Li, W.B. Zhou, and X.P. Zhang, “Low cycle fatigue performance of ball grid array structure Cu/Sn-3.0Ag-0.5Cu/Cu solder joints”, *Microelectronics Reliability*, vol. 54, No. 12, pp. 2911-2921, 2014.
- [1.5] Q.K. Zhang, H.F. Zou, and Z.F. Zhang, “Tensile and Fatigue Behaviors of Aged Cu/Sn-4Ag Solder Joints”, *Journal of Electronic Materials*, vol. 38, No. 6, pp. 852-859, 2009.
- [1.6] C.K. Chung, Y.J. Chen, T.L. Yang, and C.R. Kao, “Reactions of Sn-4.0Ag-0.5Cu on Cu and Electroless Ni Substrate in Premelting Soldering Process”, *Journal of Electronic Materials*, vol. 42, No. 6, pp. 1254-1259, 2013.
- [1.7] H.W. Zhang and N.C. Lee, “High reliability high melting mixed lead-free solder paste system”, in *Proceedings of 35th IEEE/CPMT International Electronic Manufacturing Technology Symposium (IEMT)*, pp. 1-7, 2012.

Chapter 2

Literature Review

This chapter contains the review of previous researches and their related challenges in the field of high temperature electronic packaging, high temperature solders, under bump metallisation, joining processes, interfacial reactions and mechanical properties of typical high temperature lead-free solders joints.

2.1 High temperature electronics packaging

2.1.1 High temperature electronics

Over the past several years, there has been a growing demand for hybrid automotive electronics that can operate reliably at elevated temperature (above 300 °C) [2.1]. Therefore, the conventional Si-based components (operation temperature: 125 °C [2.2]) have been replaced with wide-bandgap semiconductor materials, such as GaAs, SiC and GaN. SiC semiconductors show excellent reliability operated under high power voltage and high operation temperature (above 500 °C) [2.3]. However, the present high temperature electronic packaging processes including materials and integration technologies still have many challenges with the increasing operation temperature.

2.1.2 High temperature electronics packaging

High temperature electronic (HTE) packaging plays a critical role in the performance of electronic assemblies. The main functions of HTE packaging include: 1) providing protection to SiC chips; 2) establishing mechanical and electrical interconnections between SiC chips and substrates; 3) dissipating the heat generated from chip; 4) protecting electronic devices from voltage, vibration, and impact of application environment.

In electronic devices, electronic packaging is normally categorised into three levels as presented in figure 2-1. In first-level packaging, SiC chips are fabricated from wafer, and then connected to the metallisation or the leadframe on ceramic substrates through die bonding or wire bonding, respectively. The interconnections between the ceramic components and baseplate with heatsink are formed in second-level packaging. For instance, manufacturing a power module, which is second-level packaging and the core part in HTE packaging, is normally via reflowing or sintering. Finally, the power modules are assembled onto motherboards to complete the packaging process. The interconnection units and methods for each packaging level are listed in table 2-1.

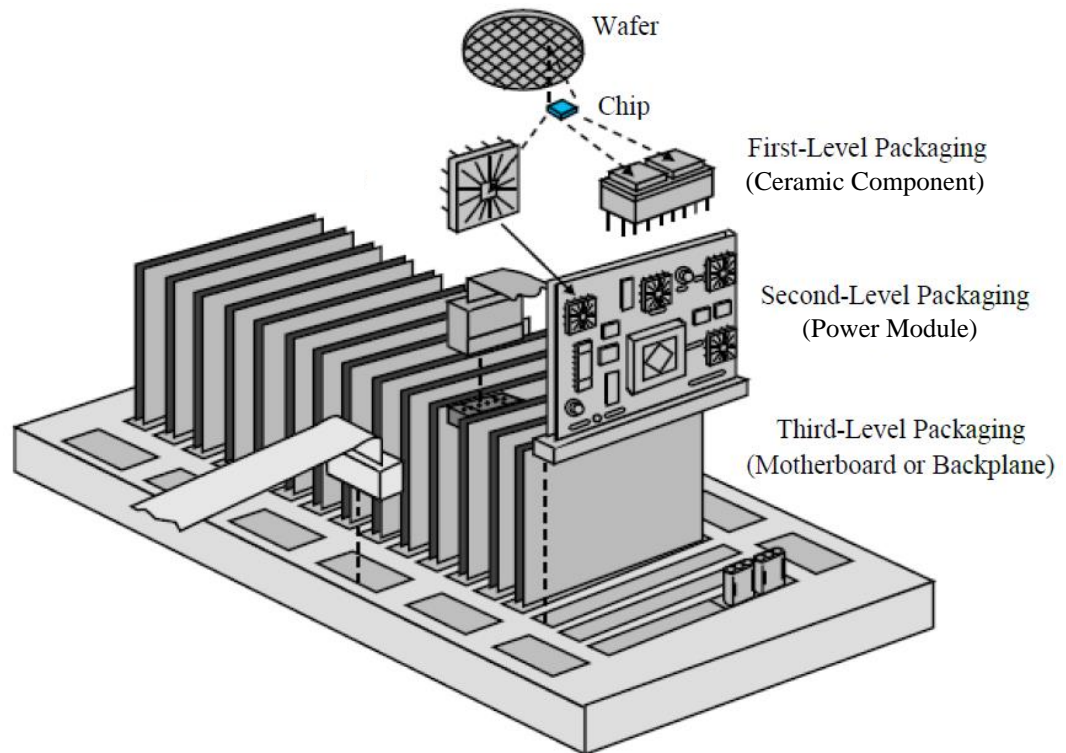


Figure 2-1 Electronic packaging hierarchy with first-, second-, third-level packages [2.4].

Table 2-1 A summary of typical packaging hierarchy for electronics assemblies [2.5].

Packaging level	Interconnection Units	Interconnection approaches
First-level	IC fabrications	Wire bonding
	Ceramic components	Die bonding
Second-level	Power modules	Soldering
		Sintering
Third-level	Motherboard	Cure

The cross section of a typical power electronic module beneath the encapsulate cover is schematically shown in figure 2-2. The main components and corresponding functions in this electronic packaging are:

1. **Wide-bandgap semiconductor chips**. They provide an electrical switching function.
2. **Die attachment**. It provides mechanical and electrical connection within the device and thermal dissipation path.
3. **Wire-bonds**. They mainly provide electrical contact between the chip and substrate.
4. **Baseplate**. It provides mechanical support for power module and heat transferring to the external heatsink for heat dissipation.

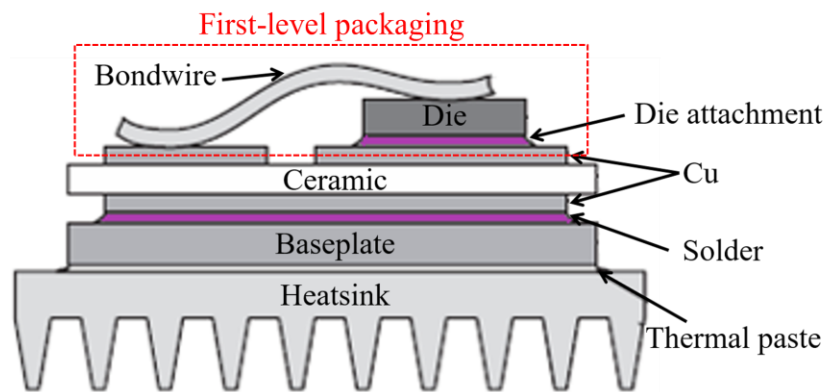


Figure 2-2 A schematic diagram revealing the cross section of a typical power modules.

2.1.3 First-level packaging

The first-level packaging (highlighted in figure 2-2) is the most critical part in high temperature power electronic package since it provides not only the electrical and mechanical interconnections, but also the thermal dissipation paths.

Wire bonding has been widely used in first-level interconnection over six decades with fine metal wires (Au, Cu, Al or Ag [2.6-8]) to provide electrical interconnection between integrated circuit (IC) chip and associate substrate. The intensity and numbers of wire bonds in high temperature power electrical device have been continuous growing due to a significant increase of electrical power conversion for several years [2.9]. Subjected to thermal cycles resulting from power conversion, wire bonds are prone to crack or lift-out due to the mechanical stress [2.10]. Moreover, wire bonds may contact with each other under vibration, causing short circuit and failure issues

[2.11]. Recently, a new package technology has been proposed to eliminate wire bonds by incorporation of die attachments from both sides of IC chips [2.12].

Die attachment is one of the most critical parts in high temperature power electronic packaging. To assure the reliability of connections, the die attachment must meet many requirements, such as good adhesion properties with IC chips and substrates, reasonable cost, suitable melting temperature range (at least above 300 °C), good thermal and electrical conductivity, compliant coefficient of thermal expansion (CTE), good ductility, low toxicity and simple soldering process. The mostly used die attach materials fall into following four categories:

1. **Ag-filled organic die-attach materials**. It can be used at a temperature range of -60 - 225 °C, which is not suitable for current HTE due to their low glass transition temperature (below 300 °C [2.13]) and thermal conductivity.
2. **High temperature solders**. It is the most common die-attach materials in HTE. It is required that the melting temperature of these solders are at least 125% of operate temperature (in K unit) to decrease the degradation possibility due to creep effects [2.14, 2.15].
3. **Mixture materials for transient liquid phase bonding**. They are generally consisted of two alloys with low melting temperature (In, Sn) and high melting temperature (Au, Ag, Cu, Ni). As a result, die attachments were produced in a form of IMCs at a low temperature (above the melting temperature of In or Sn) and can withstand harsh conditions for the high melting temperature of IMCs. However, the brittle nature and varying mechanical properties of IMCs may induce cracks and deteriorate the reliability of die attachments [2.16].
4. **Nanosilver pastes**. They were produced by mixing Ag powders, dispersant, binder, and thinner for screen printing on ceramic substrates, followed with sintering at around 250 °C [2.17]. The re-melting temperature of this die attachment is 961 °C. Moreover, nanosilver paste has an excellent thermal conductivity (200-300 W(mK)⁻¹ [2.18-20]) and electrical conductivity (2.5-10 μΩ·cm [2.18, 2.21, 2.22]). The major drawbacks of conventional nanosilver pastes are the high pressure in sintering and high porosity after joining. Currently, Wang *et al.* reported that a

rapid pressure-less sintering process was achieved at a low temperature of 150 and 200 °C by thinning the organic shells with high shear strength [2.23].

This thesis focuses on high temperature solders for their advantages. Figure 2-3 illustrates the cross-section view of the die attachment by solder interconnection. In this die attachment, a high temperature solder is in direct contact with the metallisation on the chip (normally consists of several thin layers of refractory metal in nano-scale) and the metallisation on ceramic substrate (Cu foil). During joining process, intermetallic compounds (IMCs) can be produced by the reactions between the solder and the metallisation on chips/substrates. As such, it can provide not only the electrical and mechanical interconnections between the chip and substrate, but also the heat dissipation paths within the package.

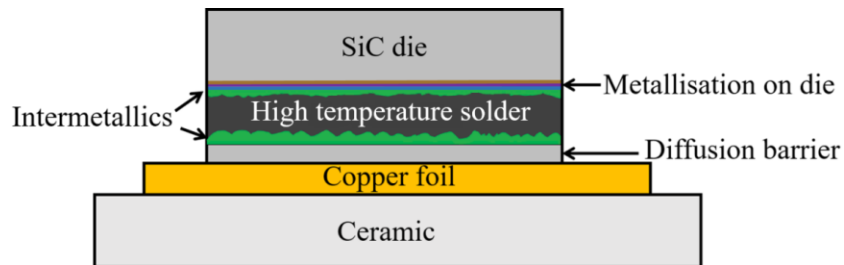


Figure 2-3 A schematic diagram revealing the cross section of a typical solder die attachment.

Although the formation of IMCs can establish a good metallurgical bond between high temperature solder and substrate, excessive growth of IMCs may deteriorate the interfacial integrity, due to their brittle nature and mismatch of physical properties (e.g. elastic moduli and coefficient of thermal expansion) with the materials involving in solder joints [2.24, 25]. This is particularly true in high temperature power electronics, because the devices normally operate at elevated temperature that can significantly facilitate the growth of IMCs. Hence, a control of the metallisation and its reactions with high temperature solder are essential to the reliability of the entire module.

2.2 High temperature solders

High temperature solders have been widely applied in advanced packaging including die attach, ball grid array (BGA), chip-scale package (CSP), and multi-chip module (MCM) [2.26]. Advanced packages with the high temperature solders were normally applied in high power modules in aircrafts, automobiles, space and drilling devices.

One of the most important roles of high temperature solders is to maintain mechanical and electrical integrity at elevated temperature. As illustrated in figure 2-2, two types of solders with different melting temperatures are usually required to bond the backside of the die to the substrate and the substrate to the baseplate afterwards in a power module. Therefore, a melting point gap between these two solders is usually necessary, at least 40 °C is desirable [2.27]. With the RoHS (Restriction of the Use of Certain Hazardous Substances) and WEEE (Waste Electrical and Electronic Equipment recycling) directive banning the use of lead, the conventional Pb-63Sn solders (melting point: 183 °C) are replaced by Sn-Ag-Cu alloy (melting point: 217 °C) for bonding baseplates, driving the melting temperature of die attachments to a higher degree (at least 260 °C).

2.2.1 High lead solders

Pb-Sn alloys with 85-95 wt.% lead are typically used in high temperature electronics for several decades on account of their proper melting point, good reliability, low cost, excellent fatigue resistance, and resistance to formation of brittle IMCs [2.28, 2.29]. The melting temperature of typical lead solders range from 288 to 314 °C [2.28]. However, lead can affect most organ systems in human health through ingestion, particularly for young children due to the damage to their central nervous systems [2.30, 2.31]. Thus, the elimination of Pb and the application of Pb-free solders are crucial especially for the applications in high temperature electronics.

2.2.2 Global legislations

Currently, two essential directives namely the WEEE and the RoHS regulations have been issued by European Union to reduce the waste of electronic equipment and to ban the use of hazardous materials [2.32, 2.33]. This drives the substitution of lead-free high temperature solders imminently. Several similar legislations were also proposed by other countries. For instance, some US non-governmental organisation provided guidance on handing specific material wastes, named as “Guidance for reporting releases and other waste management quantities of toxic chemicals: lead and lead compounds” [2.34]. Moreover, individual state (i.e. California) has set a rather strict act for electronic waste recycling. Due to the environmental destruction, the Japan Electronics and Information Technology Industries Association (JEITA) started to

implement control on releasing lead from waste disposal in the early 1990s. For the rapid growing electronic markets, a China-RoHS act has been in implementation since 2007 March [2.35]. South Korea has also issued a “Resource recycling of electrical and electronic equipment and vehicles” act for environmental issues [2.36].

However, the high lead solders were constantly exempt from these legislations since no drop-in lead-free alternatives can replace high lead solders. At present, European ELV (End of Life Vehicle) legislation will provide a future review on high-lead applications, making lead-rich solders usable until at least 2023 [2.37].

2.2.3 High temperature lead-free solder

Despite some recent efforts on high temperature lead-free solders, suitable drop-in alternatives that can take place of high-lead solders perfectly are still not proposed. The requirements for promising alternatives include:

1. Proper homologous solidus temperature (the temperature below that an alloy is completely solid) to maintain mechanical strength at high temperature;
2. Suitable IMC formation during liquid-solid reaction and solid-solid aging;
3. Excellent fatigue and creep resistance;
4. Good thermal and electrical conductivity;
5. Excellent environmental friendly and good recyclability.

Currently, the high temperature solders under investigations mainly fall into these categories: gold-rich based alloys, zinc-based alloys, bismuth-silver (Bi-Ag) alloys, and tin-antimony (Sn-Sb) alloys. This part mainly focuses on the properties (mechanical, thermal, wettability) of solders themselves, as the interfacial reactions between high temperature solders and substrates will be reviewed in Section 2.5,

2.2.3.1 Au-based solders

Gold-based solders, such as Au-Sn, Au-Ge and Au-Si, have been widely utilised in industry for their excellent mechanical properties, thermal conductivity and high reliabilities.

1. Au-Sn solder

Due to excellent mechanical and thermal properties (particularly strength and creep resistance) and fluxless bonding process, Au-Sn solder is one of the most popular in high temperature solders. However, the disadvantages of eutectic Au-Sn solder include high costs, protective bonding environment (vacuum or inert atmosphere) and complex Au-Sn IMCs.

Gnecco [2.38] investigated the wetting behaviour and the characterisation of the interfaces between liquid Au-Sn based alloys and Cu substrates, while Amore [2.39] studied the wetting behaviour of Au-Sn alloy by measuring its contact angle on Cu and Ni substrates as a function of time and temperature (between 309 °C and 427 °C). Chidambaram explored the effects of Ag and Cu addition in Au-Sn binary system on microstructure and micro-hardness after long-term aging at 150 °C and 200 °C, respectively [2.40]. Based on their work, Au-0.35Sn-0.03Ag and Au-0.33Sn-0.04Cu alloy are promising candidates for applications close to 200 °C.

Recently, enormous studies have been conducted on the transient liquid phase (TLP) bonding in Au-Sn alloy systems. Researchers in Vestfold University College (Norway) conducted systematic investigations on TLP bonding of Au-Sn system and proposed an updated Au-Sn phase diagram [2.41].

2. Au-Ge solder

Au-Ge eutectic alloy shows high melting temperature (280-400 °C), excellent thermal and electrical conductivity, good corrosion resistance [2.42-44]. Moreover, the reaction rate of Ge with common metallic substrates is rather slow. The major disadvantage of Au-Ge solder is high cost for wide-area die attachments. Low-cost metal elements can substitute Au in Au-Ge solders to solve this issue.

To replace expensive gold element in Au-Ge solder by possible low-cost alloying (Sb, Sn, Si), enormous experiments and the CALPHAD (Calculation of Phase Diagrams) approach were utilised. The essential idea of CALPHAD approach is to describe the Gibbs energies of each phase in a given system, which combines a multicomponent system to predict the phase equilibrium [2.45, 2.46]. The Au-Ge, Cu-Ge, Ge-Sb, Ge-Ni binary systems and the Au-Ge-Sb, Au-Ge-Si, Au-Ge-Sn ternary systems were all thermodynamically assessed by CALPHAD method [2.47]. Chidambaram predicted that Sb alloying to the Au-Ge eutectic solder not only decreased melting point but also

enhance ductility substantially [2.48]. However, Sb is toxic according to RoHS directive. Moreover, Au-Ge-Sb alloys were found much easier to be corroded than Au-Sn alloys due to the larger electromotive force between Au and Ge phases [2.49].

3. Au-Si solder

Although Au-Si eutectic alloy has a proper melting point of 362 °C, it is still not regarded as a potential substitution as the Au-Ge or Au-Sn alloy due to its low wetting ability. To improve its wettability, Naidich reported that the addition of Si to Au can decrease the interfacial tension and the contact angle of the Au-Si alloy on SiC monocrystal surfaces at 1500 °C [2.50].

2.2.3.2 Zn-based solders

Since pure Zn shows the advantages of low cost, excellent thermal and electrical conductivity, Zn-based alloys are regarded as potential high temperature solders. Zn-rich solders fall into two types: Zn-Al based solders and Zn-Sn solders.

1. Zn-Al solder

Zn-5Al eutectic solder with a melting point of 382 °C is a very promising substitution of high temperature applications for its low cost and good thermo-mechanical properties. However, the poor wettability, hard nature and high oxidation behaviours hinder its wide applications.

Zn-Al solders exhibited poor wettability on Al and Cu pads even with some fluxes under protective environment, especially on Cu substrates. Pstrus *et al.* reported that increasing reflow temperature could enhance the wettability [2.51]. Besides, our initial works found Zn-Al solder reacted rapidly with Cu substrate to form enormous brittle IMCs, making solder joints prone to crack.

The hard nature and high oxidation of Zn-Al based solders are also main concerns in their application. Some researchers try to find a suitable metal addition in Zn-Al solders to improve their mechanical properties. The effects of minor additions such as calcium (Ca), manganese (Mn), chromium (Cr) and titanium (Ti) on the oxidation resistance, tensile properties and microstructure of Zn have been evaluated. These minor additions are active and expected to form protective layers on the surface of Zn. Mahmudi studied the shear strength and the hardness of Zn-(4-6)Al-3Cu alloys in the

temperature range of 25 - 225 °C [2.52]. The hardness and shear strength of Zn-Al-Cu alloys would increase at room temperature and conversely decrease at high temperature with the increase of Al content. Moreover, Shimizu found that Zn-4Al-3Mg-3Ga alloy would decrease its melting point and show good reliability in thermal cycling and thermal aging tests [2.53]. But Ga was reported to cause liquid metal embrittlement and lead to failure in aluminium since the cohesion between Al grains dramatically reduced [2.54]. In addition, Kang prepared a Zn-(4-6)Al-(1-5)Cu solder with a melting point range of 382 - 400 °C for ultra-high temperature applications [2.55]. This solder shows good properties, such as high solderability, excellent electrical resistivity and mechanical property.

2. Zn-Sn solder

The Zn-Sn alloy is also a eutectic system without any Zn-Sn IMCs formation. It has various advantages including low cost, good die shear strength, good thermal conductivity, excellent electrical properties and oxidation resistance in high temperature and high humidity environments. However, the Zn-Sn alloy is prone to oxidise and has a quite wide temperature range between solid and liquid state (solidus temperature: 199 °C, liquidus temperature: ~ 360 °C). When the tin content in Zn-Sn alloy was less than 30%, Lee *et al.* found that the volume fraction of Zn-Sn liquid can be less than the liquid volume limit (around 30%) at reflow temperature around 250 °C, which makes Zn-Sn alloy a potential substitution of high lead solders [2.56]. Mahmudi examined impression creep behaviours of the Zn-Sn solders (Zn-20Sn, Zn-30Sn, Zn-40Sn solders) under constant punch stress in the range from 25 MPa to 300 MPa at a temperature from 25 °C to 152 °C [2.57]. With increasing Sn contents in the alloys, the creep resistances would decrease due to the soft Sn-rich matrix with hard Zn phase.

2.2.3.3 Bi-Ag solders

The Bi-Ag eutectic system has an acceptable melting point with 262.5 °C (eutectic composition: Bi-2.5Ag), affordable cost and proper hardness, making it another interesting die attach material for high temperature power devices. The commonly used Bi-Ag alloys are Bi-(2.5-2.6)Ag and Bi-(11-12)Ag with melting points of 263 and 360 °C, respectively [2.58]. The drawback of these alloys is poor wettability. For instance, the wetting angle of Bi-2.6Ag on Cu substrate is 39 °C, which is more than twice higher than the angle of Pb-5Sn on Cu [2.59].

The rare earth (Cs in this work) element-doped Bi-Ag solders with different Ag content are investigated by Shi *et al.* [2.60]. The wettability of Bi-Ag solders on Cu substrates and the shear strength of entire joints were both improved by adding 0.1% amount of Cs without influencing its electrical conductivity and melting point. Moreover, Zhang and Lee in Indium Corporation developed a mixed powder of BiAgX system (Bi/11Ag as a majority, Bi/42Sn as a minority with the flux) [2.61]. Its wetting behaviours, voiding performance, and mechanical strength during thermal cycling are much better than Bi-11Ag alloy.

2.2.3.4 Sn-Sb solders

The Sn-10Sb solder has a melting point of 270 °C and shows a great potential to high temperature solders [2.62]. This solder alloy has a good microstructural stability and good mechanical property. However, due to the toxicity of Sb and the low melting point [2.63], Sn-Sb alloy is not a potential low-cost high temperature solder from my perspective.

2.2.3.5 Summary of high temperature solders

According to the above literature review, table 2-2 summarises the features of typical high temperature solders for die attachment. After taking considerations of environmental friendly materials, high melting point and good mechanical properties, Au-Ge, Bi-Ag and Zn-Al solder systems were selected in this work.

Table 2-2 An overview of typical high temperature solders [2.50, 2.60, 2.64, 2.65].

Solders	Composition (wt. %)	Melting temperature	Advantages	Major issues
High-lead solders	Pb-10Sn	301 °C	High melting points, high ductility and fair thermal conductivity.	Toxicity, sensitive to Sn concentration
	Pb-5Sn	314 °C		
Au-rich solders	Au-20Sn	280 °C	High melting points, good corrosion resistance and creep behaviours.	High cost, stiff solders
	Au-12Ge	356 °C		
	Au-3Si	362 °C		
Zn-based solders	Zn-6Al	381 °C	Low cost, good thermal and electrical conductivity, high mechanical strength.	Low wettability, excessive IMC growth with Cu substrates.
	Zn-4Al-3Mg-3.2Ga	347 °C		
	Zn-(20-40)Sn	365-383 °C		
Bi-Ag solders	Bi-2.5Ag	262.5 °C	Acceptable cost, proper melting point.	Low conductivity, poor workability
	Bi-10Ag	380.6 °C		
Sn-Sb solders	Sn-5Sb	245 °C	Stable microstructure, good creep properties.	Toxic, low melting temperature.

2.3 Under bump metallisation

As discussed in above sections, high temperature electronics tend to operate at elevated temperature. Consequently, the thickness of the IMCs at solder/substrate interfaces would increase significantly due to more active interfacial reactions. Normally, the IMC layer with 1-2 μm thickness is considered as an excellent metallurgical bond for providing good mechanical and electrical interconnections [2.66]. However, Cu substrates will react rapidly with lead-free high temperature solders, particularly with Zn-based solders, inducing brittle fracture of solder joints. Therefore, to retard the rapid growth of IMCs, a diffusion barrier interlayer known as under bump metallisation (UBM) is commonly used between solders and Cu substrates. The requirements of a reliable UBM are for these aspects of: 1) good adhesion solder and substrate; 2) good solderability; 3) excellent electrical conductivity; and 4) superb diffusion barrier performance [2.67].

Ni-rich alloys are reported to have much slower reaction rates with lead-free solders in comparison with Cu substrates [2.68]. Extensive investigations have been conducted on the interfacial reactions between Ni-based metallisation and Sn-based solders [2.69-71]. Various types of Ni-based metallisation were introduced according to deposition approaches, such as physical vapour deposition (PVD), electrochemical processes and electroless plating. Among these coating techniques, electroless Ni plating is a maskless approach that is capable of generating various types of coatings and viable for batch processing of wafers, simple manufacturing without electrical energy [2.72]. The above advantages have made electroless plating an excellent method for UBM deposition.

2.3.1 Various electroless Ni-based coatings

Currently, the most widely used UBM in conventional electronic applications is electroless nickel immersion gold (ENIG) as a Ni-P alloy interlayer. However, the Ni-P diffusion barrier deteriorate rapidly once it reaches its crystallisation temperature. When reacted with solders, a crystalline Ni_3P layer exhibits a fine columnar structure and provides fast diffusion paths for solder and substrate materials [2.73]. As a result, a large number of micro-voids were found in this layer during soldering and aging as shown in figure 2-4, which degrade the reliability of the solder joints [2.69, 2.71].

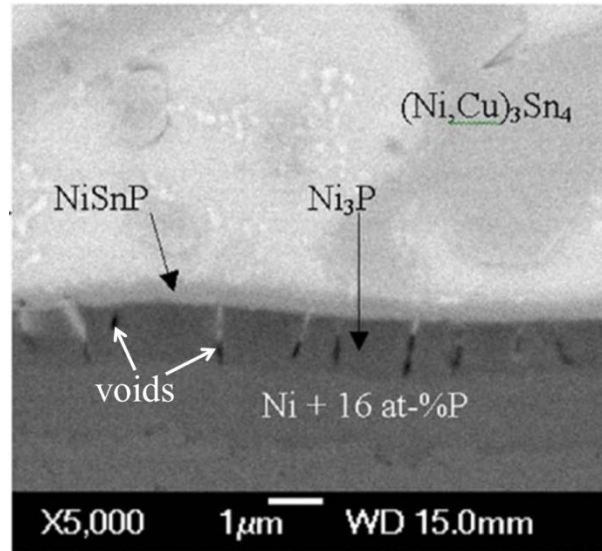


Figure 2-4 Backscattered SEM image showing voids in the Ni_3P layer at Sn-Ag-Cu/Ni(P) interface.

Therefore, to inhibit the interfacial reactions, these fast diffusion paths (Ni_3P layer) are needed to be minimised during soldering process. This demands a promising UBM material that can suppress the growth of void-embedding Ni_3P layer at elevated temperature (above 300°C) [2.74-77]. Incorporation of a third element in Ni-P compounds would be a promising way to solve these issues.

The alloy elements that can co-deposit with nickel are listed in table 2-3. Among all alloys, B, P, Fe, Co, and W elements can be deposited in a large amount by adding the corresponding salts into basic electroless Ni-P plating solution. Besides, many elements such as V, Cr, Mn, Cu, Zn, Mo, Pd, Sn, and Re can slightly co-deposit with metallic Ni. These ternary alloys have different characteristics and applications.

Table 2-3 The possible alloys that can be co-deposited with Ni in electroless plating.

IV A	V A	VI A	VII A		VIII		I B	II B	III B	IV B	V B
-	-	-	-	-	-	-	-	-	B*	C	N
-	-	-	-	-	-	-	-	-	Al	Si	P*
Ti	V•	Cr•	Mn•	Fe*	Co*	Ni	Cu•	Zn•	Ga	Ge	As
Zr	Nb	Mo•	Tc	Ru	Rh	Pd•	Ag	Cd	In	Sn•	Sb
Hf	Ta	W*	Re•	Os	Ir	Pt	Au	Hg	Tl•	Pb	Bi

Note: *This element can deposit largely with Ni; • This element can only deposit in a small amount.

Table 2-4 briefly reviews the current studies on the properties and advantages of the ternary Ni-based metallisation in comparison to binary Ni-P alloy, along with the corresponding resources for the third alloys. It shows that different ternary alloys exhibit unique influences on the performance of the entire metallisation, indicating selection of the third element generally depends on the particular application.

Table 2-4 Advantages and corresponding salts for the third alloys in ternary Ni-based metallisation.

Alloy types	Advantages compared to Ni-P alloy	Salt for third alloy
Ni-B-P	Hardness	NaBH ₄
Ni-Fe-P	Magnetic properties	FeSO ₄
Ni-Co-P	Magnetic properties	CoSO ₄
Ni-W-P	Hardness, corrosion resistance, thermal stability.	Na ₂ WO ₄
Ni-Cu-P	Corrosion protection, ductility, solderability.	NaSO ₄
Ni-Zn-P	Corrosion resistance.	ZnSO ₄
Ni-Sn-P	Corrosion resistance.	Na ₂ SnO ₃
Ni-Re-P	Thermal stability.	KReO ₄
Ni-Mo-P	Thermal stability.	Na ₂ MoO ₄

In automotive devices, the conventional Ni-P UBM is not adequate to inhibit interfacial reactions effectively since the formation of columnar structure and voids in the crystalline Ni₃P layer under elevated temperature up to 300 °C. To solve this issue, a reliable and robust ternary alloy that is capable of operating at elevated temperature (at least above 300 °C) as a diffusion barrier for high temperature solders is highly demanded.

2.3.2 Thermal stability of electroless Ni-based plating

It has been understood that the crystallisation of amorphous electroless deposit is dependent on temperature and time. At lower temperature, crystallisation can occur very slowly, but it can be much more rapid at high temperature [2.78]. Figure 2-5 reviews the crystallisation behaviours of several Ni-based alloy systems that can be

prepared with large amount of the third elements, including Ni-P, Ni-W-P, Ni-Fe-P, Ni-Co-P and Ni-B-P alloys. The incorporations of Co and B into amorphous Ni-P alloys modestly decrease the crystallisation temperature from 350 °C to 300 °C, and therefore advance the crystallisation process. In contrast, Ni-W-P and Ni-Fe-P alloys possess high crystallisation temperature above 400°C that meets the demands of high temperature electronic packaging. However, a passivating film is prone to occur on Ni-Fe-P coatings after thermal treatments, which would reduce the wettability of this ternary deposit [2.79]. Therefore, Ni-W-P alloy can be a promising candidate to high temperature UBM due to its stable structure at elevated temperature.

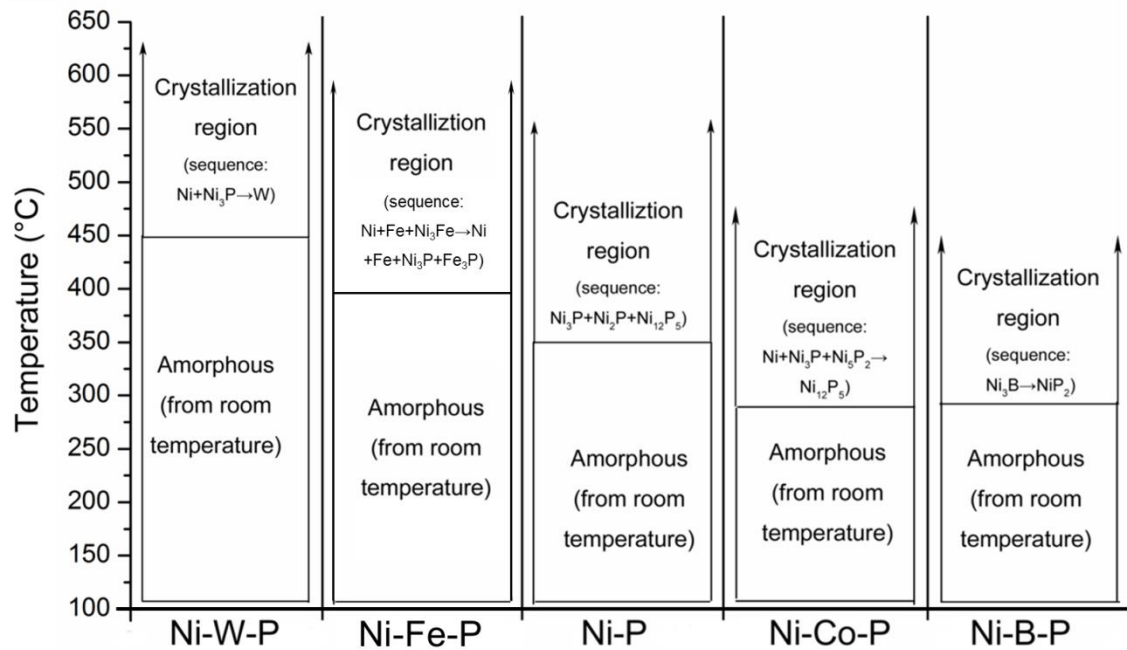


Figure 2-5 Amorphous-crystalline transition temperature in electroless Ni-based coatings.

Tien *et al.* reported that the addition of W in Ni-P compound could greatly increase the crystallisation temperature from 337 °C (Ni-8.5P) to 406 °C (Ni-10.9W-7.6P) [2.80]. This indicates the W alloy can retard the crystallisation process of Ni-W-P alloys, which agrees to various researches [2.81-83]. Moreover, the incorporation of W in the Ni-P layer also effectively improves the adhesion strength of Ni-P coating by reducing the linear crack length during scratch tests based on Tsai's work [2.84].

As listed in table 2-4, Ni-Mo-P and Ni-Re-P also show a better thermal stability than Ni-P. Cho *et al.* found that Re element can increase the crystallisation temperature of Ni-P compound for 76 °C higher [2.85]. As reported by Balaraju *et al.*, Mo alloy can also moderately improve the thermal stability of Ni-P UBM with a crystallisation

temperature of around 400 °C [2.86]. However, it is still lower than the crystallisation temperature of Ni-W-P coating.

2.3.3 Diffusion barrier properties of Ni-based metallisation

Besides thermal stability, diffusion barrier performances of these ternary alloys are also crucial. Jang and Yu have prepared various NiXP films (X = Mo, Re, Ti, Cu, W, Co, Fe, Zn, and Mn) for subsequent reactions with Sn-3.5Ag solder to examine the interfacial IMC spalling and growth behaviours [2.87].

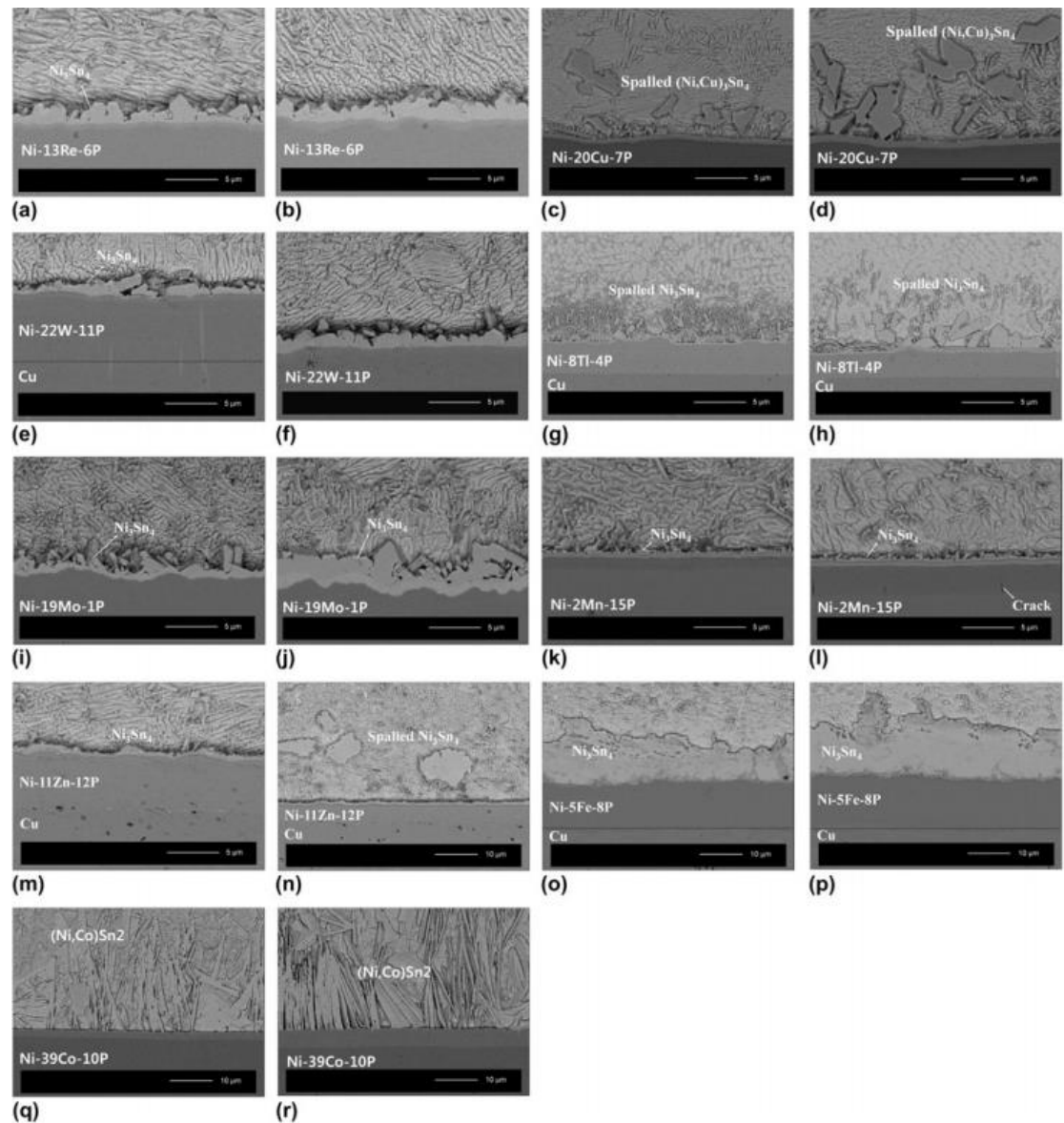


Figure 2-6 Solder joint microstructures of Sn-3.5Ag/Ni-W-P after 1 (1st, 3rd column) and 5 minutes reflow (2nd, 4th column) [2.87].

Figure 2-6 presents backscattered SEM images of the interfacial microstructure at these Sn-3.5Ag/NiXP solder interfaces after 1 and 5 minute reflowing at 260 °C. It shows that

IMC spalled from Ni-Cu-P, Ni-Tl-P, Ni-Zn-P and Ni-Co-P UBM layers after a short term soldering. This may weaken the interfacial adhesion and induce dewetting of molten solders on substrates during reflowing. Although no IMC spalling can be observed on Ni-Fe-P coated sample, the IMCs at this interface grow massively to around 10 μm and therefore cause threats to its reliability. Similarly, Ni-Mo-P also shows poor performance as a diffusion barrier, because the thickness of Ni_3Sn_4 layer grows significantly after prolonged reflowing. On the contrary, the addition of Re, Mn and W can effectively prevent the IMC spalling and suppress the growth of IMCs. It is notable that some perpendicular cracks occur along the Ni-Mn-P coating. These cracks serve as fast diffusion paths to subsequent interactions and lead to reliability deterioration. Moreover, these interior cracks would act as the initial fracture regions when subjected to external loads. According to the interfacial microstructure in different UBM systems, Ni-Re-P and Ni-W-P alloy exhibits the best performance as a diffusion barrier in Sn-rich solder at 260 $^{\circ}\text{C}$.

Considering the high price and limited storage volume of Re element, Ni-W-P is rather promising in high temperature electronics applications for not only its superb thermal stability but also excellent suppression ability in IMCs growth. The reactions between Ni-W-P and molten Sn-Bi solder and solid Sn-3.5Ag solder at 200 $^{\circ}\text{C}$ for a long-term time have been studied by Chen's and Yang's groups as shown in figure 2-7 and 2-8 [2.77, 2.78]. According to figure 2-7, a thin layer of $(\text{Ni}, \text{W})_3\text{P}$ was produced between solders and unreacted Ni-W-P coating, which was identified as amorphous structure by Jang *et al.* [2.82]. Therefore, the dense amorphous structure of the Ni-W-P that can effectively eliminate the diffusion paths or channels that normally exist in a crystalline structure such as grain boundaries, interstitials and defects [2.77].

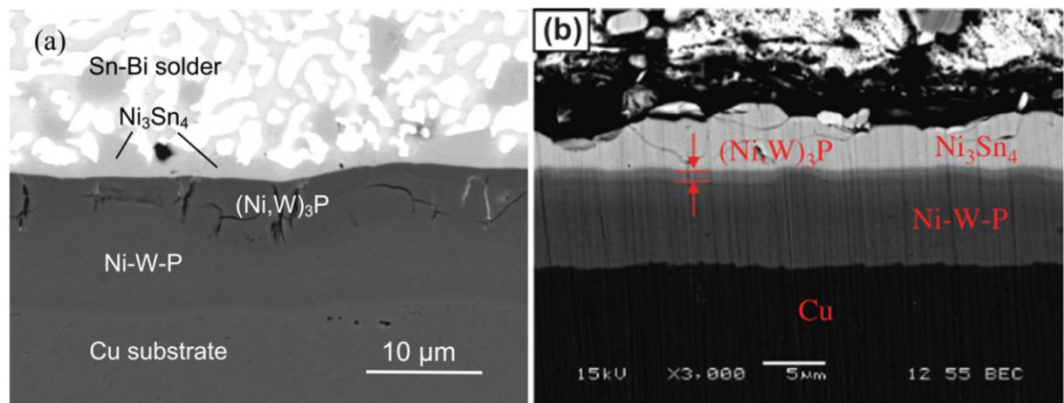


Figure 2-7 The IMCs in the a) Ni-W-P/Sn-Bi solder joint after reflowing for 28h at 200 $^{\circ}\text{C}$, and b) Ni-W-P/Sn-3.5Ag solder joints aging for 625h at 200 $^{\circ}\text{C}$ [2.77, 2.78].

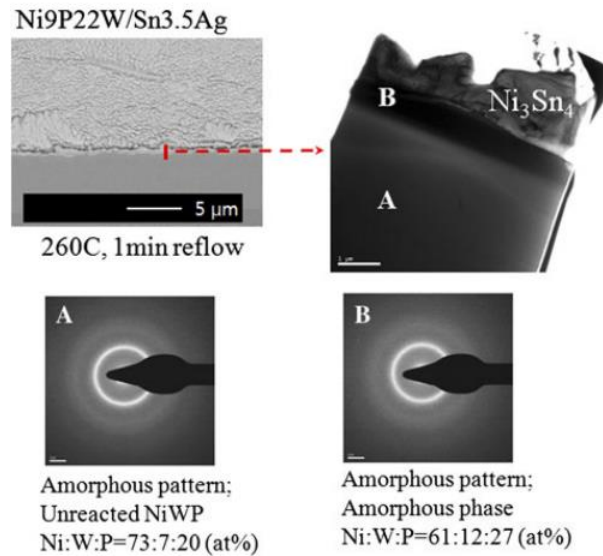


Figure 2-8 Cross-section SEM and TEM micrographs and diffraction patterns from regions A and B [2.82].

Currently, Ni-W-P coatings have not been employed in lead-free solders in high temperature electronic devices (operating above 300 °C), which are worth investigations. Moreover, it still remains unclear as to the inter-relation between coating deposition and its properties that can be achieved. Especially, how the coating composition and microstructure may ultimately govern its property as a diffusion layer; and how the deposition processes may be optimised to ensure the correct coating composition and characteristics that can meet the requirements. The mechanism of electroless Ni-W-P plating and the corresponding crucial plating parameters are reviewed as follows.

2.3.4 Electroless Ni-W-P plating

Electroless Ni-W-P plating is a chemical process for depositing Ni and W alloys from aqueous solutions onto a substrate with the energy of chemical reaction (NaH_2PO_2) rather than electric current to reduce ions into metals in the electroplate process. Pearlstein firstly prepared an electroless Ni-W-P film by adding sodium tungstate (Na_2WO_4) into the electroless nickel bath [2.88].

2.3.4.1 Pre-treatment

Prior to electroless plating, suitable pre-treatments on substrates are crucial since poor surface preparation can cause poor adhesion strength, high porosity, roughness and non-uniform thickness. In particular, for pure Cu and Al substrates that are widely used in electronic devices, they are not catalytic for spontaneous deposition and therefore

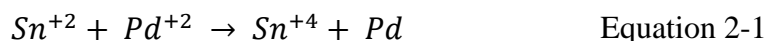
require corresponding activation treatments. According to some reported works, three approaches are possible to initiate Cu substrates catalytic as follows:

1. **Electrochemically initiating by contacting specimens with active metals (steel or Al).**

The mechanism is that the P-H bonds in the reducing agent NaH_2PO_2 only break down and then release the electron for Ni deposition on surfaces with catalytic properties. As the metal wire is attached to the Cu, the reducing agent breaks down on this wire. The released electrons flow to the Cu surface since it has a higher positive potential than this metal and are used to reduce Ni^{2+} to metallic Ni. Once the Cu surface is covered with a thin layer of Ni, the reaction can keep going without the metal wire anymore.

2. **Catalysing the surface by immersion in dilute PdCl_2 solution.**

The activation process is a two-step procedure. Step 1 was immersion in a SnCl_2/HCl solution in which stannous ions (Sn^{2+}) were adsorbed onto Cu substrates. Step 2 was immersion in a PdCl_2/HCl acid solution. When the specimens absorbed with Sn^{2+} ions were immersed in the dilute PdCl_2 solution, the Pd^{+2} ion was reduced to Pd metal and acted as a catalyst to initiate the deposition reaction according to the following reaction equation:



Flis *etc.* [2.89] reported that the activation of Cu substrate in PdCl_2/HCl solution formed separate Pd patches on these substrates. During electroless plating, the deposition rate on these Pd spots is considerably faster than that on Cu even after the deposit accumulated. This causes an unbalanced deposition reaction and further leads to the decomposition of the Ni-W-P bath.

3. **Treating the surface with a strong reducer (dimethylamine borane: DMAB).**

It is reported that the surface of Ni, Co, Cu, Pd, and *etc.* can be activated through the oxidation reaction of DMAB [2.90]. Some researchers proposed the oxidation mechanism of DMAB, the reaction pathways and the intermediates on the oxidation process of DMAB on Cu surfaces [2.91, 2.92], which was illustrated in figure 2-9. Generally, the oxidation of DMAB is produced by the substitution of H^- of the reductant by OH^- in the solvent. At the electron emitting steps, the Cu surface accepts

the electron from DMAB to form an electron transferring. Afterwards, Cu substrate can be activated.

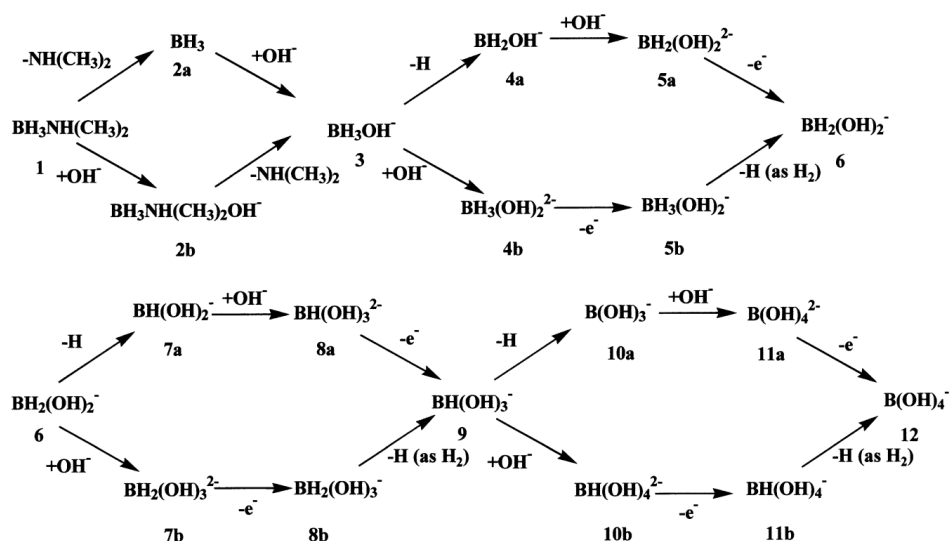


Figure 2-9 The reaction pathways for the oxidation process of DMAB via intermediates on Cu [2.91].

For Al substrate, a zincate treatment is necessary for activating substrates since Al is also not catalytic for electroless plating. Zincate treatment relies on the electrochemical reactions between zinc complexes in the solution and the Al substrate to deposit Zn particles on the Al surface at the expenses of Al dissolution [2.93]. Hutt *et al.* investigated and compared the morphologies and mechanical properties of the UBM deposited by single and double zincate process [2.94]. Double zincate treatment process can partially etch off the previous zinc layer by nitric acid and then repeat the zincate process. The experimental results from Hutt's works showed that the double zincate pre-treatment produced a thinner, denser and uniform layer, resulting in more uniform nucleation and growth of electroless Ni plating.

2.3.4.2 Electroless plating parameters

After pre-treatments, the activated samples are rinsed into electroless Ni-W-P plating bath. An electroless bath generally contains a source of metal ions, a reducing agent, a complexing agent, a buffering agent, a stabilizer, an accelerator and a brightener. Besides, pH control and reaction energy (temperature) are important to Ni-W-P deposits. Table 2-5 summarises the functions and typical materials of these plating parameters. According to reported Ni-based metallisation, these plating parameters, particularly for sources of metal ions, reducing agent, complexing agent, pH value and plating temperature, can significant affect the microstructure and composition of electroless plating [2.90, 2.95]. However, systematic investigations on these critical

parameters as to their effects on the microstructure and composition of the Ni-W-P deposits still remain to be done to obtain a comprehensive understanding of electroless Ni-W-P deposition.

Table 2-5 The functions and related materials of plating components/parameters.

Parameters	Materials	Functions
Metal ions	NiSO ₄	Source of Ni metal
	Na ₂ WO ₄	Source of W metal
Reducing agent	NaH ₂ PO ₂	Supply electrons to reduce the metal ions and also source of atomic P
Complexing agent	Na ₃ C ₆ H ₅ O ₇	Prevent excess of free metal ions concentration
Buffers	H ₃ BO ₃ +NaOH	Sustain the pH for long time
Stabilizer	Pb ²⁺ & thiourea	Stabilize the bath from decomposition by shielding catalytically active deposition
Accelerator	Amino-carboxylate	Accelerate the reducing agent and therefore increase the deposition rate
pH control	NaOH & H ₂ SO ₄	pH adjustment
Temperature	Hotplate	Energy for deposition

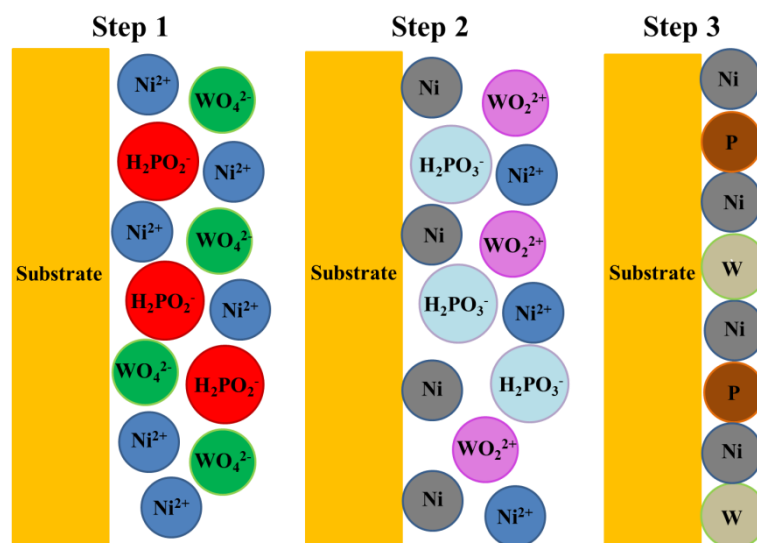
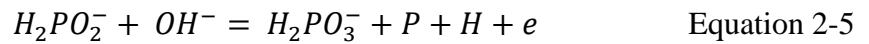
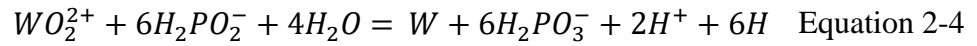
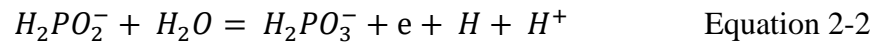
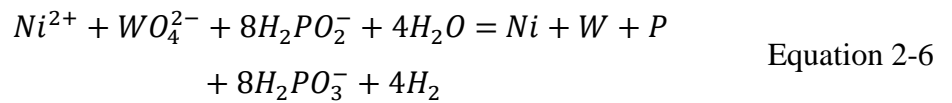


Figure 2-10 Schematic diagrams of the nickel and tungstate reduction and hypophosphite oxidation process.

After preparation of electroless Ni-W-P solution, figure 2-10 describes the process of the electroless Ni-W-P deposition. It includes three main steps: 1) the nickel source (Ni^{2+}), the tungsten source (WO_4^{2-}) and the reducing agent ($H_2PO_2^-$) are dissolved in the water solution; 2) a reduction reaction occurs on the catalytic substrate where $H_2PO_2^-$ oxidises into $H_2PO_3^-$ (Equation 2-2), providing electrons for metallic Ni on substrates (Equation 2-3). Meanwhile, WO_4^{2-} ions transform directly into WO_2^{2+} in alkaline aqueous solution [2.92]; 3) thin Ni layer serves as a catalytic layer to activate the electroless co-deposition of Ni, P and W metal during the reaction process in Equation 2-3, 2-4, and 2-5.



Therefore, the overall reaction during electroless Ni-W-P plating is shown below:



2.4 Joining process

In the past decades, various joining processes through varying tools have been proposed. Therefore, it would be rational to comprehend the nature of joining prior to discussing different joining processes. Fundamentally, a metallurgic joint would be formed when the distance between contiguous atoms decreases to a bonding distance [2.96]. The bonding distance for common metals is normally 3 Å, which is far below the thickness of oxidation layers on solid metal (3-4 nm) [2.97]. Thus, pressure and/or heating are the primary contributors to removing oxidize on substrate and solder part, making atoms from substrate and solder close enough to for a reliable bond. The commonly used joining processes are soldering, sintering and transient liquid phase (TLP) bonding.

2.4.1 Soldering

Soldering is a joining method that uses solder alloys consisting of two or more metals. The soldering process is illustrated in figure 2-11. Firstly, the solder materials in forms of foils or pastes are placed between substrates with UBMs and IC chips, followed by heating to melt the solders. The high temperature solders fully melt and wet the metallisation, leading to interfacial reactions and the formation of IMC layers. Finally, when the assembly cools down to room temperature (RT), the solder solidifies and connects the die and metallised substrate via continuous IMC layers and solder matrix. These IMC layers serve as mechanical, electrical and heat interconnections within the solder joints. Notably, the crystal structure of IMC is rather different from that of the constituents. A combination of metallic and covalent bonding leads to the formation of IMCs, which are typically brittle and hard.

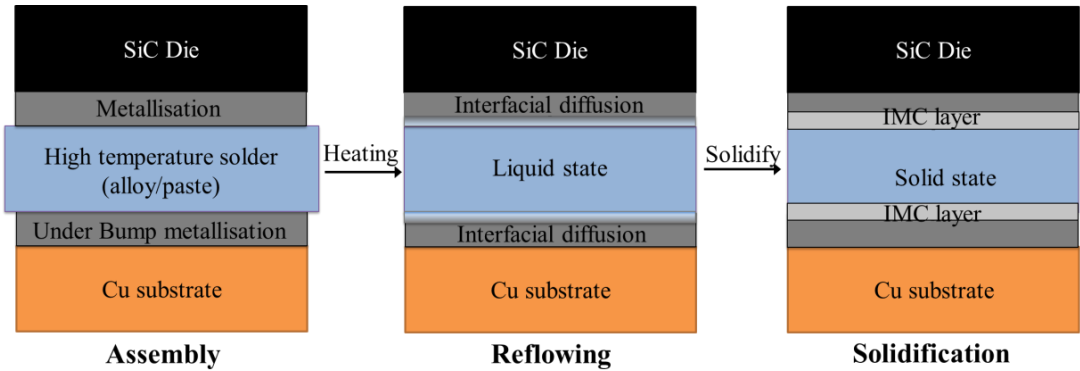


Figure 2-11 Schematic diagram of soldering process.

To form solder joints with good reliability, excellent wettability is required so that the liquid solder can spread over the metallised substrate to form IMC layers without any voids and defects. The degree of wetting is usually evaluated by the contact angles (θ) as shown in figure 2-12. When contact angles (θ) decrease to below 90° , the solder can wet the solid substrate. Moreover, the higher wettability corresponds to smaller contact angles. Young's equation (Equation 2-7) describes wetting characteristics in an equilibrium condition.

$$\cos \theta = \frac{\gamma_{sv} - \gamma_{sl}}{\gamma_{lv}} \quad \text{Equation 2-7}$$

Where θ is the contact angle, γ_{lv} , γ_{sv} , and γ_{sl} represent the liquid-vapour, solid-vapour, and solid-liquid interfacial tensions, respectively. When the wettability of solders on

metallic substrates is weak, the application of suitable flux can greatly enhance the solderability by decreasing surface tension of liquid solders.

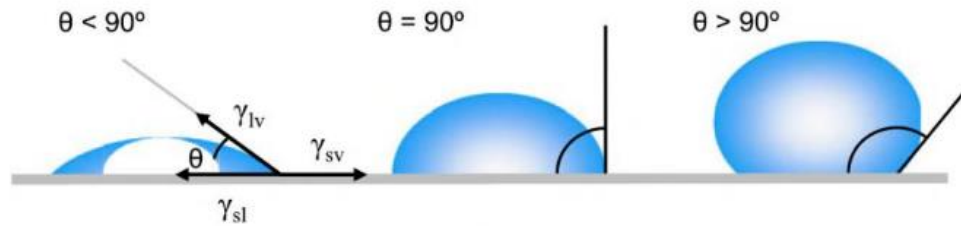


Figure 2-12 Illustration of contact angles formed by liquid drops on a smooth solid surface [2.98].

Currently, due to the toxic of Pb, conventional high lead solder needs to be replaced by lead-free high temperature solders. Though enormous efforts have been made in developing an alternative solder, no drop-in materials have been found so far.

2.4.2 Sintering

Unlike soldering in which there is a solid to liquid phase transition, sintering is a joining process for particle bonding by atomic diffusion and particle consolidation. Ag nanoparticle is normally employed in die attachments for its prominent advantage of low sintering temperature (around 250 °C [2.99]) and a high re-melting temperature (approximately 961 °C [2.100]). Moreover, Ag die attachments also exhibit high tensile strength, low fatigue failure than solders, and excellent thermal and electrical performance [2.14, 2.100, 2.101].

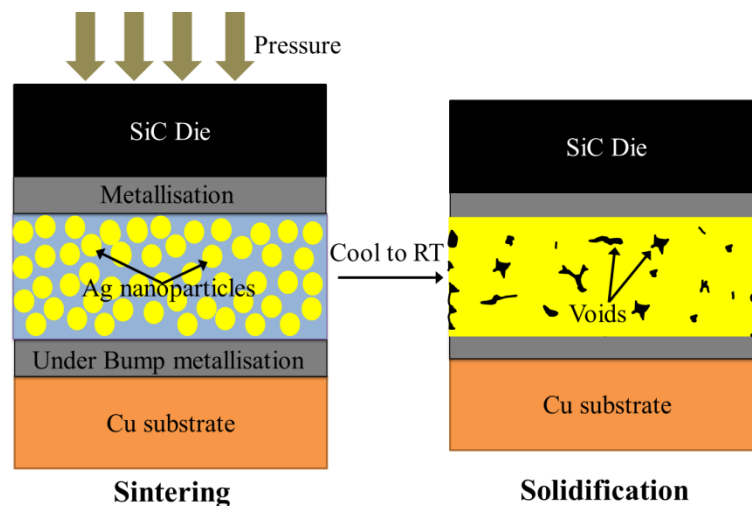


Figure 2-13 Schematic diagram of Ag sintering process.

Figure 2-13 illustrates the sintering process of Ag nanoparticles. Firstly, spherical Ag particles and a liquid binder is stencil printed on Cu substrate. The thickness of this paste layer typically ranges from 40 to 100 μm. Some metallisation are required on

both chip and substrate for Ag diffusion. During sintering, this assembly is normally heated at a peak temperature range of 200 - 300 °C for nearly 1 hour to evaporate the organic binder. During heating, a high pressure is normally applied to decreasing the joining temperature [2.100]. Joining temperature is the key factor that increases the process cost and limits the wide use of powder sintering technology. However, Wang *et al.* reported that a rapid pressure-less sintering process was achieved at a low temperature of 150 °C and 200 °C by modifying the organic shells [2.23]. After sintering, the re-melting temperature of Ag die attachment is approximately 961 °C. However, some voids can be observed within the solidified solder joints. These voids are likely to be the initial crack regions when subjected to external mechanical loads [2.15, 2.102]. Therefore, achieving a void-free die attachment with a high bonding strength through pressure-less sintering is of highly desired.

2.4.3 Transient liquid phase bonding/sintering

Transient liquid phase (TLP) bonding derives from solid-liquid interface diffusion (SLID) bonding to form high temperature phases through liquid diffusion. TLP bonding was firstly proposed and patented by Paulonis in 1972 [2.103]. TLP bonding/sintering can join materials via a thin interlayer or particles of low-melting point materials, such as tin (Sn) or indium (In) with a melting point of 231.9 °C and 156.6 °C, respectively. According to figure 2-14, the low-melting point alloy acts as a liquid phase between two solid layers or among solid particles of high-temperature materials (e.g. Au, Ag, Cu, and Ni) during joining, and then diffuses into high temperature materials to form IMCs that could stand higher temperature [2.104]. After joining, the melting temperature of the die attachment raises and the solder joint will not re-melt until reaching the melting temperature of IMC phases.

The main advantage of the TLP bonding/sintering is that the bonds can sustain under a higher operating temperature than the processing temperature [2.105]. However, several critical issues hinder the wide acceptance of TLP bonding/sintering as an alternative to conventional soldering. For TLP bonding, the drawbacks are summarised as follows: 1) the process duration could be much longer than the soldering; 2) protective atmosphere sometimes is needed to minimise the oxidation of the interlayer and the surfaces during the TLP bonding; 3) voids are prone to form at the solder joints; and 4) the IMCs at the low melting point interlayer/UBM interfaces are more brittle

than other solder alloys. However, Lee argued that there is no sufficient scientific data to support the statement “IMCs are brittle” [2.106].

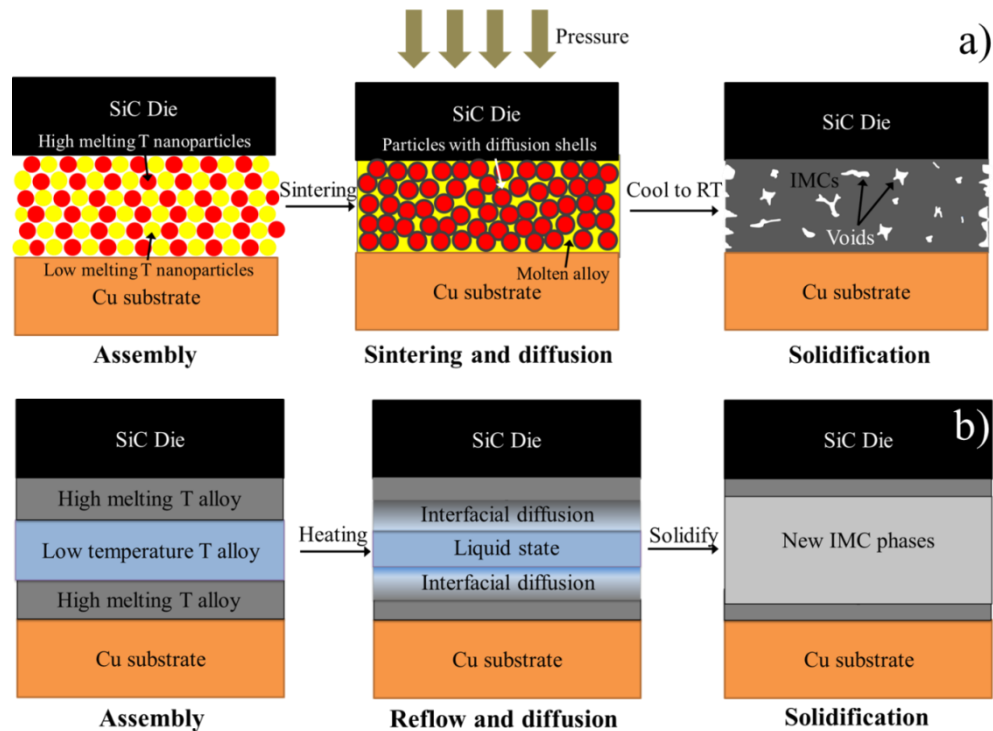


Figure 2-14 Schematic diagrams of a) transient liquid phase sintering, b) transient liquid phase soldering.

The nano-particle technology can also combine with TLP technology, namely transient liquid phase sintering (TLPS). It uses mixed powders with low and high melting temperatures by a flux. The powders with low melting point would melt firstly and afterward react with powders with high melting temperature to form IMCs that can stand high temperature. For instance, Au-Sn alloy nanoparticles (16 - 67 % Sn content) synthesized by Tabatabaei started melting from 187 °C and then formed a solder joint that can withstand a temperature up to 420 °C [2.107].

The potential application of TLP bonding in microelectronic assembly has been seen over years and there has been significant advancement in lead-free soldering and three-dimension (3-D) chip stacking [2.108]. The reported TLP bonding systems include Cu-Sn, Au-In, Ni-Sn, Au-Sn and Ag-Sn systems.

2.4.4 Other novel joining approaches

Besides the above interconnection processes, some novel joining approaches were proposed to form solder joints by electrical current, exothermic reaction film,

ultrasound vibration and impact, which could be very promising in the high temperature electronic packaging.

Liu *et al.* reported that a full Cu-In IMCs can be rapidly produced as a die attachment under a current density of $1.76 \times 10^4 \text{ A/cm}^2$ for 300ms [2.109]. Thus, the die attachments with a $\text{Cu}_4\text{In}/\text{Cu}_7\text{In}_3/\text{Cu}_4\text{In}$ structure can operate under 504 °C.

Self-propagating reaction of Al/Ni multilayer film can selectively melt the adjacent solders in solder assembly in thermally sensitive devices. This reaction can be easily initiated with a small electrical spark or laser. It has various advantages, such as, rapid heating, fast exothermic propagation, limited reaction zone and simple process [2.110]. Thin solder films of Au-20Sn and Sn-3.5Ag alloys were soundly soldered on steel, Al and Si substrates through self-propagation method [2.111-114].

Ultrasonic bonding can realise a sandwich-structured assembly by transforming entire Sn interlayer into Cu_3Sn layer embedded with some voids after 4 seconds vibration under a pressure of 0.6 MPa [2.23]. Moreover, cone bumps of high melting temperature materials (Cu and Au) were applied in 3D packaging by ultrasonic bonding in room temperature [2.115, 2.116]. In addition, ultrasonic can be employed to remove the oxidations of Zn-based solders to form Zn-Al solder joints in high temperature power electronics [2.117].

In 2D power package, solder alloys on substrates with poor wettability can be bonded through cold spray. For instance, Li *et al.* deposited Sn powers on pure Al and direct bond copper (DBC) substrates for the subsequent 3D stacking [2.118].

In future, it is very likely to present novel joining processes for high temperature power electronic applications. However, despite all apparent changes in joining processes, the joining nature remains essentially the same.

2.5 Interfacial reactions between high temperature solders and metallisation

In electronic devices, the interfacial reactions between substrates/metallisation and solders are essential to form metallurgical bonds between the solders and substrates by the IMC layers in the middle. However, it has been widely accepted that the excessive

growth of IMC layers can significantly deteriorate the reliability of solder joints, which is more likely to happen in high temperature power electronics due to the elevated temperature. Hence, a solid understanding on interfacial reactions between high temperature solders and metallisation/substrates is critical to develop the novel UBM and its application with low-cost high temperature solders such as Zn-Al, Au-Ge and Bi-Ag solders.

2.5.1 Interfacial reactions in Zn-Al-based solder joints

Takaku *et al.* investigated the interfacial reactions between Zn-4Al solder and pure Cu or Ni substrates during soldering and aging [2.75]. According to figure 2-15 and figure 2-16, Ni substrate can significantly retard the interfacial reactions and IMCs growth. However, when soldering temperature increased to 450 °C, some micro-sized dispersive Al_3Ni_2 particles scattered within the solder matrix. The reaction zone extended up to 250 μm in figure 2-16 (c) [2.119]. They also reported the IMC growth during soldering and aging process is all controlled by the volume diffusions of constituent elements. Our initial works also found that electroless Ni-P could prohibit the rapid growth of Cu-Zn IMCs, leading to higher shear strength of approximately 76.4 MPa in Ni-P/Zn-5Al solder joints. However, part of the Ni-P coating failed due to Cu-Zn IMCs in Ni-P/Zn-Al samples [2.120]

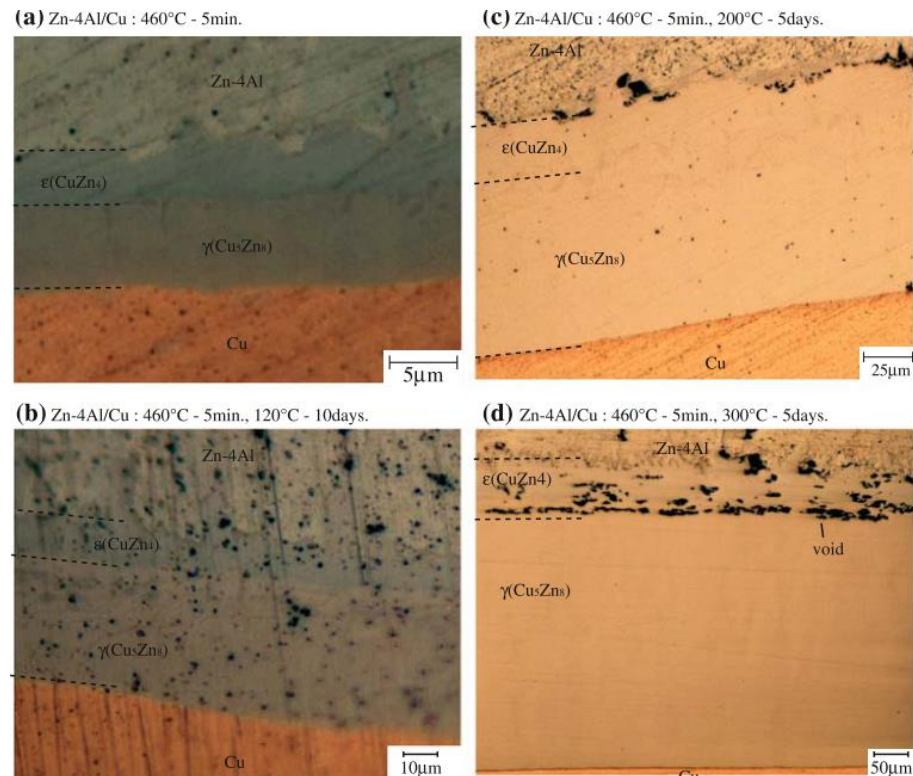


Figure 2-15 Microstructures of (a) Cu/molten Zn-4Al at 460 °C for 5 minutes, and Cu/IMCs/ Zn-4Al

aged at (b) 120 °C for 10 days, (c) 200 °C for 5 days, and (d) 300 °C for 5 days [2.75].

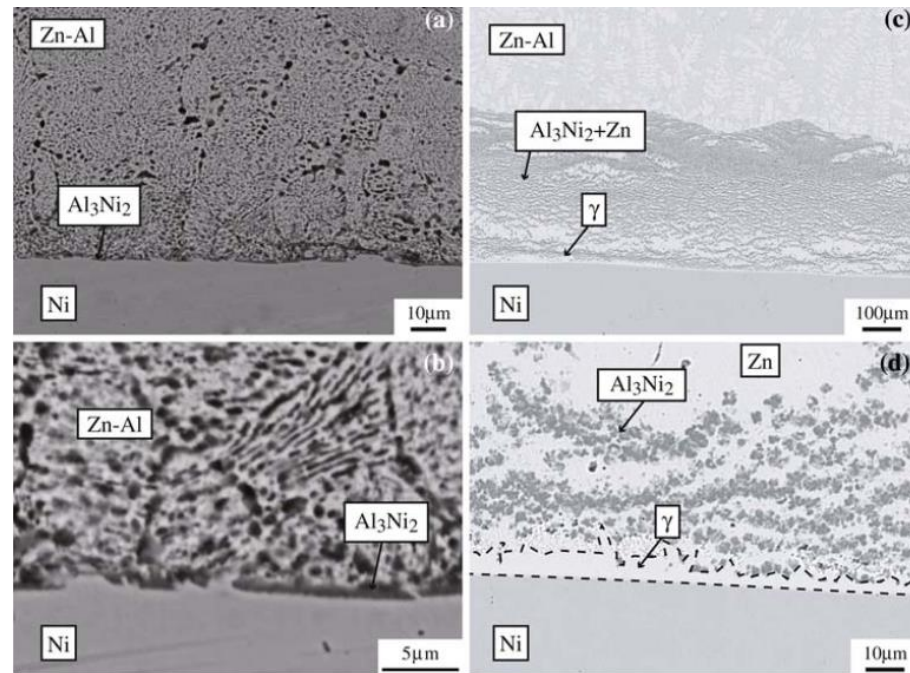


Figure 2-16 Back scattered electron (BSE) images of microstructure of (a) Ni/molten Zn-4Al soldered at 420 °C for 5 minutes; (b) enlarged image of (a); (c) Ni/molten Zn-4Al soldered at 450 °C for 5 minutes; and (d) enlarged image of (c) at the interfaces among Al_3Ni_2 , hcp-Zn, γ and Ni [2.119].

Furthermore, some researchers have studied the effects of Ag, Cu, In, Ce, Mg and Ga additions in Zn-Al solders on interfacial reactions with different metallic substrates. Pstrus reported that Cu addition retards the growth of brittle CuZn phase [2.121]. According to Gancarz's work, the addition of In leads to higher electrical resistivity and better wettability of Zn-Al-In alloys at a cost of decreasing melting temperature [2.122]. Moreover, Ce addition can improve the oxidation resistance of Zn-22Al solders and therefore increase the spreadability of molten Zn-Al-Ce solders on Cu substrates. However, some brittle Ce-bearing IMCs particles generated at the solder interfaces, weakening Zn-Al-Ce solder joints from Feng's findings [2.123]. Haque's group found that Zn-Al-Mg-Ga solder wetted well on Cu lead-frame at joining temperatures of 380 and 390 °C with an average shear strength range of 21.8 to 29.4 MPa [2.124].

2.5.2 Interfacial reactions in Au-Ge solder joints

Au-Ge solders are regarded as one of the alternatives to Pb-rich solders for their good corrosion resistance, proper melting temperature, excellent thermal and electrical conductivity. Based on Leinenbach's work, Au-Ge solder reacts rapidly with Cu substrate and produce about 30 µm thick Au-20Cu-6Ge (at.%) bulk phase as shown in

figure 2-17 [2.125]. Therefore, it is crucial to reduce the thickness of interfacial IMCs. And Ni material was found to have a small dissolution into Au-Ge solder.

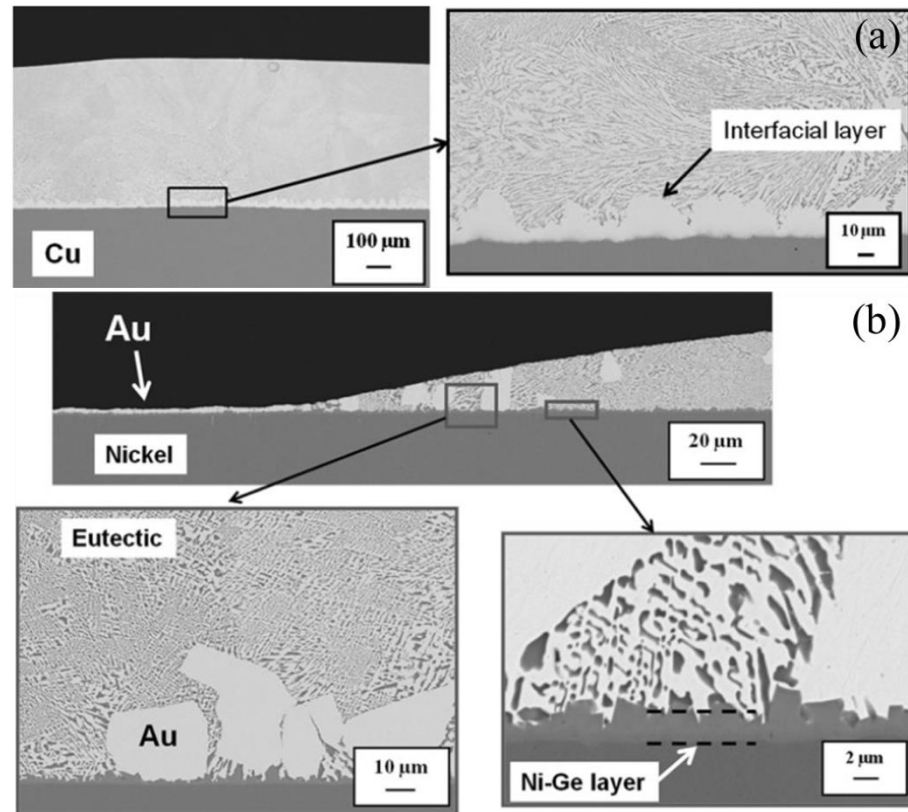


Figure 2-17 Cross-section and formation of reaction layer in the vicinity of the: (a) Cu/Au-Ge solder interface; (b) Ni/Au-Ge solder interface [2.125].

Moreover, Lin's group found that (Au, Ni, Ge)/NiGe alternating layers formed at the Au-Ge/Ni interface after reacting at 400 °C for 4 hours, as shown in figure 2-18 [2.126]. Two layers of FCC-(Au, Ge, Ni) and Ni-Ge IMCs were alternately produced around the Ni substrate. Due to the accumulation of Ge, the NiGe/Ni₂Ge interfaces are not stable and prone to ripen. This induces the fast diffusion of Au and Ge atoms from solders for nucleation and formation of new alternating layer of (Au, Ge, Ni) phase.

Chidambaram *et al.* reported that electroless Ni-P UBM was a promising diffusion barrier for suppressing the interfacial reactions even subjected to elevated atmosphere at 300 °C for 500 hours [2.127]. However, when aging temperature increased to 330 °C, the electroless Ni-P layer was totally consumed after 400 hours, leading to interdiffusion reactions between Au-Ge solder and Cu layer and the dramatic decrease in solder joint integrity from Lang's work [2.128]. The shear strength of these solder joints decreased significantly due to the rapid growth of Ni-Ge IMCs and the subsequent oxidation of the Cu layer at the interfaces. Figure 2-19 schematically

presents the microstructural evolutions of the Au-Ge/Ni-P/Cu solder joints during aging. To protect the Ni-P layer from fully consumption, a thin W film (250 nm thickness) was sputtered on Ni-P layer to improve the joint strength without damaging their electrical resistance. The additional W sputtering complicates the process and increases cost of electronic packaging.

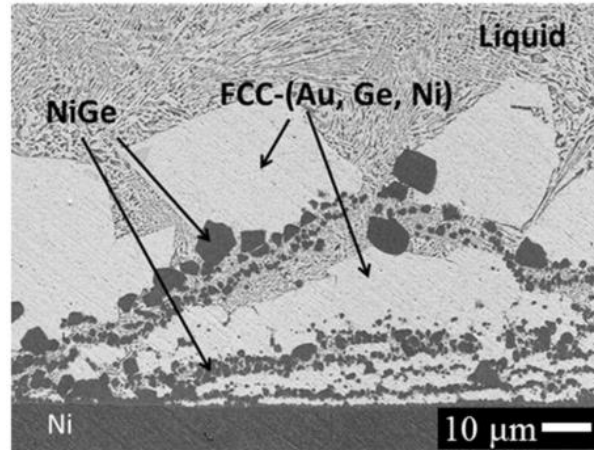


Figure 2-18 The SEM micrograph of the Au-12Ge/Ni interface reacted at 400 °C for 4 hours [2.126].

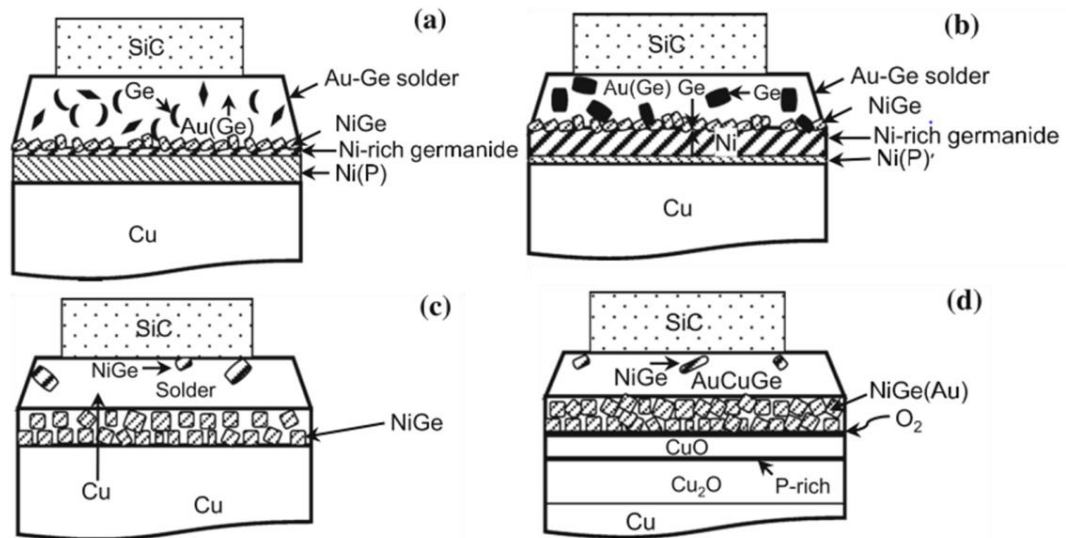


Figure 2-19 Mechanism of the microstructural evolution of the joint during high temperature aging: (a) as-reflowed; (b) initial aging stage; (c) break-up of the IMC layer; and (d) oxidation of the interface and Cu diffusion to the solder [2.128].

2.5.3 Interfacial reactions in Bi-Ag-based solder joints

Some works on interfacial reactions between Bi-Ag-based high temperature solders and metallic substrates, such as Cu and Ni, have already been reported. Song *et al.* proposed that molten Bi-Ag solder prone to penetrate into Cu grain boundaries and lead to the formation of deep boundary grooves [2.129]. This normally induces the

degradation of mechanical strength of solder joints. As for Ni substrate, a cellular layer of NiBi_3 phase perpendicular to the solder interface was produced during reflowing. During the subsequent aging, a thin NiBi layer formed between NiBi_3 and Ni substrate, as shown in figure 2-20. Owing to these brittle Ni-Bi IMCs, Bi-Ag/Ni solder joints exhibited brittle fracture mode.

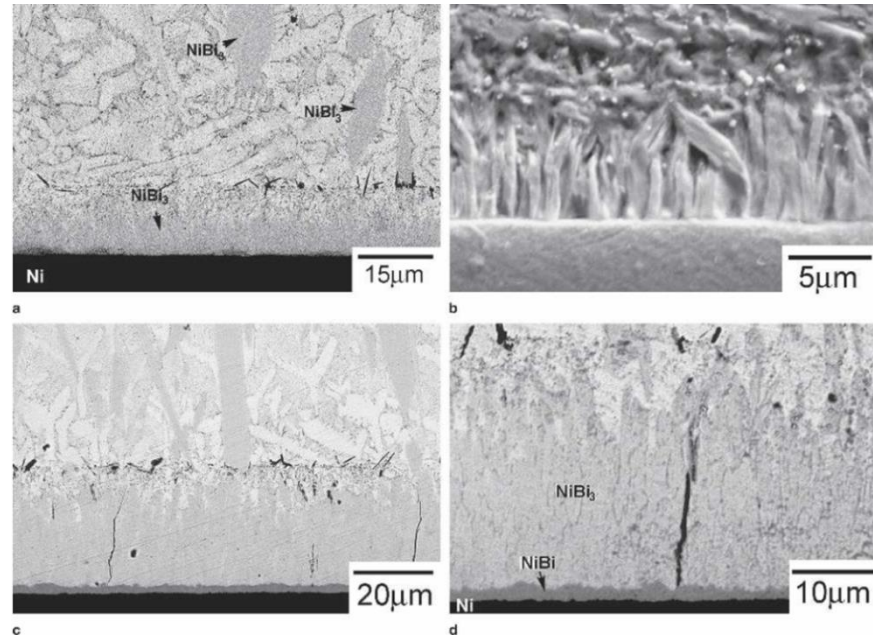


Figure 2-20 Structural feature of the Bi-2.5Ag/Ni interface after reaction at 350 °C for: (a) 1 minute; (b) magnified structure of (a) showing that only NiBi_3 was found; for (c) 5 minutes; (d) magnified structure of (c) illustrating that NiBi and intercellular cracks of NiBi_3 appeared [2.129].

Moreover, there are some major concerns on Bi-Ag solders for their low ductility and poor wetting on substrates. Increasing Ag content in Bi-Ag solder can not only improve wettability and mechanical properties of solders but also enhance the interfacial IMC microstructure at Bi-Ag solder joints [2.129, 2.130]. However, high content of Ag will increase the cost.

To find a low-cost alternative solder, Zhang and Lee in Indium Corporation have developed a BiAgX solder paste that exhibits a remarkable wetting behaviour compared to Bi-11Ag solder [2.61] as shown in figure 2-21. The solder paste mainly consists of high melting materials. Some powder and proper amount of flux were added to reduce its melting temperature to around 260 °C. Johnson's group has studied the BiAgX solder reflowed on different metallisation (Ni, Ni-P, Ni-B, Ni-Co) [2.131]. The shear strength of these solder joints gradually decrease with prolonged aging due to their increasing interfacial IMC thickness.

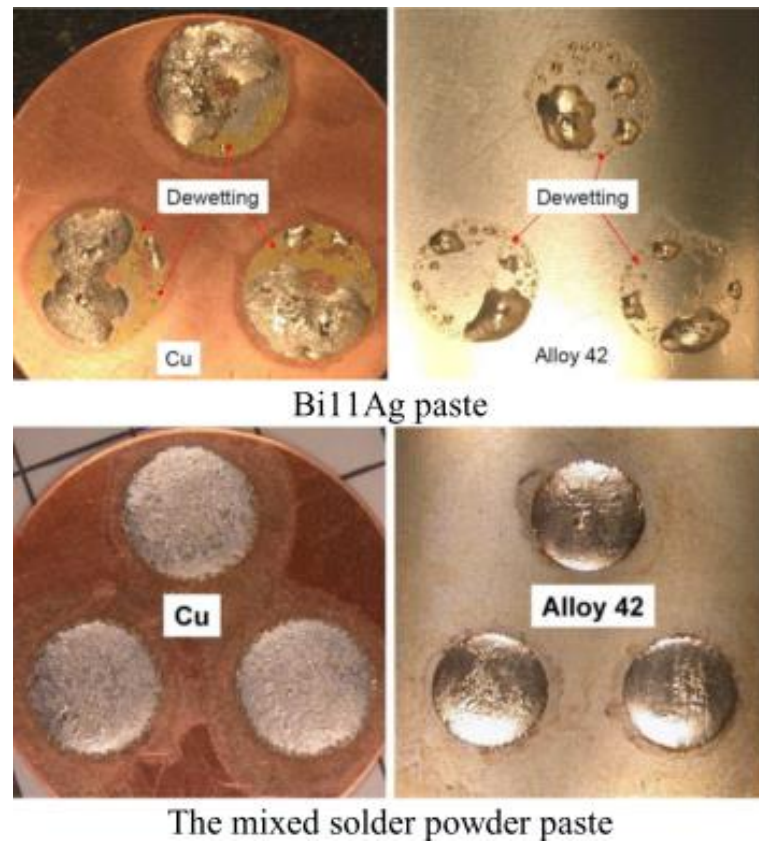


Figure 2-21 Improved wetting of the mixed solder paste comparing to Bi-11Ag paste on Cu and Alloy 42 [2.61].

Therefore, after a detailed summary of published works, it is clear that a relative low-cost diffusion barrier with a good reliability is highly demanded in high temperature applications (at least above 300 °C). Particularly, for Zn-Al-based high temperature solders, suppressing and preventing the interfacial reactions between Zn-Al-based solders and Cu substrates is extremely vital as enormous IMCs formed at Zn-Al/Cu interfaces (Figure 2-15).

2.6 Mechanical properties of high temperature solder joints

Electronic devices are subjected to different types of external loads during service. Particularly for high temperature power electronics, thermal cycling can pose significant influence on solder integrity due to the different coefficient of thermal expansion (CTE) between die, solder, and substrate. Figure 2-22 illustrates the formation of cyclic shear stresses and forces during operations. These shear stresses were prone to induce fatigue or even failure of solder joints. Therefore, to closely replicate the reality during operation, electronic industry normally conducts shear tests to obtain yield shear strength of the solder joints. These solder joints generally fracture

from the weakest regions, which can be identified through fractographic analysis and finally determine fracture modes.

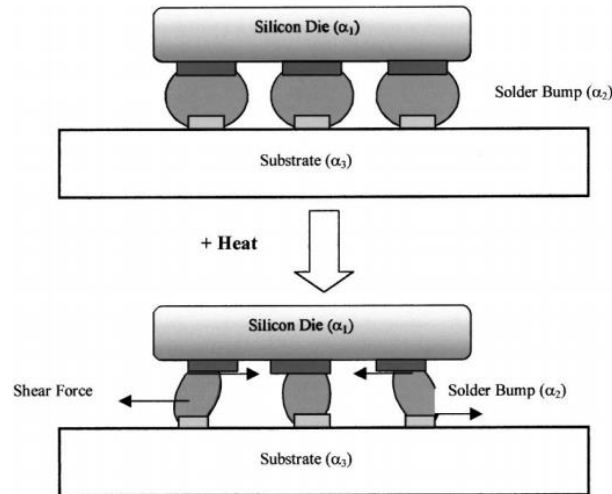


Figure 2-22 Solder joints subjected to shear strain during thermal cycling due to CTE mismatch between the Die, the solder and the substrate [2.36].

With a growing trend towards minimization, the ratio of interfacial IMCs in solders continuously increases and even fully substitutes for the entire solder matrix. Thus, obtaining a comprehensive understanding of the IMCs is quite important. A micro-scale test (e.g. nanoindentation) would be appropriate to obtain elastic moduli and hardness of these IMCs in solder joints at micro-scale.

2.6.1 Shear strength and of high temperature solder joints

Universal shear tester (DAGE 4000) is useful to evaluate shear strength of die attachments as shown in figure 2-23 a). Figure 2-23 b) schematically illustrates typical setup of shear tests. Normally, the shear height is slightly higher than the thickness of die attachment. The shear strength can be calculated through dividing the measured fracture force by the area size of the chip.

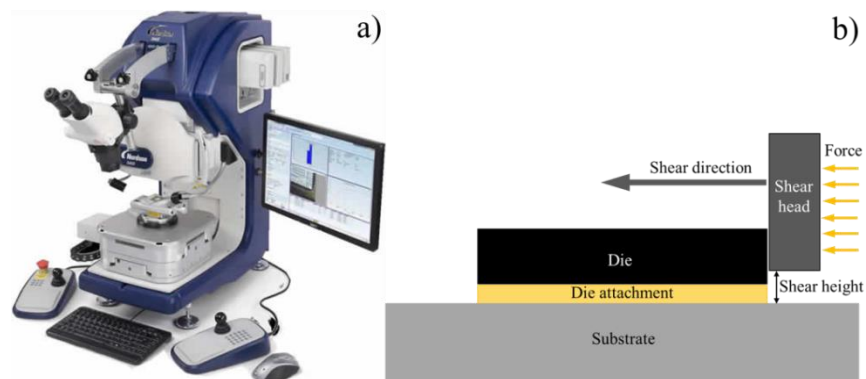


Figure 2-23 Images of: a) Universal Bond tester for measuring the shear strength of die attachment; b) schematic shear test.

Shear strengths of high temperature solder joints at room temperature are listed in table 2-6. Pb-5Sn solder joint is for comparison (25-29 MPa). It is interesting that the shear strength of Au-Ge, Zn-Al-Mg-Ga and Zn-Al solder joints varies with substrates. Electroplated Ni metallisation exhibits the weakest adhesion strength with these solders. This may attribute to the rapid reactions with solders and the resultant internal stress within Ni UBM. Therefore, electroless Ni-P UBM shows a preferable performance in improving reliability of Au-Ge and Zn-Al solder assemblies. However, with prolonged aging, Cu reacts intensively with high temperature solders and leads to enormous interfacial IMCs formations. Owing to the brittle nature of these IMCs, the joint integrity would be greatly damaged when subjected to thermal cycling and aging. In contrast, Ni-based UBM remain relatively more stable at high temperature, which agrees to a reported work [2.120]. For instance, after aging at 300 °C for nearly 60 hours, the shear strength of Au-Ge solder joints with Ni UBM can surpass the ones on Cu substrates.

Table 2-6 A summary of shear strength of current high temperature solder joints.

Solder	Substrate	Shear strength	Reference
Pb-5Sn	Cu	24.5 MPa	[2.132]
	Ni	29.3 MPa	[2.124]
Au-12Ge	Cu	25 MPa	[2.132]
Au-12Ge	Ni/Ag	11.5 MPa	[2.132]
Au-12Ge	Ni-P	60 MPa	[2.133]
Au-20Sn	Cu	41.8 MPa	[2.134]
Zn-Al-Mg-Ga	Cu	24.2 MPa	[2.135]
	Ni	20.5 MPa	[2.135]
Zn-5Al	Cu	48 MPa	[2.120]
	Ni	32.5 MPa	[2.132]
	Ni-P	76.4 MPa	[2.120]

Zn-20Sn	Cu	31-33 MPa	[2.134]
Bi-11Ag	Cu	13.28 MPa	[2.136]
BiAgX TM	Cu	43 MPa	[2.137]
Bi-20Sb-10Cu	Cu	32-35 MPa	[2.138]

Moreover, high temperature shear tests at 250 °C have been carried out to estimate the deterioration in strength of Au-based (Au-Ge and Au-Si) solders joints [2.127]. The obtained shear strength obtaining is slightly lower than shear strength at room temperature. The strength loss rate of Au-Ge and Au-Si solder joints without UBMs are around 33-50% and 20-28%, respectively. While, with the aid of UBM, the loss rate can be decreased to 20-25% for Au-Ge assemblies and 14-20% for Au-Si assemblies. This indicates a diffusion barrier can clearly avoid the degradation of joint integrity in a long-term service.

2.6.2 Fractographic analysis of high temperature solder joints

After shear tests, the fracture surface of tested specimens can be investigated by material characterisation facilities to identify the composition of fracture surface and to determine the failure modes. Generally, the failure modes of solder joints are identified with industrial test standards including MIL-STD-883H and MIL-STD-750D. However, these industry criteria cannot cover all failure modes of current die attachments in power electronic packaging. Melchor *et al.* proposed a modified criteria for failure modes, as presented in figure 2-24 [2.139]. It can be fall into four failure modes as follows:

1. **Failure mode A** (Figure 2-24 a)). Detachment of entire die-attach occurs at solder/substrate interfaces. This indicates the poor adhesion strength and mechanical properties of interfacial IMCs, corresponding to brittle fracture.
2. **Failure mode B** (Figure 2-24 b)). The solder joint fractures within the solder matrix since the adhesion strength at die/solder and solder/substrate are stronger than the mechanical strength of solders. This represents ductile failure mode.

3. **Failure mode C** (Figure 2-24 c)). The die attachment fails at solder/die interfaces due to its weakest adhesion strength among the whole solder joint. This is classified into brittle fracture.
4. **Failure mode D** (Figure 2-24 d)). This phenomenon only happens when joint strength is superb and much higher than that of entire solder joint. Therefore, the chip cracks firstly with increasing shear force.

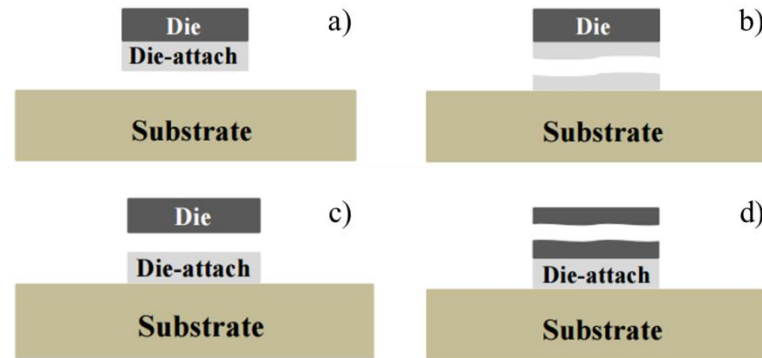


Figure 2-24 Modified fracture modes of die attachments in power electronic packaging [2.139].

Among these failure modes, the last mode is the most desirable to show excellent shear strength, which is not common for lead-free high temperature interconnections. For current high temperature solder joints, their failure modes are normally divided into two types: fracture within the solder matrix or interfacial IMC layers at solder/substrate interface. Generally, as-reflowed solder joints normally fracture at solder part as a ductile fracture. However, with continual aging or thermal cycling, the IMC layers grow gradually and therefore raise internal stresses, in which cracks are prone to initiate during service. This corresponds to brittle failure.

2.6.3 Mechanical properties of interfacial IMCs in solder joints

As discussed in Section 2.6, IMC layer is essential in solder interconnection. Due to the small scale of IMC layer (around 1 μm), conventional test methods are not able to evaluate the mechanical properties of IMCs. Nanoindentation is a favourable approach to provide mechanical properties (elastic moduli and hardness) of micro-scale IMC phases for its small indentation head and excellent position resolution [2.26, 2.64, 2.138]. Figure 2-25 illustrates the load-displacement curve with the corresponding positions of the diamond tip into samples during nanoindentation [2.140]. This curve can provide the information of nanohardness (H_N) and elastic moduli (E).

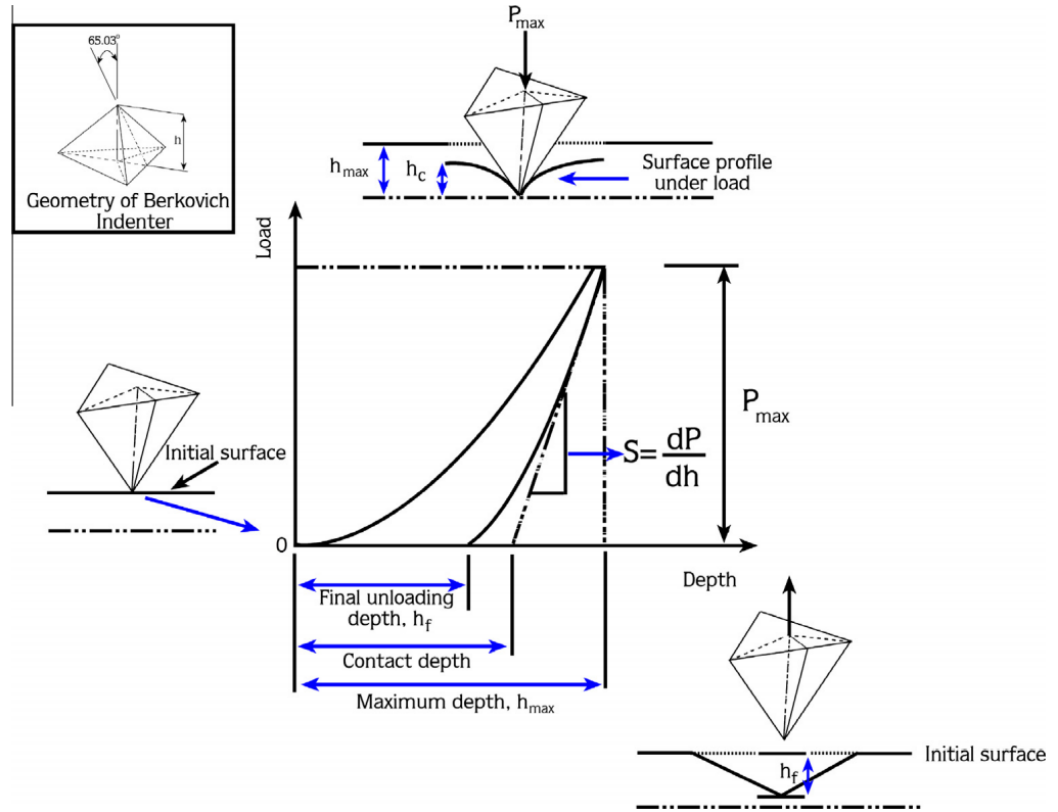


Figure 2-25 Nanoindentation depth-load curve shows the parameters for analysis of the result [2.140].

The nanohardness is defined as:

$$H_N = \frac{P_{max}}{A} \quad \text{Equation 2-8}$$

Where P_{max} is the maximum indentation load, A is the projected contact area at P_{max} .

The contact depth h_c is given by,

$$h_c = h_{max} - \beta \frac{P_{max}}{S} \quad \text{Equation 2-9}$$

Where S is the contact stiffness that can be calculated from the initial slope of the unloading curve at P_{max} , β is a constant of 1.034 for a Berkovich indenter [2.141], E_r is the reduced modulus is calculated as:

$$\frac{1}{E_r} = \frac{1 - \nu^2}{E} + \frac{1 - \nu_i^2}{E_i} \quad \text{Equation 2-10}$$

Where ν and ν_i are the Poisson's ratios of the samples and the indenter, respectively. E and E_i are the corresponding elastic moduli. The E_i and ν_i of the diamond indenter is 1141 GPa and 0.07, respectively [2.141]. Reduced elastic modulus E_r is calculated based on equation 2-11.

$$E_r = \frac{S}{2} \frac{\sqrt{\pi}}{\sqrt{24.5}h_c} \quad \text{Equation 2-11}$$

Owing to the advantages of high melting temperature and low cost, Cu-Sn and Ag-Sn IMCs have been utilised as full IMC die attachments for high temperature power electronic devices through transient liquid phase bonding and nanoparticle sintering. Table 2-7 summaries the mechanical properties of interfacial IMCs in different solder joints. From this table, even for the same IMC, the elastic moduli and hardness cannot be varying because of different solder systems, thermal treatment, loading rates, or strain rates.

Table 2-7 A summary of elastic moduli and hardness of interfacial IMCs at solder joints.

IMC type	Elastic moduli	Hardness	Reference
Cu ₆ Sn ₅	112.3 ± 5 GPa	6.38 ± 0.21 GPa	[2.142]
	125.2 – 136 GPa	6.3 – 6.5 GPa	[2.142]
	135.7 ± 5.9 GPa	5.69 ± 0.58 GPa	[2.142]
	160 ± 8 GPa	6.2 ± 0.4 GPa	[2.142]
Cu ₃ Sn	134.2 ± 6.7 GPa	6.12 ± 0.17 GPa	[2.142]
	91.7 – 108 GPa	3.6 – 5.9 GPa	[2.142]
	125 ± 6.8 GPa	6.10 ± 0.53 GPa	[2.142]
	134 ± 7 GPa	6.5 ± 0.3 GPa	[2.142]
Ag ₃ Sn	78.9 ± 3.7 GPa	3.25 ± 0.18 GPa	[2.142]
	82.3 – 90.5 GPa	2.37 – 3.13 GPa	[2.142]
	99 ± 5 GPa	2.9 ± 0.2 GPa	[2.142]
(Ag, Cu) ₃ Sn	83 GPa	2.98 GPa	[2.143]
Ni ₃ Sn ₄	140.4 ± 7.9 GPa	8.12 ± 0.62 GPa	[2.144]
Ni ₃ Sn ₄	136.4 ± 6.0 GPa	8.90 ± 0.55 GPa	[2.144]

(Cu, Ni) ₆ Sn ₅	116.77 ± 1.64 GPa	5.40 ± 0.69 GPa	[2.145]
(Cu, Ni) ₆ Sn ₅	133.8 GPa	8.21 GPa	[2.146]
CuNiSn	160 ± 4.9 GPa	7.3 ± 1.2 GPa	[2.147]
NiZn ₈	149.06 ± 3.42 GPa	7.92 ± 1.21 GPa	[2.148]
AuZn ₈	128.15 ± 4.25 GPa	6.98 ± 0.92 GPa	[2.148]
Au ₅ Sn	76 ± 5 GPa	2.5 ± 0.2 GPa	[2.149]
AuSn	87 ± 9 GPa	1.1 ± 0.06 GPa	[2.149]
AuSn ₂	103 ± 9 GPa	2.9 ± 0.4 GPa	[2.149]
AuSn ₄	39 ± 4 GPa	1.2 ± 0.2 GPa	[2.149]
(Cu, Co, Ni) ₆ Sn ₅	86.6 ± 6.5 GPa	2.12 ± 0.54 GPa	[2.150]

2.7 Summary

From the reviewed literatures in this chapter, following conclusions can be drawn:

1. Due to the environment and health concerns, high temperature lead-free solders are required to replace high lead solders in high temperature electronics. However, there is still no drop-in alternative solder system can meet all demands of high temperature electronic packaging. Among all proposed solders, Au-Ge, Bi-Ag and Zn-Al solders seems to be more promising for their advantages of high melting temperature, good electrical and mechanical properties, which demand further investigations.
2. Due to the elevated operation temperature, UBM is indispensable to suppress the growth of interfacial IMC layers at solder/substrate interfaces. The conventional electroless Ni-P UBM is not adequate to work in hybrid automotive electronics (operate above 300 °C) for the formation columnar structure and voids in the crystalline Ni₃P layer. This demands a promising UBM material that can suppress the growth of void-embedding Ni₃P layer at elevated temperature (above 300°C).

3. In terms of thermal stability, cost and production yield, it is found that electroless Ni-W-P coating is relatively more suitable than other ternary Ni-X-P metallisation to substitute current electroless Ni-P coatings as a diffusion barrier. The electroless Ni-W-P coatings only applied in low temperature (In-based) and conventional solder (Sn-based) systems and never reacted with high temperature solders to investigate their diffusion barrier properties.
4. In hybrid automotive devices, Zn-Al solders draw attention for their low cost, high mechanical strength, good thermal and electrical properties. However, the low wettability hinders the widely application of Zn-Al solders. To solve this issue, many joining processes have been proposed to check their feasibility in producing high temperature lead-free solder joints.
5. With an increasing trend towards miniaturization of microelectronic products, volume ratio of the IMCs in solder joints tends to be higher and even reach 100%. A comprehensive knowledge of mechanical properties for the interfacial IMCs in solder interconnects is beneficial to the understanding of electronics reliability. Shear strength and nanoindentation methods are common-used methods to characterise the mechanical properties of entire die attachments and the corresponding thin IMC layers, respectively.

References

- [2.1] S.W. Yoon, M.D. Glover, H.A. Mantooth, and K. Shiozaki, "Reliable and repeatable bonding technology for high temperature automotive power modules for electrified vehicles", *Journal of Micromechanics and Microengineering*, vol. 23, pp. 015017, 2013.
- [2.2] F.P. McCluskey, R. Grzybowski, and T. Podlesak, *High Temperature Electronics*, CRC Press, United State of American, 1997.
- [2.3] C. Buttay, D. Planson, B. Allard, D. Bergogne, P. Bevilacqua, and etc., "State of the art of high temperature power electronics", *Materials Science and Engineering: B*, vol. 176, No. 4, pp. 283-288, 2011.
- [2.4] R.R. Tummala, *Introduction to Microsystems Packaging, in Fundamentals of Microsystems Packaging*, McGraw-Hill, 2004.
- [2.5] H.M. Tong, "Microelectronics packaging: present and future", *Materials Chemistry and Physics*, vol. 40, No. 3, pp. 147-161, 1995.

- [2.6] H.M. Ho, W. Lam, S. Stoukatch, P. Ratchev, C. J. Vath III, and E. Beyne, "Direct gold and copper wires bonding on copper", *Microelectronics Reliability*, Vol. 43, No. 6, pp. 913-923, 2003.
- [2.7] P.A. Agyakawa, V.M.F. Marques, M.R. Corfield, J.F. Li, L. Yang, and C.M. Johnson, "Room-temperature Nanoindentation creep of thermally cycled ultrasonically bonded heavy aluminium wires", *Journal of Electronic Materials*, Vol. 42, No. 3, pp. 537-544, 2013.
- [2.8] M. S. Ramelow, C. Ehrhardt, "The reliability of wire bonding using Ag and Al", *Microelectronics Reliability*, vol. 63, pp. 336-341, 2016.
- [2.9] G. Harman, *Wire bonding in microelectronics: materials, processes, reliability and yield (3rd edition)*, McGraw-Hill, 2010.
- [2.10] J.C. Krinke, D. Dragicevic, S. Leinert, E. Friess, and J. Glueck, "High temperature degradation of palladium coated copper bond wires", *Microelectronics Reliability*, vol. 54, No. 9-10, pp. 1995-1999, 2014.
- [2.11] M. Mirgizoudi, C. Liu, and S. Riches, "Reliability Testing of Electronic Packages in Harsh Environment", in *Proceeding of 12th Electronics Packaging Technology Conference (EPTC)*, Singapore, 2010, pp. 224-230.
- [2.12] T. Kimura, O. Saitou, K. Kubo, K. Nakatsu, H. Ishikawa, and K. Sasaki, "High-power-density inverter technology for hybrid and electric vehicle applications", *Hitachi Review*, vol. 63, No. 2, pp. 96-102, 2014.
- [2.13] Cotronics Corporation, data sheet Duralco 4703. (2013). [Online]. Available: <https://www.cotronics.com/vo/cotr/pdf/4703.pdf>.
- [2.14] C. Buttay, A. Masson, J. Li, M. Johnson, M. Lazar, C. Raynaud, and H. Morel, "Die attach of power devices using silver sintering bonding process optimization and characterization," in *Proceeding of International IMAPS High Temperature Electronics*, Oxford, U.K., 2011.
- [2.15] M. Knoerr, S. Kraft, and A. Schletz, "Reliability assessment of sintered nano-silver die attachment for power semiconductors", in *Proceeding of 12th Electronic Packaging Technology Conference (EPTC)*, Singapore, 2010, pp. 56-61.
- [2.16] Zhiwen Chen, "Micro-mechanical characteristics and dimensional change of Cu-Sn interconnects due to growth of interfacial intermetallic compounds", Ph.D. thesis, Loughborough University, UK, 2015.
- [2.17] R. Khazaka, L. Mendizabal, D. Henry, and R. Hanna, "Survey of high-temperature reliability of power electronics packaging components", *IEEE Transactions on Power Electronics*, vol. 30, No. 5, pp. 2456-2464, 2015.
- [2.18] T. Wang, X. Chen, G. Q. Lu, and G.Y. Lei, "Low-temperature sintering with nano-silver paste in die-attached interconnection", *Journal of Electronic Materials*, vol. 36, No. 10, pp. 1333-1340, 2007.
- [2.19] M. Tobita, Y. Yasuda, E. Ide, J. Ushio, and T. Morita, "Optimal design of coating material for nanoparticles and its application for low-temperature interconnection", *Journal of Nanoparticle Research*, vol. 12, No. 12, pp. 2135-2144, 2010.

- [2.20] A.J. Murray, P. Jaroenapibal, and B. Koene, “Sintering of silver nanoparticles for the formation of high temperature interconnect joints”, in *Proceeding of Materials Research Society Symposium*, vol. 942, pp. 39-44, 2006.
- [2.21] C. Huang, M. F. Becker, J.W. Keto, and D. Kovara, “Annealing of nanostructured silver films produced by supersonic deposition of nanoparticles”, *Journal of Applied Physics*, vol. 102, No. 5, pp. 054308, 2007.
- [2.22] M. Jakubowski, M. Jarosz, K. Kiełbasinski, and A. Młozniak, “New conductive thick-film paste based on silver nanopowder for high power and high temperature applications”, *Microelectronics Reliability*, vol. 51, No. 7, pp. 1235-1240, 2011.
- [2.23] S. Wang, M.Y. Li, H.J. Ji, and C.Q. Wang, “Rapid pressureless low-temperature sintering of Ag nanoparticles for high-power density electronic packaging”, *Scripta Materialia*, vol. 69, pp. 789-792, 2013.
- [2.24] H.B. Qin, W.Y. Li, W.B. Zhou, and X.P. Zhang, “Low cycle fatigue performance of ball grid array structure Cu/Sn-3.0Ag-0.5Cu/Cu solder joints”, *Microelectronics Reliability*, vol. 54, No. 12, pp. 2911-2921, 2014.
- [2.25] Q.K. Zhang, H.F. Zou, and Z.F. Zhang, “Tensile and Fatigue Behaviors of Aged Cu/Sn-4Ag Solder Joints”, *Journal of Electronic Materials*, vol. 38, No. 6, pp. 852-859, 2009.
- [2.26] A. Kroupa, D. Andersson, N. Hoo, J. Pearce, A. Watson, A. Dinsdale, and S. Muchleohn, “Current Problems and Possible Solutions in High-Temperature Lead-free Soldering”, *Journal of Materials Engineering and Performance*, vol. 21, No. 5, pp. 629-637, 2011.
- [2.27] W.W. Sheng, and R.P. Colino, *Power Electronic Modules: Design and Manufacture (1st edition)*, CRC Press, USA, 2005.
- [2.28] S. Menon, E. George, M. Osterman, and M. Pecht, “High lead solder (over 85%) solder in the electronics industry: RoHS exemptions and alternatives”, *Journal of Material Science: Materials in Electronics*, vol. 26, No. 6, pp. 4021-4030, 2015.
- [2.29] V.R. Manikam, and K.Y. Cheong, “Die attach materials for high temperature applications: a review”, *IEEE Transactions on Components, Packaging and Manufacturing Technology*, vol. 1, No. 4, pp. 457-478, 2011.
- [2.30] H. Sunil, “Review: Green Electronics through Legislation and Lead Free Soldering”, *Clean*, vol. 36, No. 2, pp. 145-151, 2008.
- [2.31] K.J. Puttlitz, and K.A. Salter, *Handbook of lead-free solder technology for microelectronic assemblies*, Marcel Dekker Incorporation, USA, 2004.
- [2.32] Directive 2011/65/EU of the European Parliament and the Council of 8 June 2011 on the restriction of the use of certain hazardous substances in electrical and electronic equipment: compliance and guidance, 2011. <http://eur-lex.europa.eu/legal-content/en/TXT/?uri=celex%3A32011L0065>. Accessed 20 October 2016.
- [2.33] Directive 2012/19/EU of the European Parliament and the Council of 4 July 2012 on Waste Electrical and Electronic Equipment Recycling (WEEE), 2012.

- <http://eur-lex.europa.eu/legal-content/EN/TXT/?uri=celex%3A32012L0019>. Accessed 20 October 2016.
- [2.34] EPA 260-B-01-027 of the Emergency Planning and Community Right-to-know Act – Section 313: Guidance for Reporting Releases and Other Waste Management Quantities of Toxic Chemicals: Lead and Lead Compound, 2001. <https://www.epa.gov/sites/production/files/documents/2001lead.pdf>. Accessed 20 October 2016.
 - [2.35] X. Zeng, J. Li, A.L.N. Stevels, and L. Liu, “Perspective of electronic waste management in China based on a legislation comparison between China and the EU”, *Journal of Cleaner Production*, vol. 51, pp. 80-87, 2013.
 - [2.36] M. Abtew and G. Selvaduray, “Lead-free solders in microelectronics”, *Materials Science and Engineering: R*, vol. 27, No. 5-6, pp. 95-141, 2000.
 - [2.37] C.O. Gensch, Y. Baron, and K. Moch, “8th Adaptation to scientific and technical progress of exemptions 2(c), 3 and 5 of Annex II to Directive 2000/53/EC(ELV): Final Report for the European Commission DG Environment under Framework Contract: Evaluation of ELV Exemptions”, N0 ENV. C.2/FRA/2011/0020”, 2016.
 - [2.38] F. Gnecco, E. Ricci, and S. Amore, “Wetting behavior and reactivity of lead free Au-In-Sn and Bi-In-Sn alloys on copper substrates”, *Journal of Adhesion and Adhesives*, vol. 27, No. 5, pp. 409-416, 2006.
 - [2.39] S. Amore, and E. Ricci, “Wetting behavior of lead-free Sn-based alloys on Cu and Ni substrates”, in *Proceeding of 5th International Conference on HTC-2007*, Alicante, Spain, vol. 495, No. 1-2, 2008, pp. 108-112.
 - [2.40] V. Chidambaram, J. Hattel, J. Hald, “Design of lead-free candidate alloys for high-temperature soldering based on the Au-Sn system”, *Journal of Materials and Design*, vol. 31, No. 10, pp. 4638-4645, 2010.
 - [2.41] T.A. Tollefsen, A. Larsson, O.M. Lovvik, and K.E. Aasmundtveit, “High temperature interconnect and die attach technology: Au-Sn SLID bonding”, *IEEE Transactions on Components, Packaging and Manufacturing Technology*, vol. 3, No. 6, pp. 904-914, 2013.
 - [2.42] G. Humpston and D.M. Jacobsen, “Gold in gallium arsenide die-attach technology”, *Gold Bulletin*, vol. 22, No. 3, pp. 79-91, 1989.
 - [2.43] H. Takiguchi and Z. Yoshikawa, “The Role of Au in the Thermoelectric Properties of Amorphous Ge/Au and Si/Au Thin Films”, *Journal of Electronic Materials*, vol. 39, No. 9, pp. 1627-1633, 2010.
 - [2.44] T.S. Abhilash and C.H.R. Kumar, “Nickel dissolution into AuGe in alloyed AuGe/Ni/Au Ohmic contacts on GaAs/AlGaAs multilayer structure”, *Thin Solid Films*, vol. 518, No. 19, pp. 5576-5578, 2010.
 - [2.45] H.L. Lukas, S.G. Fries and B. Sundman, *Computational Thermodynamics, the CALPHAD Method*, Cambridge University Press, 2007.
 - [2.46] J.M. Joubert, “CALPHAD Modelling of Metal-Hydrogen Systems: A Review”, *Journal of the Minerals, Metals & Materials Society*, vol. 64, No. 12, pp. 1438-1447, 2012.

- [2.47] C. Leinenbach, S. Jin, J. Wang, and H.R. Elsener, “Au-Ge based alloys for novel high-T lead free solder materials- fundamentals and applications”, in *Proceedings of the 5th IBSC*, Las Vegas, USA, 2012, pp. 196-201.
- [2.48] V. Chidambaram, J. Hald and J. Hattel, “Development of Au-Ge based candidate alloys as an alternative to high-lead content solders”, *Journal of Alloys and Compounds*, vol. 490, No. 1-2, pp. 170-179, 2010.
- [2.49] V. Chidambaram, J. Hald, and R. Ambat, “A Corrosion Investigation of Solder Candidates for High-temperature Applications”, *JOM*, vol. 61, No. 6, pp. 59-65, 2009.
- [2.50] Y.V. Naidich, V. Zhuravlev, and N. Krasovskaya, “The wettability of silicon carbide by Au-Si alloys”, *Journal of Material Science Engineering*, vol. 245, No. 2, pp. 293-299, 1998.
- [2.51] J. Pstruś, P. Fima, and T. Gancarz, “Wetting of Cu and Al by Sn-Zn and Zn-Al Eutectic Alloys”, *Journal of Materials Engineering and Performance*, vol. 21, No. 5, pp. 606-613, 2012.
- [2.52] R. Mahmudi and S. Alibabaei, “Elevated-temperature shear strength and hardness of Zn-3Cu-xAl ultra-high-temperature lead-free solders”, *Materials Science and Engineering: A*, vol. 559, pp.421-426, 2013.
- [2.53] T. Shimizu, H. Ishikawa, I. Ohnuma and K. Ishida, “Zn-Al-Mg-Ga Alloys as Pb-Free Solder for Die-Attaching Use”, *Journal of Electronic Materials*, vol. 28, No. 11, pp. 1172-1176, 1999.
- [2.54] H.S. Nam and D.J. Srolovitz, “Effect of material properties on liquid metal embrittlement in Al-Ga system”, *Acta Materialia*, vol. 57, No. 5, pp. 1546-1553, 2009.
- [2.55] N. Kang, H.S. Na, S.J. Kim, and C.K. Kang, “Alloy design of Zn-Al-Cu solder for ultra high temperatures”, *Journal of Alloys and Compounds*, vol. 467, pp. 246-250, 2009.
- [2.56] J.E. Lee, K.S. Kim, K. Suganuma, M. Inoue, and G. Izuta, “Thermal Properties and Phase Stability of Zn-Sn and Zn-In Alloys as High Temperature Lead-free Solder”, *Materials Transactions*, vol. 48, No. 3, pp. 584-593, 2007.
- [2.57] R. Mahmudi and M. Eslami, “Impression Creep Behavior of Zn-Sn High-Temperature Lead-Free Solders”, *Journal of Electronic Materials*, vol. 39, No. 11, pp. 2495-2502, 2009.
- [2.58] R. Koleňák and M. Chachula, “Characteristics and properties of Bi-11Ag solder”, *Soldering & Surface Mount Technology*, vol. 25, No. 2, pp. 68-75, 2013.
- [2.59] V. Chidambaram, J. Hattel, and J. Hald, “High-temperature lead-free solder alternatives”, *Microelectronic Engineering*, vol. 88, No. 6, pp. 981-989, 2011.
- [2.60] Y. Shi, W. Fang, Z. Xia, Y. Lei, F. Guo and X. Li, “Investigation of rare earth-doped BiAg high-temperature solders”, *Journal of Materials Science: Materials in Electronics*, vol. 21, No. 9, pp. 875-881, 2010.

- [2.61] H.W. Zhang and N.C. Lee, “High reliability high melting mixed lead-free solder paste system”, in *Proceedings of 35th IEEE/CPMT International Electronic Manufacturing Technology Symposium (IEMT)*, 2012, pp. 1-7.
- [2.62] S.F. Corbin, “High-temperature variable melting point Sn-Sb lead-free solder pastes using transient liquid-phase powder processing”, *Journal of Electronic Materials*, vol. 34, No. 7, pp. 1016-1025, 2005.
- [2.63] G. Zeng, S. McDonald, and K. Nogita, “Development of high-temperature solders: Review”, *Microelectronics Reliability*, vol. 52, No. 7, pp. 1306-1322, 2012.
- [2.64] A.R. Geranmayeh, R. Mahmudi, F. Khalatbari, N. Kashi, and G. Nayyeri, “Indentation Creep of Lead-free Sn-5Sb solder alloy with 1.5 wt% Ag and Bi additions”, *Journal of Electronic Materials*, vol. 43, No. 3, pp. 717-723, 2014.
- [2.65] J.H. Kyle, P.L. Breuer, K.G. Bunney, and R. Pleysier, “Review of trace toxic elements (Pb, Cd, Hg, As, Sb, Se, Te) and their deportment in gold processing: Part II: Deportment in gold ore processing by cyanidation”, *Hydrometallurgy*, vol. 111-112, pp. 10-21, 2012.
- [2.66] P. Xue, B.L. Xiao, D.R. Ni, and Z.Y. Ma, “Enhanced mechanical properties of friction stir welded dissimilar Al-Cu joint by intermetallic compounds”, *Materials Science and Engineering A*, vol. 527, pp. 5723-5727, 2010.
- [2.67] T.H. Ming, Y.S. Lai, and C.P. Wong, *Advanced Flip Chip Packaging*, Springer New York Heidelberg Dordrecht London, 2013.
- [2.68] K.N. Tu and K. Zeng, “Tin-lead (SnPb) solder reaction in flip chip technology”, *Materials Science and Engineering: R*, vol. 34, No. 1, pp. 1-58, 2001.
- [2.69] K. Chen, C. Liu, D. Whalley, and D. Hutt, “A comparative study of the interfacial reaction between electroless Ni-P coatings and molten tin”, *Acta Materialia*, vol. 56, pp. 5668-5676, 2008.
- [2.70] C.E. Ho, Y.C. Lin and S.J. Wang, “Sn-Ag-Cu solder reaction with Au/Pd/Ni(P) and Au/Pd(P)/Ni(P) platings”, *Thin Solid Films*, vol. 544, pp. 551-556, 2013.
- [2.71] V. Vuorinen, T. Laurila, H. Yu, and J.K. Kivilahti, “Phase formation between lead-free Sn-Ag-Cu solder and Ni(P)/Au finishes”, *Journal of Applied Physics*, vol. 99, pp. 023530, 2006.
- [2.72] K.H. Krishnan, S. John, K.N. Srinivasan, J. Praveen, M. Ganesan, and P.M. Kavimani, “An overall aspect of electroless Ni-P depositions - A Review Article”, *Metallurgical and Materials Transactions A*, vol. 37, No. 6, pp. 1917-1926, 2006.
- [2.73] C.K. Chung, Y.J. Chen, T.L. Yang, and C.R. Kao, “Reactions of Sn-4.0Ag-0.5Cu on Cu and Electroless Ni Substrate in Premelting Soldering Process”, *Journal of Electronic Materials*, vol. 42, No. 6, pp. 1254-1259, 2013.
- [2.74] Y. Takaku, I. Ohnuma, Y. Yamada, Y. Yagi, I. Nakagawa, T. Atsumi, and K. Ishida, “A review of Pb-free high temperature solders for power semiconductor devices: Bi-base composite solder and Zn-Al solder”, *Journal of ASTM International*, vol. 8, pp. 1-18, 2011.

- [2.75] Y. Takaku, L. Felicia, I. Ohnuma, R. Kainuma, and K. Ishida, "Interfacial Reaction between Cu Substrates and Zn-Al Base High-Temperature Pb-free Solders", *Journal of Electronic Materials*, vol. 37, pp. 314-323, 2008.
- [2.76] J.X. Li, B.W. Wen, S. Krishnan, and B. Knight, "Advanced materials for drop in solution to Pb in high temp solders: The next generation of zinc based solder alloy", in *Proceedings of 63rd Electronic Components and Technology Conference (ECTC)*, Las Vegas, USA, 2013, pp. 1628-1633.
- [2.77] K. Chen, C. Liu, D.C. Whalley, D.A. Hutt, J.F. Li, and S.H. Mannan, "Electroless Ni-W-P Alloys as Barrier Coatings for Liquid Solder Interconnects", in *Proceeding of 1st Electronics System integration Technology Conference (ESTC)*, Dresden, Germany, 2006, pp. 421-427.
- [2.78] Y. Yang, J.N. Balaraju, Z. Tsakadze, and Z. Chen, "Electroless Ni-W-P alloy as a more enduring and reliable soldering metallization", in *Proceeding of 13th Electronics Packaging Technology Conference (EPTC)*, Singapore, 2011, pp. 44-48.
- [2.79] G.F. Huang, W.Q. Huang, L.L. Wang, B.S. Zou, D.P. Chen, and etc., "Effects of complexing agents on the corrosion resistance of electroless Ni-Fe-P alloys", *International Journal of Electrochemical Science*, vol. 2, pp. 321-328, 2007.
- [2.80] S.K. Tien, J.G. Duh, and Y.I. Chen, "Structure, thermal stability and mechanical properties of electroless Ni-P-W alloy coatings during cycle test", *Surface and Coatings Technology*, vol. 177-178, pp. 532-536, 2004.
- [2.81] J.N. Balaraju, Kalavati, N.T. Manikandanath, and V.K.W. Grips, "Phase transformation behavior of nanocrystalline Ni-W-P alloys containing various W and P contents", *Surface and Coatings Technology*, vol. 206, No. 10, pp. 2682-2689, 2012.
- [2.82] D.M. Jang, and J. Yu, "Tungsten alloying of the Ni(P) films and the reliability of Sn-3.5Ag/NiWP solder joints", *Journal of Materials Research*, vol. 26, No. 7, pp. 889-895, 2011.
- [2.83] Y.J. Hu, T.X. Wang, J.L. Meng, and Q.Y. Rao, "Structure and phase transformation behaviour of electroless Ni-W-P on aluminium alloy", *Surface and Coatings Technology*, vol. 201, pp. 988-992, 2006.
- [2.84] Y.Y. Tsai, F.B. Wu, Y.I. Chen, P.J. Peng, J.G. Duh, and S.Y. Tsai, "Thermal stability and mechanical properties of Ni-W-P electroless deposits", *Surface and Coatings Technology*, vol. 146-147, pp. 502-507, 2001.
- [2.85] J.K. Cho, M.T. Kim, and S.G. Kang, "Thermal stability of electrodeposited Ni-Re-P diffusion barrier for Cu interconnection", *Journal of the Korean Institute of Metals and Materials*, vol. 45, No. 5, pp. 300-304, 2007.
- [2.86] J.N. Balaraju, N. Raman, and N.T. Manikandanath, "Nanocrystalline electroless nickel poly-alloy deposition: incorporation of W and Mo", *The International Journal of Surface Engineering and Coatings*, vol. 92, No. 3, pp. 169-176, 2013.
- [2.87] D.M. Jang and J. Yu, "Intermetallic compound spalling characteristics of Sn-3.5Ag solder over ternary electroless Ni under-bump metallurgy", *Journal of Materials Research*, vol. 26, pp. 3032-3037, 2011.

- [2.88] F. Pearlstein and R.F. Weightman, “Electroless deposition of nickel alloys”, *Electrochemistry Technology*, vol. 6, No. 11-12, pp. 427-430, 1968.
- [2.89] J. Flis and D.J. Duquette, “Initiation of electroless nickel plating on copper, palladium-activated copper, gold, and platinum”, *Journal of the Electrochemical Society*, vol. 131, No. 2, pp. 254-260, 1984.
- [2.90] G.O. Mallory and J.B. Hajdu, *Electroless Plating: Fundamentals and Applications*, William Andrew Publishing, USA, 1990.
- [2.91] T. Homma, I. Komatsu, A. Tamaki, H. Nakai, and T. Osaka, “Molecular orbital study on the reaction mechanisms of electroless deposition processes”, *Electrochimica Acta*, vol. 47, pp. 47-53, 2001.
- [2.92] B. Zhang, *Amorphous and Nano Alloys Electroless Depositions: Technology, Composition, Structure and Theory*, Chemical Industry Press, USA, 2016.
- [2.93] G. Qi, X. Chen, and Z. Shao, “Influence of bath chemistry on zincate morphology on aluminium bond pad”, *Thin Solid Films*, vol. 406, No. 1-2, pp. 204-209, 2002.
- [2.94] D.A. Hutt, C. Liu, P.P. Conway, D.C. Whalley, and S.H. Mnan, “Electroless nickel bumping of aluminium bondpads - part I: surface pretreatment and activation”, *IEEE Transactions on Component and Packaging Technologies*, vol. 25, No. 1, pp. 85-97, 2002.
- [2.95] J. Sudagar, J. Lian, and W. Sha, “Electroless nickel, alloy, composite and nano coatings - A critical review”, *Journal of Alloys and Compounds*, vol. 571, pp. 183-204, 2013.
- [2.96] E.J. Mittemeijer, *Fundamentals of Materials Science: The Microstructure-Property Relationship Using Metals as Model System*, Springer, 2011.
- [2.97] U.C. Jindal, *Material Science and Metallurgy*, Pearson India, 2012.
- [2.98] G. Bracco and B. Holst, *Surface science techniques*, Springer, USA, 2013.
- [2.99] C. Yang , H. Gu , W. Lin , M.M. Yuen , C.P. Wong, and *etc.*, “Silver nanowires: from scalable synthesis to recyclable foldable electronics”, *Advanced Materials*, vol. 23, No. 7, pp. 3052-3056, 2011.
- [2.100] W. Sabbah, S. Azzopardi, C. Buttay, R. Meuret, and E. Woiregard, “Study of die attach technologies for high temperature power electronics: Silver sintering and gold-germanium alloy”, *Microelectronic Reliability*, vol. 53, pp. 1617-1621, 2013.
- [2.101] J. Kä, A. Stranz, E. Peiner, and A. Waag, “Sinter-Attach of High-Temperature Sensors for Deep-Drilling Monitoring”, *Packaging Technology*, vol. 1, pp. 1594-1599, 2012.
- [2.102] K. Xiao, J.N. Calata, H. Zheng, K.D.T. Ngo, and G. Lu, “Large-area Nanosilver Die-attach by Hot-pressing Below 200°C and 5 MPa”, in *Proceeding of HITEC*, Baltimore, United States, 2012, pp. 129-134.
- [2.103] D. Paulonis, D.S. Duvall, and W.A. Owczarski, *Diffusion bonding utilizing transient liquid phase*, US Patent US3678570 A, 1972.

- [2.104] E. Lugscheider, “Solder deposition for transient liquid phase (TLP) bonding by MSIP-PVD process”, *Journal of Surface and Coatings Technology*, vol. 174, pp. 704-707, 2003.
- [2.105] G.O. Cook III and C.D. Sorensen, “Overview of transient liquid phase and partial transient liquid phase bonding”, *Journal of Materials Science*, vol. 46, No. 16, pp. 5306-5323, 2011.
- [2.106] C.C. Lee, P.J. Wang, and J.S. Kim, “Are intermetallics in solder joints really brittle”, in *Proceeding of 57th Electronic Components and Technology Conference (ECTC)*, New York, USA, 2007, pp. 648-652.
- [2.107] S. Tabatabaei, A. Kumar, H. Ardebili, P.J. Loos, and P.M. Ajayan, “Synthesis of Au–Sn alloy nanoparticles for lead-free electronics with unique combination of low and high melting temperatures”, *Microelectronics Reliability*, vol. 52, No. 11, pp. 2685-2689, 2012.
- [2.108] C. Ko and K. Chen, “Low temperature bonding technology for 3D integration”, *Journal of Microelectronics Reliability*, vol. 52, No. 2, pp. 302-311, 2012.
- [2.109] B. Liu, Y. Tian, Y. Liu, and C. Wang, “Rapid formation of full Cu-In intermetallic compounds (IMCs) joints under electric current”, in *Proceeding of 65th Electronic Component and Technology Conference (ECTC)*, San Deogo, USA, 2015, pp. 1780-1784.
- [2.110] J. Wang, E. Besnoin, A. Duckham, S. J. Spey, M. E. Reiss, and etc., “Room-temperature soldering with nanostructured foils”, *Applied physics letters*, vol. 83, No. 19, 2003, PP. 3987-3989.
- [2.111] T. Namazu, K. Ohtani, S. Inoue, and S. Miyake, “Influences of exothermic reactive layer and metal interlayer on fracture behaviour of reactively bonded solder joints”, *Journal of Engineering Materials and Technology*, vol. 137, pp. 031011, 2015.
- [2.112] J. Wang, E. Besnoin, O. M. Knio, and T. P. Weihs, “Investigating the effect of applied pressure on reactive multilayer foil joining”, *Acta Materialia*, vol. 52, pp. 5265-5274, 2014.
- [2.113] S. Kanetsuki, S. Miyake, K. Kuwahara, and T. Namazu, “Influence of bonding pressure on thermal resistance in reactively-bonded solder joints”, *The Japan Society of Applied Physics*, vol. 55, pp. 06GP17, 2016.
- [2.114] S. Ito, S. Inoue, and T. Namazu, “The size limit of Al/Ni multilayer rectangular cuboids for generating self-propagating exothermic reaction on a Si wafer”, *Transducers 2013*, Barcelona, Spain, 2013, pp. 1927-1930.
- [2.115] L.J. Qiu, A. Ikeda, K. Noda, S. Nakai, and T. Asano, “Room-temperature Cu microjoining with ultrasonic bonding of Cone-shape bump”, *Japanese Journal of Applied Physics*, vol. 52, No. 45, pp. 04CB10, 2013.
- [2.116] B.T. Tung, M. Suzuki, F. Kato, S. Nemoto, N. Watanabe, and M. Aoyagi, “Sub-micro-accuracy gold-to-gold interconnection flip-chip bonding approach for electronics - optics heterogeneous integration”, *Japanese Journal of Applied Physics*, vol. 52, No. 4S, pp. 04CB08, 2013.

- [2.117] Y. Xiao, H. Ji, M. Li, and J. Kim, “Ultrasound-assisted brazing of Cu/Al dissimilar metals using a Zn–3Al filler metal”, *Materials & Design*, vol. 52, pp. 740-747, 2013.
- [2.118] J.F. Li, P.A. Agyakwa, C.M. Johnson, D. Zhang, T. Hussain, and D.G. McCartney, “Characterization and solderability of cold sprayed Sn-Cu coatings on Al and Cu substrates”, *Surface and Coatings Technology*, vol. 204, pp. 1395-1404, 2010.
- [2.119] Y. Takaku, K. Makino, K. Watanabe, I. Ohnuma, R. Kainuma, Y. Yamada, and edc., “Interfacial reaction between Zn-Al-based high-temperature solders and Ni substrate”, *Journal of Electronic Materials*, vol. 38, No. 1, pp. 54-60, 2009.
- [2.120] L. Liu, L. Zhou, and C. Liu, “Electroless Ni-W-P Alloy as a Barrier Layer between Zn-based High Temperature Solders and Cu Substrates,” in *Proceeding of 64th Electronic Components and Technology Conference (ECTC)*, Orlando, USA, pp. 1348-1353, 2014.
- [2.121] J. Pstruś, and T. Gancarz, “Interfacial phenomena in Al/Al, Al/Cu, and Cu/Cu joints soldered using an Al-Zn alloy with Ag or Cu additions”, *Journal of Materials Engineering and Performance*, vol. 23, pp. 1614-1624, 2014.
- [2.122] T. Gancarz, J. Pstruś, P. Fima, and S. Mosińska, “Thermal Properties and Wetting Behavior of High Temperature Zn-Al-In Solders”, *Journal of Materials Engineering and Performance*, vol. 21, pp. 599-605, 2012.
- [2.123] J. Feng, X. Songbai, and D. Wei, “Reliability studies of Cu/Al joints brazed with Zn-Al-Ce filler metals”, *Materials & Design*, vol. 42, pp. 156-163, 2012.
- [2.124] A. Haque, B.H. Lim, A.S.M.A. Haseeb, and H.H. Masjuki, “Die attach properties of Zn-Al-Mg-Ga based high-temperature lead-free solder on Cu lead-frame”, *Journal of Materials Science: Materials in Electronics*, vol. 23, no. 1, pp. 115-123, 2012.
- [2.125] C. Leinenbach, F. Valenza, D. Giuranno, H.R. Elsener, S. Jin, and R. Novakovic, “Wetting and Soldering Behavior of Eutectic Au-Ge Alloy on Cu and Ni Substrates”, *Journal of Electronic Materials*, vol. 40, No. 7, pp. 1533-1541, 2011.
- [2.126] S. Lin, M. Tsai, P. Tsai, and B. Hsu, “Formation of alternating interfacial layers in Au-12Ge/Ni joints”, *Scientific Reports*, vol. 4, pp. 4557, 2014.
- [2.127] V. Chidambaram, H.B. Yeung, and G. Shan, “Reliability of Au-Ge and Au-Si eutectic solder alloys for high-temperature electronics”, *Journal of Electronic Materials*, vol. 41, pp. 2107-2117, 2012.
- [2.128] F. Lang, H. Yamaguchi, H. Ohashi, and H. Sato, “Improvement in joint reliability of SiC power devices by a diffusion barrier between Au-Ge solder and Cu/Ni(P)-metalized ceramic substrates”, *Journal of Electronic Materials*, vol. 40, No. 7, pp. 1563-1571, 2011.
- [2.129] J.M. Song, H.Y. Chuang, and Z.M. Wu, “Interfacial reactions between Bi-Ag high-temperature solders and metallic substrates”, *Journal of Electronic Materials*, vol. 35, No. 5, pp. 1041-1049, 2006.

- [2.130] M. Shimoda, T. Yamakawa, K. Shiokawa, H. Nishikawa, and T. Takemoto, “Effects of Ag Content on the Mechanical Properties of Bi-Ag Alloys Substitutable for Pb based Solder”, *Transactions of JWRI*, vol. 41, pp. 51-54, 2012.
- [2.131] J. Cui, R.W. Johnson, and M. Hamilton, “Investigation into the role of different Ni compositions and plating methods on die attach reliability”, in *Proceeding of HiTEM*, Oxford, UK, 2015.
- [2.132] S. Egelkraut, L. Frey, M. Knoerr, and A. Schletz, “Evolution of shear strength and microstructure of die bonding technologies for high temperature applications during thermal aging”, in *Proceeding of 12th Electronics Packaging Technology Conference (EPTC)*, 2010, pp. 660-667.
- [2.133] F.Q. Lang, H. Yamaguchi, H. Nakagawa, and H. Sato, “Solid-State Interfacial Reaction between Eutectic Au-Ge Solder and Cu/Ni(P)/Au Metalized Ceramic Substrate and Its Suppression”, *Journal Materials Science Technology*, vol. 31, No. 5, pp. 445-452, 2015.
- [2.134] S. Kim, K. S. Kim, S. S. Kim, and K. Suganuma, “Interfacial reaction and die attach properties of Zn-Sn high-temperature solders”, *Journal of Electronic Materials*, vol. 38, No. 2, pp. 266-272, 2009.
- [2.135] A. Haque, Y.S. Won, B.H. Lim, A.S.M.A. Haseeb, and H.H. Masjuki, “Effect of Ni Metallization on Interfacial Reactions and Die Attach Properties of Zn-Al-Mg-Ga High Temperature Lead-free Solder”, in *Proceeding of 34th International Electronic Manufacturing Technology Conference*, 2010.
- [2.136] J.N. Lalena, N.F. Dean, and M.W. Weiser, “Experimental investigation of Ge-doped Bi-11Ag as a new Pb-free solder alloy for power die attachment”, *Journal of Electronic Materials*, vol. 31, No. 11, pp. 1244-1249, 2002.
- [2.137] R.W. Johnson and M.C. Hamilton, “SiC Power Device Die Attach for Extreme Environments”, *IEEE Transactions Electron Devices*, vol. 62, No. 2, pp. 346-353, 2015.
- [2.138] J. Cho, S. Mallampati, H. Schoeller, L. Yin, and D. Shaddock, “Developments of Bi-Sb-Cu alloys as a high-temperature Pb-free solder”, in *Proceeding of 65th Electronic Components Technology Conference*, Las Vegas, USA, pp. 1251-1256, 2015.
- [2.139] L.A.N. Melchor, Evaluation of die attach materials for high temperature power electronics applications and analysis of the Ag particles sintering solution, Thesis doctoral.
- [2.140] A.E. Ozmetin, O. Sahin, E. Ongun, and M. Kuru, “Mechanical characterisation of MgB₂ thin films using nanoindentation technique”, *Journal of Alloys and Compounds*, vol. 619, pp. 262-266, 2015.
- [2.141] A.C. Fischer-Cripps, *Nanoindentation (3rd edition)*, Springer, USA, 2011.
- [2.142] M.A. Dudek and N. Chawla, “Nanoindentation of rare earth-Sn intermetallics in Pb-free solders”, *Intermetallics*, vol. 18, pp. 1016-1020, 2010.

- [2.143] T. Takahashi, S. Komatsu, H. Nishikawa, and T. Takemoto, “High-temperature resistant intermetallic compound joints for Si chips and Cu substrates”, *Journal of Electronic Materials*, vol. 39, No. 10, pp. 2274-2280, 2010.
- [2.144] G.Y. Jang, J.W. Lee, and J.G. Duh, “The nanoindentation characteristics of Cu₆Sn₅, Cu₃Sn, and Ni₃Sn₄ intermetallic compounds in the solder bump”, *Journal of Electronic Materials*, vol. 33, No. 10, pp. 1103-1110, 2004.
- [2.145] D. Li, C. Liu, and P.P. Conway, “Characteristics of intermetallics and micromechanical properties during thermal ageing of Sn–Ag–Cu flip-chip solder interconnects”, *Materials Science and Engineering: A*, vol. 391, pp. 95-103, 2005.
- [2.146] H. Tsukamoto, Z. Dong, H. Huang, T. Nishimura, and K. Nogita, “Nanoindentation characterization of intermetallic compounds formed between Sn-Cu (-Ni) ball grid arrays and Cu substrates”, *Materials Science and Engineering: B*, vol. 164, No. 1, pp. 44-50, 2009.
- [2.147] F.X. Che and J.H.L. Pang, “Characterization of IMC layer and its effect on thermomechanical fatigue life of Sn-3.8Ag-0.7Cu solder joints”, *Journal of Alloys and Compounds*, vol. 541, pp. 6-13, 2012.
- [2.148] K.M. Kumar, V. Kripesh, L. Shen, K. Zeng, and A.A. Tay, “Nanoindentation study of Zn-based Pb free solders used in fine pitch interconnect applications”, *Materials Science and Engineering: A*, vol. 423, No. 1-2, pp. 57-63, 2006.
- [2.149] R.R. Chromik, D.N. Wang, A. Shugar, L. Limata, M.R. Notis, and R.P. Vince, “Mechanical properties of intermetallic compounds in the Au-Sn system”, *Journal of Materials Research*, vol. 20, No. 8, pp. 2161-2172, 2005.
- [2.150] F. Gao, T. Takemoto, H. Nishikawa, and A. Komatsu, “Microstructure and Mechanical Properties Evolution of Intermetallics between Cu and Sn-3.5Ag Solder Doped by Ni-Co Additive”, *Journal of Electronic Materials*, vol. 35, No. 5, 2006.

Chapter 3

Deposition and Analysis of Electroless Ni-W-P Coatings

This chapter serves as an introduction to electroless Ni-W-P plating on the aspects of the plating process and main plating parameters. Critical parameters of the electroless plating process were systematically investigated as to their effects on the microstructure and composition of the Ni-W-P coating. Finally, a developed deposition process was established to precisely control the composition of Ni-W-P coatings with reasonable deposition rates.

3.1 Introduction

As discussed in Chapter 2, electroless Ni plating is widely used in microelectronics as a metallisation process due to its low cost, simple process route and uniform metallic coating on various substrates. Pearlstein firstly prepared electroless ternary Ni-W-P films by adding Na_2WO_4 into electroless Ni-P aqueous solution in order to codeposit W with Ni [3.1]. Electroless Ni-W-P plating is a chemical reduction process via chemical reducing agent (NaH_2PO_2) without the aid of external electrical energy in electroless solution. Compared to conventional Ni-P under bump metallisation (UBM), the diffusivity of the atoms in Ni-W-P coatings would be rather low due to the infusibility of W, leading to a slower interfacial reaction with lead-free solders [3.2, 3.3]. Moreover, Ni-W-P coatings also show their improved characteristics in terms of corrosion resistance [3.4, 3.5], hardness [3.5, 3.6], wear [3.4, 3.7] and adhesion strength [3.8]. Therefore, electroless Ni-W-P coatings can be proposed as a good candidate of UBM and worthy to be investigated and further developed in this thesis.

Currently, effects to utilise Ni-W-P coatings as a diffusion barrier in microelectronic packaging were made by some researchers. For instance, Chen *et al.* firstly employed

Ni-W-P coatings (W contents: 14 and 21 wt.%) in molten Sn-58Bi solder with a control specimen of Ni-P alloy [3.2]. It is found that the Ni-W-P with a high W content exhibits superiority to Ni-P UBM for increasing the service lifetime of these solder joints. Moreover, Ni-W-P coatings with varying W contents also reacted with Sn-3.5Ag solders along with their drop/impact test reported by Jang *et al.* [3.9]. Yang *et al.* extended the study to investigate the growth mechanisms of the IMCs formed at the Ni-W-P/Sn-3.5Ag solder interface as well as the tensile strength of these solder joints [3.3]. In addition, some works reported that electroless Ni-W-P alloys show excellent thermal stability at elevated high temperature (400 °C) [3.5, 3.6, 3.9-12], which is considerably suitable for high temperature electronics. However, the interfacial reactions between electroless Ni-W-P coatings and high temperature lead-free solders have not been reported to the author's knowledge yet.

In electroless Ni-W-P plating, the conventional pre-treatment is PdCl₂ activation. However, using this pre-treatment, the plating solution easily decomposed when heated up to 85 °C at a high pH value (above 8.5) for 30 minutes from our initial experiments. This situation frequently happened if the Ni-W-P alloys with high W contents are required. The reason for this decomposition is that the deposition rates on the Pd metal are considerably faster than the rates on Cu surface even after the thickness of Ni-W-P deposits accumulated [3.13]. Therefore, a developed pre-treatment process was in highly demands. Moreover, the effects of various plating parameters, such as plating temperature, plating pH, additives and all constituents in electroless solution, on characteristics of Ni-W-P coatings have not been systematically studied. Particularly for obtaining the Ni-W-P coatings with required compositions in acceptable deposition rates.

In this work, a systematic study was carried out with regard to the effects of electroless plating parameters on characteristics of the Ni-W-P coatings. Their surface morphology and composition were examined with scanning electron microscopes (SEMs) incorporated with energy dispersive X-ray detector (EDX) equipment. Meanwhile, the thicknesses of each Ni-W-P coatings were measured through SEM observations. Hence, the correlation between the properties of these coating including composition, surface evenness, and plating parameters can be established. According to it, an electroless Ni-W-P plating process was developed and optimised to achieve

precise chemical compositions with reasonable deposition rates. Furthermore, the plating mechanisms of Ni-W-P deposit were also discussed.

3.2 Development of electroless Ni-W-P plating

For the initial electroless Ni-W-P plating with a conventional pre-treatment (dilute SnCl_2 and PdCl_2 solution), the solution easily decomposed after 30 minutes when plating temperature and pH value exceed $85\text{ }^\circ\text{C}$ and 8.5. The primary task is to develop an electroless plating process with an excellent stability under harsh conditions (temperature: $90\text{ }^\circ\text{C}$, pH value: 9). This task can be completed through modified pre-treatments in this work. In addition, it is observed that a series of small pinholes or pores occurred in Ni-W-P coatings. Though no works reported the effects of these defects on the performances of diffusion barrier, it still would be ideal to eliminate these defects for their potential bad influence. To prepare a pore-free metallisation, a pin-reliever (sodium lauryl sulphate, SLS) was added in electroless solution.

3.2.1 Experimental details

3.2.1.1 Preparation of electroless Ni-W-P solution

The experimental system for electroless Ni-W-P plating consists of a hotplate embedded with a thermal couple (IKA C-MAG HS 7), water bath in a beaker, sample holders and a high temperature glass pH probe that can work under $95\text{ }^\circ\text{C}$ (Shanghai Boqu Instrument CPH5806-K8S) as illustrated in figure 3-1.

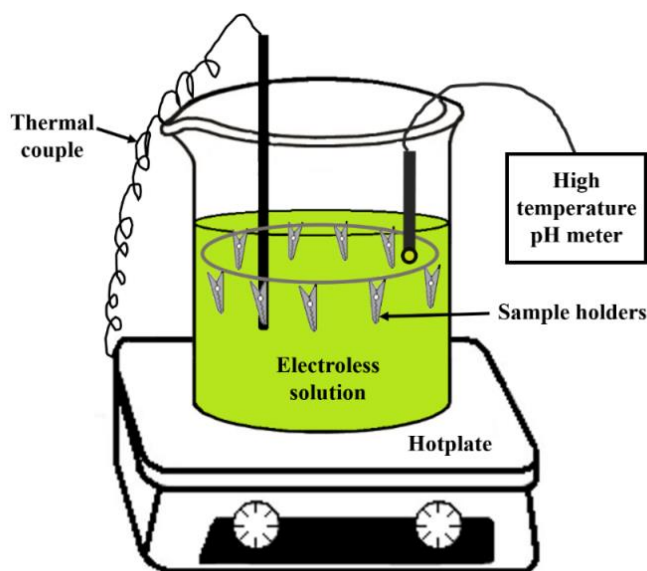


Figure 3-1 Experimental setup of the electroless Ni-W-P plating system.

The real-time temperature of the water bath was constantly monitored with a thermal couple to provide a feedback to the hotplate for temperature control. Meanwhile, the pH value of the water bath was measured and adjusted within a narrow window through the addition of acid (if pH value went high) or alkali solution (if pH value was low). Ten clamps attached to a steel circle wire worked as the sample holders to fix Cu substrates. So a load of small pieces of samples can be deposited in an electroless solution at same time, guaranteeing the consistency of their composition and properties.

The constituents of the electroless Ni-W-P solution include sources of Ni and W ions (nickel sulfate and sodium tungstate), a reducing agent (sodium hypophosphite), and a suitable complexing agent (sodium citrate). Because several chemicals were involved in the electroless bath, the procedure of preparing the solution is quite vital. During the preparation, all chemical reagents dissolved into warm deionized (DI) water (60 °C) for better solubility, and the steps illustrated in figure 3-2 include:

1. Firstly, the specific amounts of nickel sulfate hexahydrate ($\text{NiSO}_4 \cdot 6\text{H}_2\text{O}$) and sodium tungstate dihydrate ($\text{Na}_2\text{WO}_4 \cdot 2\text{H}_2\text{O}$) were weighted by a precise weighting balance and then formed a suspension liquid solution marked A.
2. Then, solution A and sodium citrate dehydrate ($\text{Na}_3\text{C}_6\text{H}_5\text{O}_7 \cdot 2\text{H}_2\text{O}$) solution were mixed together as solution B.
3. After a complete dissolution of all chemicals in solution B, sodium hypophosphite ($\text{NaH}_2\text{PO}_2 \cdot \text{H}_2\text{O}$) solution was slowly added into solution B to obtain the electroless plating solution (solution C) for the following deposition tests. Sodium hypophosphite solution must be added in the final step to prevent decomposition of the bath.

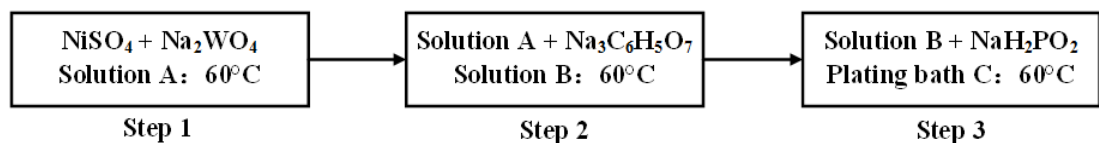


Figure 3-2 Procedures of making up the electroless Ni-W-P plating solution.

3.2.1.2 Pre-treatment

In electroless plating of Ni-W-P UBM with hypophosphite electroless Ni-based solutions, proper pre-treatments on Cu substrates were necessary to catalytically

initiate the substrate. Three approaches were estimated on Cu substrates (length \times width \times thickness: 10 mm \times 10 mm \times 1 mm, 5 pieces for each test) in this work:

1. Catalysing the Cu surface by dilute palladium chloride (PdCl_2) solution.
2. Electrochemically initiating by contacting Cu substrates with active metals (Al).
3. Immersing Cu substrates in a strong reducer (dimethylamine borane: DMAB).

For pre-treatment tests, the formulations and plating conditions of the deposition bath are listed in table 3-1. The stability of plating solution was evaluated with different pre-treatments under a harsh condition (plating temperature: 95 °C, pH value: 9.5) for 2 h.

Table 3-1 Formulations and plating conditions of electroless Ni-W-P plating with various pre-treatments.

Chemical reagents	Composition (g/L)
$\text{NiSO}_4 \cdot 6\text{H}_2\text{O}$	7
$\text{Na}_2\text{WO}_4 \cdot 2\text{H}_2\text{O}$	35
$\text{NaH}_2\text{PO}_2 \cdot \text{H}_2\text{O}$	10
$\text{Na}_3\text{C}_6\text{H}_5\text{O}_7 \cdot 2\text{H}_2\text{O}$	40
Variable (Pre-treatments)	PdCl_2 solution, Al wire, DMAB solution
Plating condition	Temp: 95 °C, pH: 9.5, Time: 2 hours

After the deposition of Ni-W-P metallisation, the adhesion qualities were tested with 3M Scotch 600 and 3M-56 tapes to evaluate the adhesion strength between the coating and substrate after deposition with different pre-treatment methods. The tests complied with ASTM D3359-02 standard [3.14]. Figure 3-3 schematically shows the tape test. Cross cuts were made through the film to the substrates with a gap of 1-2 mm. Then, a tape was applied over the cuts and then stripped off the substrate, providing the qualitative assessment of adhesion quality by the percent of the areas from the detached coating. Table 3-2 provides the classification of adhesion test results in accordance with the areas of detached coating.

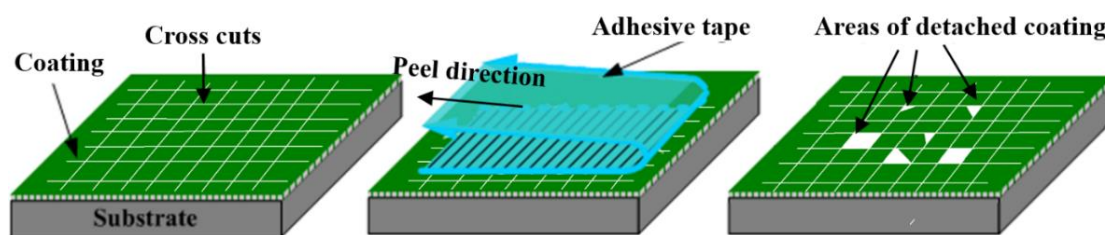


Figure 3-3 The schematic diagram of the tape test on adhesion strength of the Ni-W-P coatings.

Table 3-2 Classification of adhesion test results [3.14].

Classification	Percent area removed
5B	0% None
4B	Less than 5%
3B	5 - 15%
2B	15- 35%
1B	35 – 65%
0B	Greater than 65%

3.2.1.3 Pinhole reliever (sodium lauryl sulphate)

In the trial coatings with various pre-treatment methods, Ni-W-P metallisation embeds numerous voids. Hence, proper methods to eliminate these voids in coatings are essential to ensure the quality of Ni-W-P deposits. Sodium lauryl sulphate (SLS, $\text{NaC}_{12}\text{H}_{25}\text{SO}_4$) was added in plating solution as a pinhole reliever. The effects of SLS content on electroless Ni-W-P coatings were investigated by running the deposition tests with progressively increasing contents of SLS in electroless solution under the same plating conditions. The specific formulations and plating conditions of this bath solution are listed in table 3-3. The substrates for electroless plating were Cu sheets (length \times width \times thickness: 5 mm \times 5 mm \times 1 mm, eight pieces for each test). The surface morphology, composition and thickness of these Ni-W-P deposits were analysed by a FEG-SEM (FEI, Sirion 200 SEM) incorporated with EDX equipment. At least three random EDX points were severally selected on three samples for a same type of Ni-W-P deposits to obtain reliable composition results.

Table 3-3 Formulations and plating conditions of electroless Ni-W-P plating with different SLS concentrations.

Chemical reagents	Composition (g/L)
$\text{NiSO}_4 \cdot 6\text{H}_2\text{O}$	7
$\text{Na}_2\text{WO}_4 \cdot 2\text{H}_2\text{O}$	35
$\text{NaH}_2\text{PO}_2 \cdot \text{H}_2\text{O}$	10
$\text{Na}_3\text{C}_6\text{H}_5\text{O}_7 \cdot 2\text{H}_2\text{O}$	40
Variable (SLS)	0.1, 0.3, 0.5, and 1 mg/L
Plating condition	DMAB pre-treatment, pH: 9, 90 °C, 30 minutes

3.2.2 Results and discussions

3.2.2.1 Effects of pre-treatments

The first pre-treatment approach was electrochemically initiation by contacting specimens with active metals (Al wire). As an Al wire was attached to Cu surfaces, the reducing agent broke down on this wire. The released electrons flow to the surface of Cu since it has a more positive potential than this metal and are used to reduce Ni^{2+} to metallic Ni. Once the Cu surface was covered with a thin layer of Ni, the reaction can keep going without the wire anymore. This approach is the simplest and cheapest method for initiating the electroless Ni-W-P plating on Cu specimens with a large area. However, for small samples (length < 20mm), the metal wire was hard to be fixed at the Cu surfaces for their initiation reactions. Based on the experimental results, the deposition can keep reacting for 2 hours at a temperature and pH value of 95 °C and 9.5, respectively.

For the samples with small dimensions (length < 20mm), DMAB was employed as a pre-treatment. The oxidation reaction of DMAB initiates on the Cu surface to provide electrons, which were then accepted by Cu substrates to form an electron transferring. Thus, Cu substrates were finally activated to be successfully deposited with Ni-W-P coatings. It is also observed that the electroless Ni-W-P solution can keep stable for at least 2 hours under the harsh plating condition. Because DMAB (boiling point: 62 °C)

is easy to evaporate under a warm temperature, leaving no rooms for the aggregation centres for the deposition of Ni-W-P alloys in the bath solution. These approaches both simplified the process of pre-treatment from two steps (sensitisation with dilute stannous chloride solution and then activation with dilute palladium chloride solution) of the PdCl_2 approach to only one catalytic step.

In addition, the adhesion qualities of the Ni-W-P coatings with above pre-treatments were assessed by tape tests (illustrated in figure 3-3). After tape tests, all samples exhibit a same characteristic as shown in figure 3-4. The edges of the cuts were smooth and none of the squares of the lattices was detached (0% area removed), which can be classified as the best quality: Classification 5B according to ASTM D3359-02 standards (Table 3-2).

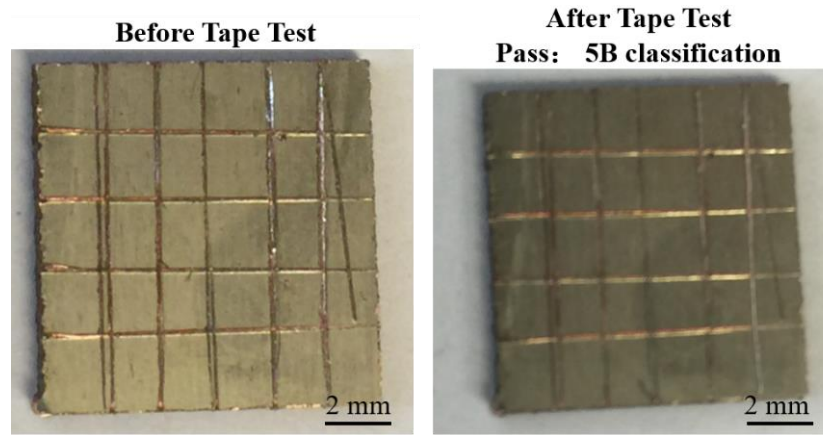


Figure 3-4 An example of the tape test results on Ni-W-P coatings ($\sim 10 \mu\text{m}$ thickness).

According to experimental results, the advantages and disadvantages of the above approaches are summarised and listed in table 3-4.

Table 3-4 Comparisons of the different pre-treatment approaches.

Methods	Advantages	Disadvantages	Substrates size
PdCl_2	Suitable for various substrates, conventional usage.	Unstable bath solution, unstable deposition.	Samples with various sizes.
Al wire	Simple process, cheap, stable deposition.	Unsuitable for small specimens.	Large-area samples
DMBA	Simple process, stable deposition.	DMAB chemical needs to be storage in a fridge	Samples with various sizes.

After comparing these pre-treatment methods, DMAB acting as a strong reducing agent was used in this thesis for its advantages of simple process, good adhesion strength and excellent improvement in bath stability. The procedures of all electroless Ni-W-P plating are summarised in figure 3-5. Prior to catalytic reaction, the oil, oxidise and contaminations on Cu substrates need to be totally removed. After storing samples in DMAB solution for 5 minutes, these samples can be electroless plated in plating bath. After electroless plating, the Ni-W-P deposits are cleaned and dried for the following observations.

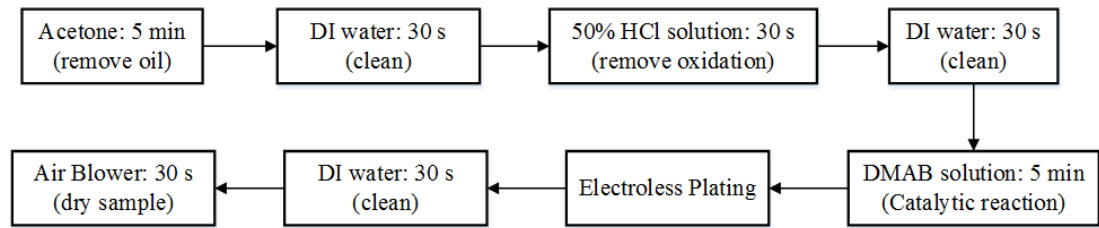


Figure 3-5 Procedures of pre-treatment process of electroless Ni-W-P plating on Cu substrates.

3.2.2.2 Effects of sodium lauryl sulphate (SLS)

In figure 3-6 a), a number of nano-sized pinholes and small pores were observed on Ni-W-P deposits. These defects attribute to the absorption of hydrogen bubbles within the surface of deposits. To obtain pore-free Ni-W-P coatings, a pin-reliever (SLS) was added in electroless solution to investigate its effects on microstructure of Ni-W-P deposits.

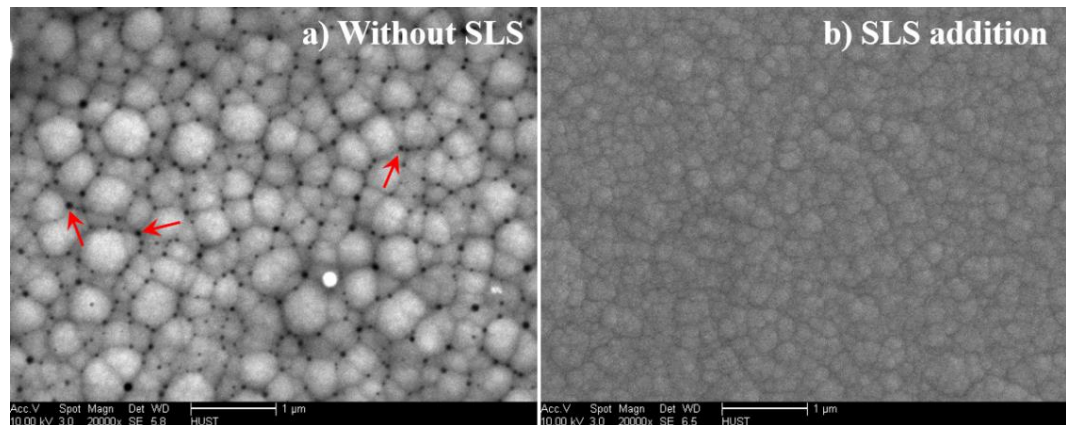


Figure 3-6 The surface morphologies of the Ni-W-P coatings with a) no additives; b) SLS addition (concentration: 0.3 mg/L).

The surface morphologies of the electroless Ni-W-P metallisation with and without SLS additive are presented in figure 3-6. A lot of pinholes or pores were observed on deposition surface, which generally form along the boundaries of Ni-W-P nodules

(nodule size: $\sim 0.4 \mu\text{m}$) as indicated with red arrows in figure 3-6 a). With a tiny amount of SLS (concentration: 0.3 mg/L), the Ni-W-P layer shows a rather compact structure, and is free from any pores or pinholes. Moreover, the surface of Ni-W-P metallisation is smoother with a smaller size of the Ni-W-P nodules ($0.15 \mu\text{m}$ approximately).

The effects of SLS concentration on composition and deposition rates of the Ni-W-P coatings are shown in figure 3-7. Each point was collected from three random samples with at least nine different evaluations. The error bars in W and P contents represent standard deviations. It can be found that the contents of P and W remain stable, at about 10 wt.% and 22 wt.%, respectively, with the concentration of SLS addition increased from 0 to 1 mg/L. This indicated that the addition of SLS has a minimal effect on the composition of the Ni-W-P deposits. However, SLS concentration posed a notable effect on the deposition rate. The deposition rate rises to the highest ($14 \mu\text{m/h}$) when SLS concentration reaches 0.3 mg/L , and then decreases to $9 \mu\text{m/h}$ with more addition of SLS up to 1 mg/L .

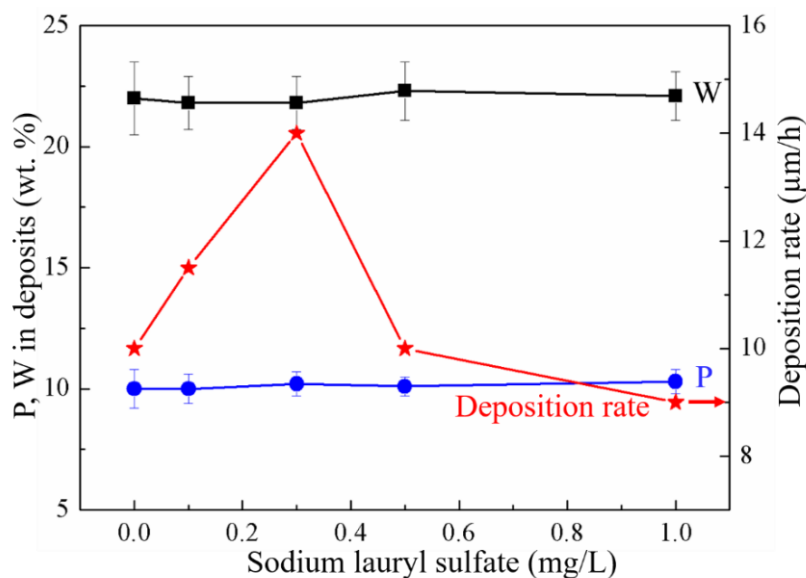


Figure 3-7 Effects of SLS concentration on composition and deposition rate of the Ni-W-P deposits.

3.3 Effects of plating parameters on electroless Ni-W-P deposits

After establishing a proper electroless plating process, it is essential to elaborate the effects of various coating parameters, such as formulations of the bath, plating temperature and plating pH, on the compositions and deposition rates of Ni-W-P

deposits. As such, electroless Ni-W-P metallisation with various compositions can be prepared for further investigations.

3.3.1 Experimental details

3.3.1.1 Constituents of electroless Ni-W-P plating solution

The plating solution composed with $\text{NiSO}_4 \cdot 6\text{H}_2\text{O}$, $\text{Na}_2\text{WO}_4 \cdot 2\text{H}_2\text{O}$, $\text{NaH}_2\text{PO}_2 \cdot \text{H}_2\text{O}$, $\text{Na}_3\text{C}_6\text{H}_5\text{O}_7 \cdot 2\text{H}_2\text{O}$, and trace additive of SLS ($\text{NaC}_{12}\text{H}_{25}\text{SO}_4$). To investigate the effects of these main chemicals in the plating solution, a set of electroless Ni-W-P plating with various formulations were conducted on Cu sheets (length \times width \times thickness: 5 mm \times 5 mm \times 1 mm) as listed in table 3-5. According to previous works [3.15], the range of the $\text{NiSO}_4 \cdot 6\text{H}_2\text{O}$, $\text{Na}_2\text{WO}_4 \cdot 2\text{H}_2\text{O}$, $\text{NaH}_2\text{PO}_2 \cdot \text{H}_2\text{O}$ and $\text{Na}_3\text{C}_6\text{H}_5\text{O}_7 \cdot 2\text{H}_2\text{O}$ were set to be 7-40 g/L, 35-75 g/L, 10-30 g/L, and 40-100 g/L, respectively. This is for achieving good coating performance, acceptable deposition rate and stability of plating solution. From table 3-5, by analysing the deposition results from the group consisting B, F, G and H, the effects of NiSO_4 can be investigated. Similarly, the effects of Na_2WO_4 , NaH_2PO_2 , and $\text{Na}_3\text{C}_6\text{H}_5\text{O}_7$ in Ni-W-P deposits can be studied by the result analysis among these groups of (A, D, E), (G, I, J, K) and (A, B, C), respectively.

Table 3-5 Formulations and plating conditions of electroless Ni-W-P plating solution (unit: g/L).

Chemicals	A	B	C	D	E	F	G	H	I	J	K
$\text{NiSO}_4 \cdot 6\text{H}_2\text{O}$	7	7	7	7	7	20	30	40	30	30	30
$\text{Na}_2\text{WO}_4 \cdot 2\text{H}_2\text{O}$	35	35	35	55	75	35	35	35	35	35	35
$\text{NaH}_2\text{PO}_2 \cdot \text{H}_2\text{O}$	10	10	10	10	10	10	10	10	18	25	30
$\text{Na}_3\text{C}_6\text{H}_5\text{O}_7 \cdot 2\text{H}_2\text{O}$	40	75	100	40	40	75	75	75	75	75	75
SLS	3×10^{-4}										
Parameter	DMAB pre-treatment, 90 °C, pH: 8, Plating time: 30 minutes.										

3.3.1.2 Plating temperature

The effects of plating temperature ranging from 70 °C to 90 °C on electroless Ni-W-P deposits were also investigated. The specific formulations of this bath solution are A solution listed in table 3-5. The plating pH value is 9 and the plating time is 30 minutes.

Eight pieces of Cu substrates (1 mm thickness) with an area size of 5mm × 5mm were used for each type of deposition tests.

3.3.1.3 pH of electroless Ni-W-P solution

Similarly, the formulation of the electroless solution to investigate the effects of pH values on composition and microstructure of Ni-W-P coatings was also Solution A in table 3-5. The plating temperature and plating time is 90 °C and 30 minutes, respectively. The plating pH values of the deposition bath were controlled precisely at 7, 8, and 9 with a narrow window of 0.2 by additions of dilute H₂SO₄ or NaOH solution. For each deposition tests, eight pieces of Cu sheets (1mm thickness, 99.9% purity) were used as substrates.

3.3.2 Results

3.3.2.1 The effects of nickel sulfate

Figure 3-8 shows the surface morphologies of Ni-W-P coatings with varying nickel sulfate concentrations (7, 20, 30, 40 g/L). The surfaces of all Ni-W-P deposits exhibit smooth morphologies with few scattered nodules. It is a quite common phenomenon for nodules formation during electroless plating. Limited pores were observed at the boundaries of Ni-W-P nodules, which resulting from the aggregations of hydrogen bubbles on Ni-W-P surface during deposition [3.2]. It is noteworthy that the Ni-W-P deposit with a NiSO₄ concentration of 40 g/L shows a ‘cauliflower’ morphology with the finest nodules (< 160 nm). The nodules size is significantly smaller than the one of the other Ni-W-P coatings (ranges from 300 nm to 1 μm) in figure 3-8 a-c).

The changes in the surface morphologies of these Ni-W-P coatings may attribute to their P contents. It is widely known that the P content in the electroless Ni-P coatings has a great influence in determining its structure. For instance, if the P content exceeds 8 wt.%, the lattice strain of Ni (1 1 1) grains increases [3.16], leading to a Ni-P deposit with an amorphous structure. As for the ternary Ni-W-P metallisation, a mix structure (amorphous/nanocrystalline) appears when its P content decreases to 8 wt.% [3.17]. The P content of the Ni-W-P deposit corresponding to figure 3-8 d) is approximately 6.5 wt.%, certainly revealing a mix structure.

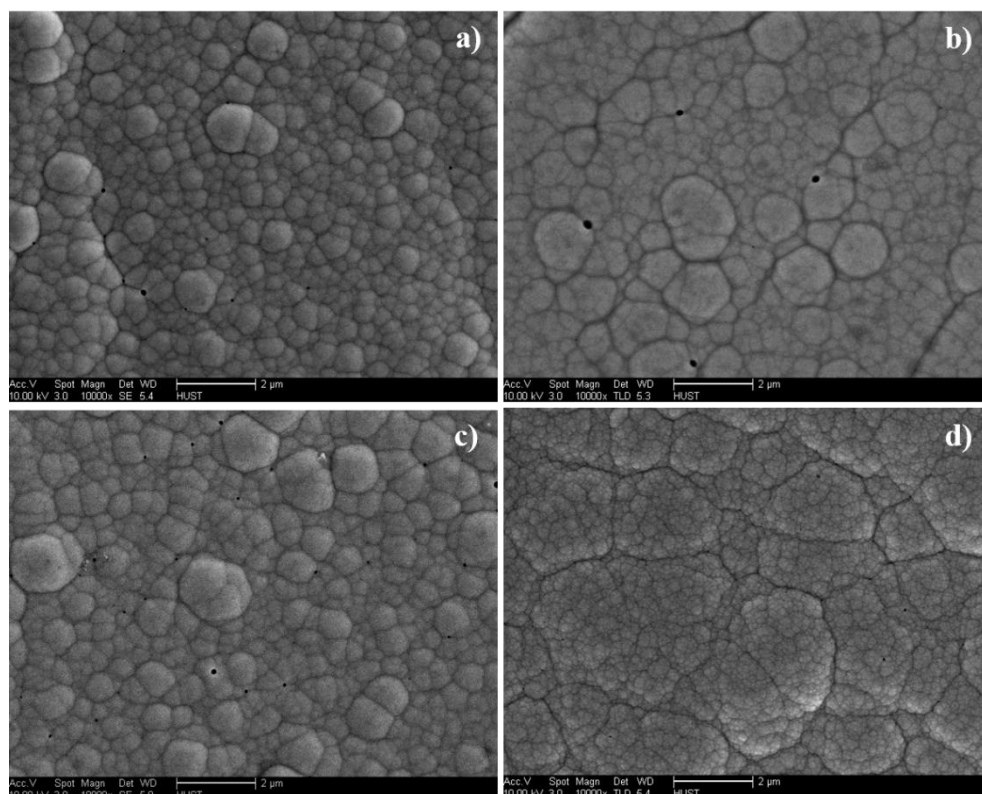


Figure 3-8 The surface morphologies of the Ni-W-P deposits using different concentrations of $\text{NiSO}_4 \cdot 6\text{H}_2\text{O}$: a) 7 g/L, b) 20 g/L, c) 30 g/L, d) 40 g/L.

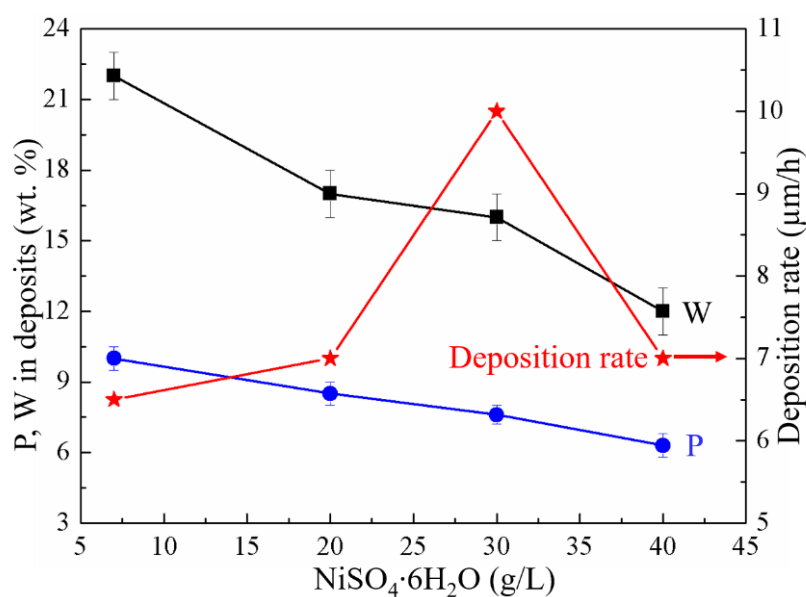


Figure 3-9 Effects of $\text{NiSO}_4 \cdot 6\text{H}_2\text{O}$ concentration on composition and deposition rate of the Ni-W-P deposits.

Figure 3-9 illustrates the influence of NiSO_4 on the composition of electroless coating and deposition rate. From figure 3-9, the increase in NiSO_4 concentration from 7 to 40 g/L leads to a continuous declination in the W and P content of the Ni-W-P deposits. However, the deposition rate rises to a maximum of 10 $\mu\text{m/h}$ at 30 g/L NiSO_4 .

concentration, and then sharply decreases to 7 $\mu\text{m/h}$ when NiSO_4 concentration continually increases to 40 g/L.

3.3.2.2 The effects of sodium tungstate

The surface morphologies of Ni-W-P deposits with different concentrations of sodium tungstate (35, 55, 75 g/L) are shown in figure 3-10. Generally, all Ni-W-P coatings consist of nodular structures, and the size ranges of nodular diameters are within 0.5 - 1 μm . The differences in their microstructure are hardly distinguished among these ternary Ni-W-P deposits as the P contents in these deposits are similar.

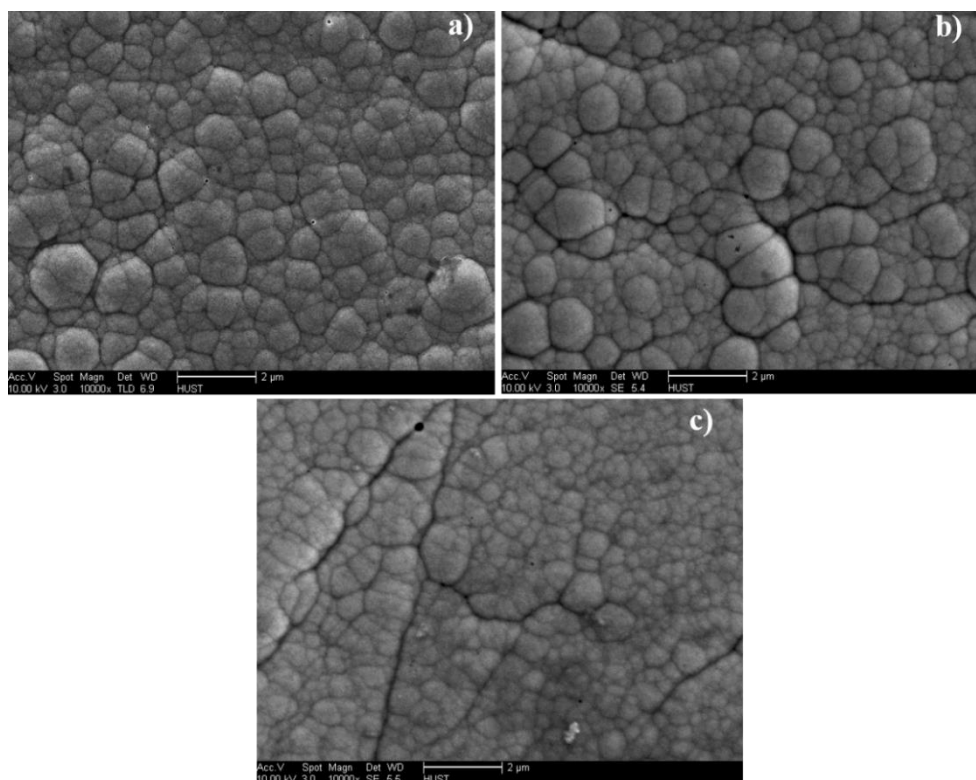


Figure 3-10 The surface morphologies of the Ni-W-P deposits using different concentrations of $\text{Na}_2\text{WO}_4 \cdot 2\text{H}_2\text{O}$: a) 35 g/L, b) 55 g/L, c) 75 g/L.

Figure 3-11 illustrates the influence of Na_2WO_4 on the composition of Ni-W-P coatings and deposition rate. With an increase in Na_2WO_4 concentration, the W content of Ni-W-P deposits increases gradually from 19 to 27 wt.%. But the P content in these coatings was relatively stable, about 8 wt.% in all deposited specimens. It is also found that the Na_2WO_4 concentration can alter the deposition rate significantly. The deposition rate peaked at Na_2WO_4 concentration of 55 g/L (15 $\mu\text{m/h}$) and then dropped greatly when addition of Na_2WO_4 reached 75 g/L (12 $\mu\text{m/h}$).

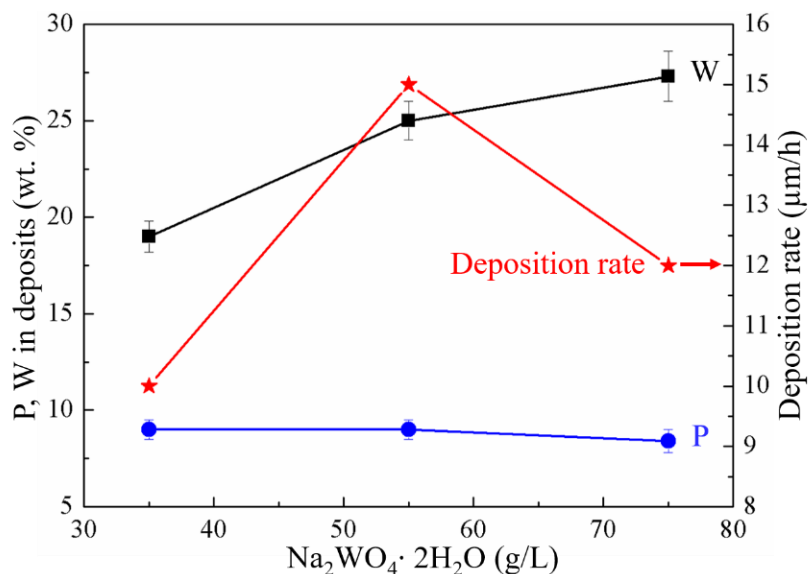


Figure 3-11 Effects of $\text{Na}_2\text{WO}_4 \cdot 2\text{H}_2\text{O}$ concentration on composition and deposition rate of the Ni-W-P deposits.

3.3.2.3 Effect of sodium hypophosphite

The surface morphologies of the Ni-W-P coatings with varying sodium hypophosphite concentrations are presented in figure 3-12.

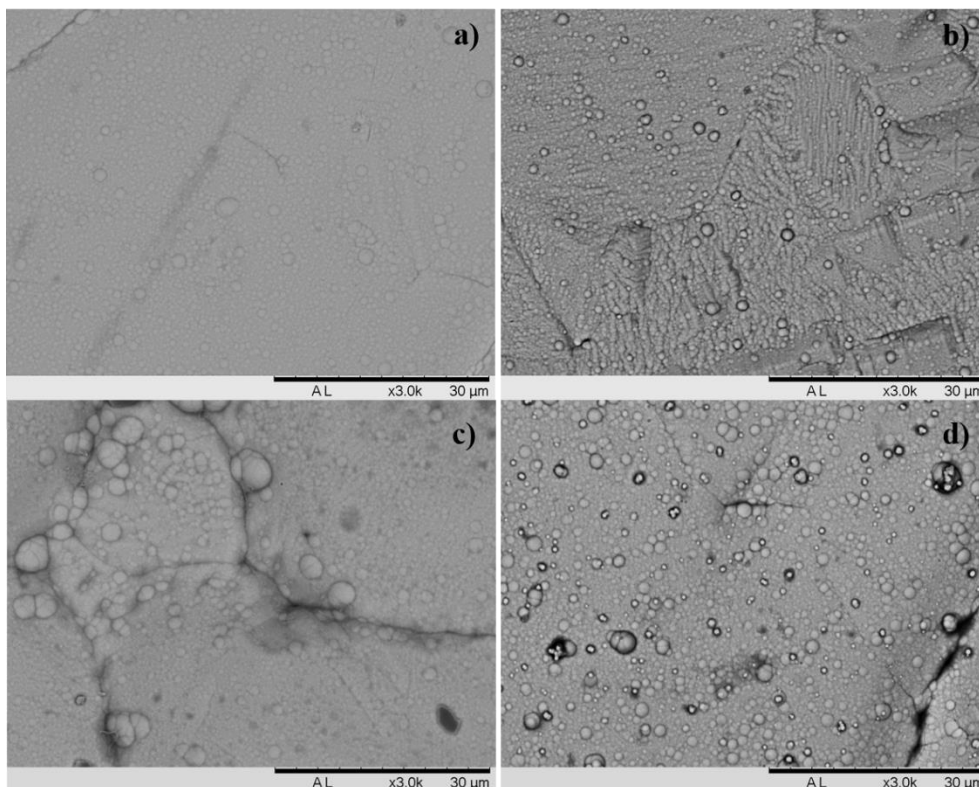


Figure 3-12 The surface morphologies of the Ni-W-P coatings using different concentrations of $\text{NaH}_2\text{PO}_2 \cdot \text{H}_2\text{O}$: a) 10 g/L, b) 18 g/L, c) 25 g/L, d) 30 g/L.

All surfaces contain a great number of individual and agglomerated nodules. However, some scattered nodules are observed with a bigger size ($\sim 6 \mu\text{m}$) on the Ni-W-P

coatings corresponding to figure 3-12 c). Notably, the substrate for this deposition was rough copper foils on ceramic substrates, which contributes to some tiny grooves on deposit surfaces.

Figure 3-13 illustrates the effects of NaH_2PO_2 concentration on the deposition of Ni-W-P coatings. It is shown that the P content and the deposition rate of the Ni-W-P coatings both grow continually with the increasing NaH_2PO_2 concentration (10-30 g/L). The P content increases from 8 to 15 wt.% and the deposition rate raises from 9 to 16 $\mu\text{m/h}$ when NaH_2PO_2 concentration grows to 30 g/L. In contrast, the W content declined gradually from 16 wt.% to 7 wt.% approximately.

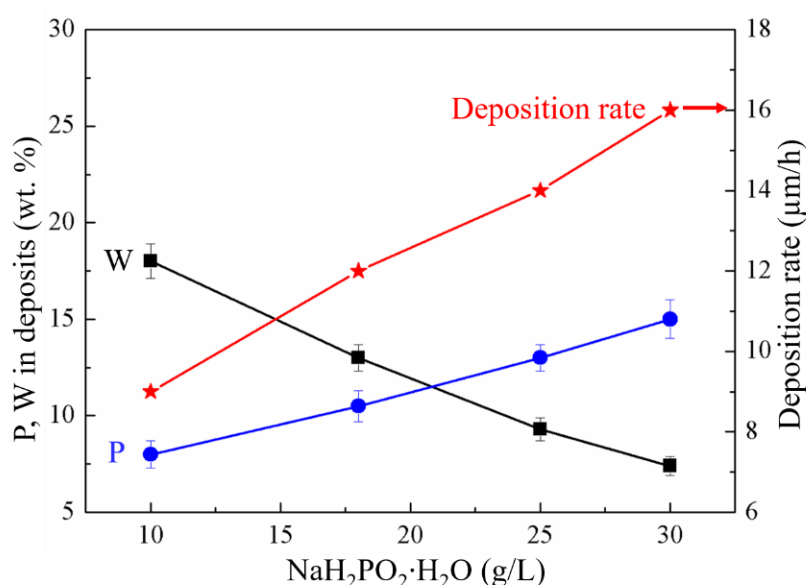


Figure 3-13 Effects of $\text{NaH}_2\text{PO}_2 \cdot \text{H}_2\text{O}$ concentrations on composition and deposition rate of the Ni-W-P deposits.

3.3.2.4 The effects of sodium citrate

In figure 3-14, the surface morphologies of the Ni-W-P coatings using different concentration of sodium citrate (40, 75, 100 g/L) are presented. Besides some tiny bumps occurred in figure 3-14 c), the surface morphologies of all Ni-W-P coatings are quite similar to the others with nodular sizes ranging from 0.5 to 1.5 μm .

Figure 3-15 illustrates the effects of $\text{Na}_3\text{C}_6\text{H}_5\text{O}_7$ concentration on the electroless Ni-W-P deposits. When $\text{Na}_3\text{C}_6\text{H}_5\text{O}_7$ concentration raises from 40 to 100 g/L, the contents of W and P in Ni-W-P alloys grow continuously to 26 wt.% and 11 wt.%, respectively. However, the deposition rate dropped sharply from 10 to 5 $\mu\text{m/h}$ with increasing concentration of $\text{Na}_3\text{C}_6\text{H}_5\text{O}_7$. This decrease in the deposition rate can be explained by

the buffering function of $\text{Na}_3\text{C}_6\text{H}_5\text{O}_7$ for coordination with nickel ions (Ni^{+2}). Therefore, the Ni^{+2} concentration in the bath solution decreased significantly, resulting in a significant decrease of Ni content in the Ni-W-P coatings and the distinct impediment on the deposition reaction. Notably, in previous tests, addition of another buffering agent, ammonium sulfate ($(\text{NH}_4)_2\text{SO}_4$), in plating bath can achieve a low W content (around 5 wt.%) with a good surface finishing, which was utilised in Chapter 4.

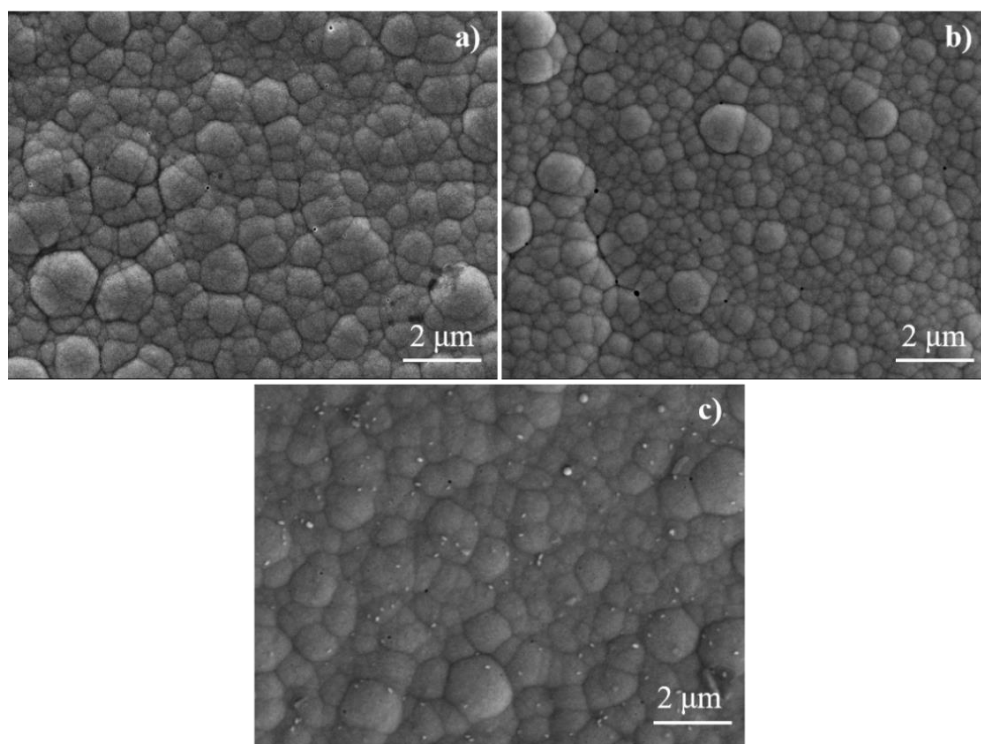


Figure 3-14 The surface morphologies of the Ni-W-P coatings using different concentrations of $\text{Na}_3\text{C}_6\text{H}_5\text{O}_7 \cdot 2\text{H}_2\text{O}$: a) 40 g/L, b) 75 g/L, c) 100 g/L.

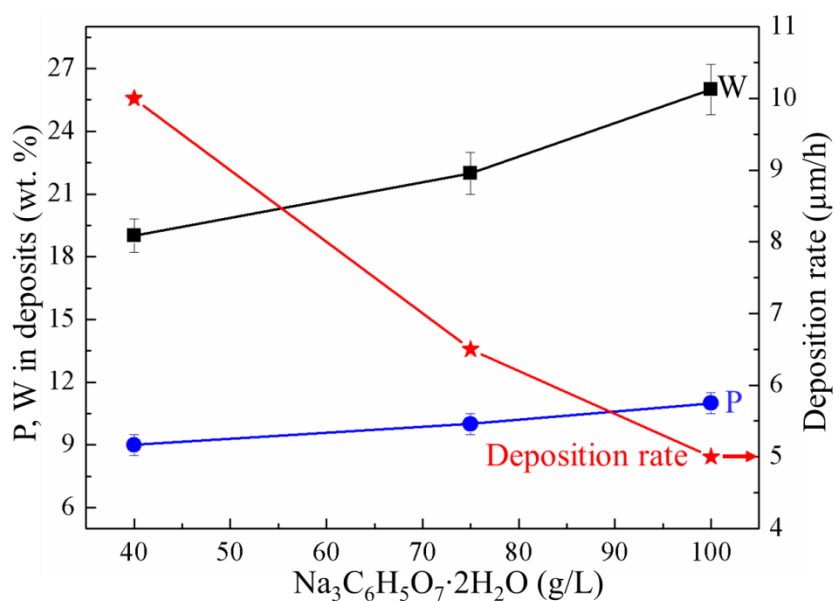


Figure 3-15 Effects of $\text{Na}_3\text{C}_6\text{H}_5\text{O}_7 \cdot 2\text{H}_2\text{O}$ concentrations on chemical composition and deposition rate of the Ni-W-P deposits.

3.3.2.5 Effects of plating temperature

The surface morphologies of the ternary Ni-W-P alloys deposited under various plating temperature (70, 80, and 90 °C) were observed with a FEG-SEM, and the corresponding microstructure are shown in figure 3-16. When electroless plated at the lowest temperature of 70 °C, the surface of the Ni-W-P coating shows a rather smooth and almost nodules-free morphology. If plating temperature increased to 80 °C, a number of nodules with a bigger size (around 1.3 μm) start to emerge on Cu substrate. For Ni-W-P deposited at the highest temperature (90 °C), the surface of the Ni-W-P samples is fully covered with the nodules. Moreover, this nodular size of ternary Ni-W-P deposit is coarser (nodular size: 3 μm approximately) as compared to the smoother deposit (nodule size: ~1.3 μm) obtained from ternary Ni-W-P plating bath in 80 °C.

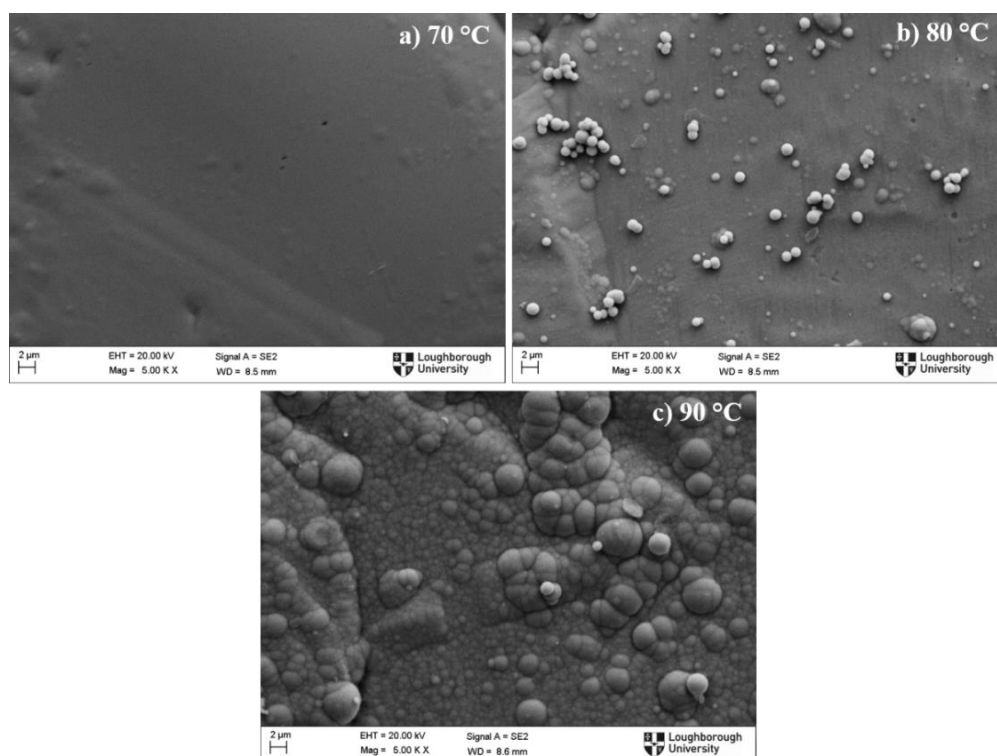


Figure 3-16 The surface morphologies of the Ni-W-P coatings with different plating temperature: a) 70 °C; b) 80 °C; c) 90 °C.

The increase in modulus size can be explained by the significant increase of the deposition rate from 4 to 10 μm/h with an increasing plating temperature as illustrated in figure 3-17. The rapid formation of nuclei and subsequent growth of the electroless Ni-W-P coatings promote the nodularity of deposits. Figure 3-17 illustrates the effects of temperature on Ni-W-P deposits. The W content increases slightly from 18 to 22 wt.% with an increasing plating temperature from 70 to 90 °C. Generally, the plating

temperature does not have a great influence on P content in the deposited Ni-W-P alloys as all P contents is around 10 wt.%.

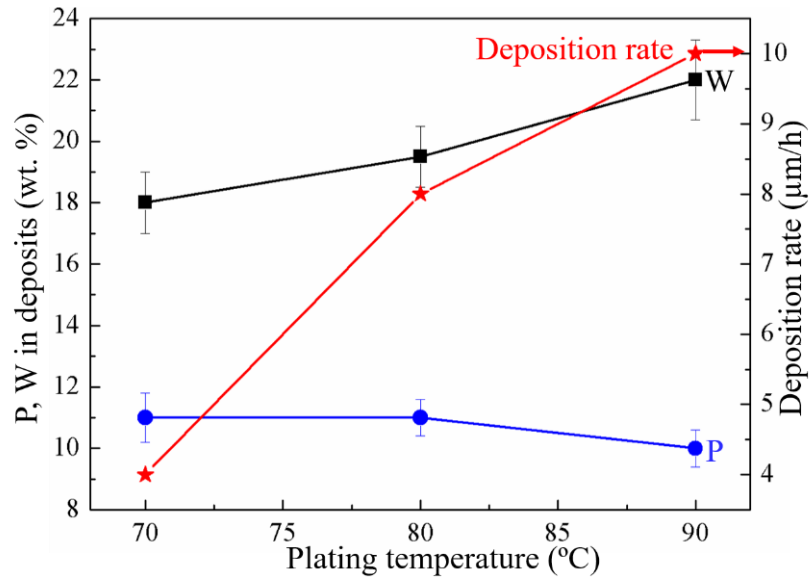


Figure 3-17 Effects of plating temperature on composition and deposition rate of the Ni-W-P deposits.

3.3.2.6 Effects of pH values

The effects of plating pH on the microstructure and composition of Ni-W-P alloys are both presented in figure 3-18 and figure 3-19. Notably, due to the spontaneous decompositions of Ni-W-P solution when pH value exceeds 9.5, only the Ni-W-P samples deposited with the pH values ranging from 7-9 are discussed in this section.

In figure 3-18, the surface morphologies of the Ni-W-P coatings plated with different pH values (7, 8, and 9) are quite similar in their nodules characteristics. The average sizes of the nodules in these Ni-W-P deposits moderately decreased from 1.2 μm to 0.7 μm with increasing pH values. This may attribute to the slight decrease of P content of these Ni-W-P deposits.

In figure 3-19, an increasing pH value from 7 to 9 leads to a significant increase in the W content ranging from 4.5 to 22 wt.% in the Ni-W-P deposits. This can be explained that the reduction ability of sodium hypophosphite declines for the less Ni deposition, resulting in a relatively high content of tungsten. Moreover, the weakening reduction ability also leads to a slight decrease of P in the Ni-W-P deposits from 12 to 10 wt.%. Under various pH values, a maximum deposition rate (12 μm/h) can be achieved at pH 7, whilst the deposition rate decreases at pH 9 as the coordinating ability of sodium citrate with nickel ions deteriorates under higher pH values.

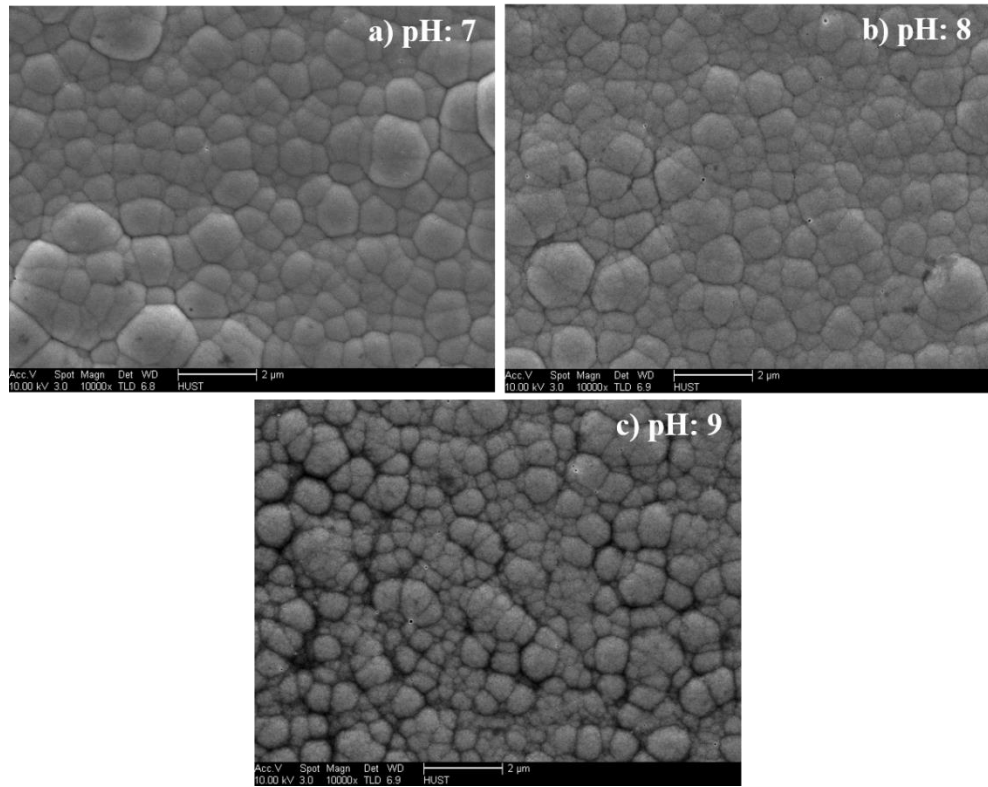


Figure 3-18 The surface morphologies of the Ni-W-P coatings with different pH: a) 7; b) 8; c) 9.

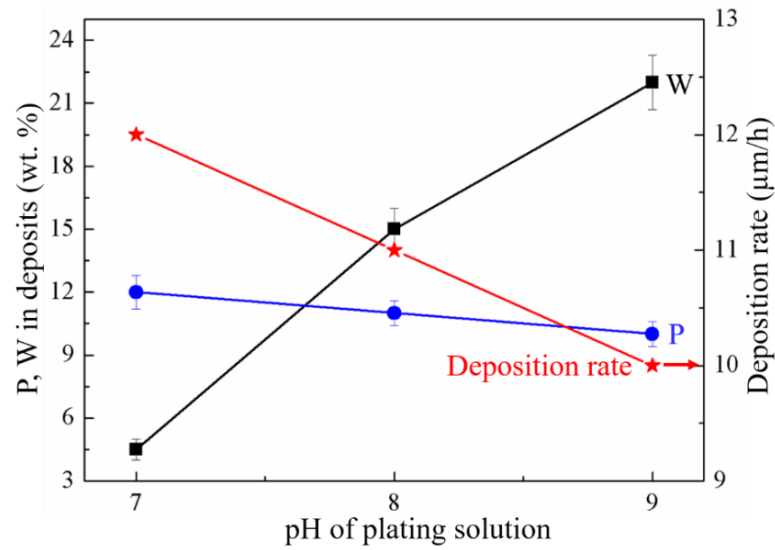


Figure 3-19 Effects of pH values on composition and deposition rate of the Ni-W-P deposits.

3.3.3 Discussions

3.3.3.1 Control of tungsten content in Ni-W-P coatings

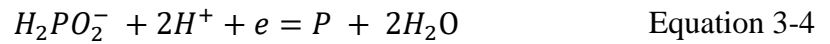
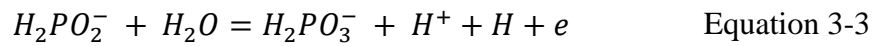
From the experimental results, the W contents of the electroless Ni-W-P deposits were precisely controlled through the adjustments of plating parameters, such as plating

temperature, plating pH, and the chemical concentrations of Ni-W-P plating solution. Among these parameters discussed above, only the trace additive of SLS has no effects on W content of the Ni-W-P deposits.

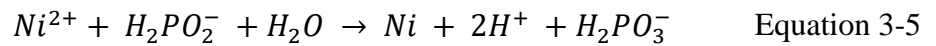
During electroless Ni-W-P plating, W atoms are incorporated into nickel matrix based on the catalytic reaction in equation 3-2.



The electrons for reduction of metallic tungsten are derived from $H_2PO_2^-$ of sodium phosphorus as described in equation 3-3, which means the addition of NaH_2PO_2 can provide more electrons for W reductions. Instead, as observed in figure 3-13, the W contents in the electroless Ni-W-P deposits sharply decrease from 18 to 7.5 wt.% with an increase in NaH_2PO_2 concentration from 10 to 30 g/L. This can be explained by the absorption electrons for the depositions of phosphorus substance. Equation 3-4 also describes the reduction phenomenon of $H_2PO_2^-$ into P substance.



Similarly, the increasing concentration of nickel sulfate also significantly decrease the W contents from 22 to 12 wt.%. The concentration of Ni^{2+} increases and therefore consumes the $H_2PO_2^-$ concentration in the electroless solution. This will reduce the free electrons for the reduction reaction of WO_4^{2-} into metallic W.



Moreover, the formation of the complex between $Na_3C_6H_8O_7$ and Ni^{2+} causes a largely decrease in the dissociative Ni^{2+} concentration in the electroless Ni-W-P solution when $Na_3C_6H_8O_7$ concentration increased from 40 to 100 g/L (see figure 3-15). Therefore, the relative concentration of WO_4^{2-} among all free radicals (Ni^{2+} , WO_4^{2-} , $H_2PO_2^-$, e and etc.) raised and induced a increasing W content in Ni-W-P deposits from 19 to 26 wt.%.

Besides, the addition of Na_2WO_4 can directly increase the concentration of free WO_4^{2-} in electroless Ni-W-P solution. This leads to a growing content of metallic tungsten in electroless Ni-W-P alloys. When the Na_2WO_4 concentration grows from 35 to 75 g/L, the W content in the Ni-W-P deposits increases from 19 and 27 wt.%.

Apart from the chemical reagents of electroless Ni-W-P solution, the pH values and plating temperature also demonstrate their abilities in rising W content of Ni-W-P alloys. The pH value of the plating bath has the strongest ability in increasing W content as the W content in the deposits sharply increased from 4.5 wt.% at pH 7 to 22 wt.% at pH 9 (see figure 3-19). The W content and deposition rate both rise with an increasing temperature up to 90 °C, which attribute to the increasing driving force of the reducing agent [3.18]. Hung *et al.* [3.19] reported a similar result in another alkaline bath solution deposited in a temperature range from 50 °C to 90 °C at pH 9.

Hence, the effects of various factors that may affect the percentage of W in Ni-W-P electroless coating are summarised in table 3-8.

Table 3-6 Summary of coating parameters on the proportion of W in Ni-W-P deposits.

	NaH ₂ PO ₂	NiSO ₄	Na ₂ WO ₄	Na ₃ C ₆ H ₅ O ₇	Temperature	pH values
W Content	Negative correlation	Negative correlation	Positive correlation	Positive correlation	Positive correlation	Positive correlation

3.3.3.2 Control of phosphorus content in Ni-W-P coatings

The control of phosphorus content in electroless Ni-W-P deposits is rather crucial as the P content plays a vital role in the crystal structure of the coating. High P content (above 10 wt.%) in Ni-W-P deposit can lead to formations of amorphous structure in the metallisation, while low content of P results in a crystalline structure.

Among the plating parameters, SLS and sodium acetate barely affect the co-deposition of P in electroless Ni-W-P metallisation. For plating temperature and pH, they both have slight effects on the increase of P content in Ni-W-P alloys. The increase in temperature and pH value of the bath can improve the driving force of the reducing agent (NaH₂PO₂). However, NaH₂PO₂ is the supplier of electrons and phosphorus substance in electroless plating process. Hence, the rise in temperature and pH value would reduce the amount of free H₂PO₂⁻ for P deposition in the solution. And it leads to a small reduction in P contents of the ternary alloys.

Moreover, the constituents of electroless plating solution can also alter the content of P in the coating. The deposition of P atoms arises from the catalytic reaction (Equation 3-

2 and 3-3), which derives from the electron and H_2PO_2^- of NaH_2PO_2 . Figure 3-13 illustrated that the P content significantly increases from 7.5 wt.% to 14 wt.% with the increasing nickel phosphate concentration in electroless solution. The deposition rate is nearly proportional to the concentration of NaH_2PO_2 reagent, which is also found in the electroless Ni-P system by Gutzeit *et al.* [3.20]. This indicates that the reaction mechanisms of ternary Ni-W-P and binary Ni-P are similar.

The nickel sulfate can also affect the content of P in Ni-W-P deposits. When the amount of NiSO_4 in the water bath decreases, the concentration of Ni^{2+} atoms falls and therefore increases the possibility of the available H_2PO_2^- to gain electrons for more P element deposition (Figure 3-9) in Equation 3-4. Overall, the concentration of H_2PO_2^- in the electroless solution is the critical factor in the determination of P content.

Furthermore, it is rather interesting that W is co-deposited with Ni without affecting the content of P in the Ni-W-P deposits when sodium tungstate (ranging from 35 to 75 wt.%) was added in the alkaline bath. Hence, it is reasonable to assume that there is no competitive reaction between W and P to inhibit the P content to co-deposit in this alloy matrix, at least in formulation and plating conditions of this electroless bath. This result is different from the acid bath solution. Some previous studies [3.21, 3.22] reported that the addition of sodium tungstate leads to the rapid decrease of P content by co-deposition of W. The bath solution they used is acid bath containing aminoacetic acid as a complexing agent at 75 °C.

Therefore, the effects of various factors that may affect the percentage of P in Ni-W-P coatings are summarised in table 3-9.

Table 3-7 Summary of coating parameters on the proportion of P in Ni-W-P deposits.

	NaH_2PO_2	NiSO_4	$\text{Na}_3\text{C}_6\text{H}_8\text{O}_7$	Temperature	pH values
P	Positive	Negative	Positive	Negative	Negative
Content	correlation	correlation	correlation	correlation	correlation

3.4 Summary

In this work, a series of experiments on electroless Ni-W-P metallisation were conducted to develop a proper deposition procedure and to analyse the effects of

various plating parameters on the deposition characteristics. Based on the above experimental results and discussions, the conclusions can be achieved as follows.

1. Prior to electroless plating, dimethylamine borane (DMAB: $(\text{CH}_3)_2\text{NHBH}_3$) and metallic wire can successfully initiate the deposition reactions on Cu substrates and prevent the plating solution from decomposition at a high temperature (below 95°C) and a pH value (below 9.5) for a long plating time (at least 2 hours). Moreover, adhesion strength of Ni-W-P coatings on Cu substrates after DMAB pre-treatment was evaluated to be the best qualification 5B in tape tests.
2. An SLS concentration of 0.3 mg/L can greatly improve the surface quality and moderately increase the deposition rate of Ni-W-P deposits without any changes in compositions of these ternary deposits.
3. Phosphorus content is vital in control the microstructure and crystallinity of electroless Ni-W-P deposits. The P content in Ni-W-P coatings significantly increase with the growing concentration of NaH_2PO_2 with an accelerating deposition rate. While, the increasing $\text{Na}_3\text{C}_6\text{H}_8\text{O}_7$ concentration only raises the P content at an expense of slow deposition rate. However, the factors including NiSO_4 concentration, plating temperature, and plating pH correlate negatively with the P content.
4. The effects of W contents in crystallisation behaviours of electroless Ni-W-P coatings are remain uncertain. Increasing Na_2WO_4 concentration (35 - 75 g/L) shows a significant positive effect on raising the W content, while the fastest deposition rate reaches in 55 g/L concentration of Na_2WO_4 . The W content correlates positively with plating temperature, plating pH value, and the concentration of $\text{Na}_3\text{C}_6\text{H}_8\text{O}_7$. Moreover, plating temperature also speed up the deposition rate. On the contrary, the correlations between sodium phosphate (NaH_2PO_2) and nickel sulfuric (NiSO_4) concentration and W content are negative.

References

- [3.1] Pearlstein, R.F. Weightman, "Electroless Deposition of Nickel Alloys", *Electrochemical Technology*, vol. 6, No. 11-12, pp. 427-430, 1968.
- [3.2] K. Chen, C. Liu, D.C. Whalley, and D.A. Hutt, "Electroless Ni-W-P alloys as

- barrier coatings for liquid solder interconnects”, in *1st Electronics System Integration Technology Conference (ESTC)*, Dresden, Germany, 2006, pp. 421-427.
- [3.3] Y. Yang, J.N. Balaraju, S.C. Chong, H. Xu, C. Liu, V.V. Silberschmidt, and Z. Chen, “Significantly retarded interfacial reaction between an electroless Ni–W–P metallization and lead-free Sn–3.5Ag solder”, *Journal of Alloys and Compounds*, vol. 565, pp. 11–16, 2013.
 - [3.4] F.J. He, Y.Z. Fang, and S.J. Jin, “The study of corrosion-wear mechanism of Ni-W-P alloy”, *Wear*, vol. 311, pp 14-20, 2014.
 - [3.5] S.K. Tien, J.G. Duh, and Y.I. Chen, “The influence of thermal treatment on the microstructure and hardness in electroless Ni–P–W deposit”, *Thin Solid Films*, vol. 469-470, pp. 333–338, 2004.
 - [3.6] Y.J. Hu, T.X. Wang, J.L. Meng, and Q.Y. Rao, “Structure and phase transformation behaviour of electroless Ni-W-P on aluminium alloy”, *Surface and Coatings Technology*, vol. 201, No. 3-4, pp. 988–992, 2006.
 - [3.7] J. Li, X. Hu, and D. Wang, “Effects of codeposited tungsten on the properties of low-phosphorous electroless nickel coatings”, *Plating Surface Finishing*, vol. 83, pp. 62-64, 1996.
 - [3.8] Q. Zhou, W.C. Sun, M. Zhu, and M.F. Tan, “Fabrication and corrosion behaviour of electroless Ni-W-P coating on magnesium alloy”, *Advanced Materials Research*, vol. 79-82, pp. 997-1000, 2009.
 - [3.9] D.M. Jang, and J. Yu, “Tungsten alloying of the Ni(P) films and the reliability of Sn–3.5Ag/NiWP solder joints”, *Journal of Materials Research*, vol. 26, No. 7, pp. 889-895, 2011.
 - [3.10] S.K. Tien, and J.G. Duh, “Thermal reliability of electroless Ni-P-W coating during the aging treatment”, *Thin Solid Films*, vol. 469-470, pp. 268–273, 2004.
 - [3.11] Y.Y. Tsai, F.B. Wu, Y.I. Chen, P.J. Peng, J.G. Duh, and S.Y. Tsai, “Thermal stability and mechanical properties of Ni–W–P electroless deposits”, *Surface and Coatings Technology*, vol. 146-147, pp. 502–507, 2001.
 - [3.12] S.K. Tien, J.G. Duh, and Y.I. Chen, “Structure, thermal stability and mechanical properties of electroless Ni-P-W alloy coatings during cycle test”, *Surface and Coatings Technology*, vol. 177-178, pp. 532-536, 2004.
 - [3.13] J. Flis, and D.J. Duquette, “Initiation of Electroless Nickel Plating on Copper, Palladium-Activated Copper, Gold, and Platinum”, *Journal of Electrochemistry Society*, vol. 131, No. 2, pp. 254-260, 1984.
 - [3.14] ASTM Standard D3359-02, “Standard Test Methods for Measuring Adhesion by Tape Test”, ASTM International, West Conshohocken, PA, 2010.
 - [3.15] N. Li, Z.M. Tu, *Practical technology of electroless plating*, Chemical Industry Press, Beijing, China, 2003.
 - [3.16] D.B. Lewis, and G.W. Marshall, “Investigation into the structure of electrodeposited nickel-phosphorus alloy deposits”, *Surface and Coating Technology*, vol. 78, pp. 150-156, 1996.
 - [3.17] J.N. Balaraju, Kalavati, N.T. Manikandanath, and V.K. William Grips, “Phase transformation behavior of nanocrystalline Ni-W-P alloys containing various W

- and P contents”, *Surface and Coating Technology*, vol. 206, No. 10, pp. 2682–2689, 2012.
- [3.18] Z.A. Hamid, “Mechanism of electroless deposition of Ni-W-P alloys by adding surfactants” *Surface and Interface Analysis*, vol. 35, pp. 496-501, 2003.
- [3.19] A. Hung, “Effects of thiourea and guanidine hydrochloride on electroless copper plating”, *Journal of The Electrochemical Society*, vol. 132, No. 5, pp. 1047-1049, 1985.
- [3.20] G. Gutzeit, *Plating*, 46, 1158, 1275, 1317 (1959); 49, 63 (1960).
- [3.21] B. Szczygieł, and A. Turkiewicz, “Aminoacetic acid as complexing agent in baths for electroless deposition of Ni-W-P coatings”, *Transactions of the Institute of Metal Finishing*, vol. 84, No. 6, pp 309-312, 2006.
- [3.22] T. Osaka, H. Sawai, F. Otoi, and K. Nihei, “Autocatalytic (electroless) nickel-tungsten-phosphorus plating”, *Metal Finishing*, vol. 80, No. 8, pp. 31-35, 1982.

Chapter 4

Thermal Stability and Phase Transformation Behaviours of Ni-W-P Coatings

In this chapter, the microstructure and phase transformation behaviours of Ni-W-P coatings were investigated using scanning electron microscopy (SEM), differential scanning calorimetry (DSC), X-ray diffraction (XRD) and atomic force microscope (AFM). Moreover, the thermal stability of cross-section electroless Ni-W-P coatings on Cu substrate was evaluated by comparing with electroplated Ni-W coatings.

4.1 Introduction

The barrier material in application of high temperature power electronics has to fulfil strict demands, including high melting point, high electrical conductivity, low or no reactivity with substrate and solder. Currently, electroless Ni-P alloy has been widely used as a diffusion barrier in Sn-based solder joints for various advantages, including selective deposition, uniform thickness, good wettability, good corrosion resistance, and low reaction rate with solders [4.1-4]. However, Ni-P coatings normally crystallise below 300 °C to form crystalline Ni₃P with a columnar structure at solder interfaces, the boundaries of which act as diffusional pathways for the reactions between atoms of solders and substrate [4.4, 4.5]. This certainly deteriorates the function of Ni-P under bump metallisation (UBM), leading to excessive IMC formation at UBM/solder interfaces and therefore decreasing the reliability of the solder joints [4.6, 4.7].

Therefore, a novel metallisation that can keep stable under relatively high temperature (at least above 300 °C) is highly desirable in application of hybrid automotive electronics. Incorporation of a refractory metal element (W) in binary Ni-P alloy through electroless deposition was reported to significantly enhance the crystallisation behaviours and thermal stability of binary Ni-P alloy [4.8-10]. Moreover, electroplated

Ni-W alloy shows a good thermal stability and low diffusion rate, which is also proposed to be a potential diffusion barrier [4.11, 4.12].

This chapter aims at evaluating the effects of tungsten that added in Ni-P coating on the thermal stability of Ni-W-P UBM. The thermal stability and phase transformation behaviours of ternary Ni-W-P alloys after thermal treatments were investigated using X-ray diffractograms (XRD), differential scanning calorimetry (DSC), and atomic force microscopy (AFM) apparatus. Moreover, an *in-situ* thermal treatment was conducted on cross sections of Ni-W-P and Ni-W coatings on Cu substrates to evaluate their thermal stability via high temperature optical microscopy (HTOM).

4.2 Experimental details

In this work, electroless Ni-P and electroless Ni-W-P coatings with varying W contents were prepared to investigate the effects of W element on thermal stability of ternary Ni-W-P alloys. Moreover, the electroless Ni-W-P and electroplated Ni-W coatings were also prepared and compared using HTOM method. For different purposes, the experimental details with different Ni-based metallisation were described as follows.

4.2.1 Electroless Ni-W-P and Ni-P coatings

Two substrates were used for electroless Ni-W-P and Ni-P plating; Cu sheets (1 mm thickness, 99.9% purity) with an area size of 5 mm × 5 mm and Al foils (50 µm thickness, 99% purity). The coatings on Al foils were for DSC and XRD specimens since Al can dissolve in NaOH solution to obtain pure Ni-W-P films, so that the influences of substrates on X-Ray diffraction analysis can be excluded.

Before electroless plating, Cu sheets were polished and then etched with HCl solution (50% by volume) for 30 s, followed with final cleaning in deionized water. The Cu substrates were then rinsed in a DMAB solution to be activated for following depositions. For Al substrates, a double zincate treatment [4.13] was employed in the pre-treatment process of Al substrates as described in table 4-1.

Table 4-1 Procedures of pre-treatment process for aluminium substrate prior to electroless plating.

Process	Chemicals	Time	Purpose
Clean	Acetone	3-5 mins	Get an oil-free surface
Clean	Deionised water	5-10 s	Clean the surface
Etch	5% sodium hydroxide solution	5-30 s	Etch the surface
Clean	Deionised water	5-10 s	Remove chemicals
Desmut	50 % nitric acid	20 s	Desmut
Clean	Deionised water	5-10 s	Remove chemicals
1 st Zincate	Alkaline zincate solution	1 min	Deposit zinc layer
Clean	Deionised water	5-10 s	Remove chemicals
Etch	50 % nitric acid	10-20 s	Etch the zinc layer
Clean	Deionised water	5-10 s	Remove chemicals
2 nd Zincate	Alkaline zincate solution	1 min	Deposit zinc layer
Clean	Deionised water	5-10 s	Remove chemicals

In this chapter, three different Ni-W-P coatings with varying W contents were electroless plated in self-prepared alkaline solutions. The formulations and the plating conditions of these water baths are all listed in table 4-2.

Table 4-2 Formulations and plating conditions of three electroless Ni-W-P baths (wt. %).

Bath Composition (g/L)	Ni-W-P-I	Ni-W-P-II	Ni-W-P-III
NiSO ₄ •6H ₂ O	20	25	7
Na ₂ WO ₄ •2H ₂ O	10	30	75
NaH ₂ PO ₂ •H ₂ O	20	12	10
Na ₃ C ₆ H ₅ O ₇ •2H ₂ O	35	10	40
(NH ₄) ₂ SO ₄	30	/	/
Plating condition	pH: 9; T: 85±2 °C	pH: 9; T: 90±2 °C	pH: 8; T: 85±2 °C

Meanwhile, an electroless Ni-P coating was also prepared in comparison with the above ternary Ni-W-P coatings, so as to investigate the effect of W on their crystallisation behaviours. The formulations and plating conditions of the electroless Ni-P bath are listed in table 4-3.

Table 4-3 Formulations and plating conditions of the electroless Ni-P bath (wt.%).

Bath Composition (g/L)	Ni-P
$\text{NiSO}_4 \cdot 6\text{H}_2\text{O}$	30
$\text{NaH}_2\text{PO}_2 \cdot \text{H}_2\text{O}$	25
$\text{C}_2\text{H}_5\text{NO}_2$	20
$\text{Na}_3\text{C}_6\text{H}_5\text{O}_7 \cdot 2\text{H}_2\text{O}$	20
Plating condition	pH: 5.5; T: 85 ± 2 °C

After electroless plating, all Al specimens were rinsed in a high-concentration NaOH solution (80 g/L) to dissolve the Al substrates without damaging the ternary Ni-W-P films. Using this approach, pure Ni-W-P films can be obtained for following tests and analysis. Firstly, the phase transition temperature of these as-deposited Ni-based coatings during heating were analysed with a thermal gravimetric analyser (TGA, Netzsch STA 409 PC). The heating temperature ranged from room temperature (20 °C) to 550 °C with a heating rate of 10 °C/min at an inert atmosphere (N_2).

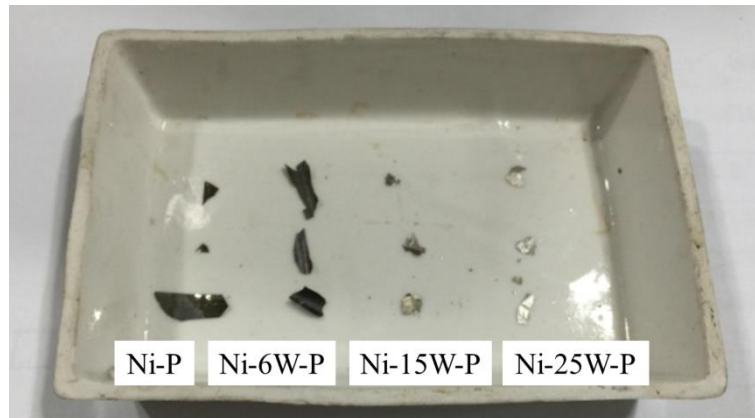


Figure 4-1 The electroless Ni-based deposits with different W contents in ceramic boat for subsequent thermal treatments.

Moreover, these Ni-based coatings were annealed in a vacuum furnace (vacuum degree $< 10^{-3}$ Pa) at a peak temperature of 400 °C, 450 °C, and 750 °C for 2 hours. As illustrated in figure 4-1, the Ni-W-P films with various W contents (6, 15, and 25 wt.% tungsten

content) and the control sample (Ni-10P films) were put together in a ceramic boat for this thermal treatment.

The temperature profile of the annealing treatments is illustrated in figure 4-2. The initial heating rate from room temperature to a pre-set temperature (50 °C gap below the peak temperature) was 10 °C/minute. Then all samples were stored at this temperature for 5 minutes to prevent overheating. Afterwards, the samples were heated with a heating rate of 5 °C/minute to reach and then stay at the peak temperature for two hours.

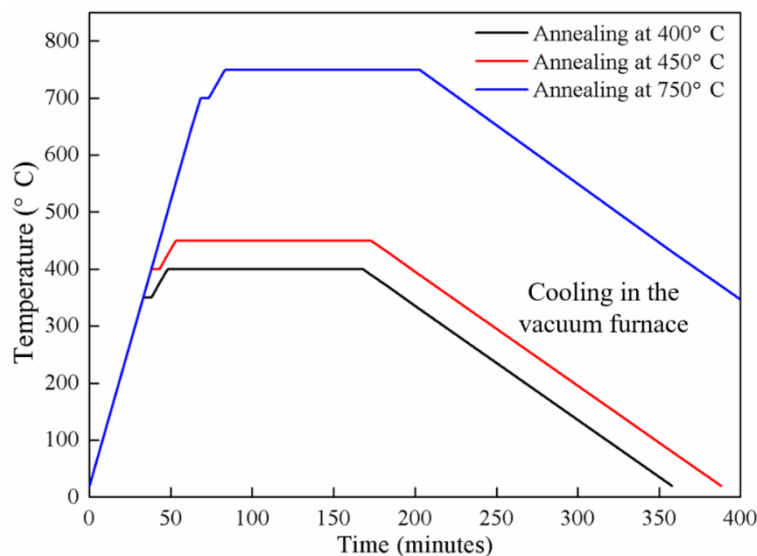


Figure 4-2 Temperature profile of annealing treatments at the peak temperature of 400, 450 and 750 °C.

The phase identifications of the Ni-based films before and after thermal treatments were analysed by X-ray diffraction (XRD, X'pert Pro XRD, PANalytical BV) with a diffractometer using Cu K α radiation. The XRD analysis was conducted at the scanning angles ranging from 30 to 60° (2θ) with a scanning rate of 2°/min. The morphological features of electroless Ni-W-P coatings before and after thermal treatments were observed through two FEG-SEMs (FEI Sirion 200 and Carl Zeiss 1530 VP) using EDX (energy dispersive X-ray analysis, Oxford) equipment. Moreover, the surface morphology and the roughness of as-deposited and annealed Ni-15W-P coatings were evaluated by an atomic force microscopy (AFM, Nanoscope II Digital Instruments, CA) with a tapping mode. At least three AFM images were taken for the Ni-15W-P coatings to obtain a precise surface roughness. In AFM analysis, the surface area of tested coatings was about 2 $\mu\text{m} \times 2 \mu\text{m}$.

4.2.2 Electroplate Ni-W coating

To testify the thermal stability of electroless Ni-W-P coatings in cross-sectional view, a Ni-W coating was electroplated from an aqueous solution as a control sample, with the formulations and plating conditions listed in table 4-4. Chemicals of reagent grade and ultrapure water were utilised to make up the electrolytes for minimising contaminations. The pH value of the plating bath was adjusted to 8.0 by dilute NaOH and H₂SO₄ solutions. Pure Cu sheets with a surface area of 16 cm² and a pure Ni substrate were used as working electrode and auxiliary electrode, respectively. The composition of W in Ni-W alloy was measured to be 29 wt.%.

Table 4-4 Formulations and plating conditions of the electroplate Ni-W bath.

Bath Composition (g/L)	Ni-W
NiSO ₄ •6H ₂ O	26
Na ₂ WO ₄ •2H ₂ O	132
Na ₃ C ₆ H ₅ O ₇ •2H ₂ O	147
NaBr	15.4
Plating condition	pH: 8; Temperature: 15 °C; Current density: 5 mA/cm ²

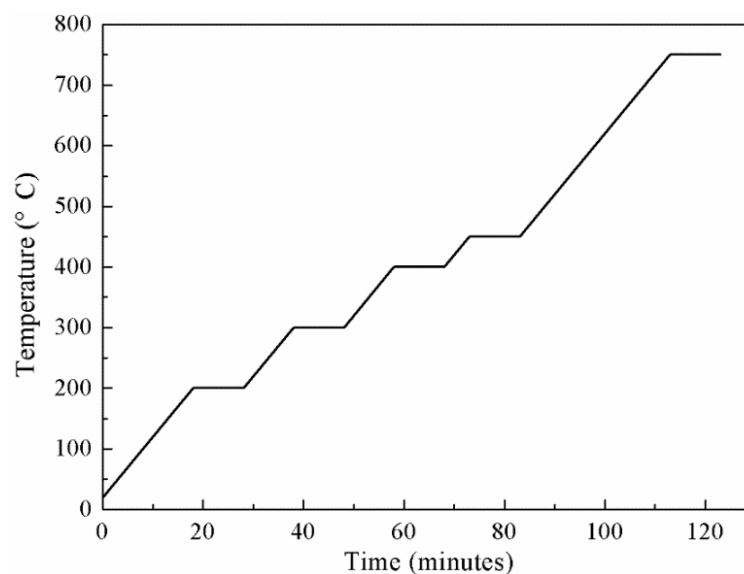


Figure 4-3 The temperature profile for the Ni-W-P coatings in high temperature optical microscopy.

A high temperature microscopy (Carl Zeiss, AxioVert A1) was used in observing the *in-situ* cross-sectional microstructure of Ni-25W-P and Ni-29W coatings during heating with a $\times 500$ magnification. The temperature profile of thermal treatment is shown in figure 4-3. The thickness of these coatings is approximately 15 μm . This is to test the thermal behaviours of the cross-sectional Ni-W-P coatings.

4.3 Results and discussions

4.3.1 Composition and phase analysis

The EDX results of electroless Ni-W-P coatings are listed in table 4-5. The thickness of all coatings was approximately 6 μm . The W element with a high melting point (3422 $^{\circ}\text{C}$) can be successfully co-deposited with Ni from an aqueous solution containing sodium tungstate. With an increasing concentration of sodium tungstate (from 10 g/L to 75 g/L), the W content increased significantly from 5.5 to 25.3 wt.%. Meanwhile, to acquire coatings with a similar structure, the P content was controlled within a narrow window (8.6-9.5 wt.%) by adjusting deposition parameters such as plating temperature, pH value and concentration of chemical constituents.

Table 4-5 Chemical composition of as-plated Ni-W-P coatings (wt.%).

Type of coatings	W	P
Ni-P	-	10.2 ± 1.2
Ni-W-P-I	5.5 ± 0.7	8.6 ± 1.3
Ni-W-P-II	15.2 ± 1.9	9.5 ± 1.1
Ni-W-P-III	25.3 ± 2.6	9.3 ± 1.1

As metastable alloys are thermodynamically unstable, the structure of amorphous Ni-W-P coatings can be transformed into a completely stable crystalline structure under thermal treatments [4.10]. The phase transformation behaviours of these Ni-W-P alloys were studied with a TGA/DSC equipment. The DSC thermograms of ternary Ni-W-P coatings were recorded over a temperature range of 100 $^{\circ}\text{C}$ to 550 $^{\circ}\text{C}$ at a heating rate of 10 $^{\circ}\text{C}/\text{min}$. Figure 4-4 shows the obtained DSC results. A sharp exothermic peak occurs in all electroless Ni-based coatings, corresponding to their crystalline temperature. The crystalline temperature ranges from 350 to 420 $^{\circ}\text{C}$, which attributes to the crystallisation

transition of the amorphous phases to the formation of Ni and Ni₃P phases [4.8, 4.10, 4.14]. However, another modest exothermic peak can be observed in the Ni-6W-9P coating at approximately 300 °C as its structure would be a mixture with amorphous phases and nanocrystalline phases. This slight exothermic peak represents the initial-stage crystallisation of metastable phases, resulting from atomic movements to eliminate the point defects and dislocations within the Ni-W-P coatings [4.10, 4.15].

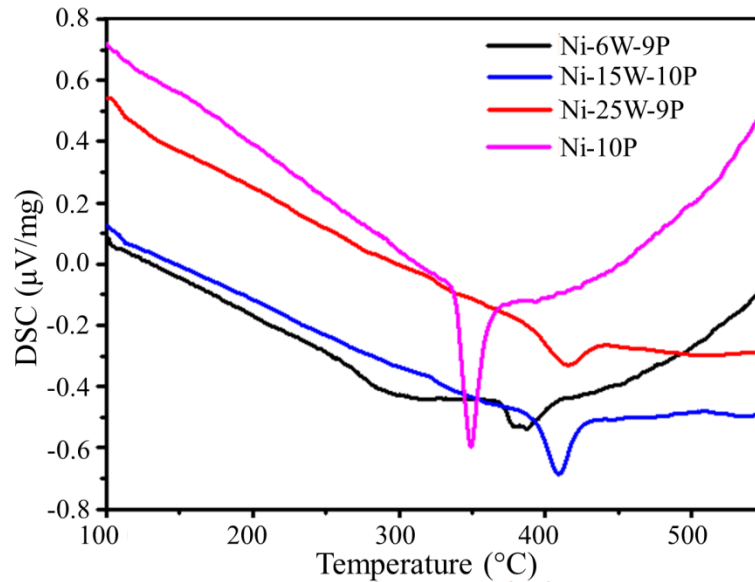


Figure 4-4 DSC thermograms obtained for the electroless Ni-based metallisation with various W contents (0, 5.5, 15.2, and 25.3 wt.%)

Table 4-6 lists the crystallisation temperatures of the electroless Ni-10P coating and the electroless Ni-W-P coatings with different W contents. For Ni-W-P alloys, crystallisation temperatures continue to rise with increasing W contents. It can be found that with a small addition of W (5.5 wt.%) into electroless Ni-P coatings, the crystallisation temperature can be significantly increased from 347 °C to 390 °C approximately. The reason for the higher crystallisation temperature of these Ni-W-P coatings is the lower rate of elemental diffusion due to the incorporation of W material (melting point: 3422 °C [4.16]). When the W content in Ni-W-P coatings increases to 15.2 wt.%, the crystallisation temperature grows to 410 °C. This crystallisation temperature exceeds 400 °C and meets general requirements in application of high temperature electronics. However, the rise speed of crystallisation temperature clearly slows down (only increase 6 °C), even though the W content in Ni-W-P coatings clearly increases from 15.2 to 25.3 wt.%.

Table 4-6 Crystallisation temperatures of the Ni-based metallisation obtained in DSC results.

Coating type	Crystallisation temperature (°C)
Ni-10P	347
Ni-5.5W-9P	390
Ni-15.2W-10P	410
Ni-25.3W-9P	416

4.3.2 Phase transformation behaviours of Ni-based coatings

To investigate the effect of W content on the phase transformation behaviours of electroless Ni-based coatings, XRD analysis were conducted on Ni-W-P coatings with different W contents (5.5, 15.2, and 25.3 wt.%) before and after various thermal treatments (400, 450, and 750 °C) for 2 hours.

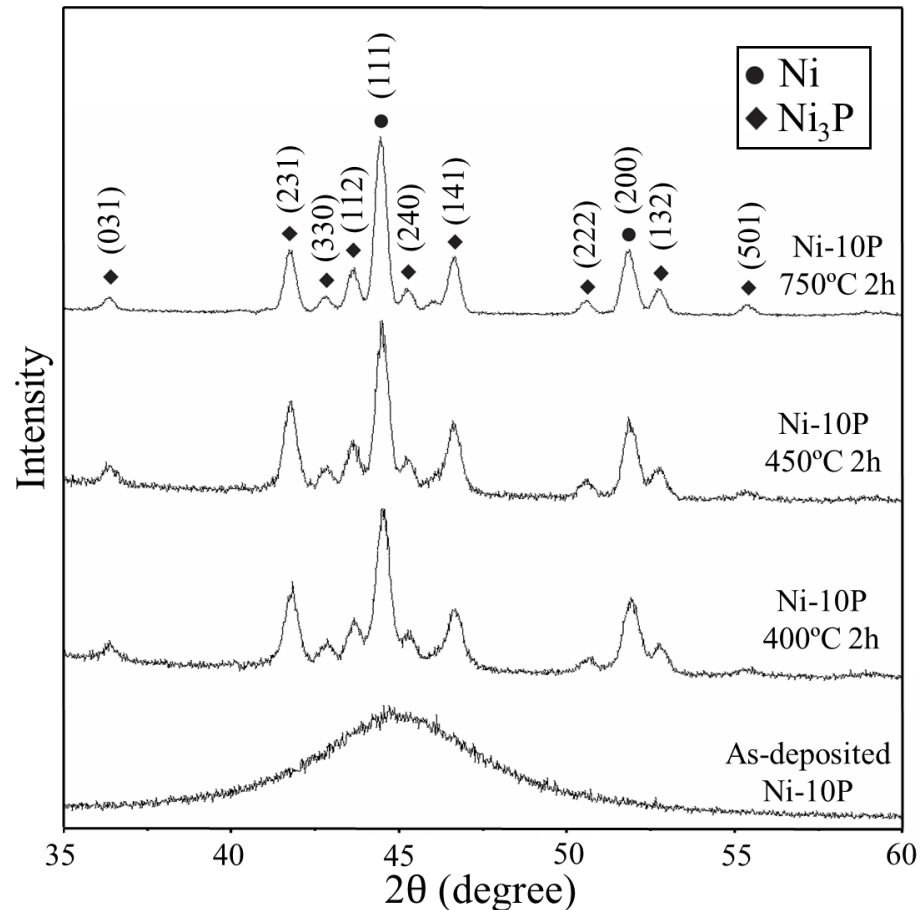


Figure 4-5 XRD diffraction patterns of the Ni-10P coating annealed for 2 hours at various temperature.

Figure 4-5 and figure 4-6 shows the X-ray diffraction patterns of electroless Ni-P and Ni-W-P coatings before and after annealing for 2 hours at different temperatures (400,

450, and 750 °C). All Ni-based alloys mainly exhibit an amorphous structure, since only one broad peak (40 - 50 °) exist in their XRD patterns. These single curves of the broad peak are around 44 ° 2θ , which are ascribed to Ni (111) plane. For Ni-10P alloy, the atomic radius of P and Ni are 2.20, and 2.49 Å, respectively [4.17]. Thus, P can dissolve into Ni matrix and replace with some Ni grains in (1 1 1) orientation, leading to a shrinkage of the Ni lattice according to Bragg Equation (Equation 4-1).

$$2d \sin \theta = \lambda \quad \text{Equation 4-1}$$

Where d is interplanar crystal spacing, θ is diffraction angle, λ is wavelength of incident wave.

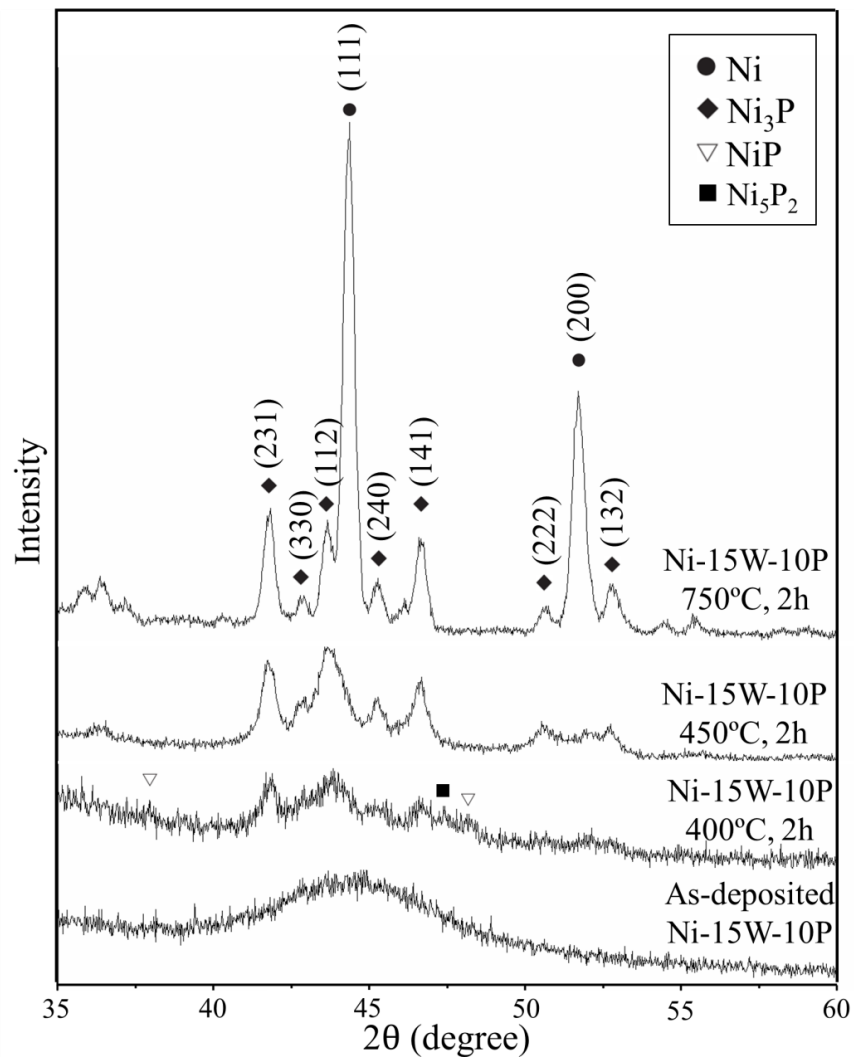
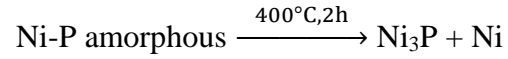


Figure 4-6 XRD diffraction patterns of the Ni-15W-10P coating annealed for 2 hours at various temperature.

After annealing at 400 °C for 2 hours, the amorphous Ni-P alloy fully transferred to a stable body centered tetragonal Ni₃P phase, and no metastable phases were discovered.

In addition to stable Ni_3P phase, face centered cubic Ni phase was also found in this Ni-P coating after annealing at 400 °C for 2 h. When annealing temperature increased to 450 and 750 °C, no new phases or Ni_3P phases with different orientations were formed. Thus, it can be concluded that this amorphous Ni-P coating crystallised completely after annealing at 400 °C for 2 hours as shown as follows.

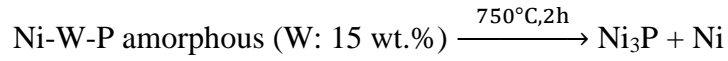
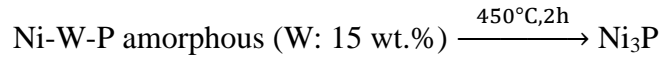
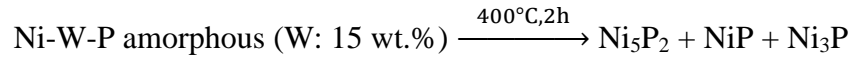


As for electroless Ni-W-P coatings, the exothermic peak of P and W cannot be found in figure 4-6, indicating that the P and W solute in the Ni lattices. The atomic radius of W is 2.78 Å [4.18], which is lightly larger than Ni element (2.49 Å). Therefore, W lattice can also solute into Ni matrix to substitute Ni (1 1 1) oriented lattices, resulting in an expansion of Ni lattice [4.17] for the bigger size of W lattice. According to Bragg Equation, the angle θ corresponding to Ni (1 1 1) plane should be shift towards a slight lower angle (from 44.5 ° in Ni-P alloy to 44.2 ° in Ni-W-P alloy), which agrees with a published work [4.19].

After a thermal treatment at 400 °C for 2 hours, metastable phases of Ni_5P_2 and NiP are identified according to the XRD patterns. Moreover, stable crystalline Ni_3P phase was also found, resulting from these metastable phases is partly transformed into stable crystalline Ni_3P phase at 400 °C. When the annealing temperature grew to 450 °C, all metastable Ni_5P_2 and NiP phases transformed into crystalline Ni_3P phase after 2 hours annealing. However, only crystalline phases such Ni (1 1 1) and Ni_3P peaks were formed after annealing at 750 °C, which is as same as the Ni-10P film annealed in a same heating condition (750 °C, 2h). Therefore, the addition of W into the Ni-10P can greatly improve the thermal stability of Ni-15W-10P coatings by postponing the phase transformation of Ni_3P and Ni crystalline phases.

Overall, the crystallisation process of Ni-W-P alloy is divided into two major stages. Firstly, the heating energy activates the local atomic movements, resulting in an incipient crystallisation into metastable crystalline structures (Ni_5P_2 , NiP). Then, a high annealing temperature and elongated thermal heating time can lead to a thermal migration of the atoms in metastable Ni_5P_2 and NiP phases and consequently transformed into stable Ni_3P crystalline phase.

The crystallisation process of amorphous Ni-W-P compound is as shown as follows:



To clarify the effect of W contents on crystallisation behaviours of electroless Ni-based coatings, the XRD results of these alloys heated at 400 °C for 2 h are summarised in figure 4-7. Generally, the increase in W content significantly retards the crystallisation formation of equilibrium phases (Ni₃P and Ni) in amorphous Ni-P compound.

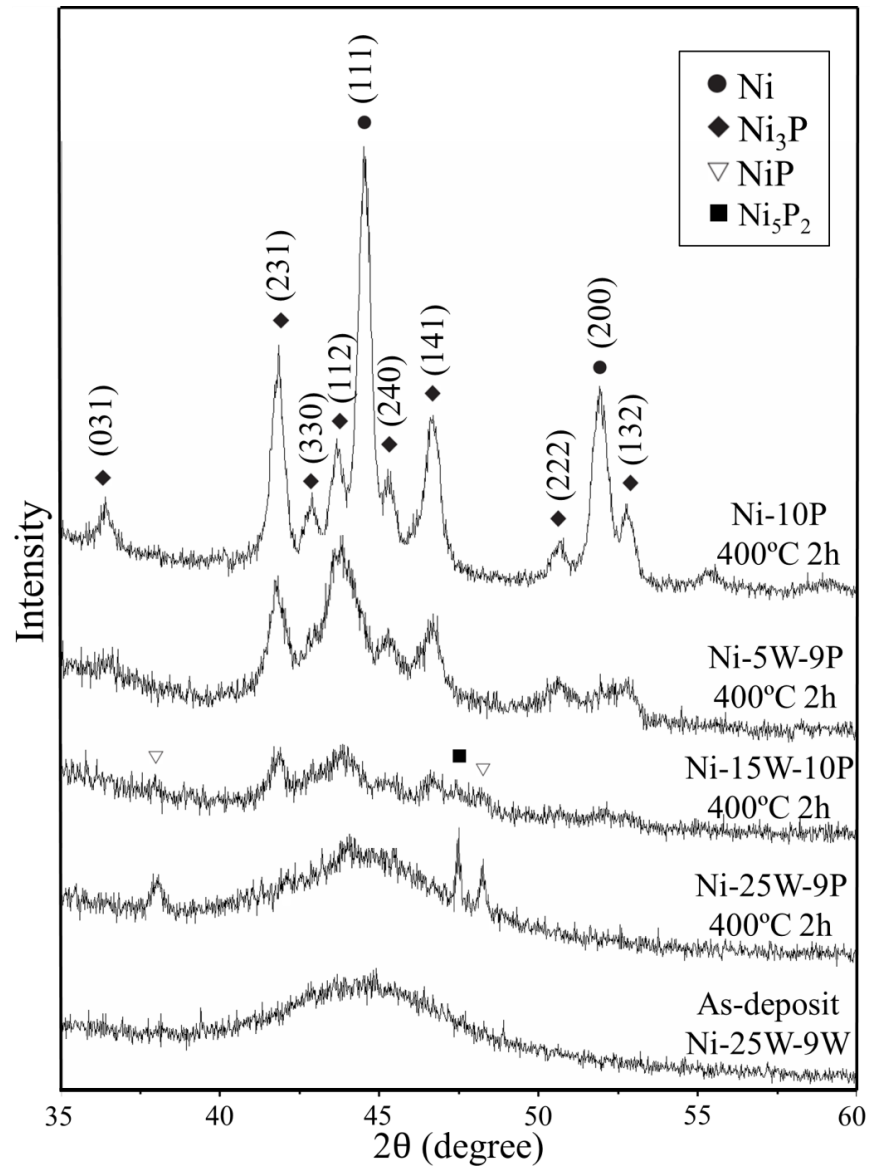


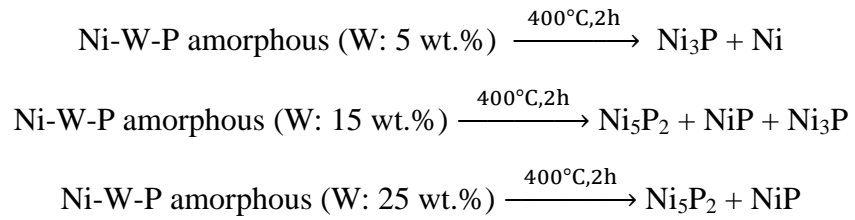
Figure 4-7 XRD diffraction patterns of various Ni-based coatings annealed at 400 °C for 2 hours.

For the electroless Ni-W-P coatings with a low W content (~ 5.5 wt.%) annealed at 400 °C for 2 hours, fully transformation of metastable Ni₅P₂ and NiP phases into stable

crystalline Ni_3P phases could be observed. Moreover, a NiP phase in (2 0 0) orientation also occurred with a low intensity. Besides the inhibition of NiP (2 0 0) phase, the small addition of tungsten (~5.5 wt.%) also retarded the formation of Ni (1 1 1) peak compared to the Ni-10P coating in the same thermal treatment.

When the W content rises to 15.3 wt.%, metastable phases of Ni_5P_2 and NiP phase as well as stable crystalline Ni_3P phase are observed in the XRD pattern. However, if W content increases to a max degree of 25.3 wt.%, this Ni-W-P alloy exhibits a almost amorphous structure. Only metastable Ni_5P_2 and NiP phases can be found in this Ni-W-P coating, demonstrating the highest thermal stability among all these Ni-based metallisation.

Overall, tungsten can clearly improve the thermal stability of these Ni-W-P coatings and their crystallisation process of amorphous Ni-W-P alloy with different W contents is summarised as follows:



4.3.3 Surface morphology of Ni-W-P alloys after thermal treatments

Figure 4-8 shows the SEM and the corresponding AFM images of amorphous Ni-15W-10P coatings after the storages at room temperature (20 °C), 400 °C, and 750 °C for 2 hours. The surface roughness was measured at these Ni-W-P coatings in an area size of $2\text{ }\mu\text{m} \times 2\text{ }\mu\text{m}$. The average surface roughness (R_a) of these Ni-W-P coatings are listed in table 4-7. The as-deposited Ni-15W-10P coating exhibited a nodule-like morphology and the average surface roughness was $5.6 \pm 1.4\text{ nm}$. According to the XRD pattern as shown in figure 4-6, the as-deposited Ni-W-P coatings were consisted of amorphous Ni-P compounds with W atoms dissolvent and substitution for Ni atoms.

After heating at 400 °C for 2 hours, the grain boundaries of annealed Ni-W-P coating became more obvious. But generally, the surface morphology is quite stable with a similar modulus characteristic. Simultaneously, the surface roughness slightly increased to $7.5 \pm 1.6\text{ nm}$ as presented in figure 4-8 b). Based on its corresponding

XRD patterns in figure 4-6, some metastable and stable crystalline phases such as Ni_5P_2 , NiP and Ni_3P emerge within the amorphous Ni-W-P coatings, contributing to the slight increase in its surface roughness.

When the Ni-15W-10P coating was heated at 750 °C for 2 hours, all amorphous nodule features completely turned out to be a great number of nano-sized crystalline grains, as shown in figure 4-8. These crystalline grains corresponding to stable Ni_3P and Ni phases lead to a significant increase in average surface roughness ($23.8 \pm 3.5 \text{ nm}$).

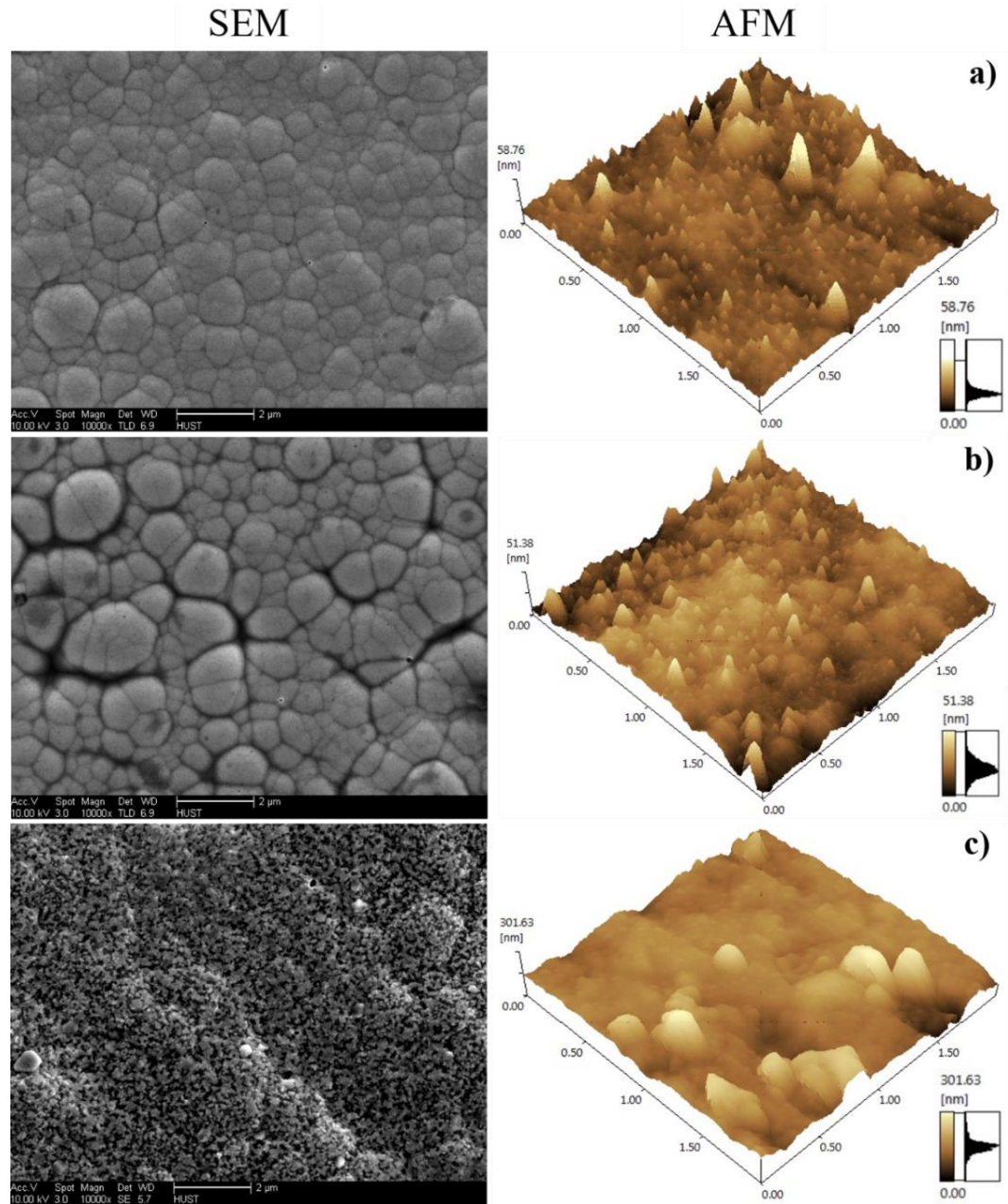


Figure 4-8 SEM and AFM images of electroless Ni-15W-10P coatings after 2 hours annealing at: a) room temperature (20 °C); b) 400 °C; c) 750 °C.

Therefore, even though the electroless Ni-15W-10P coating started to crystallise at 400 °C, the surface morphology and roughness of this coating almost remained steady, indicating that no individual crystalline particles have been transformed from amorphous Ni(W)-P compounds. Generally, the Ni-W-P coatings are clearly stable at elevated temperature and are capable to be applied in applications of high temperature electronics.

Table 4-7 The surface roughness of the Ni-15W-10P coatings after thermal treatments.

Thermal treatments	Roughness, R_a (nm)
20 °C	5.6 ± 1.4
400 °C	7.5 ± 1.6
750 °C	23.8 ± 3.5

4.3.4 Cross-section morphology of Ni-based coatings during *in-situ* heating

Electroplated Ni-W coatings are also regarded as a promising diffusion barrier operated under high temperature for their high crystallisation temperature, low diffusion rate, and compact structure [4.11, 4.12]. To testify the thermal stability of electroless Ni-25W-P and electroplated Ni-29W coatings in a cross-section view, an *in-situ* observations on the cross-section microstructure of these coatings (thickness: ~ 15 µm) on Cu substrates were conducted by a high temperature optical microscopy (HTOM). The temperature profile of the heating treatment in the HTOM equipment is illustrated in figure 4-3.

Figure 4-9 presents the cross-section microstructure of electroless Ni-25W-10P plating during the *in-situ* heating for different durations. It is observed that the cross-section microstructure of this Ni-25W-P coating remained unaltered after heating at 400 °C for 10 minutes, which agrees with the above XRD results (Figure 4-7). When the ambient temperature raised, the thickness of the interaction layer (the arrow in figure 4-9 f)) between electroless Ni-W-P coating and Cu substrate gradually increased. During the heating process with an increasing temperature, some dark particles emerged within the coating, corresponding to the crystalline phases. When ambient temperature reached and kept at 750 °C, enormous crystalline grains were scattered within the amorphous Ni-W-P coating, which are pointed out by the white arrows in figure 4-9 g).

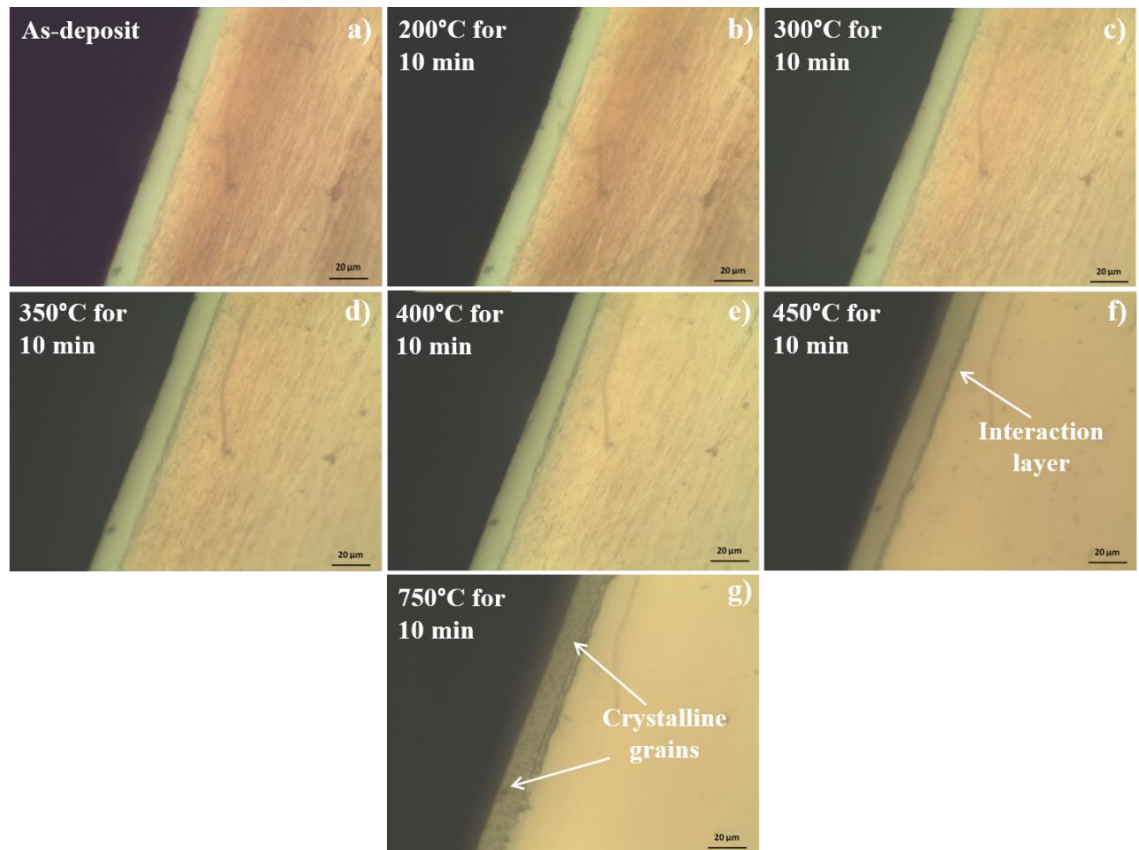


Figure 4-9 The cross-section images of microstructure of electroless Ni-25W-9P coating during *in-situ* thermal treatments.

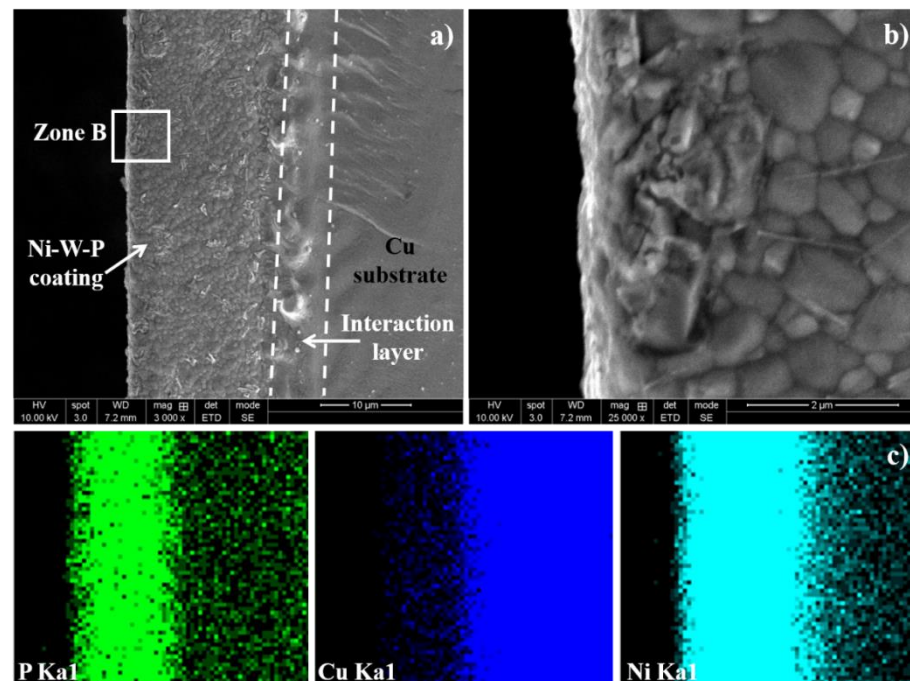


Figure 4-10 The cross-sectional microscopy of crystallised Ni-25W-9P coating on Cu substrates after observations in high temperature optical microscopy.

After the *in-situ* observation under high temperature, this Ni-25W-9P sample was taken out from the chamber of HTOM and then observed with a FEG-SEM to provide its

cross-sectional microstructure as shown in figure 4-10. Some crystalline particles in filiform and granulate shapes are observed in the cross-section structure. In addition, Ni atoms in electroless Ni-W-P coatings reacted with Cu atoms in Cu substrate to form an interaction layer composing with Cu-Ni IMCs, according to the elemental mapping results in figure 4-10 c).

For electroplated Ni-29W coatings, figure 4-11 shows the observations on its cross-section microstructure under an *in-situ* heating treatment for different time. Although no dark crystalline particles can be observed in this coating at a heating temperature under 500 °C, the electroplated coating started to crack when the temperature just reached 200 °C. This is like to be attributed to the high residual stress as well as the mismatch of coefficient of thermal expansion (CTE) between the electroplated Ni-29W coating and Cu substrate. Consequently, though the electroplated Ni-W coatings have high crystallisation temperatures, they are still not appropriate for high temperature electronics due to its fragility.

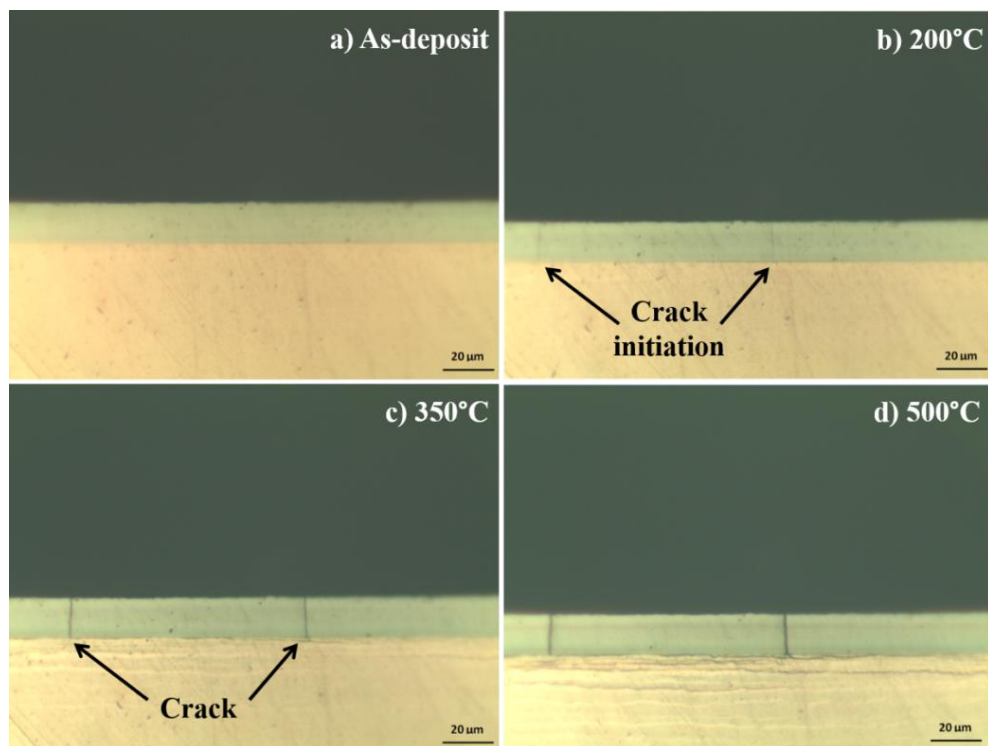


Figure 4-11 The *in-situ* cross-section images of microstructure of electroplated Ni-29W coating during thermal treatments

This electroplated Ni-29W coating before and after *in-situ* HTOM observation was investigated through SEM in a back-scattered mode. The dash line represents the edge of Ni-W coating since the Ni-W plane is not horizontal to its base. A micro crack with

a width of 8 μm is formed at this coating as indicated in figure 4-11. In addition to micro cracks, the microstructure of the Ni-29W metallisation after the thermal treatment in HTOM chamber was quite similar to the as-deposited coating, which contain some Ni grains perpendicular to Cu substrate prior to and after thermal treatment, leading to diffusion paths. As observed in figure 4-12 b), Cu atoms diffuse into the Ni-29W layer according to the elemental line results. No interaction layer between Cu and Ni-W layer was found in this electroplate Ni-W coating. On the contrary, when the electroless Ni-25W-9P coatings crystallised, their microstructure turned to be shapes of filiform and granulate from amorphous nodules, which are still quite compact and uniform. Compared to the compact Ni-W-P coatings, the perpendicular structure in electroplate Ni-29W coating is more likely to induce cracks when subject to the horizontal stress due to thermal expansion of materials under elevated temperature (up to 200 $^{\circ}\text{C}$).

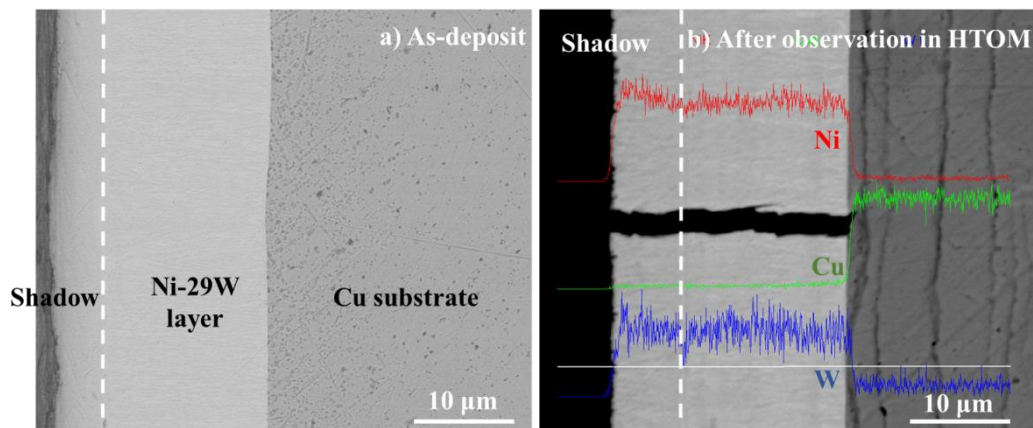


Figure 4-12 The cross-section microscopy of the Ni-W coating on Cu substrates: a) As-deposit; b) After *in-situ* observation in high temperature optical microscopy (In back-scattered mode).

4.4 Summary

The as-deposited electroless Ni-W-P coatings with different W contents were prepared and their thermal stability and phase transformation behaviours were investigated by comparing with electroless Ni-10P coatings and electroplated Ni-29W coatings as control samples. The main findings are summarised as follows:

1. Various Ni-based coatings including electroless Ni-10P, Ni-6W-9P, Ni-15W-10P, Ni-25W-9P, and electroplated Ni-29W alloys were prepared with different deposition parameters.

2. Increasing the W contents in Ni-W-P coatings can clearly improve their thermal stability and postpone their crystallisation process. A small addition of W element (5.5 wt.%) can effectively elevate the crystallisation temperature of amorphous Ni-P compound from 347 °C to 390 °C. The crystallisation temperatures of electroless Ni-W-P coatings continued to rise with increasing W contents. However, the rise rate of their crystallisation temperature gradually slowed down.
3. The crystallisation process of electroless Ni-W-P coatings can be divided into two major stages. Firstly, it crystallises into metastable crystalline structures (Ni_5P_2 , NiP) at lower temperature. Then, a high annealing temperature and elongated thermal heating time can lead to a thermal migration of the atoms in metastable Ni_5P_2 and Ni-P phases and transformed into stable Ni_3P crystalline phase.
4. After 2 hours annealing at 400 °C for 2 hours, the surface morphology of Ni-15W-P coating still exhibited a similar nodules characteristics to as-deposited coatings. The surface roughness of annealed coatings increased slightly from 5.6 ± 1.4 nm to 7.5 ± 1.6 nm. When the annealing temperature increased to 750 °C, all amorphous nodule features completely turned out to be enormous nano-sized crystalline grains, and the surface roughness increased to 23.8 ± 3.5 nm.
5. In the cross-sectional view, the microstructure of electroless Ni-25W-9P coating remains stable when temperature was below 400 °C. In contrast, though no dark crystalline particles were observed in the electroplated Ni-29W coating up to 500 °C, this coating started to crack at 200 °C, deteriorating the diffusion barrier property and reliability of Ni-W UBMs.

References

- [4.1] M.O. Alam, Y.C. Chan, and K.N. Tu, “Effect of reaction time and P content on mechanical strength of the interface formed between eutectic Sn–Ag solder and Au/electroless Ni(P)/Cu bond pad”, *Journal of Applied Physics*, vol. 94, No. 6, pp. 4108-4115, 2003.
- [4.2] K. Zeng, V. Vuorinen, and J.K. Kivilahti, “Interfacial reactions between lead-free SnAgCu solder and Ni(P) surface finish on printed circuit boards”, *IEEE Transactions of Electronics Packaging Manufacturing*, vol. 25, No. 3, pp. 162-167, 2002.

- [4.3] Y.D. Jeon, K.W. Paik, K.S. Bok, W.S. Choi, and C.L. Cho, “Studies of electroless nickel under bump metallurgy - Solder interfacial reactions and their effects on flip chip solder joint reliability”, *Journal of Electronic Materials*, vol. 31, No. 5, pp. 520-528, 2002.
- [4.4] M. He, Z. Chen, and G. Qi, “Solid state interfacial reaction of Sn–37Pb and Sn–3.5Ag solders with Ni–P under bump metallization,” *Acta Materialia*, vol. 52, No. 7, pp. 2047-2056, 2004.
- [4.5] Y.D. Jeon, K.W. Paik, K.S. Bok, W.S. Choi, and C.L. Cho, “Studies of electroless nickel under bump metallurgy - Solder interfacial reactions and their effects on flip chip solder joint reliability”, *Journal of Electronic Materials*, vol. 31, No. 5, pp. 520-528, 2002.
- [4.6] M. He, Z. Chen, and G. Qi, “Mechanical strength of thermally aged Sn–3.5Ag/Ni-P solder joints”, *Metallurgical and Materials Transactions A*, vol. 36A, pp. 65–75, 2005.
- [4.7] Y.C. Sohn, J. Yu, S.K. Kang, D. Shih, and T. Lee, “Spalling of intermetallic compounds during the reaction between lead-free solders and electroless Ni-P metallization”, *Journal of Material Research*, vol. 19, No. 8, pp. 2428–2436, 2004.
- [4.8] S.K. Tien, J.G. Duh, and Y.I. Chen, “The influence of thermal treatment on the microstructure and hardness in electroless Ni–P–W deposit”, *Thin Solid Films*, vol. 469-470, pp. 333–338, 2004.
- [4.9] D.M. Jang, and J. Yu, “Tungsten alloying of the Ni(P) films and the reliability of Sn–3.5Ag/NiWP solder joints”, *Journal of Materials Research*, vol. 26, No. 7, pp. 889-895, 2011.
- [4.10] J.N. Balaraju, Kalavati, N.T. Manikandanath, and V.K. William Grips, “Phase transformation behavior of nanocrystalline Ni-W-P alloys containing various W and P contents”, *Surface and Coatings Technology*, vol. 206, No. 10, pp. 2682–2689, 2012.
- [4.11] N.C. Lee, *Reflow soldering processes and troubleshooting: SMT, BGA, CSP, and flip chip technologies*, Newnes, 2002.
- [4.12] L. Wang, T. Chen, T. Feng, Y. Chen, W. Que, L. Lin, and Z. Sun, “Effect of sputtered Cu film’s diffusion barrier on the growth and field emission properties of carbon nanotubes by chemical vapor deposition”, *Applied Physics A Materials Science & Processing*, vol. 90, pp. 701-704, 2008.
- [4.13] D.A. Hutt, C. Liu, P.P. Conway, D.C. Whalley, and S.H. Mannan, “Electroless nickel bumping of aluminium bondpads - part I: surface pretreatment and activation”, *IEEE Transactions on Component and Packaging Technologies*, vol. 25, No. 1, pp. 85-97, 2002.
- [4.14] X. Zhan and F. Ernst, “Crystallization micro-mechanism of near-eutectic amorphous Ni-P,” *Acta Materialia*, vol. 104, pp. 274-282, 2016.
- [4.15] K.G. Keong, W. Sha, and S. Malinov, “Crystallisation kinetics and phase transformation of electroless nickel-phosphorus deposits with high phosphorus content”, *Journal of Alloys and Compound*, vol. 334, No. 1-2, pp. 192-199, 2002.

- [4.16] A. Cezairliyan, "Measurement of melting point and electrical resistivity (above 3600 K) of Tungsten by a pulse heating method", *High Temperature Science*, vol. 4, pp. 248-252, 1972.
- [4.17] Y.J. Hu, T.X. Wang, J.L. Meng, and Q.Y. Rao, "Structure and phase transformation behaviour of electroless Ni-W-P on aluminium alloy," *Surface & Coatings Technology*, vol. 201, pp. 988-992, 2006.
- [4.18] A. Allouche, and C. Linsmeier, "Quantum study of tungsten interaction with beryllium (0001)", *Journal of Physics: Conference Series*, vol. 117, 012002, 2008.
- [4.19] S.K. Tien and J.G. Duh, "Thermal reliability of electroless Ni-P-W coating during the aging treatment", *Thin Solid Films*, vol. 469-470, pp. 268-273, 2004.

Chapter 5

Formations and Characteristics of Zn-Al Solder Interconnects

In this chapter, different joining processes, including soldering, gas dynamic cold spray, and self-propagation processes, were developed and applied in enhancing the solderability of Zn-Al solders on various substrates (Cu, Ni-based, or SiC chip with metallisation). As a result, Zn-Al solder interconnects were formed successfully, followed with characterisations on their interfacial reactions.

5.1 Introduction

Considering human health and natural protection, environmental legislations and restrictions (RoHS and WEEE directives) banned the use of hazardous substances (Pb) in electronic devices. Recently, numerous high temperature lead-free solders have been developed to replace the high-lead solders (Pb-10Sn, Pb-5Sn) in die attachments, such as Au-based solders, Bi-Ag-based solders, and Zn-Al-based solders. Among them, Zn-Al high-temperature solders exhibit various advantages such as low cost, reasonable melting temperature, excellent mechanical property (shear strength can reach 90 MPa in Ni-P/Zn-Al joints in our previous work [5.1]), good thermal and electrical conductivity [5.2-4]. However, it is difficult to form Zn-Al interconnects owing to the low oxidation resistance and poor wettability. To solve these issues, proper joining methods were required to achieve a good solderability of Zn-Al solders on metallised substrates.

Conventionally, a flux can reduce oxidation on the metallisation and solder surface during flux activation to achieve an optimal solderability. Nevertheless, there is no commercial flux for Zn-Al solder so far since its activation temperature ranges between 350 and 450 °C, while operating temperature of most fluxes are below 250 °C or over 500 °C for Sn-based solder and Al-based solder, respectively. In addition, a flux usually

causes cleaning problems by using detergents after solder joint formations [5.5]. Besides, the reflowing temperature of Zn-Al solder is relatively high which also arouses reliability issues for electrical components. Some process methods have drawn wide interests in academic and industry fields with the attempts to not only lower the processing temperature but also enhance the wettability of solders during joining. Recently, some novel joining methods have been reported (Reviewed in Section 2.4), including gas dynamic cold spray and self-propagation process, to form solder joints at a relatively lower temperature in air [5.6-8]. So far, no works have been reported in terms of applying self-propagation method to prepare Zn-Al solder interconnects.

Therefore, various joining methods including soldering, gas dynamic cold spray, and self-propagation processes were utilised to form Zn-based solder interconnects in this chapter. Notably, for conventional soldering, a flux was prepared to obtain Zn-Al solder interconnects with a good solderability in air. The interfacial microstructure and the defects of these solder interconnects fabricated by various processes were studied. Overall, advantages and disadvantages of these process methods are discussed and summarised in this chapter.

5.2 Soldering process with a self-developed flux

5.2.1 Experimental details

5.2.1.1 Development of the soldering flux

Due to the lack of commercial fluxes for Zn-based solder, a new flux was particularly developed for Zn-Al solder in this work. The flux was to improve the wettability of Zn-Al solder alloy on Cu and electroless Ni-W-P plated substrates at approximately 400 °C in air. The requirements of this flux are listed below based on flux specifications from the Institute for Interconnecting and Packaging Electronic Circuits (IPC) [5.9, 5.10].

1. To remove oxides prior to soldering.
2. To maintain an oxide-free surface during the soldering process.
3. To lower the surface tension at the substrate/solder interface.

Generally, a soldering flux is composed with activators, oxidation remover and basic components [5.11]. To determine the flux formulation, some potential chemical

reagents were considered for their effects of eliminating Zn-Al oxidizes and modulating the melting point. Zn-Al alloys tend to react with oxygen and moisture in air, forming an oxidation layer on the metal surface (Figure 5-1 [5.12]). The oxidation layer of Zn-Al alloys is quite complex with high melting points and compact structures, composing with Al_2O_3 , ZnO , ZnAl_2O_4 , and etc. KF is an efficient oxidation remover, especially for the compact Al_2O_3 layer in this work. ZnCl_2 , LiCl and KCl are also the key constituents in the flux. ZnCl_2 shows abilities of removing the oxidation layer, decreasing the melting point, and increasing the wettability of the flux. The addition of LiCl can improve the wettability and decrease the melting point of the flux. KCl in the flux is for the decrease in the melting point and surface tension of the flux. The physical properties of main constituents of this flux are listed in table 5-1.

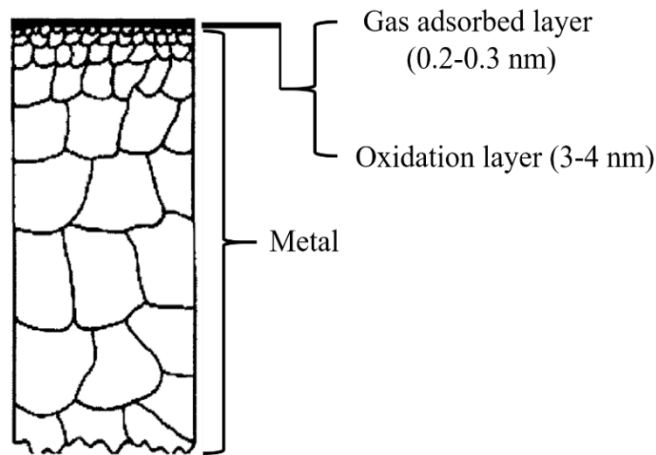


Figure 5-1 Surface structure of solid metal [5.12].

Table 5-1 The physical properties of main chemicals in the flux.

Chemical	Melting Point	Boiling Point
ZnCl_2	318 °C	730 °C
LiCl	613 °C	-
KCl	768 °C	-
KF	857 °C	1505 °C

After determining the flux constituents, the most vital factor of soldering flux is its melting temperature. The flux needs to be melt and spread over substrate prior to soldering of Zn-5Al alloy (melting point: 382 °C). The flux system is polybasic, involving several binary and ternary phase diagrams. In figure 5-2 [5.12], the melting

temperature of LiCl-KCl eutectic system is 355 °C (LiCl: 60 mol%). The triangulation of ZnCl_2 -LiCl-KCl ternary system is presented in figure 5-3 [5.13]. In this figure, two eutectic temperatures can be found in this ternary system, 325 °C at ZnCl_2 content of 71.4% and 289 °C at ZnCl_2 content of 48%. Figure 5-4 [5.13] presents the pseudo-binary diagrams of LiCl-(2ZnCl_2 -KCl) and LiCl-(ZnCl_2 -2KCl) system. For each system, there are two eutectic points. In figure 5-4 a), the eutectic points are 222 °C (22.7% LiCl) and 198 °C (47.3% LiCl) in LiCl-(2ZnCl_2 -KCl) system. Similarly, the eutectic points are 435 °C (77.7% LiCl) and 327 °C (44% LiCl) in LiCl-(ZnCl_2 -2KCl) system.

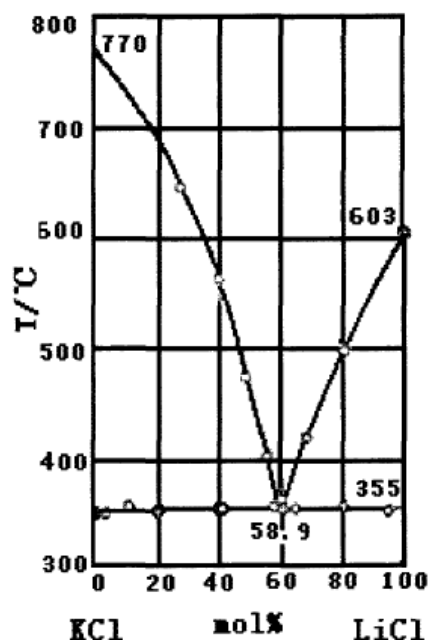


Figure 5-2 The binary phase diagram of LiCl-KCl system [5.12].

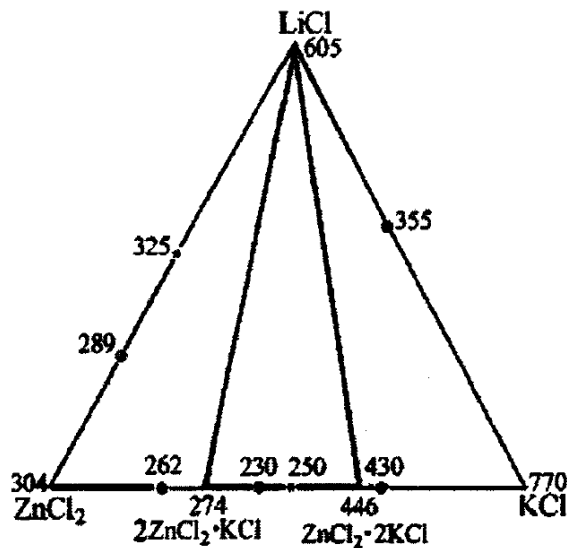


Figure 5-3 The triangulation of ZnCl_2 -LiCl-KCl ternary system [5.13].

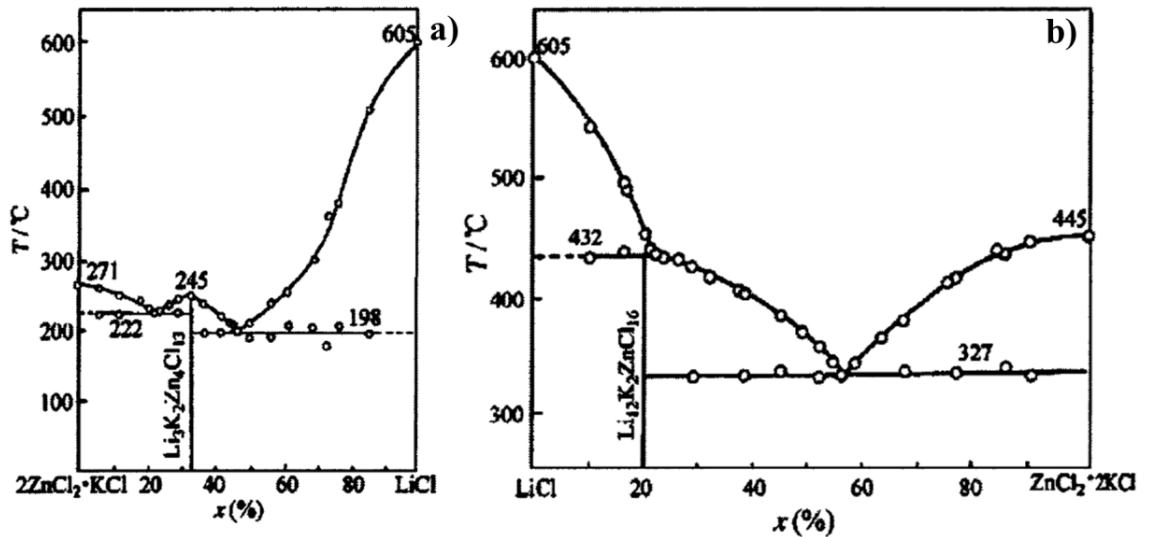


Figure 5-4 Pseudo-binary diagrams of: a) $\text{LiCl}-(2\text{ZnCl}_2\text{-KCl})$ system; b) $\text{LiCl}-(\text{ZnCl}_2\text{-}2\text{KCl})$ system [5.13].

With a comprehensive understanding of these phase diagrams, many eutectic systems can be formed in $\text{ZnCl}_2\text{-LiCl}$, LiCl-KCl , $\text{LiCl}-(2\text{ZnCl}_2\text{-KCl})$ and $\text{LiCl}-(\text{ZnCl}_2\text{-}2\text{KCl})$ systems. The base component of this flux is $\text{LiCl}-(\text{ZnCl}_2\text{-}2\text{KCl})$ system with a LiCl content of 44%; its melting temperature is 327 $^{\circ}\text{C}$. Beside the basic constituent, small amount of KF was added into the flux matrix as an oxidation remover, especially for the compact Al_2O_3 layer. In preparation of this flux, all constituents were dissolved into an absolute ethanol to mix uniformly. As ZnCl_2 exhibits a strong hygroscopicity, the flux dehydrated from 100 to 125 $^{\circ}\text{C}$ to achieve a solid flux. The developed flux was tested in soldering Zn-Al solder in air. The Zn-Al solder interconnects with good bonding were finally achieved.

5.2.1.2 Soldering of Zn-Al alloy with flux

A Zn-5Al eutectic solders (melting point: 382 $^{\circ}\text{C}$, supplied by Brock Metal Company Limited) were diced into small pieces with the weight of approximately 0.15 g. These solder pieces were polished by 1 μm alumina powder to remove the oxides on their surface and then rinsed in absolute ethanol to prevent further oxidation prior to soldering. Cu sheets were cut into 20 mm \times 20 mm squares and then ultrasonically cleaned in acetone for 5 minutes to serve as the substrates. After that, all Cu substrates were polished and then etched with 50% HCl solution (by volume) for 30 s to remove oxidation.

Prior to electroless plating, half of the Cu sheets were immersed in DMAB solution for 5 minutes. Substituents of the plating bath and major coating parameters are listed in table 5-2. The plating solution was an alkaline bath making up with deionized water and sodium tungstate (7 g/L), nickel sulphate (35 g/L), sodium hypophosphite (12 g/L) and sodium acetate (40 g/L). The plating temperature was 88 ± 2 °C and the plating time was 20 minutes. The pH of the bath was controlled in a narrow window around 8.2 by dilute H_2SO_4 and NaOH solution during the plating process.

Table 5-2 The formulations and plating conditions of the electroless Ni-W-P plating.

Chemicals	Concentration (g/L)
$\text{NiSO}_4 \cdot \text{H}_2\text{O}$	7
$\text{Na}_2\text{WO}_4 \cdot \text{H}_2\text{O}$	35
$\text{NaH}_2\text{PO}_2 \cdot \text{H}_2\text{O}$	12
$\text{Na}_3\text{C}_6\text{H}_5\text{O}_7 \cdot \text{H}_2\text{O}$	40
$\text{NaC}_{12}\text{H}_{25}\text{SO}_4$ (SLS)	3×10^{-4}
Plating conditions	Temperature: 88 ± 2 °C, pH: 8.2

For soldering, the Zn-Al solder pieces were placed on the substrates that were covered with the developed flux and heated on the hotplate (IKA C-MAG HP4) at 450 °C in air. After soldering, all specimens were mounted, grinded and polished to reveal the cross section of the Zn-Al interconnects. The interfacial microstructure of the solder interconnects was observed with scanning electron microscopy (SEM: Carl Zeiss, Stereoscan 360, Cambridge) and the composition of each IMCs at the interfaces was examined by energy dispersive X-ray technique (EDX) incorporated with the SEM.

5.2.2 Solderability of Zn-Al/Cu and Zn-Al/UBM Solder

With the developed flux, the Zn-Al interconnects can be prepared in air up to 450 °C. The composition of deposited Ni-W-P layer was measured as 6-7 wt.% of phosphorous and 18-19 wt.% of tungsten by EDX.

The wetting angles of Zn-Al solder on Cu substrates with and without Ni-W-P coatings were measured in the cross-section micrographs as shown in figure 5-5. The average wetting angles of Ni-W-P/Zn-Al interconnects were approximately 32°, and the

wetting angles of Cu/Zn-Al samples were lower at about 26° . It indicates that the solderability of Zn-Al solder on Ni-W-P UBM was smaller than that on Cu substrates. However, the solderability of Zn-Al solder on both Cu and Ni-W-P substrates is good since all wetting angles were less than 40° [14]. Moreover, no massive voids or cracks can be found within the Cu/Zn-Al and Ni-W-P/Zn-Al solder interconnects after liquid-solid reaction at 450°C up to 30 minutes, which will be further discussed in Chapter 6. This also verifies the advantages of this developed flux in enhancing the solderability of Zn-Al solders.

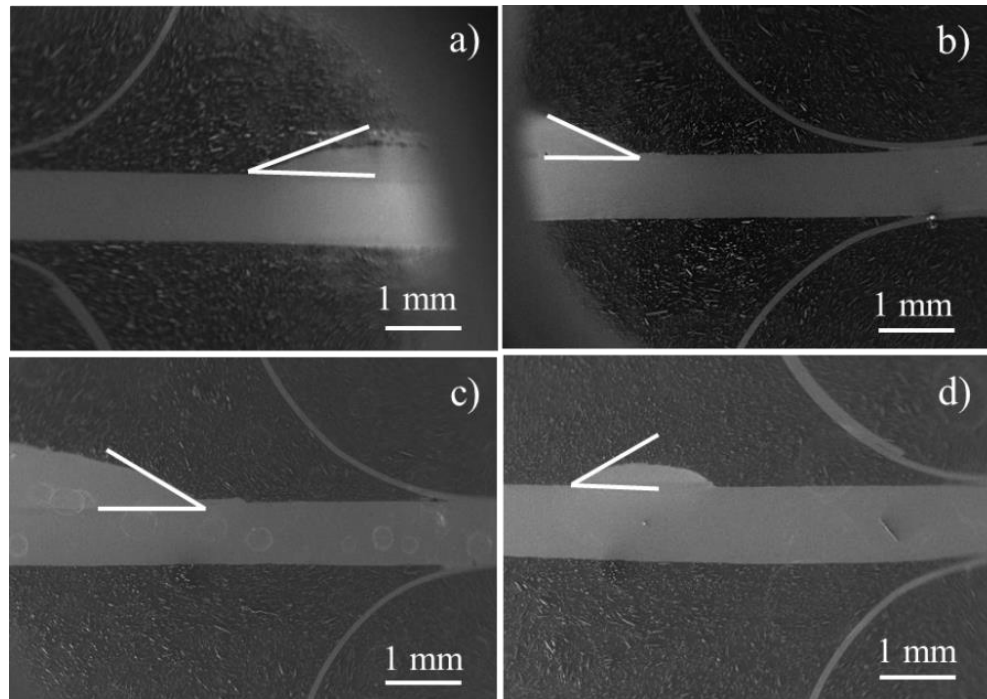


Figure 5-5 Wetting angles of Zn-Al solder on (a) Cu substrate after 5 minutes soldering; (b) Cu substrate after 30 minutes; (c) Ni-W-P/Cu substrate after 5 minutes soldering; (d) Ni-W-P/Cu substrate after 30 minutes soldering.

5.2.3 Interfacial microstructure at Cu/Zn-Al and Ni-W-P/Zn-Al interfaces

The cross-section microstructure at as-soldered Cu/Zn-Al interface was shown in figure 5-6. According to the EDX results, $\epsilon\text{-CuZn}_4$ phase formed in dendritic shape adjacent to the Zn-5Al solder. Meanwhile, $\gamma\text{-Cu}_5\text{Zn}_8$ clearly formed as a levelled interlayer between $\epsilon\text{-CuZn}_4$ and Cu substrate. The thickness of $\epsilon\text{-CuZn}_4$ and $\gamma\text{-Cu}_5\text{Zn}_8$ were measured to be approximately $2.57\ \mu\text{m}$ and $6.69\ \mu\text{m}$, respectively.

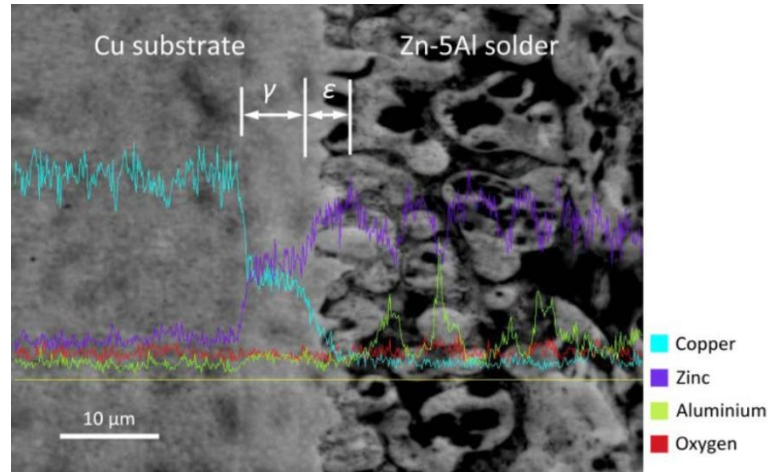


Figure 5-6 Back-scattered SEM image showing Cu-Zn IMCs formed at the as-soldered Cu/Zn-Al interface with line-scanned EDX results.

Figure 5-7 shows the interfacial microstructure of the as-soldered Ni-W-P/Zn-Al interface soldered at 450 °C. The EDX line results indicates that the Zn, Al, Cu atoms were effectively blocked by the electroless Ni-W-P coatings. Therefore, Zn and Cu could not directly react with each other to form brittle Cu-Zn IMCs. According to the related researches and EDX analysis [5.2, 5.15, 5.16], only $\gamma\text{-Ni}_5\text{Zn}_{21}$ and Al_3Ni_2 may generate at Ni-W-P/Zn-Al interfaces. However, the thickness of the interfacial IMC layer in the as-soldered Zn-5Al solder interconnects with Ni-W-P UBM was too thin ($< 1 \mu\text{m}$) to be identified by EDX. This also indicates an excellent property for diffusion barrier characteristics of Ni-W-P UBM by suppressing the IMC thickness from around 9 μm to below 1 μm in as-built Zn-Al solder interconnects.

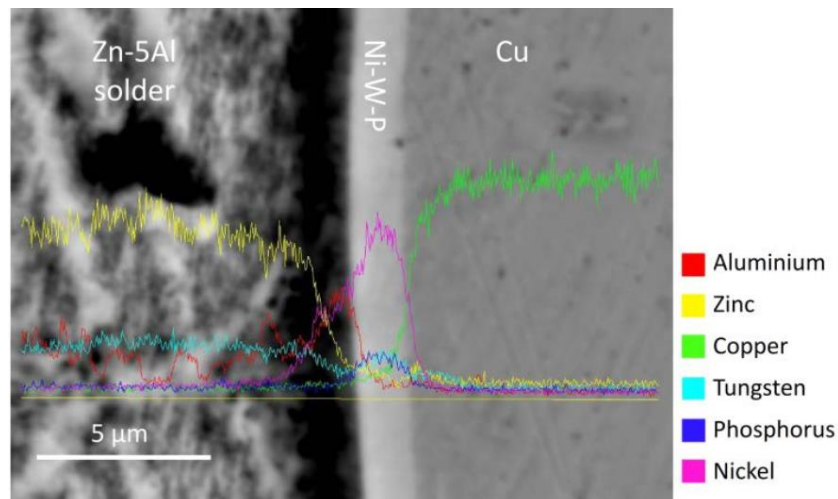


Figure 5-7 Back-scattered SEM image showing the IMCs formed at the as reflowed Ni-W-P/Zn-5Al interface with line-scanned EDX results.

The interfacial reactions and microstructure of Zn-Al solder interconnects with and without Ni-W-P coatings will be further discussed in Chapter 6 to elaborate the formation mechanisms and mechanical characteristics of the interfacial IMCs layers.

5.3 Gas Dynamic Cold Spray

Gas dynamic cold spray (GDCS) is a deposition method to obtain a compact coating with a relative low content of oxygen at lower temperature [5.17, 5.18]. This method has been utilised to deposit solder alloys in electronic packaging as reported in some works [5.8, 5.19].

Figure 5-8 illustrates a typical GDCS system. In the chamber of GDCS equipment, solid solder powders (with a diameter from 1 to 50 μm) are accelerated to 500 - 1000 m/s in a supersonic gas jet [5.20, 5.21]. Once they hit the substrate, particles undergo plastic deformation and adhere to the surface. If the particle velocity exceeds its critical velocity, the solder particles and substrate can be bonded firmly. The spray nozzle scanned along the substrate to cover the entire surface. In GDCS process, the deposition parameters that affect the performances of the Zn-Al coatings include spray distance, pre-heat temperature, gas pressure and the feed rate of Zn-Al powders.

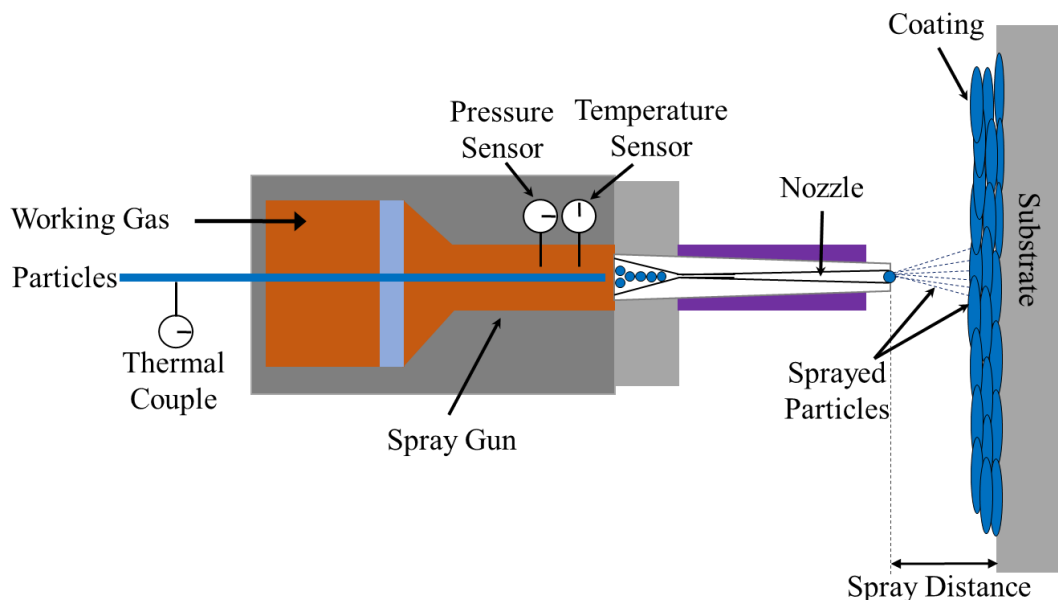


Figure 5-8 A schematic diagram of gas dynamic cold spray system.

In this work, eutectic Zn-5Al solder particles were deposited on Cu and electroless Ni-W-P plated substrates, respectively. Thus, the solderability of Zn-Al solder was

evaluated by observing the interfacial microstructure at the solder interfaces during reflowing.

5.3.1 Experimental details

Copper sheets with a dimension of 30 mm × 80 mm × 1 mm were used as the substrates. All Cu substrates were polished and etched with 50% HCl solution (by volume) for 30 s to remove the surface oxides. Afterwards, half of the specimens were activated in DMAB solution for 5 minutes and then quickly immersed into an alkaline Ni-W-P plating bath for 45 minutes. The composition of this plating solution was exactly as same as the bath condition listed in table 5-2. The pH value of the bath was 8.2 and the plating temperature was 88 ± 2 °C. A layer of Ni-W-P UBM can thus be finally electroless plated on the substrate.

Eutectic Zn-5Al powders (99.9% purity, Tianjiu Metal Materials Co. Limited) were cold sprayed on Cu substrates with and without Ni-W-P coatings with a high-pressure cold spray system (CS2000, Xi'an Jiaotong University) using nitrogen as the process gas. The particle size distribution was analysed by a particle size analyser (Mastersizer 3000, Malvern).

In this GDCS system, the solder particles were fed by a powder feeder (Plasma 1000, Japan), and preheated in a preheating chamber (length: 120 mm) fixed behind a nozzle. The particles were then sprayed onto substrates by this de Laval nozzle. The dimensions of the nozzle are listed in table 5-3. The spraying can be manipulated by the controller of the nozzle.

Table 5-3 Dimensions of the nozzle.

Part of nozzle	Length
Throat diameter	2 mm
Outlet diameter	6 mm
Divergent section length	100 mm

To obtain an optimised Zn-Al coatings on Ni-W-P UBM with a high deposition rate, high deposition efficiency and good integrity, a pre-set of cold spray tests were conducted to optimise the process. Major process parameters of these cold spray pre-

tests are listed in table 5-4. After trial tests, parameters of Test Cu-1 and Test NiWP-1 were found to be optimal for Cu and Ni-W-P deposited substrates, respectively.

Table 5-4 The process parameters for GDCS pre-tests.

Test	Temperature ($^{\circ}\text{C}$)	Spray distance (mm)	Pressure (MPa)	Gun Speed (mm/s)	Thickness (mm/10 times)
Cu-1	190	20	1.9	100	0.25
Cu-2	250	20	1.9	60	0.17
Cu-3	250	20	2.2	20	0.23
Cu-4	250	40	2.2	20	To thin
NiWP-1	240	20	1.9	20	0.58
NiWP-2	250	20	2.2	20	0.68

After the preparation of Cu/Zn-Al and Ni-W-P/Zn-Al solder interconnects by GDCS method, these interconnects were then reflowed with the temperature profile (Figure 5-9) to test the solderability.

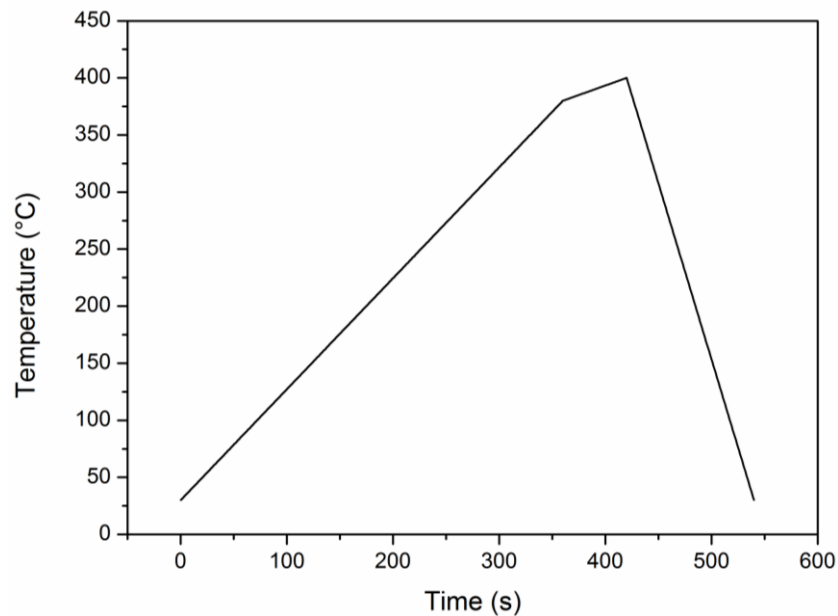


Figure 5-9 The reflow profile for the cold sprayed samples

A FEG-SEM (Mira 3 LMH, Tescan, Czech Republic) was utilised to characterise the morphology and interfacial microstructure of the Zn-Al solder particles, as-deposited Zn-Al interconnects, and as-reflowed Zn-Al interconnects. The porosity of Zn-Al

interconnects before and after soldering were observed with a C mode scanning acoustic microscope (C-SAM).

5.3.2 Characteristics of Zn-Al solder particles

The morphology of original Zn-Al solder particles was observed with a FEG-SEM in a back-scattered image mode, as shown in figure 5-10. The average diameter of the particles is around 40 μm , which meets the particle requirement for GDCS process. Some dark Al particles pointed out with arrows disperse into this particle matrix, and were identified to be oxydic Al in figure 5-10 c). The white particles are Zn-5Al solder with a diameter range of 3-90 μm .

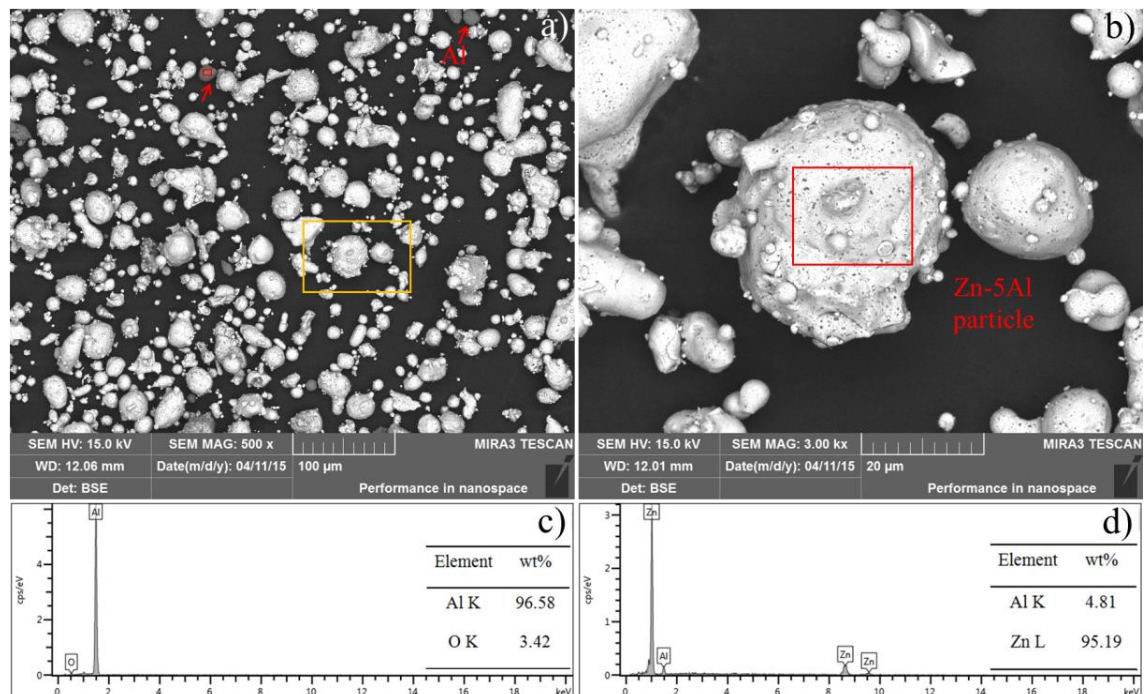


Figure 5-10 Back-scattered images of the morphology of Zn-Al solder particles with elemental results: a) overview image; b) typical Zn-Al particles (enlarged view of the highlight region in figure 5-10 a)); c) EDX spectrum on dispersive Al particles; d) EDX spectrum on Zn-Al particles.

However, small solder particles ($< 10 \mu\text{m}$) lead to the blockage of the nozzle in its throat region and significantly weaken the deposition effectiveness. Therefore, a sleeve (mesh size: 15 μm) was used to remove the smaller solder particles before GDCS process. After the screening, an analysis of particle sizes on Zn-Al solder particles was conducted again. Figure 5-11 illustrates the comparison between the original particles and screened particles. It is found that the volume mean diameters of original and screened Zn-Al particles are the same of 40.9 μm . The amount of small particles (diameter size $< 10 \mu\text{m}$) significantly decreases in the particle matrix.

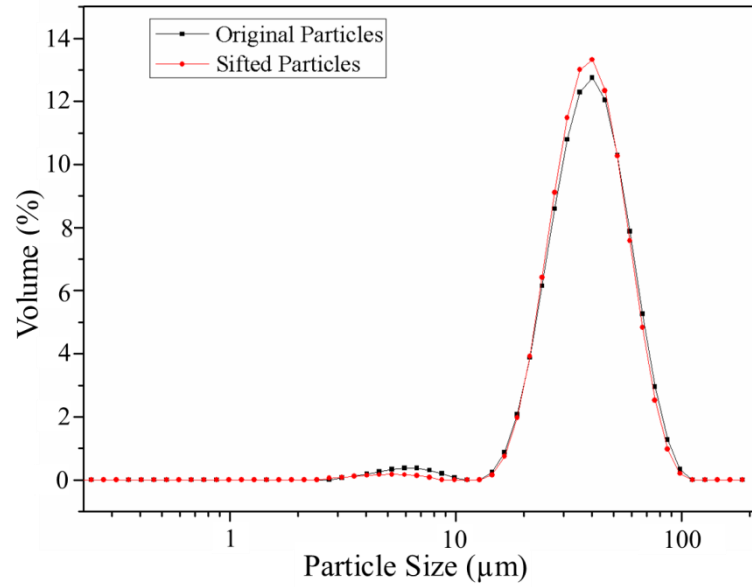


Figure 5-11 The particle size distribution of Zn-5Al solder particles.

5.3.3 Microstructure of the as-deposited samples

In cold spray process, Zn-Al particles before impacting onto substrates were solid with the temperature between 190 and 240 °C, which is lower than the melting point of Zn-5Al eutectic solder (382 °C).

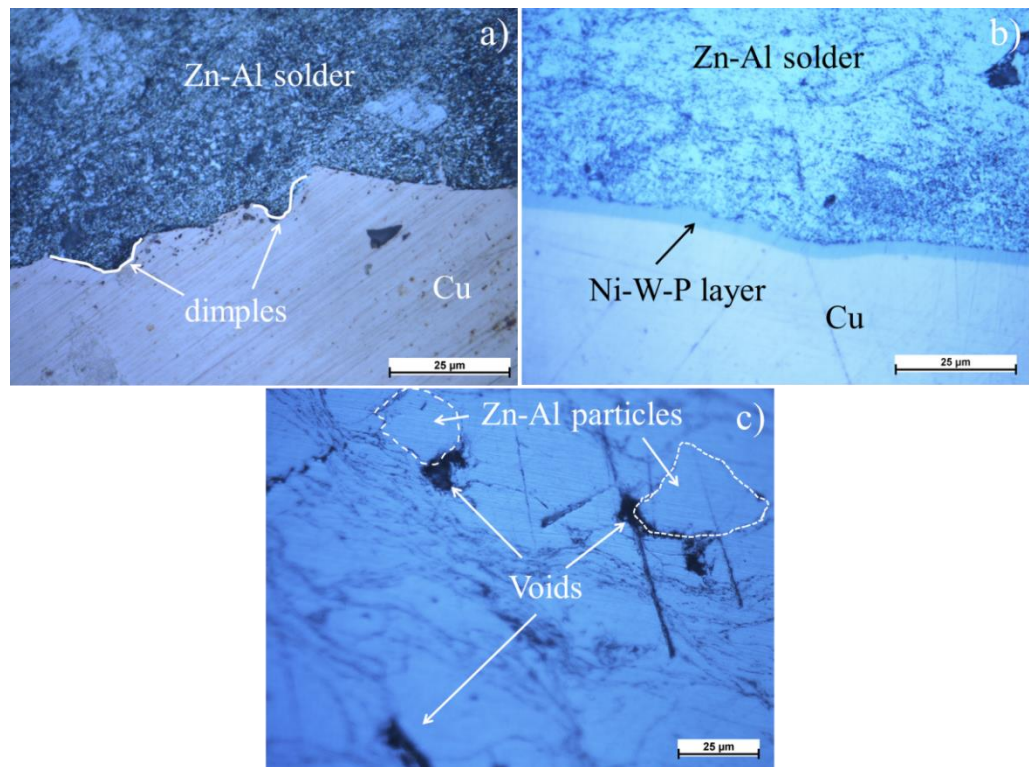


Figure 5-12 Cross-sectional image of as-deposited Zn-Al coatings: a) on Cu substrate; b) on Ni-W-P plated Cu substrate; c) with distinct voids and boundaries of Zn-Al solder particles.

Figure 5-12 shows the cross-section micrographs of Cu/Zn-5Al and Cu/Ni-W-P/Zn-5Al interconnects prepared by cold spraying. The un-etched Zn-Al coatings exhibit a relatively dense structure with some voids at the boundaries of Zn-Al particles, as illustrated in figure 5-12 c). At the Cu/Zn-Al interface, some dimples were formed due to the impact of the supersonic Zn-Al particles with the aid of propellant gas. In contrast, the cross section of Ni-W-P UBM in figure 5-12 b) is relatively smoother since the hardness of Ni-W-P alloy is much higher than that of Zn-Al solder.

Figure 5-13 shows the typical surface morphology of the Zn-Al coatings deposited at 190 °C in N₂ atmosphere. The Zn-Al particles experienced intensive plastic deformation during cold spraying. Moreover, a number of micro-pores were also observed on the surface of Zn-Al coatings.

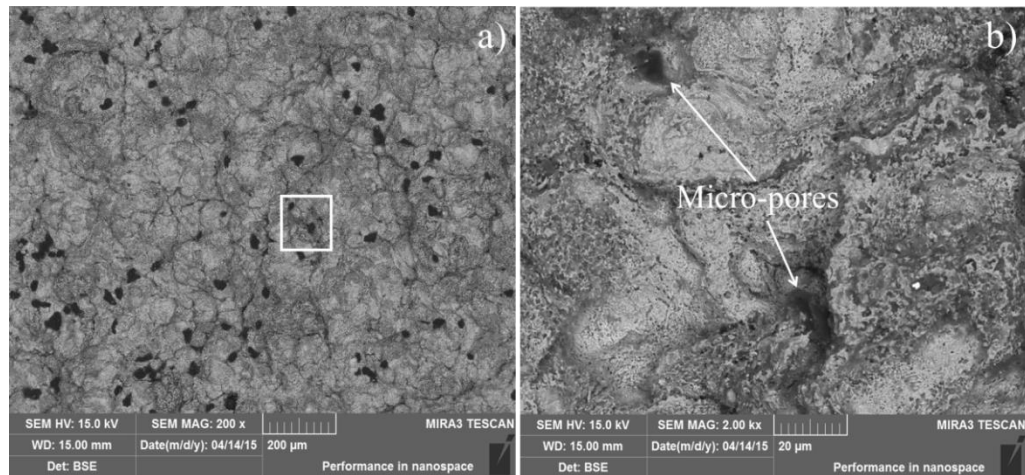


Figure 5-13 Surface morphology of cold-sprayed Zn-Al coating in N₂ atmosphere at a temperature of 190 °C: a) Overview image; b) Enlarged view of the region highlighted in figure 5-13 a).

5.3.4 Microstructure of as-reflowed Zn-Al solder interconnects

The as-deposited Cu/Zn-Al and Cu/Ni-W-P/Zn-Al solder interconnects were cut into small pieces in a dimension of 5 × 5 × 1 mm for subsequent soldering tests. After soldering, the interfacial microstructures of Zn-Al coating are presented in figure 5-14. It is observed that some Zn-5Al solder particles did not melt together owing to their oxidation layers on particle surfaces as highlighted in dash lines (Figure 5-14 a)), along with bright Zn-rich phases and dark eutectic Zn-Al alloy existing in the solder particles. In figure 5-14 b), dispersive Al particles also did not melt during the soldering process at a maximum temperature of 400 °C, inducing voids due to the extruded oxides moving in the solder matrix.

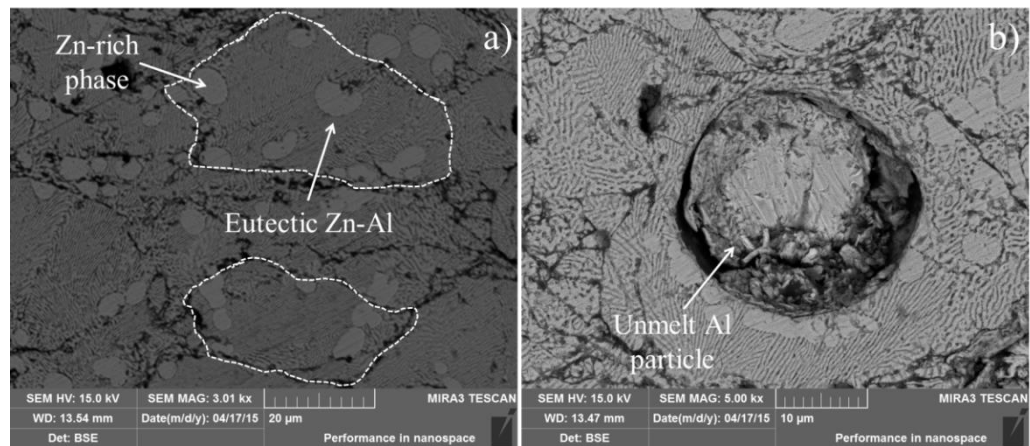


Figure 5-14 Interfacial microstructures of as-soldered Zn-Al coatings. a) Overview image showing the Zn-Al particle grains; b) The unmelt Al particle embedded in Zn-Al coating matrix.

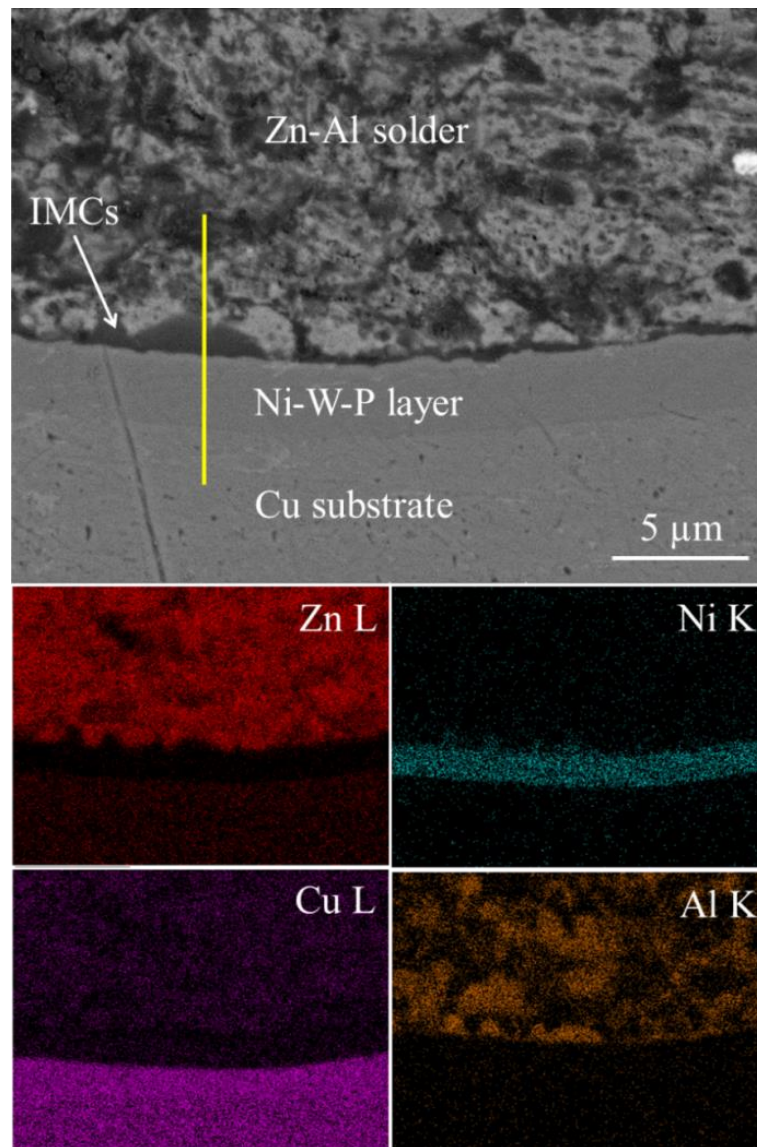


Figure 5-15 As-soldered Ni-W-P/Zn-Al solder interconnects with elemental mapping results.

Though the Zn-Al solder particles posed great impacts on electroless Ni-W-P UBM, no visible cracks were seen in most regions of this Ni-W-P layer. Because the impact was neutralised by the significant deformations of softer Zn-Al solders, not the Ni-W-P coatings. However, mutual diffusion of Cu and Zn into the opposite side can be still identified from the elemental mapping results (Figure 5-15). It indicates that some defects or pores may occur in the entire Ni-W-P coatings after the GDCS process.

Figure 5-16 illustrates the elemental line scan results at Ni-W-P/Zn-Al interface. According to the elemental results, the IMC interlayer is Al_3Ni_2 phase, which is discontinuous with a maximum height of approximately 2 μm . The black particles near the Cu substrate are Al-rich phase instead of voids.

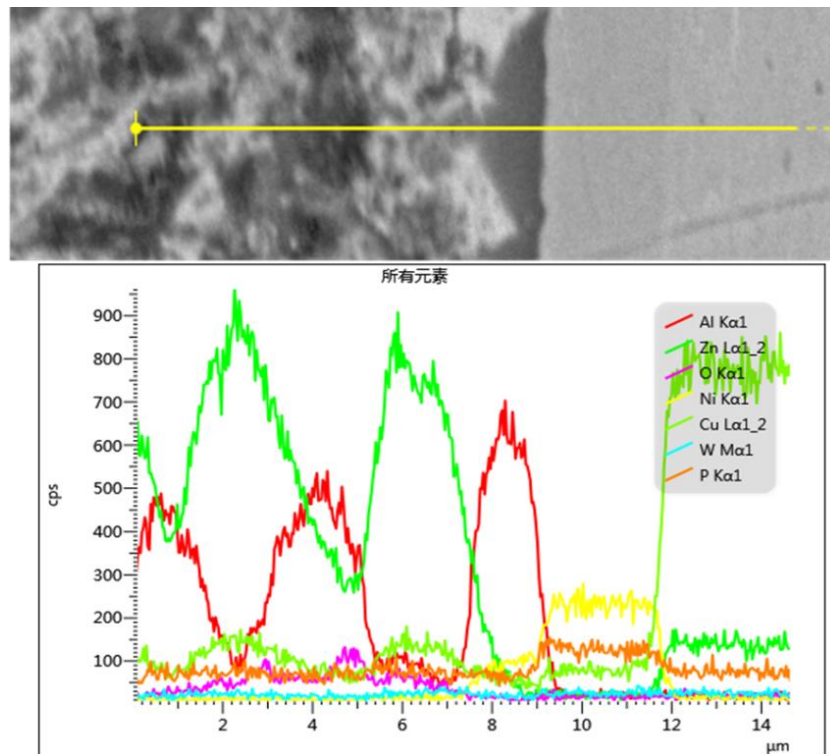


Figure 5-16 The interfacial microstructure at Ni-W-P/Zn-Al interface with elemental line results.

Figure 5-17 presents the fractures and cracks in the as-reflowed Cu/Zn-Al solder interconnects. Massive cracks and voids exist within the Zn-Al solder matrix, as shown in figure 5-17 a). This is partly due to the residual stresses from the plastic deformation of the Zn-Al coating in cold spraying, agreeing to previous works [5.22, 5.23]. Moreover, during cold spraying, the Zn-Al solder were deposited layer by layer with the scanning of the nozzle. Hence, the first layer of Zn-Al solder could be in contact with Cu substrate free of oxides. However, the other surface on the first layer of Zn-Al solder was exposed to the air at slightly elevated temperature (around 150 $^{\circ}\text{C}$). Thus, it

is highly likely to be oxidised. The oxides will lead to the poor adhesion, and therefore induce the cracks between Zn-Al solder layers.

Similarly, after the cold spraying, the Zn-Al solder on Cu substrate is more like multi-layer structure with oxide layers between them. Consequently, during reflowing, the first layer of Zn-Al solder was mainly consumed by the reaction with Cu substrate. Because of the blockage of oxides, incomplete melting of the Zn-Al solder and trapped air within the solder, the supplement of solder from the 2nd layer of Zn-Al solder was mostly suppressed. Meanwhile, the reaction between the first layer of Zn-Al solder and Cu substrate could lead to volume shrinkage and height reduction due to the formation of IMCs. Consequently, the gap between the 1st and 2nd layers of Zn-Al solder expands with the growth of Zn-Cu IMCs at the solder/Cu interface. Figure 5-17 b) shows another micro-crack penetrated adjacent to the Zn-Cu IMCs, which was formed by the consumption of the Zn-Al solder particles during the growth of Cu-Zn IMCs.

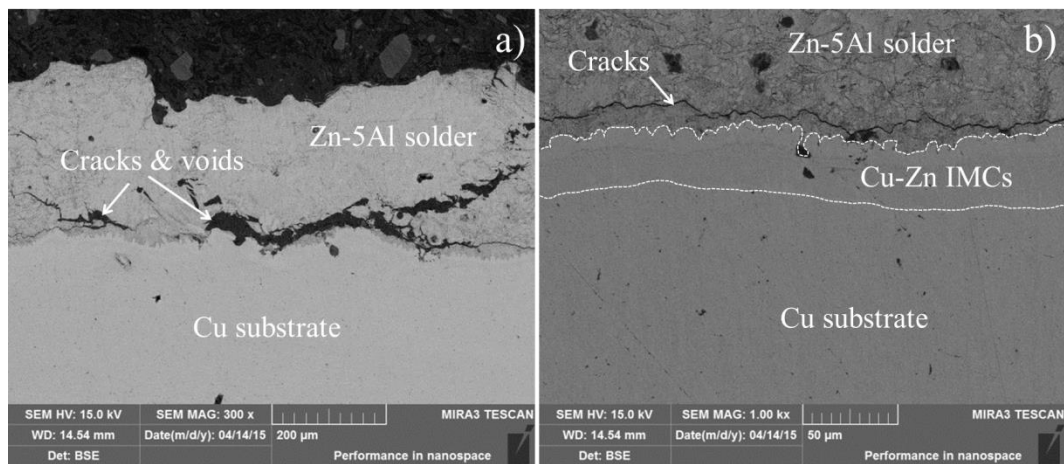


Figure 5-17 Fracture at Cu/Zn-Al solder interconnects: a) massive cracks and voids formed within the solder joint; b) penetrating cracks near the Cu-Zn IMCs.

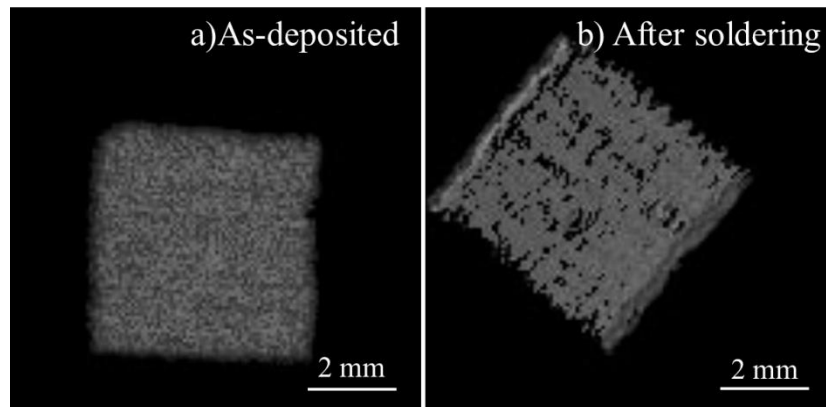


Figure 5-18 SAM images of the Cu/Zn-Al solder interconnects: a) As-deposited specimen; b) After soldering process.

As many voids formed in the Cu/Zn-Al solder interconnects, a C mode scanning acoustic microscope (C-SAM) was employed to analyse the porosity features within the Zn-Al solder interconnects. In figure 5-18, the small voids in as-deposited Cu/Zn-Al interconnects gathered together and led to a significant increase of the void size, which is identical to a typical 2D C-SAM images.

5.4 Self-propagation method

As discussed in Section 5.1, the highly oxidation and high processing temperature of Zn-5Al solder prohibit its wide application in high temperature packaging, especially in 3D stacking. Self-propagation method through Al/Ni multilayer can be an applicable option since exothermic multilayer can produce sufficient heat immediately to break the oxidation of solders and to form solder joints [5.24-27]. Moreover, self-propagation can selectively melt the adjacent solder rather than heating up the entire sample, causing less damage to entire devices. The exothermic reaction is easy to be initiated by ignition sources, such as electric spark or laser light. Once the reaction in Ni/Al films starts, the Ni/Al film can be serve as a local heat source with a maximum temperature at around 1400 °C [5.28]. Hence, the solder film close to Ni/Al multilayer melts and leads to a formation of solder joint without any external heat sources and fluxes [5.29, 5.30]. In this study, Ni/Al exothermic reaction was conducted on formation of Zn-Al solder joints at a relative low temperature.

5.4.1 Experimental details

In this research, a 40 µm thick Al-Ni multilayer foil (Nanofoil[®], Indium Corporation) was selected to serve as the heat source for soldering. Figure 5-19 illustrates the schematic structure of this Al-Ni multilayer. In this Nanofoil, the thicknesses of Al and Ni nanolayers were 30 and 20 nm, respectively. Therefore, the overall atomic ratio of Al and Ni was 1:1, which produces the highest heat during the self-propagation reactions of different Al-Ni IMCs. Besides, vanadium (V) with an atomic ratio of 5 % was co-deposited in this Al-Ni Nanofoil to refine the reaction products and thus ensure high mechanical performance of the foil after reaction. In addition, the top and bottom surfaces of Ni/Al Nanofoil were covered with a thin Ag layer (1 µm thickness) to improve wettability.

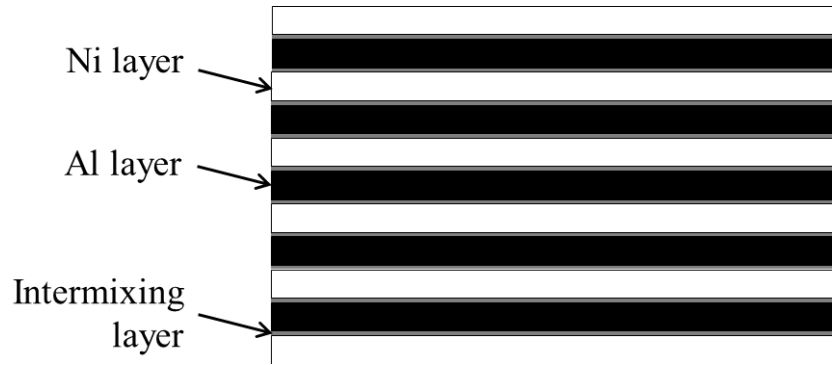


Figure 5-19 Schematic microstructure of the Al-Ni Nanofoil used for reactive bonding.

The Al/Ni Nanofoils were cut into $5\text{ mm} \times 7\text{ mm}$ by a scalpel. During cutting, the Nanofoils were placed on metal (Cu or Al) plates with good heat conductivity to avoid ignition. The sizes of Al/Ni Nanofoils were designed to be slightly wider than the joining area ($5\text{ mm} \times 5\text{ mm}$) to provide enough spaces for contacting the ignition source. As-cast Zn-Al solder was compressed into $25\text{ }\mu\text{m}$ thick foils by cold rolling. These solder foils were then cut into a square size of $5\text{ mm} \times 5\text{ mm}$ for sample preparation. Prior to bonding, the solder films were stored in a vacuum jar to minimize the oxidations. Some Si chips with a $5\text{ mm} \times 5\text{ mm}$ size area were prepared by Harbin Tebo Technology Co., Ltd for the bonding substrates in this work. Some metallisation layers, including a 50 nm thick Cr layer followed with a 300 nm Ni layer and a 50 nm thick Au layer, were on the surface of Si wafer. The functions of Cr, Ni, and Au layer act as an adhesive layer, diffusion barrier, and wetting layer, respectively. Moreover, the Au layer on the top surface also protect underlying materials from oxidizing during storage and heating due to its outstanding oxidation resistance.

The prepared Al/Ni Nanofoil, Zn-Al films and Si chips were then stacked into Si/Zn-Al/Al-Ni/Zn-Al/Si sandwich structure, as illustrated in figure 5-20. A pressure of 1 MPa was applied on the top chip while the bottom chip was placed on a hotplate heating at $150\text{ }^{\circ}\text{C}$, which was below the direction ignition temperature of Ni/Al Nanofoil ($200\text{ }^{\circ}\text{C}$) [5.30]. To initiate a self-propagation reaction, an electric spark (DC current: 5 V , 1 A) was applied by two electrode probes. Exothermic heats generated locally at the Ni/Al Nanofoil position and melt the adjacent Zn-Al solder foils immediately. Consequently, the sandwich-structured joints formed instantly after the rapid solidification of the Zn-Al solders.

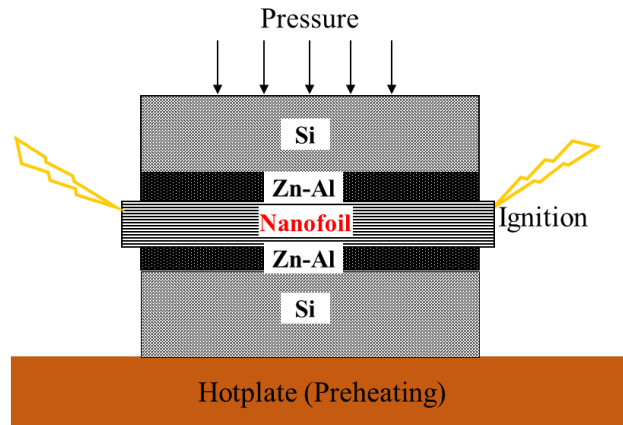


Figure 5-20 Schematic diagram of self-propagation test.

After sample preparations, the interfacial microstructure and IMC morphology in the cross-section solder joints were characterised by an optical microscopy (Leica DM6000M) and a FEG-SEM (Carl Zeiss, Stereoscan 360). A thin transmission electron microscope (TEM, JEOL 2000FX) samples with a thickness of 150 nm was prepared with a dual-beam focus ion beam (FIB, FEI Nova 600 Nanolab Dual Beam) in the Si/Zn-Al/Ni-Al solder interconnect as marked in figure 5-21 b).

5.4.2 Interfacial microstructure of Zn-Al solder joints

Figure 5-21 shows the cross-section micrographs of Zn-Al solder joints. In the Zn-Al solder joints, the Ni/Al Nanofoil turned into AlNi crystalline particles after the self-propagation reaction and was partially broken due to its brittleness. By comparing the Zn-Al solder after reaction in figure 5-21 b) and before reaction in figure 5-21 c), it can be confirmed that the Zn-Al solder film fully melted across the entire solder joints during the rapid self-propagation reaction. Afterward, the Zn-Al solders solidified surround the AlNi layer, guaranteeing the mechanical strength and ductility of this solder joints.

Metastable interfacial IMC layers are located at the NiAl/Zn-Al and Zn-Al/Au metallisation interfaces due to the wide temperature range of 400 - 1400 °C. TEM sample was prepared by FIB milling at the location highlighted in figure 5-21 b) for further analysis of the microstructure and composition at these interfaces. The overview image of this TEM sample is presented in figure 5-22. The thickness of melted Zn-Al solder layer is approximately 11 µm. The Si chip with Cr/Ni/Au metallisation and the reacted Al/Ni Nanofoil (AlNi phase) are located at the right and

left side of Zn-Al solder, respectively. The white area in figure 5-22 represents the materials with a lowest density within this solder system. This indicates that a large number of voids and oxides scattered into the Zn-Al solder matrix, which agrees with the SEM mapping results in figure 5-21. During the exothermic reaction, the Al atoms in Al/Ni Nanofoil firstly melt into liquid drops and immediately reacted with the nearby Ni atoms from the solid Ni films. Thus, the structure of Al/Ni multilayer altered from multilayers to granules.

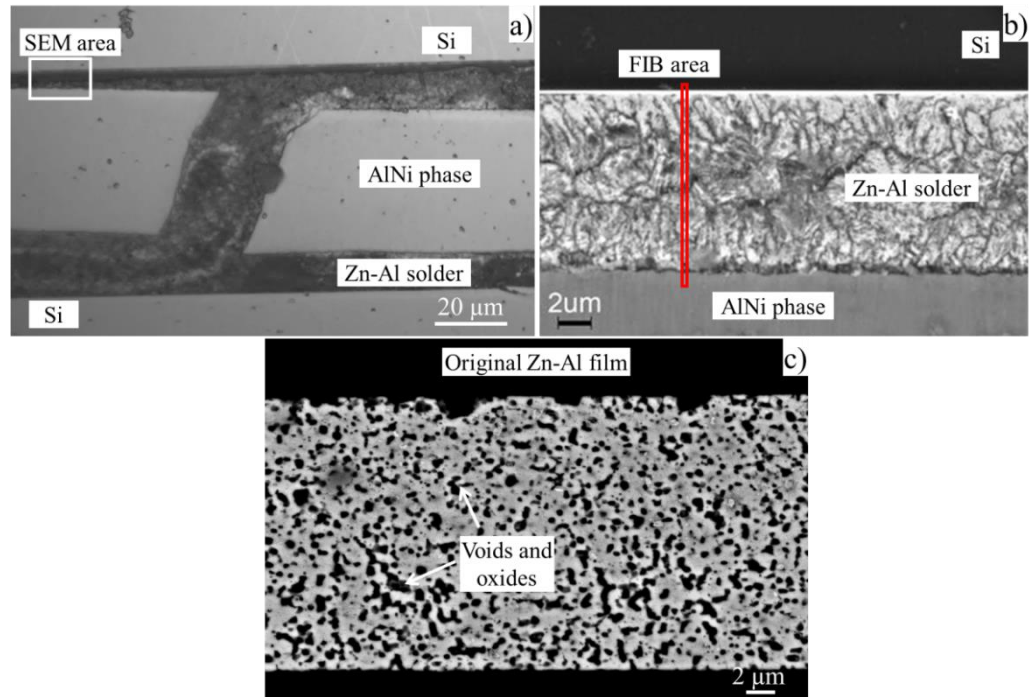


Figure 5-21 SEM images of the Zn-Al solder joints: a) entire solder joint; b) enlarged image at the Si/Zn-Al/AlNi interface highlighted in figure 5-21 a); c) The original microstructure of the original (unreacted) Zn-Al solder film.

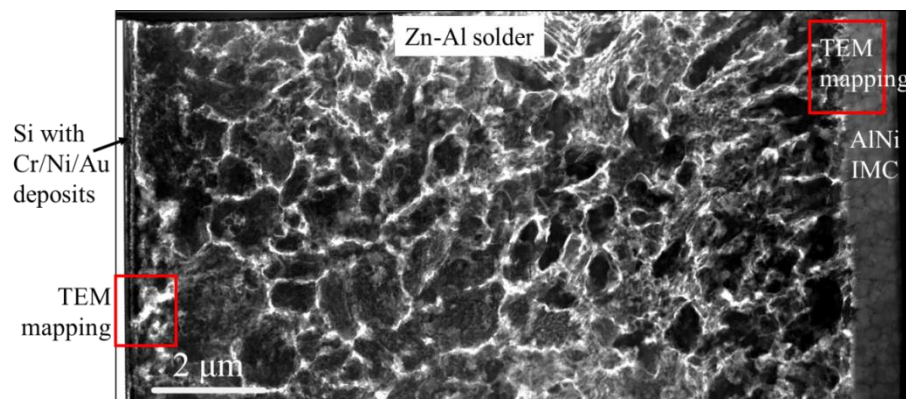


Figure 5-22 TEM image of the morphology at the SiC/ZnAl/AlNi interfaces.

To elaborate the interfacial microstructure and composition at the solder interface, two regions at the Si/Zn-Al and Zn-Al/AlNi interface were both investigated with TEM

elemental techniques as highlighted in figure 5-22. Figure 5-23 and table 5-5 present the TEM mapping results at the Si/Zn-Al interface and the EDX results of spectrums indicated in figure 5-23. Firstly, the thin Au metallisation on Si die diffused into Zn-Al solder to form AuZn (Spectrum 57). After the instant dissolvent of Au, Zn atoms quickly reacted with revealed Ni thin film, forming a discontinuous ZnNi thin layer proven by EDX results of Spectrum 55 and Spectrum 72. In the meanwhile, most Zn atoms remained in solder matrix without reaction based on the Zn K mapping image and the composition of Spectrum 58. Furthermore, the Al material in Zn-Al solder would react with Ni and produce AlNi phase. Overall, the possible phases at the Si/Zn-Al interface contain Zn, ZnNi, AlNi, and AuZn.

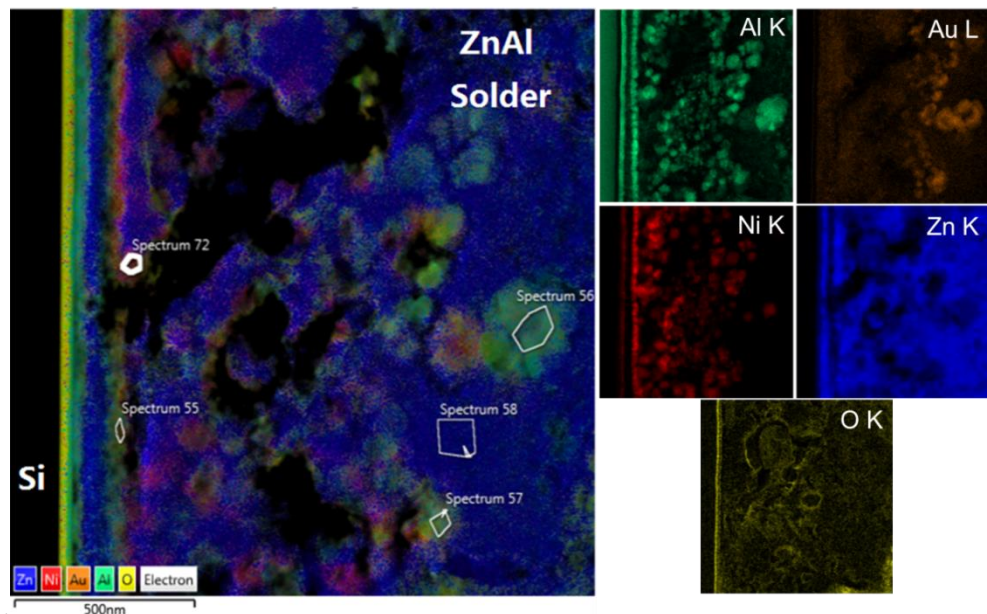


Figure 5-23 The TEM elemental mapping results at the Si/Zn-Al solder interface.

Table 5-5 The composition of spectrums indicated in figure 5-23 (at.%).

Spectrums	Al	Ni	Zn	Ag	Au	O	Possible Phase
55	20.63	32.92	33.08	-	10.28	3.08	ZnNi + AlNi + Zn + AuZn
56	12.84	6.61	46.94	6.35	26.22	1.02	
57	8.65	1.51	39.87	4.50	44.26	1.20	
58	1.61	0.1	80.45	9.53	7.28	1.02	
72	11.38	30.79	39.38	4.58	12.96	0.91	

The interfacial microstructure and composition at the Nanofoil/Zn-Al solder interface are also shown in figure 5-24 and table 5-6, respectively. The Ag coating on Al/Ni Nanofoil diffused into the Zn-Al solder matrix and the generated IMCs since all spectrums contain varying amounts of Ag. As similar to the mapping results in figure 5-23, the major part of Zn-Al solder matrix is composed with dispersive Zn material based on the elemental results such as the Zn K mapping image in figure 5-24 and the Spectrum results (61, 66, and 68) in table 5-6. Besides the Zn, Ni granules can be found in the Nanofoil adjacent to Zn-Al solder (Spectrum 59). The molten Zn-Al can react with Ni metallisation to form AlNi and ZnNi IMCs, which is similar to some IMCs at Si/Zn-Al interfaces (Figure 5-23). Moreover, due to the high oxidation of Zn-Al solder foil, Al_2O_3 and ZnO phases scattered within the bulky Zn-Al solders as listed in table 5-6. Generally, the possible phases at the Nanofoil/Zn-Al interface contain ZnNi, AlNi, Al_2O_3 , ZnO, Ni, and Zn.

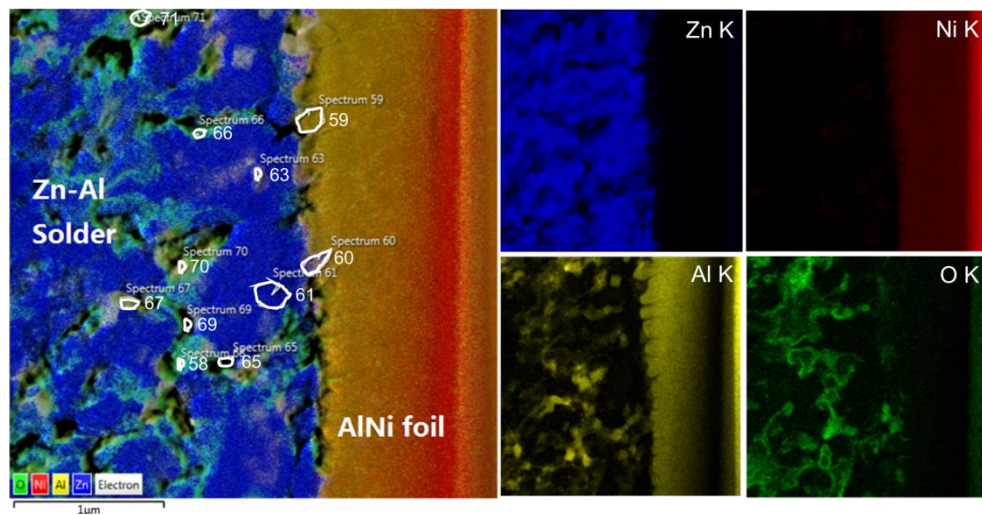


Figure 5-24 The TEM elemental mapping results at the AlNi Nanofoil/Zn-Al solder interface.

Table 5-6 The composition of spectrums indicated in figure 5-24 (at.%).

Spectrums	Al	Ni	Zn	Ag	O	Possible Phase
59	19.01	71.85	7.80	0.52	0.52	ZnNi
60	7.44	42.43	47.97	1.53	0.63	+ AlNi
61	0.78	2.59	79.83	16.39	0.42	+ Al_2O_3
63	10.10	16.41	69.17	4.32	-	+ ZnO

65	10.10	2.32	62.79	2.62	15.33	+ Ni
66	5.42	1.72	68	2.04	10.3	+ Zn
67	22.80	1.51	64.12	10.06	1.52	
68	4.87	0.53	63.91	18.12	12.57	
69	19.41	1.47	53.93	14.69	10.51	
70	18.60	19.94	52.17	8.48	0.81	
71	13.75	8.26	53.27	11.63	13.09	

5.5 Discussions

In this chapter, three joining processes, including soldering, GDCS, and self-propagation approaches, were employed in enhancing the solderability of Zn-Al solders on metallic substrates (Cu, Ni-based, or Si chip). Zn-Al solder interconnects can be achieved by all these methods. The characteristics of these joining approaches are summarised in table 5-7.

Although soldering is a widely used approach in industry for its simple process, the high process temperature and long reflow duration have bad influence on electronic components. Moreover, due to the poor solderability of Zn-Al solder, a flux is required to remove the oxides on solders and substrates. In this work, the self-prepared flux is composed with toxic fluorides and chlorides that can cause environment pollutions. Moreover, the residuals of oxides and flux may lead to a corrosion phenomenon and voids within Zn-Al solder joints. Compared to soldering, GDCS method is a green technology for producing Zn-5Al solder interconnects without any fluxes. However, due to the immature process parameters, voids and cracks in varying sizes occurred at as-soldered Cu/Zn-Al interfaces. Moreover, the pressure gas is possible to damage electroless Ni-W-P diffusion barrier somehow for the strong impact. Among these joining methods, self-propagation using Al/Ni Nanofolios was proven viable in forming reliable Zn-Al solder joints. It is a promising way to prepare Zn-Al solder joints due to its low process temperature and less requirements of the experimental setup, which is worth further investigations.

Table 5-7 The characteristics of these joining approaches.

Approach	Process temperature	Time	Flux	Pressure	Complexity of rigs	Defects	Packaging
Soldering	400 °C	Long	Yes	No	Low	Residuals, toxic flux	2D
Gas dynamic cold spray	190-240 °C	Medium	No	N ₂ gas	High	Voids, oxides and cracks	2D
Self-propagation	150 °C	Short	No	Weight	Medium	Oxides	3D

5.6 Conclusions

In this chapter, three joining methods, soldering, gas dynamic colder spray and self-propagation, were employed in preparing Zn-Al solder interconnects. After joining process, the interfacial microstructures at the Zn-Al solder interfaces were examined to evaluate the feasibility of these joining methods. From the experimental results and discussions, the following conclusions can be made.

1. The developed flux ($\text{LiCl-ZnCl}_2\text{-KCl-KF}$ constitutions) can greatly enhance the wettability of Zn-5Al solder on Cu and electroless Ni-W-P plated substrate by effectively removing the oxides of Zn-Al solders during the soldering.
2. The average wetting angle of Ni-W-P/Zn-5Al interconnects was approximately 32° , while the average wetting angle of Cu/Zn-5Al samples was lower at around 26° . Both wetting angles indicate that the wettability of Zn-Al solder is good on these substrates.
3. For soldering process, both dendritic $\epsilon\text{-CuZn}_4$ phase and levelled $\gamma\text{-Cu}_5\text{Zn}_8$ layer can be identified at the as-soldered Cu/Zn-Al interface. The thicknesses of $\epsilon\text{-CuZn}_4$ and $\gamma\text{-Cu}_5\text{Zn}_8$ were $2.57\text{ }\mu\text{m}$ and $6.69\text{ }\mu\text{m}$, respectively. When introduced electroless Ni-W-P UBM in Zn-Al solder joints, $\gamma\text{-Ni}_5\text{Zn}_{21}$ and Al_3Ni_2 may produce in as-reflowed Zn-Al/Ni-W-P solder interconnects. However, the thickness of the Ni-based IMC layers was too thin ($< 1\text{ }\mu\text{m}$) to be verified by EDX in SEM, which will be further elaborated in Chapter 6 using TEM technique.
4. In the initial Zn-Al solder interconnects prepared by gas dynamic cold spray, part of the Zn-Al/Cu interface was curved due to the impact of the supersonic Zn-Al particles accelerated by propellant gas. In contrast, the Ni-W-P/Zn-Al interface was relatively smoother.
5. When cold sprayed samples reflowed, massive voids and cracks can be found within the Zn-Al solders near Cu/Zn-Al interfaces. In contrast, with electroless Ni-W-P coatings, only discontinuous Al_3Ni_2 layer with a max thickness of $2\text{ }\mu\text{m}$ can be found at Ni-W-P/Zn-Al interfaces after reflow. Besides, the whole solder joints still remain intact.
6. Self-propagation with Al/Ni Nanofoil was proven to be viable in forming reliable

Zn-Al solder joints at a low joining temperature and less requirement of experimental setup. However, the high cost and complexity of interfacial microstructure in the solder joints can still be critical concerns in industry use.

References

- [5.1] L. Liu, M. Mirgizoudi, P. Zhang, L. Zhou, and C. Liu, “Mechanical and Interfacial Characteristics of Zn-Al solder joints under elevated temperature and vibration conditions”, in *5th Electronics System Integration Technology Conference (ESTC)*, Helsinki, Finland, 2014, pp. 1-5.
- [5.2] A. Haque, B.H. Lim, A.S.M.A. Haseeb, and H.H. Masjuki, “Die attach properties of Zn-Al-Mg-Ga based high-temperature lead-free solder on Cu lead-frame”, *Journal of Materials Science: Materials in Electronics*, vol. 23, No. 1, pp. 115–123, 2012.
- [5.3] M. Nobumasa, N. Shuichi, Japan Patent 2006-320913 (2006)
- [5.4] T. Gancarz, J. Pstruś, P. Fima, and S. Mosińska, “Thermal Properties and Wetting Behavior of High Temperature Zn-Al-In Solders”, *Journal of Material Engineering Performance*, vol. 21, No. 5, pp. 599–605, 2012.
- [5.5] M. McCormack, S. Jin, and H.S. Chen, “New lead-free, Sn-Zn-In solder alloys”, *Journal of Electronic Materials*, vol. 23, No. 7, pp. 687-690, 1994.
- [5.6] J. Wang, E. Besnoin, A. Duckham, S.J. Spey, M.E. Reiss, and etc., “Room-temperature soldering with nanostructured foils”, *Applied Physics Letters*, vol. 83, No. 19, pp. 3987-3989, 2003.
- [5.7] Y.P. Zhang, Y.Q. Yang, J.L. Yi, and H.C. Hu, “Diffusion Bonding of Cu-Cu with Al-Ni Nano Multilayers”, *Materials Transactions*, vol. 54, No. 6, pp. 931-933, 2013.
- [5.8] J.F. Li, P.A. Agyakwa, C.M. Johnson, D. Zhang, T. Hussain, and D.G. McCartney, “Characterization and solderability of cold sprayed Sn-Cu coatings on Al and Cu substrates”, *Surface and Coatings Technology*, vol. 204, No. 9-10, pp. 1395-1404, 2010.
- [5.9] Flux specification of the Institute for Interconnecting and Packaging Electronic Circuits (IPC), ANSI/IPC-SF-818, “General Requirements for Electronic Soldering Fluxes”.
- [5.10] L.A. Guth, 'Post-Solder Cleaning Consideration', in 'Solder Joint Reliability: Theory and Application', edited J. H. Lau, Van Nostrand Reinhold, New York, pp. 143-172, 1991.
- [5.11] F.G. Yost, F.M. Hosking and D.R. Frear, *The Mechanics of Solder Alloy: Wetting and Spreading*, Van Nostrand Reinhold, New York, 1993.
- [5.12] Q.Y. Zhang, H.S. Zhuang, *Brazing and Soldering Manual*, China Machine Press, Beijing, 1999.
- [5.13] L.B. Jiang, A.H. Meng, and Q.Y. Zhang, “The three pseudo-side binary system in $\text{LiCl}-(2\text{ZnCl}_2\cdot\text{KCl})-(\text{ZnCl}_2\cdot 2\text{KCl})$ system”, *Acta Physico-Chimica*

- Sinica*, vol. 22, No. 2, pp. 131-134, 2006.
- [5.14] E.P. Lopez, P.T. Vianco, J.A. Rejent, J.J. Martin, "Solderability study of 63Sn-37Pb on Zinc-plated and Cadmium-plated stainless steel for the MC4636 Lighting arrestor connector", *Sandia National Laboratories Report*, 2004.
- [5.15] M. Rettenmayr, P. Lambracht, B. Kempf, C. Tschudin, "Zn-Al Based Alloys as Pb-Free Solders for Die Attach", *Journal of Electronic Materials*, vol. 31, No. 4, pp. 278-285, 2002.
- [5.16] Y. Takaku, I. Ohnuma, Y. Yamada, S.W. Dean, "A review of Pb-free high temperature solders for power semiconductor devices: Bi-based composite solder and Zn-Al solder," *Journal of ASTM International*, vol. 8, No. 1, pp. 1-18, 2011.
- [5.17] S. Marx, A. Paul, A. Khler, and G. Hüttl, "Cold spray – innovative layers for new applications", in *Proceedings of the International Thermal Spray Conference and Exposition (ITSC2005)*, Basel, Switzerland, 2005, pp. 209-215.
- [5.18] F. Gärtner, T. Stoltenhoff, T. Schmidt, and H. Kreye, "The cold spray process and its potential for industrial applications", in *Proceedings of the International Thermal Spray Conference and Exposition (ITSC2005)*, Basel, Switzerland, 2005, pp. 158-163.
- [5.19] X.J. Ning, J.H. Jang, H.J. Kim, C.J. Li, and C. Lee, "Cold spraying of Al-Sn binary alloy: Coating characteristics and particle bonding features", *Surface and coatings technology*, vol. 202, No. 9, pp. 1681-1687, 2008.
- [5.20] A.P. Alkimov, A.N. Papyrin, V.F. Kosarev, N.I. Nesterovich, and M.M. Shushpanov, U.S. Patent 5 302 414, April 12 (1994).
- [5.21] V.F. Kosarev, S.V. Klinkov, A.P. Alkimov, A.N. Papyrin, "On some aspects of gas dynamic principles of cold spray process", *Journal of Thermal Spray Technology*, vol. 12, No. 2, pp. 265-281, 2003.
- [5.22] G. Shayegan, H. Mahmoudi, R. Ghelichi, J. Villafuerte, J. Wang, and etc., "Residual stress induced by cold spray of magnesium AZ31B extrusion", *Materials & Design*, vol. 60, pp. 72-84, 2014.
- [5.23] J. Cizek, O. Kovarik, J. Siegl, K. A. Khor, and I. Dlouhy, "Influence of plasma and cold spray deposited Ti layers on high-cycle fatigue properties of Ti6Al4V substrates", *Surface and Coatings Technology*, vol. 217, pp. 23-33, 2013.
- [5.24] L. Wang, B. He, and X. H. Jiang, "Modelling the velocity of self-propagating exothermic reactions in multilayer foils", *Combustion Science and Technology*, vol. 182, pp. 1000-1008, 2010.
- [5.25] E. Ma, C.V. Thompson, L.A. Clevenger, and K.N. Tu, "Self-propagating explosive reactions in Al/Ni multilayer thin films", *Applied Physics Letter*, vol. 57, pp. 1262-1264, 1990.
- [5.26] F.Z. Chrifi-Alaoui, M. Nassik, K. Mahdouk, and J.C. Gachon, "Enthalpies of formation of the Al-Ni intermetallic compounds", *Journal of Alloys Compound*, vol. 364, No. 1-2, pp. 121-126, 2004.
- [5.27] T.P. Weihs, A.J. Gavens, M.E. Reiss, D.Van Heerden, A. Draffin, and D. Stanfield, *Chemistry and Physics of Nanostructured and Related Non Equilibrium Materials* (TMS, Warrendale, PA, 1997) p. 75.

- [5.28] V.P. Korzhov, V.M. Kiiko, and M.I. Karpov, “Structure of multilayer microcomposite Ni/Al obtained by diffusion welding”, *Inorganic Materials: Applied Research*, vol. 3, No. 4, pp. 314-318, 2012.
- [5.29] T. Namazu, K. Ohtani, K. Yoshiki, and S. Inoue, “Crack-less wafer layer packaging using flash heating technique for micro devices”, *Materials Science Forum*, vol. 706–709, pp. 1979-1983, 2012.
- [5.30] E.V. Levchenki, A.V. Evteev, D.P. Riley, I.V. Belova and G.E. Murch, “Molecular dynamic simulation of the alloying reaction in Al-coated Ni nanoparticle”, *Computational Materials Science*, vol. 47, No. 3, pp. 712-720, 2010.

Chapter 6

Microstructural Characteristics of Zn-Al Solder Interconnects

With the developed reflow process proposed in Chapter 5, the interfacial reactions and IMC morphologies in Zn-Al solder interconnects with or without electroless Ni-W-P coatings subjected to different liquid-solid reaction durations (1, 5, 15, and 30 minutes) at 450 °C were investigated in this chapter. Moreover, nanoindentation tests were performed to evaluate the micro-mechanical properties (elastic moduli and hardness) of Al_3Ni_2 and Cu-Zn intermetallic compounds (IMCs) in the Zn-Al solder interconnects.

6.1 Introduction

As discussed in previous chapters, Zn-5Al alloy was a potential lead-free candidate for high temperature solders. However, Zn-based solders react actively with Cu substrates, forming excessive Cu-Zn IMCs at elevated temperature. This makes the solder joints brittle and prone to fracture [6.1]. Figure 6-1 presents a typical fractured Zn-Al solder interconnect.

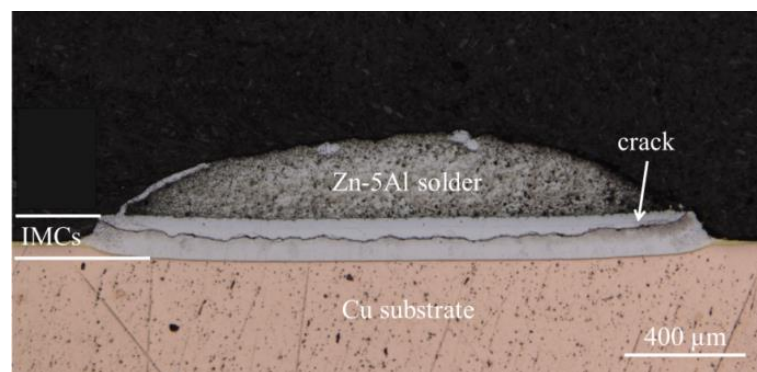


Figure 6-1 Cross section of the Cu/Zn-5Al solder interconnect with a crack.

To solve these challenges, a diffusion barrier can be utilised to prevent the excessive growth of Cu-Zn IMCs in Zn-based solder joints. In industry, electroless Ni-P coating was normally applied as the diffusion barrier to significantly decrease the growth rate

of IMCs. However, Ni-P alloy is not suitable for high temperature electronics due to its low crystalline temperature, weak thermal stability, and voids in crystalline Ni₃P layer in reflowed solder joints [6.2, 6.3]. As investigated in Chapter 4, electroless Ni-W-P coatings are rather promising in high temperature electronics since Ni-W-P alloys possess better heat-resistivity with a stable microstructure at elevated temperature (up to 400 °C).

During reflow, the IMCs formed between solders and substrates provide mechanical and electrical interconnections of electronic components. However, excessive growth of IMCs would deteriorate the interfacial integrity, due to their brittle nature and mismatches of physical properties (e.g. elastic moduli and coefficient of thermal expansion) with solders and substrates [6.4-6]. Thus, it is crucial to control the thickness of IMCs in a small value to reduce the internal stresses during operation. Moreover, knowledge of the mechanical properties for the interfacial IMCs in Zn-Al solder interconnects is also beneficial to the understanding of electronics reliability.

Bulk IMCs were prepared through casting and annealing processes to enable mechanical tests at a macro-scale [6.7, 6.8], but residual porosity and oxides may emerge from these processes, degrading applicability of the results. Besides, the microstructure of bulk IMC samples are considerably different from interfacial IMCs layers in solder joint. Therefore, a micro-scale test, e.g. nanoindentation, would be appropriate to obtain elastic moduli and hardness of these IMCs in solder joints at micro-scale [6.9-11].

With an increasing trend towards miniaturization of microelectronic products, volume ratio of the IMCs in solder joints tends to be higher, which affects their mechanical integrity significantly [6.12, 6.13]. Li *et al.* reported that solder interfaces consisting of IMCs fully act as entire interconnections through transient liquid phase bonding, targeting for three-dimension (3D) integration [6.14, 6.15]. Moreover, Zhong *et al.* found that Cu₆Sn₅ nanoparticles (< 10 nm) exhibit superplastic and super-uniform that can form die attachments through sintering process [6.16].

In this work, to clarify the effect of electroless Ni-W-P coatings as a diffusion barrier for high temperature solders in harsh conditions, Zn-Al solder interconnects with and without Ni-W-P UBM under liquid-solid reactions were prepared. The interfacial

reactions in these solder interconnects were examined. Mechanical properties of each IMCs in the Zn-Al solder joints were also investigated by nanoindentation.

6.2 Experimental details

6.2.1 Preparations of Ni-W-P/Zn-Al solder joints

The preparations of electroless Ni-W-P coatings and formation of Zn-Al solder joints with flux are described in Section 5.2.1.2. The reflow was conducted on a hotplate attached with a temperature control unit to perform a reflow profile. The real-time temperature of the samples was measured with a K-type thermal couple. The liquid-solid reactions ranged from 1 to 30 minutes and their reflow temperature profiles were illustrated in figure 6-2.

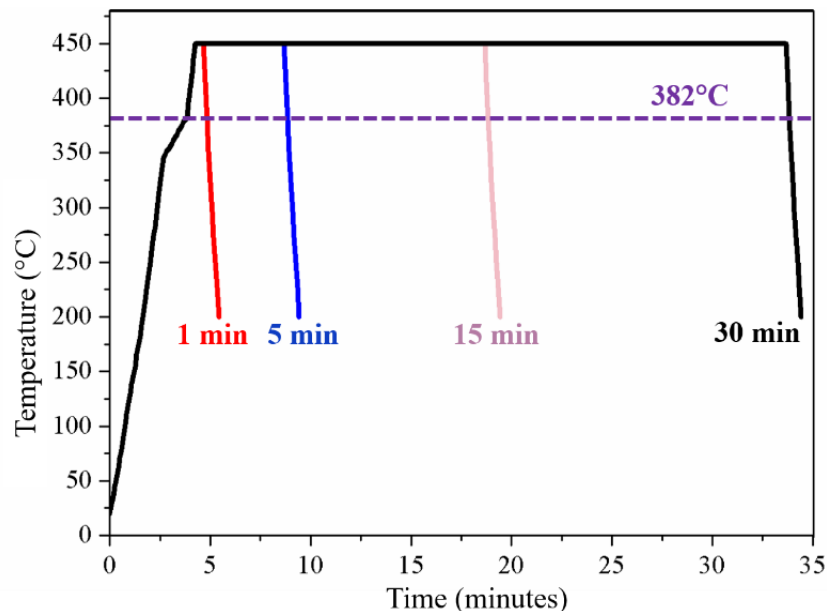


Figure 6-2 Reflow profiles of the Zn-Al solder interconnects.

6.2.2 Morphological and Microstructural Observations

After reflow, the specimens were cold mounted, ground and polished to reveal their cross-section microstructure. The microstructure of interfacial IMCs at the Cu/Zn-5Al and Cu/Ni-W-W/Zn-5Al interfaces were investigated by scanning electron microscopy (SEM, Cambridge Stereoscan 360) incorporated with energy dispersive X-ray detector (EDX). The thickness of Ni-W-P coatings and IMCs layers were measured with Image J software. This can be associated with diffusion barrier properties of Ni-W-P coatings. Overall, the reactions and morphologies of the IMCs at Cu/Zn-5Al interfaces were

compared with that at Cu/Ni-W-P/Zn-5Al interfaces in the same conditions. Moreover, the top-view morphology of the IMCs formed in Ni-W-P/Zn-Al solder interconnects were also examined by etching Zn-Al solders with NaOH solution (20 g/L).

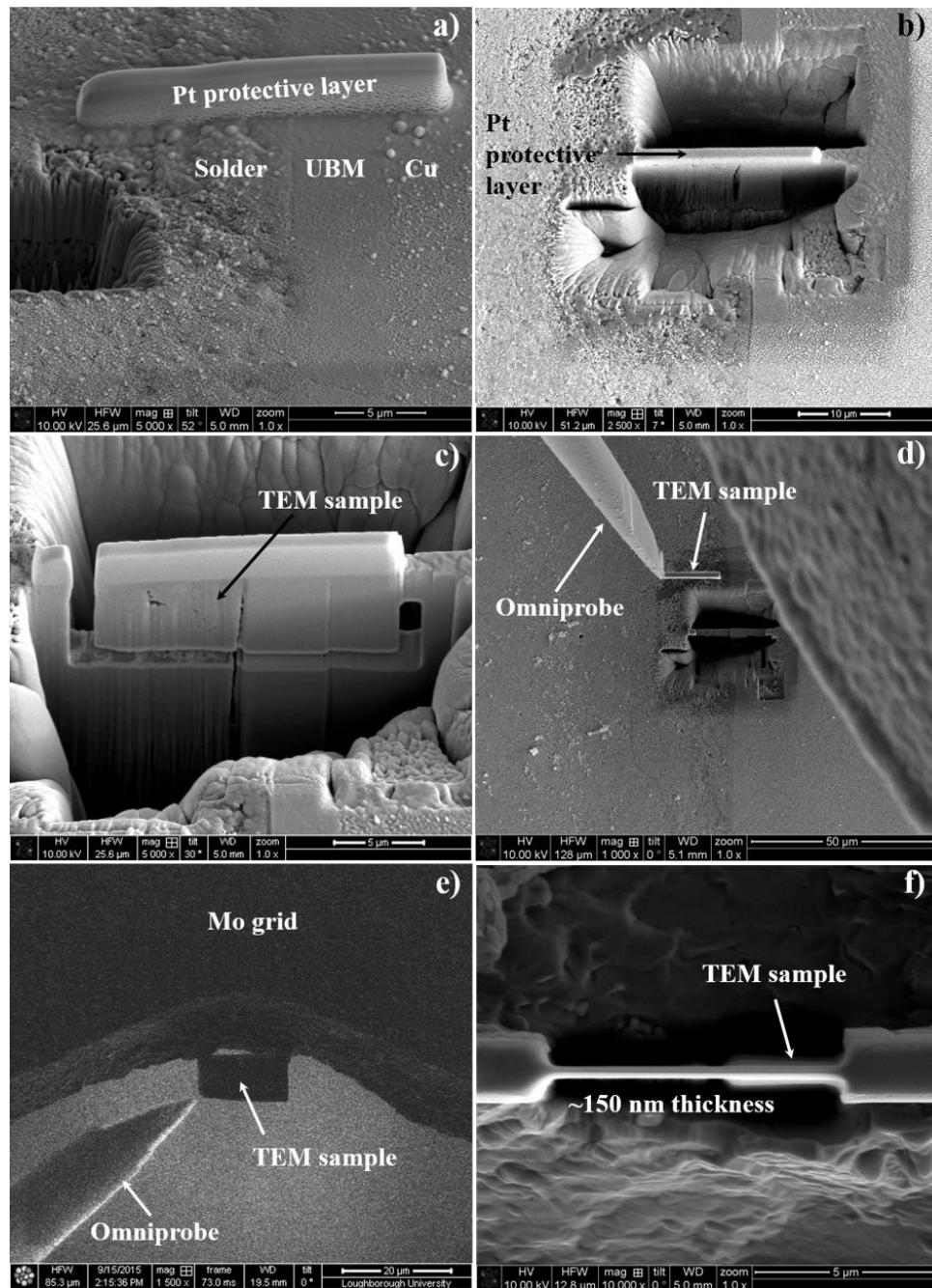


Figure 6-3 Micro-machining process by Dual FIB for TEM sample preparation. a) Pt layer deposited on top of the region of interest; b) two rectangular trenches fabricated on both sides of the Pt layer for preparation of the TEM sample; c) “U” cut of the TEM sample to be lifted up; d) Foil attached to the omniprobe and lifted up; e) TEM sample attached to the Mo grid holder by Pt deposition; f) TEM sample further thinning to electron transparency.

Transmission electron microscopy (TEM, JEOL 2000FX TEM with EDX) and focus ion beam (FIB, FEI Nova 600 Nanolab dual beam FIB) were used to investigate the crystallisation characteristics of electroless Ni-W-P coatings and interfacial evolution

in the solder interconnects after reflow process. The preparation of TEM samples by FIB milling is illustrated in figure 6-3. Firstly, to protect the area of interest (solder interface), a Pt layer is deposited on the surface with a thickness of around 2 μm . Then, two rectangular trenches are gradually milled by Ga ion beams (Current: decreased from 7 nA to 3 nA), leaving an approximately 1.5 μm wide foil between them (figure 6-3 b)). A lamella is then chopped near the area of interest, consisting of Zn-Al solder, interfacial IMCs, Ni-W-P coating and Cu substrate, with a “U” cut (figure 6-3 c)). A tungsten omniprobe is used to transfer the TEM lamella to sample grids. In figure 6-3 d), the omniprobe is attached to the lamella with the aid of Pt deposition and ion milling. In this work, a molybdenum (Mo) grid instead of a Cu grid was used to avoid X-ray energy overlaps as Cu is involved in the Zn-Al solder interconnects. The TEM lamella is lifted out from the bulk materials, and then contacts the Mo grid using the omniprobe. Once the TEM lamella is attached to the Mo grid by ion beam Pt deposition, the connection between the omniprobe and the TEM specimen is removed by ion milling. In the end, a low current ion beam (10 kv, 100 Pa) is employed to final clean the sample surface (in the middle or edge of the TEM lamella) and decreases its thickness to approximately 150 nm [6.17]. Thus, a sample free of stresses and contaminations is ready for following TEM observations.

TEM analysis was then performed using either a JEOL 2000FX TEM equipped with Oxford Instrument INCA EDX spectroscopy, or and FEI Tecnai F20 high resolution TEM (HRTEM) with Oxford Instrument INCA EDX system and 80 mm² X-Max silicon drift detector. The voltage for selected area diffraction pattern (SADP), EDX, and image acquisition was 20 kV. The apertures of SADP range from 0.2 to 1.4 μm for inspecting the crystallographic structure of sample area at a micro-scale.

6.2.4 Nanoindentation tests

A nanoindenter (Micro Materials NanoTest 600) was utilised to measure the elastic moduli and hardness of the IMCs formed at the Cu/Zn-Al and Ni-W-P/Zn-Al interfaces after liquid-solid reaction at 450 $^{\circ}\text{C}$ for 30 minutes. The drift rate of the nanoindenter system was calibrated to be less than 0.05 nm/s prior to indentation tests. A Berkovich diamond indenter (tip radius: ~ 50 nm) was employed at ambient temperature. The indenters held at their peak loads for 10 s to avoid the creep influences on unloading characteristics [6.18]. Six indents were conducted on each type of the IMCs. The

distance between each indents in Cu/Zn-Al solder interconnects was 10 μm to minimised the mutual interaction due to the deformation of conducted indents. However, the distance between adjacent indents was set to be 5 μm for Ni-W-P/Zn-Al samples since the thickness of Al_3Ni_2 layer is quite thin ($\sim 2\text{ }\mu\text{m}$). To reveal more IMCs, the Ni-W-P/Zn-Al samples were etched with dilute HCl solution (4 %) for 3s by removing solders.

Table 6-1 Major parameters of nanoindentation.

Interface type	Loading rate	Peak load	Duration time	Unloading rate
Cu/Zn-Al	1 mN/s	10 mN	10 s	1 mN/s
Ni-W-P/Zn-Al	1 mN/s	10 mN	10 s	1 mN/s

6.3 Results & Discussions

6.3.1 As-deposit Ni-W-P UBM

The as-deposited Ni-W-P coatings consisted of 7-8 wt.% of P and 18-19 wt.% of W. In figure 6-4 a), the surface of this coatings exhibits a pore-free morphology with nodular features in varying sizes (size range: 1 - 1.5 μm). The reason for the existence of these nodules is the aggregations of Ni-W-P compounds. The thickness of Ni-W-P coating was approximately 2 μm in figure 6-4 b). This coating was firmly adhered to Cu substrate as no visible pores can be seen at the interface. Overall, the coatings were crack-free, compact and adherent, showing good qualities as a barrier layer.

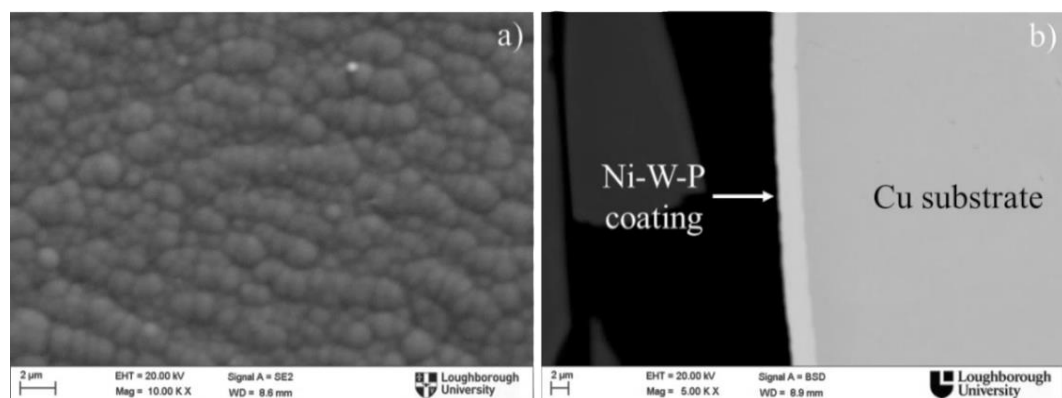


Figure 6-4 Micrographs of as-deposit Ni-W-P coatings: a) surface morphology; b) cross-section morphology.

6.3.2 Interfacial microstructure of Zn-Al solder interconnects

During the soldering process, Zn-5Al solder melt at 450 °C and then held up to 30 minutes to facilitate the interfacial reactions at the Cu/Zn-5Al and Ni-W-P/Zn-5Al interfaces. According to Cu-Zn phase diagrams (Figure 6-5 [6.19]), three IMCs, β -CuZn, γ -Cu₅Zn₈, ϵ -CuZn₄ can be produced in the Cu/Zn-Al solder joints when reflowed at 450 °C. Based on the related Ni-Zn and Ni-Al phase diagrams (Figure 6-6 [6.20, 6.21]), the interfacial reactions between Zn-5Al solders and Ni-W-P substrates would be more complicated than that on Cu substrates. For instance, β_1 -NiZn, γ -Ni₅Zn₂₁ and δ -NiZn₈ in the Ni-Zn system, and Al₃Ni, Al₃Ni₂, Al₃Ni₅ and AlNi₃ in the Ni-Al system are stable at the temperature studied herein.

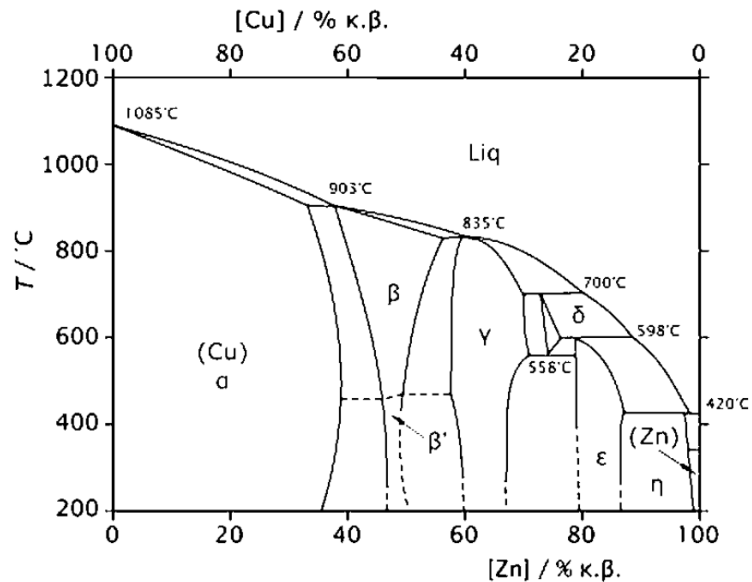


Figure 6-5 Phase diagram of Cu-Zn binary system [6.19]

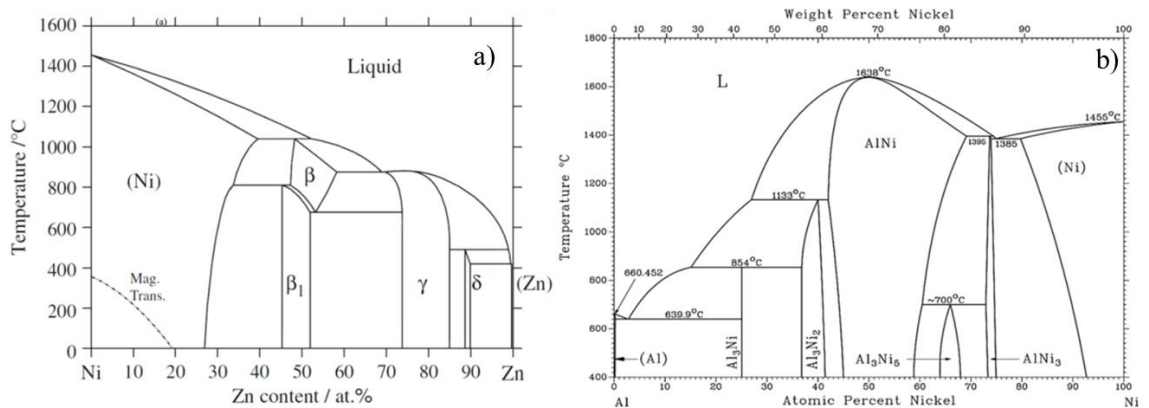


Figure 6-6 Phase diagram of a) Ni-Zn binary system, b) Ni-Al binary system [6.20, 6.21].

Figure 6-7 presents the back-scattered cross-section micrographs of the IMCs formed between Zn-5Al solder and Cu substrate with or without Ni-W-P coatings for different liquid-solid reaction at 450 °C. In figure 6-7 a), two distinct layers can be identified at the Zn-Al solder interface. The upper layer adjacent to Zn-Al solder was dendritic ϵ -CuZn₄ layer according to EDX analysis. A level γ -Cu₅Zn₈ interlayer was formed between CuZn₄ and Cu substrate. The activation energy for the formation of CuZn₄ and Cu₅Zn₈ have been reported to be 29.54 and 42.38 kJ/mol, respectively [6.22]. Therefore, it can be predicted that ϵ -CuZn₄ is the first IMC generated at the Zn/Cu interface by the mutual diffusions of Zn and Cu atoms. After a liquid-solid reaction for 5 minutes, a new thin layer of β' -CuZn (thickness: < 1 μ m) emerged between CuZn₄ and Cu substrate in figure 6-7 b), which agrees to a previous work [6.23].

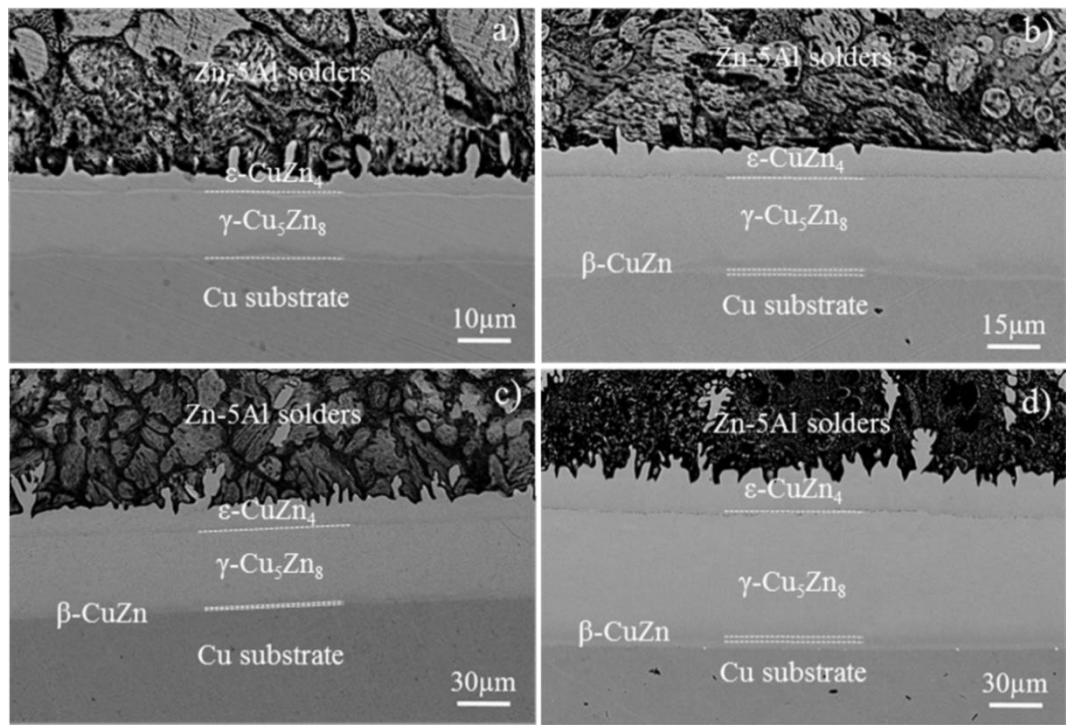


Figure 6-7 Back-scattered SEM images showing IMCs at Zn-Al/Cu interfaces after liquid-solid reaction for: a) 1 minute; b) 5 minutes; c) 15 minutes; d) 30 minutes.

Notably, some Kirkendall voids were observed near the boundaries of CuZn interlayer as shown in figure 6-8, which is similar to the observations of accumulating voids in Cu₃Sn layer in aged Cu/Sn solder joints [6.24]. The formation of these nano-sized voids is due to the difference in the intrinsic diffusivities between Cu and Zn. The Cu/CuZn and CuZn/Cu₅Zn₈ interfaces served as locations for the agglomeration of the defects into nano/micro-voids (Kirkendall voids) near the interfaces. These voids can seriously degrade reliability of solder joints by providing a crack initiation region when subjected to external loads [6.25]. Moreover, during service, these voids were likely to

propagate with the growth of CuZn and aggregate into larger sizes, resulting in significant mechanical and electrical degradation of the solder joints [6.26, 6.27]. Some Kirkendall voids were also found at the $\text{Cu}_5\text{Zn}_8/\text{CuZn}_4$ interface, which agrees with a reported work in Zn-Sn-Cu-Bi solder system [6.28].

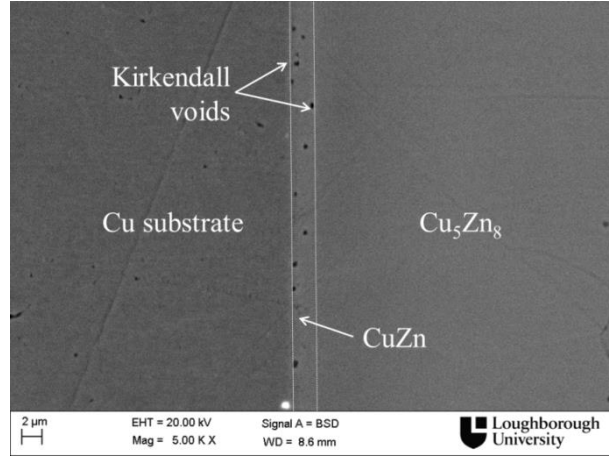


Figure 6-8 Kirkendall voids formed around the CuZn interlayer at the Cu/Zn-Al interface after 30 minutes reaction at 450 °C.

After the above discussions, the interfacial microstructure and Cu-Zn IMC evolutions after prolonged reactions is summarised in figure 6-9. The sequence of Cu-Zn IMCs formation are described as follow: At first, zinc atoms in liquid Zn-5Al alloy react with copper substrate directly and lead to formation of $\epsilon\text{-CuZn}_4$ interlayer, which hinders the direct reaction between Zn solders and Cu substrate. Then, with continuous growth of $\epsilon\text{-CuZn}_4$, Zn atoms in $\epsilon\text{-CuZn}_4$ diffuse into Cu and generate $\gamma\text{-Cu}_5\text{Zn}_8$ interlayer between $\epsilon\text{-CuZn}_4$ and Cu substrate. Finally, small amount of Zn atoms in $\gamma\text{-Cu}_5\text{Zn}_8$ layer diffuse continuously into Cu to form a thin layer of $\beta'\text{-CuZn}$. However, due to the different diffusion rates of Cu and Zn, the Kirkendall voids accumulate around the CuZn layer as well as at the $\text{Cu}_5\text{Zn}_8/\text{CuZn}_4$ interface. This can induce degradation in reliability of this solder joints.

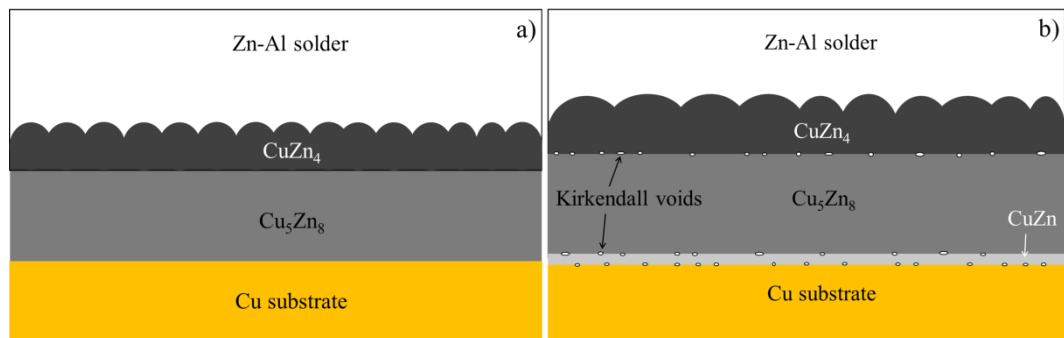


Figure 6-9 Schematic diagram illustrating the interfacial microstructure and IMC evolutions after liquid-solid reactions at 450 °C for: a) 1 minute; b) 30 minutes.

In the Zn-Al solder interconnects with electroless Ni-W-P coatings, figure 6-10 shows the cross-section microstructure at Ni-W-P/Zn-5Al interfaces and the morphology of the IMC from the top view.

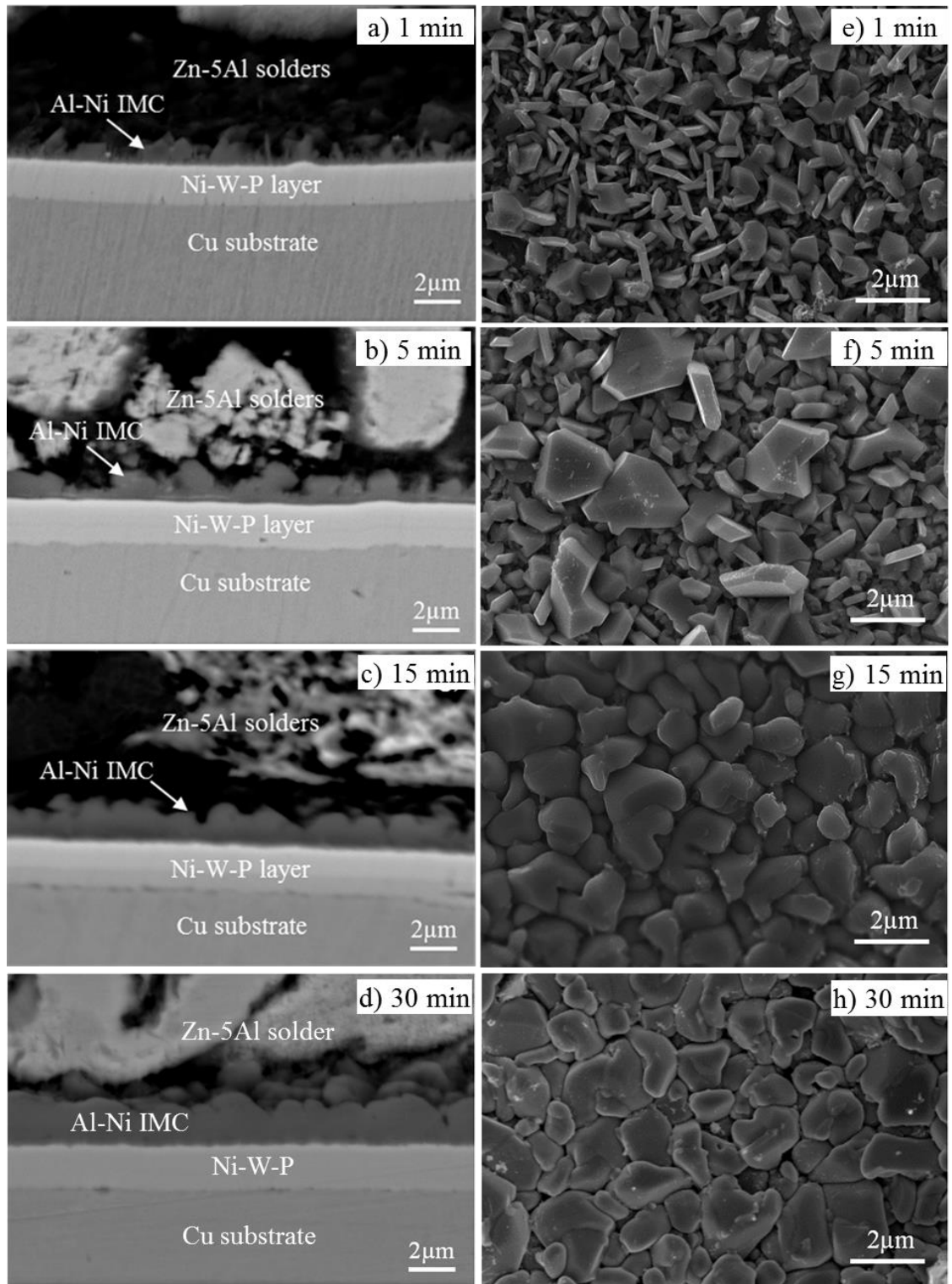


Figure 6-10 SEM images showing the morphology and size of the Al_3Ni_2 particles observed at the Ni-W-P/Zn-Al interfaces from cross-section view after liquid-solid reactions at 450 °C for: a) 1 minute; b) 5 minutes; c) 15 minutes; d) 30 minutes, and from top view: e) 1 minute; f) 5 minutes; g) 15 minutes, h) 30 minutes.

In figure 6-10 a) - d), a thin IMC layer generated between Zn-Al solder and electroless Ni-W-P coating continued to grow from approximately 0.5 to 2.1 μm thickness with an increasing liquid-solid reaction duration. To identify the thin IMC layer, elemental analysis was conducted in the Ni-W-P/Zn-Al solder interconnects after the longest reaction time (30 minutes) as presented in figure 6-11. From the mapping results of this solder interconnect, it is clear that Ni atoms in Ni-W-P coatings diffuse out and react with Al atoms from Zn-Al solders to form Ni-Al IMCs. This IMC was identified as Al_3Ni_2 phase through elemental pointing analysis. On the contrary, the W and P elements remained in Ni-W-P coating without diffusing into Zn-Al solder part. Thus, Ni-W-P UBM shows an excellent diffusion barrier property in preventing the reactions between Zn-Al solder and Cu substrate. Takaku *et al.* reported that Al_3Ni_2 grains grew and dispersed into Zn-4Al solder matrix after 5 minutes reaction at 450 $^{\circ}\text{C}$ in Ni/Zn-4Al solder interconnects, leading to a thick influencing zone [6.29]. This phenomenon did not occur in this Ni-W-P/Zn-5Al system, even after liquid-solid reaction at 450 $^{\circ}\text{C}$ for 30 minutes. This observation also verified the excellent properties of electroless Ni-W-P diffusion barrier compared to electroplated Ni coating.

In figure 6-10 e), after 1 minute reaction, a very thin layer of Al_3Ni_2 (thickness: $\sim 0.5 \mu\text{m}$) generated in prism-like or plate-like shapes. When the reaction time increased to 5 minutes, the average size of Al_3Ni_2 was 0.9 μm approximately. The plate-like IMC turned to be rod-like, while the prism-like IMC continuously grew with a larger size of approximately 2 μm (Figure 6-10 f)). After liquid-solid reaction for 15 minutes, some Al_3Ni_2 grains in bigger size ($\sim 2 \mu\text{m}$) continued to grow into a round scallop shape by merging the adjacent smaller Al_3Ni_2 grains ($\sim 0.2 \mu\text{m}$), resulting in a continuous Al_3Ni_2 layer as presented in figure 6-10 c). The size of these round scallop IMCs was in the range of 1 - 2.1 μm . After 30 minutes reaction, faceted scallops in polygon-like shape were observed with a slightly increased grain size (up to 2.5 μm).

Overall, for reflowed Ni-W-P/Zn-Al solder interconnects, the Al_3Ni_2 layer became thicker and the Al_3Ni_2 /Zn-5Al interface tended to be more planar after the liquid-solid reaction duration from 1 minute to 30 minutes. The shapes of Al_3Ni_2 grains transformed from prism-like or plate-like shapes into rod-like shape, and grew to be scallop shape.

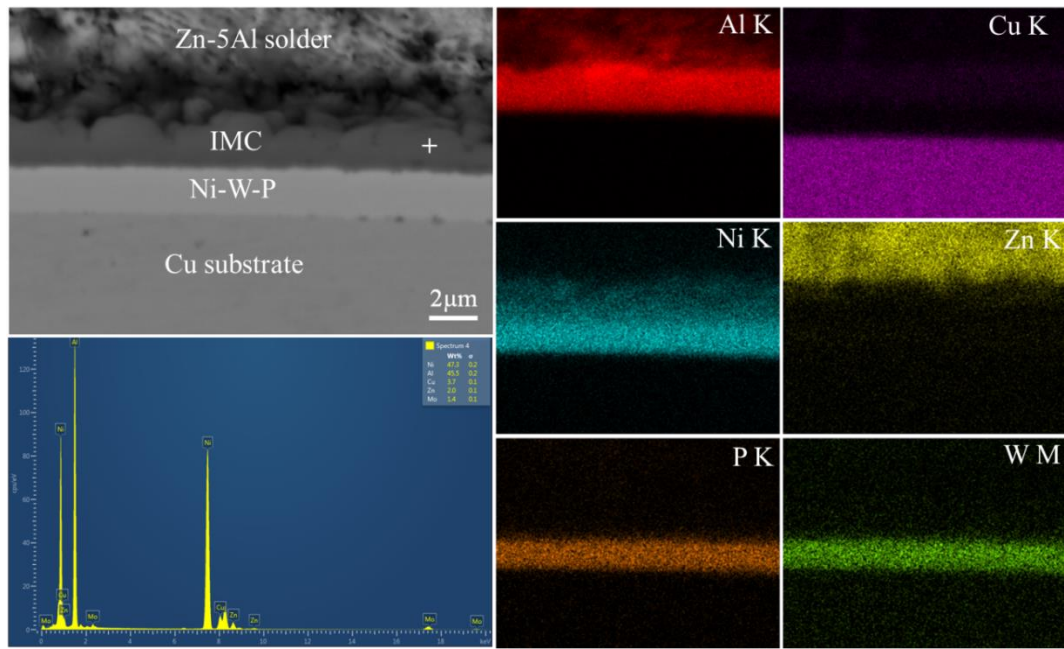


Figure 6-11 Elemental mapping and pointing analysis of the Ni-W-P/Zn-Al interface after 30 minutes liquid-solid reactions at 450 °C.

6.3.3 Growth mechanisms of IMC layers during reaction

The reactions between molten Zn-5Al solders and solid Cu or Ni-W-P plated substrates are shown in figure 6-7 and 6-10, respectively. Various IMC layers were formed and continued to grow with an increasing reaction time.

In figure 6-7, all three Cu-Zn IMCs continuously grow when the liquid-solid reaction time increases from 1 minute to 30 minutes. The thickness of total Cu-Zn IMC layers ranges from approximately 17 μm (after 1 minute reaction) to 94 μm (after 30 minutes reaction). Among these Cu-Zn IMCs, γ -Cu₅Zn₈ interlayer is the thickest layer, showing the strongest relationship with the increasing reaction time. In contrast, the growth rate of Al₃Ni₂ is the slowest. For the reflowed Zn-5Al solder interconnects with Ni-W-P coatings, only Al₃Ni₂ layer was formed at Ni-W-P/Zn-Al interfaces with an increasing thickness from 0.5 to 2.15 μm as shown in figure 6-10.

Figure 6-12 shows a parabolic relationship between the thickness of all IMCs and the liquid-solid reaction durations at the Cu/Zn-Al and Ni-W-P/Zn-Al interfaces reacted at 450 °C for 1, 5, 15 and 30 minutes. It is clearly observed that IMC thickness (d) increases linearly with the square root of t . This linear relationship indicates that the growth mechanisms of all IMCs are diffusion-control, which agrees to the following parabolic law.

$$d = k\sqrt{t} \quad \text{Equation 6-1}$$

Where d is the thickness of IMC layers, t is the liquid-solid reaction duration, and k represents the growth rate coefficient of each IMCs that can be calculated from the slope of the fit lines in figure 6-12.

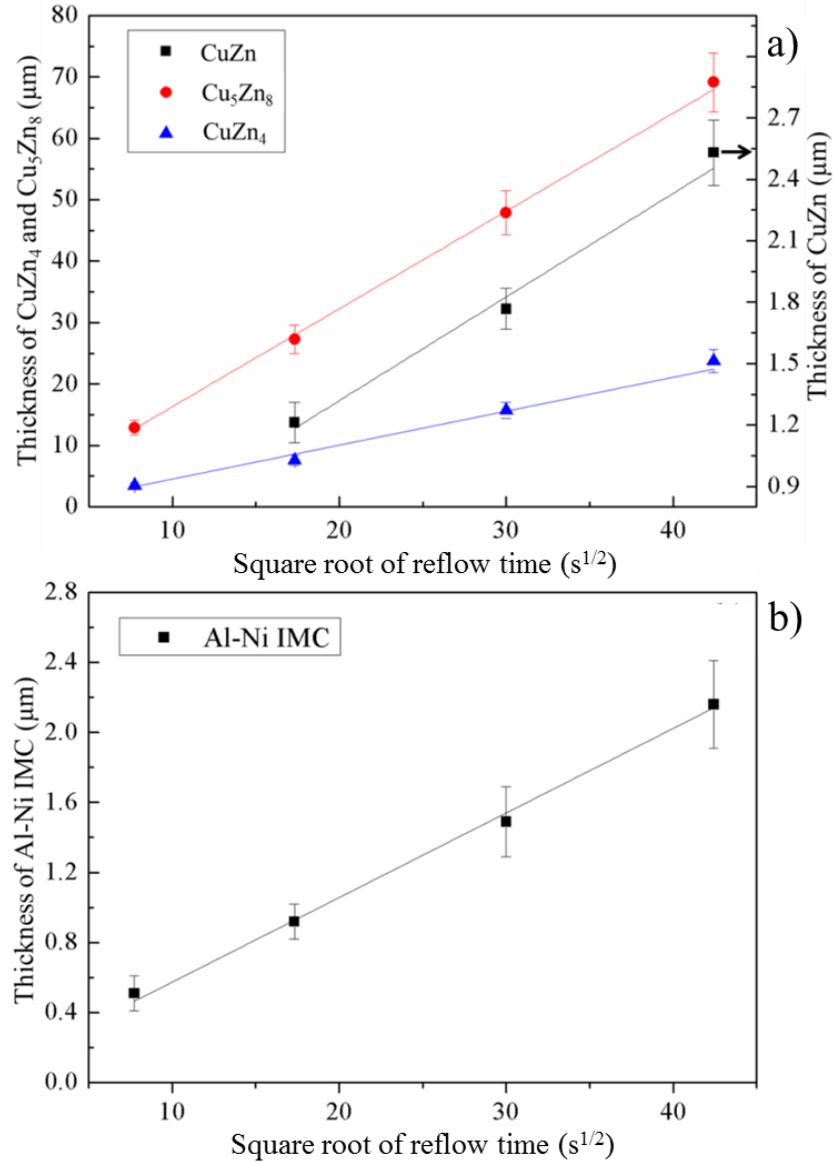


Figure 6-12 Thickness of the Zn-Cu IMCs formed after liquid-solid reactions at 450 °C for 1, 5, 15 and 30 minutes at: a) Cu/Zn-5Al interfaces; b) Ni-W-P/Zn-5Al interfaces.

Therefore, the experimental values of k for different interfacial IMCs in Zn-Al solder interconnects under harsh conditions are calculated and listed in table 6-2. The growth rate coefficient of γ -Cu₅Zn₈ interlayer is $1.573 \mu\text{m/s}^{1/2}$, which is almost three times as high as that of ϵ -CuZn₄ layer ($0.551 \mu\text{m/s}^{1/2}$). Although k of β -CuZn interlayer is considerable small, the formation of the Kirkendall voids formed around this layer are highly likely to cause reliability issues when subject to external loads.

For Zn-Al solder interconnects with Ni-W-P coatings, the growth rate (k) of Al_3Ni_2 layer is $4.90 \times 10^{-2} \mu\text{m/s}^{1/2}$ due to the slow reaction rate between Zn-Al solder and Ni-W-P coating. During the initial liquid-solid reaction (1 minute), a good metallurgical and electrical bond was achieved through a thin Al_3Ni_2 layer with a reasonable thickness ($\sim 0.5 \mu\text{m}$). It is widely known that excessive growth of IMCs has a tendency to deteriorate the mechanical reliability of solder joints [6.4-6]. Therefore, the slow growth rate of Al_3Ni_2 is regarded to be beneficial for the reliability of solder joints.

Table 6-2 Comparisons of the formation and growth of IMCs at Ni-W-P/Zn-Al and Cu/Zn-Al interconnects during liquid-solid reactions.

Solder interconnects	IMCs	$k (\mu\text{m/s}^{1/2})$	Reflowing Temperature (°C)
Ni-W-P/Zn-5Al	Al_3Ni_2	4.90×10^{-2}	450
Cu/Zn-5Al	$\varepsilon\text{-CuZn}_4$	5.506×10^{-1}	450
Cu/Zn-5Al	$\gamma\text{-Cu}_5\text{Zn}_8$	1.573	450
Cu/Zn-5Al	$\beta\text{-CuZn}$	5.607×10^{-2}	450

6.3.4 Crystallisation characteristics of Ni-W-P UBM during reactions

To further clarify the crystallisation characteristics of electroless Ni-W-P coatings, TEM analysis on this UBM reacted with molten Zn-Al solder at 450 °C for 1 and 30 minutes are both presented in figure 6-13. From figure 6-13 b) and d), this electroless Ni-W-P coating can be divided into two layers, the unreacted Ni-W-P coating near Cu substrate and a crystalline layer adjacent to Zn-Al solder highlighted between two dash lines. The formation of the crystalline layer is due to the diffusions and reactions between solders and substrates. When reacted with Zn-Al solder at 450 °C for 1 minute, the thickness of the crystalline layer is approximately 50 nm. After reacted with solders up to 30 minutes, its thickness grew to approximately 300 nm. SADP images of the unreacted Ni-W-P coatings (SADP a and b) after reaction for 1 minute and 30 minutes are both demonstrated in figure 6-13. From these SADP features, unreacted Ni-W-P coating can be regarded as a fine polycrystalline structure since few diffraction spots appeared and sharpened the diffraction rings of nickel. The grain size of the fine polycrystalline Ni particles is assumed to be below 5 nm [6.30]. Notably, the crystallinity of the unreacted Ni-W-P coatings are not further increased since there are

no difference between the SADP a and SADP b figures. According to SADP c figure, the individual spots and ring patterns represent Ni_3P and Ni (fcc lattice) and Ni_3P phases, respectively. After 30 minutes reaction with Zn-5Al solders, the grain size of this crystalline layer is approximately 100 nm, which is quite close to the grain size of bare electroless Ni-W-P layer after 4 hours aging at 600 °C. This indicate the reaction-assist crystallisation is more intense and easier to trigger than the spontaneous crystallisation.

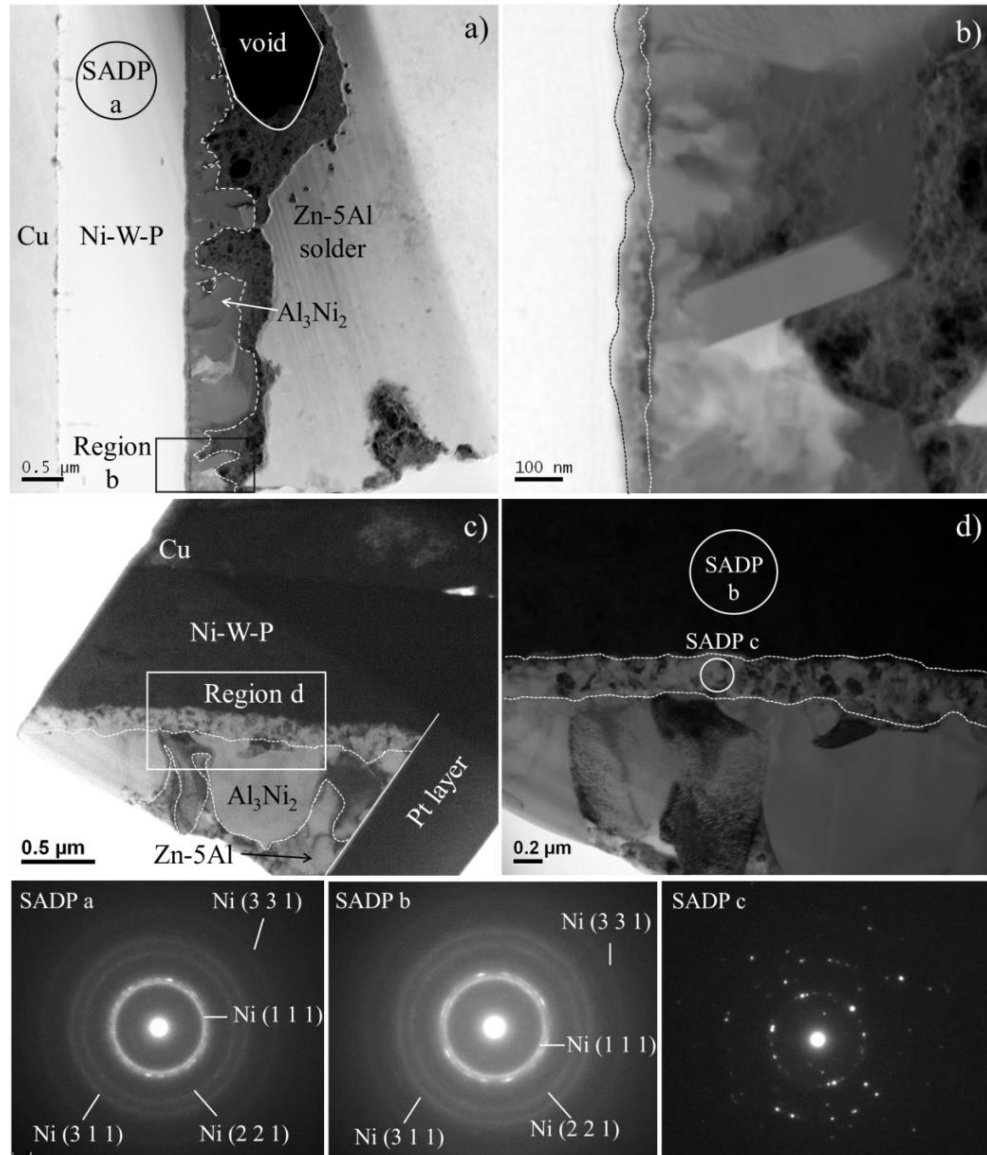


Figure 6-13 Interfacial microstructure and SADP at Ni-W-P/Zn-Al interfaces: a), b): after 1 minute liquid-solid reaction; c), d): after 30 minutes liquid-solid reaction.

Moreover, the crystalline structure of these two Ni-W-P coatings at the Ni-W-P/solder interface is quite different from some literatures. Yang *et al.* reported that an amorphous $(\text{Ni}, \text{W})_3\text{P}$ layer can be produced between the unreacted Ni-W-P coating

and Sn-based solders with electroless Ni-W-P coatings when reflowed at 260 °C [6.31]. Moreover, in Chapter 7, an amorphous interlayer can be found at Ni-W-P/Au-Ge interfaces. However, the interlayer formed at the Ni-W-P/Zn-Al interfaces were crystalline. This is likely to be attributed to the reflowing temperature (450 °C) that is above the amorphous-crystalline transition temperature (~ 400 °C).

The microstructure of the crystalline layer agrees with a study on crystalline electroless Ni-P coatings after thermal treatments [6.32]. It also shows that Ni₃P crystallites nucleated in amorphous Ni-P compounds and grew rapidly in an approximately 80 nm size by encircling nickel grains. However, when reacted with Sn-based solders, the crystallisation process of Ni-P UBM can be categorised into two types: a reaction-assist crystallisation triggered at reflow temperature (200-260 °C) [6.33, 6.34], and a spontaneous crystallisation occurred at a crystallisation temperature of Ni-P coatings [6.35] (around 350 °C obtained in Chapter 4).

Although the triggered temperature of reaction-assisted crystallisation is much lower than that of spontaneous crystallisation, the former one dominates the crystallisation process. In addition, the microstructure of crystalline Ni₃P in Ni-P layer obtained from the reaction-assist crystallisation and the spontaneous crystallisation are completely different. The crystallisation mechanism of former one leads to a Ni₃P layer with fine columnar structure [6.34, 6.36, 6.37], which can serve as a diffusion path and degrade the barrier property. In Ni-W-P/Zn-Al solder interconnects, the rate of reaction-assist crystallisation clearly exceeds the spontaneous crystallisation rate. However, the morphology and microstructure of the resultant interlayer in Ni-W-P coating are similar to that of a crystalline Ni-P coating after 2 hours thermal treatment at 450 °C [6.32]. No columnar structure or voids, acting as diffusion paths, can be found in this resultant layer. Consequently, the diffusion barrier performance of electroless Ni-W-P coatings can be significantly enhanced at elevated temperature (> 400 °C) compared to electroless Ni-P coatings.

Based on the previous discussions on Ni-W-P/Zn-Al interconnects, figure 6-14 summaries the interfacial reactions between electroless Ni-W-P coatings and Zn-Al solders, including morphology evolutions of interfacial Al₃Ni₂ grains, crystallisation characteristics of Ni-W-P coating, and interfacial microstructure at the Ni-W-P/Zn-Al interfaces after reaction at 450 °C for 1, 15, and 30 minutes.

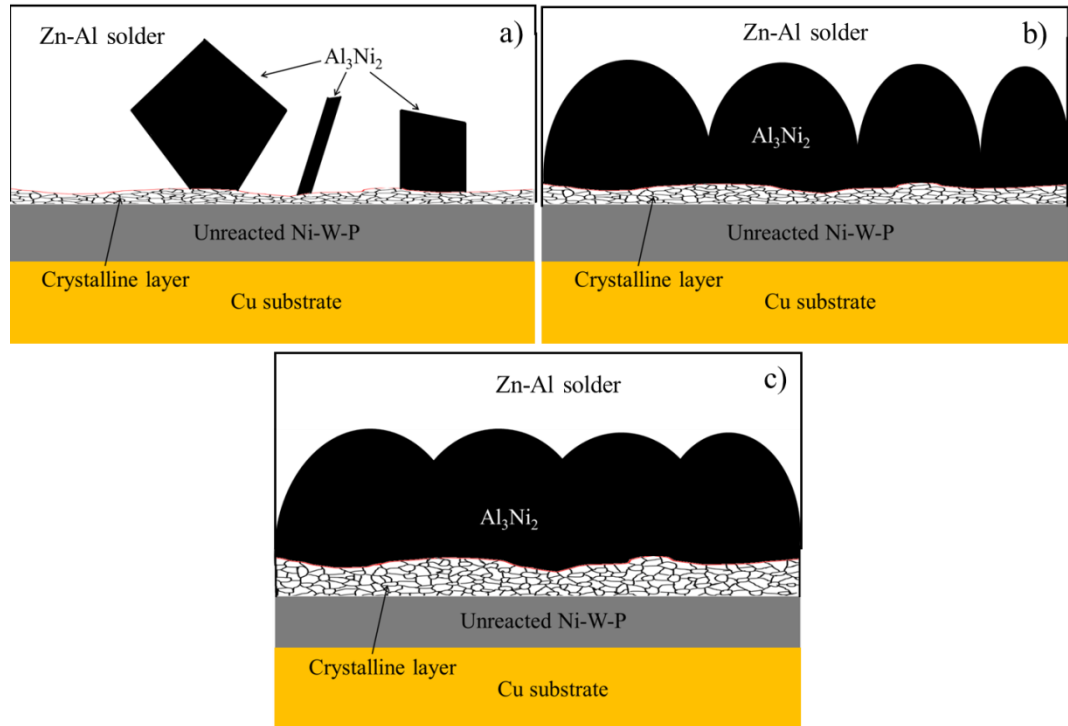


Figure 6-14 Schematic diagram illustrating the IMC evolutions and Ni-W-P crystallisations after reaction at 450 °C for: a) 1 minute; b) 15 minutes; c) 30 minutes.

When reacted with solder for 1 minute, a very thin layer of Al_3Ni_2 grains (thickness: $\sim 0.5 \mu\text{m}$) was formed in shapes of prism-like or plate-like. After 15 minutes reaction, the big Al_3Ni_2 grains (up to $2.1 \mu\text{m}$) emerged the adjacent small Al_3Ni_2 grains, forming Al_3Ni_2 particles with a scallop shape due to the volume expansion of all Al_3Ni_2 grains. The size of these round scallop-shape Al_3Ni_2 was in the range of $1 - 2.1 \mu\text{m}$, forming to a continuous Al_3Ni_2 layer from cross-section view. Finally, faceted scallop Al_3Ni_2 grains were observed in a polygon-like shape with a slightly increasing grain size (up to $2.5 \mu\text{m}$) after 30 minutes reaction. Meanwhile, the electroless Ni-W-P coatings were divided into two layers of a crystalline resultant interlayer and an unreacted Ni-W-P coating with a fine polycrystalline structure. The rate of resultant interlayer due to the reaction-assist crystallisation in entire Ni-W-P coatings continued to grow. Its structure was impact and free of voids, exhibiting a better diffusion barrier property compared to electroless Ni-P coating.

6.3.5 Nanoindentation characterisations

Figure 6-15 shows the morphologies of the indented regions and the representative indenters on CuZn_4 , Cu_5Zn_8 , CuZn and Al_3Ni_2 in the Zn-5Al solder interconnects after 30 minutes reaction at 450 °C. Notably, due to the extreme thin thickness of CuZn ($\sim 2 \mu\text{m}$), the indentations were mostly located in this IMC layer but also inevitability

involved the adjacent materials. In similar, the nanoindenter cannot be pressed into an absolute flat Al_3Ni_2 thin layer. But the nanoindenter was fully immersed in Al_3Ni_2 grains without involving any other materials as the surround solders have been removed by dilute HCl solution. The uneven surface of Al_3Ni_2 layer contributed to the unloading-displacement curve highlighted in figure 6-16.

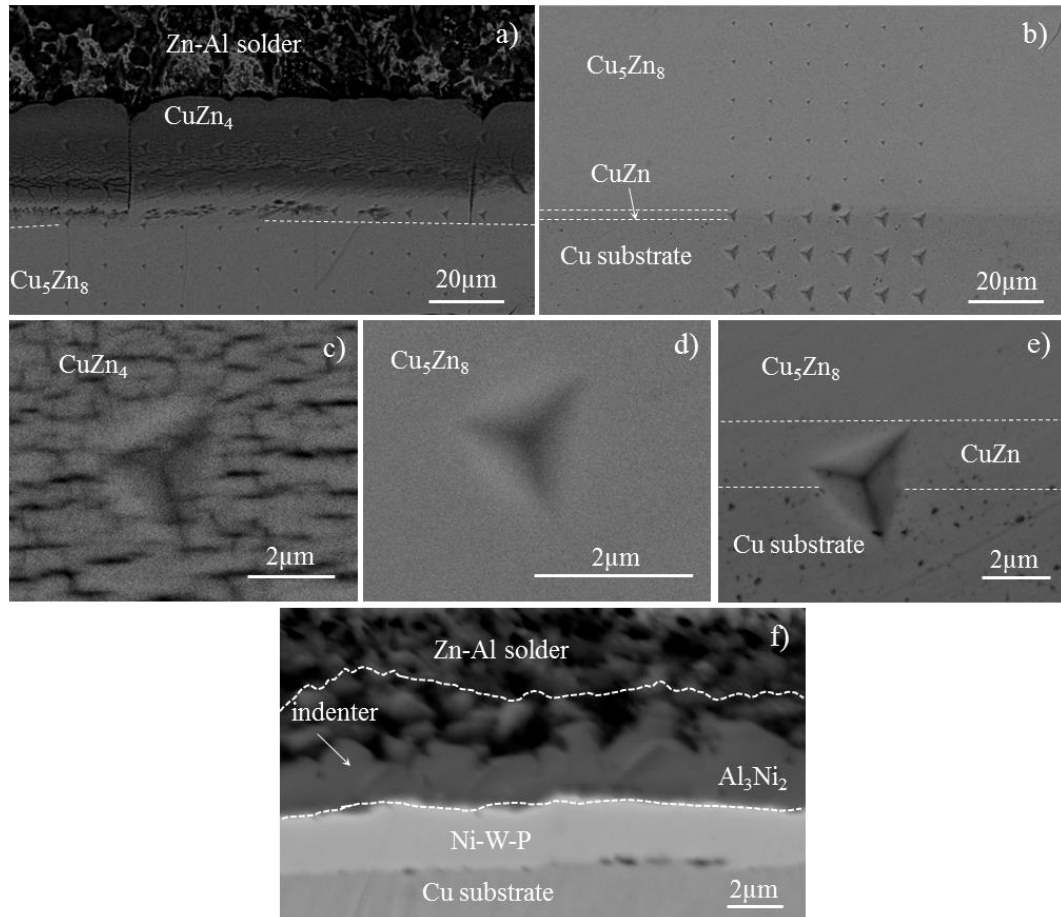


Figure 6-15 Indents on the IMC layers at the Cu/Zn-Al and Ni-W-P/Zn-Al interfaces after 30 minutes reaction at 450 °C: a) indents near Zn-Al solder; b) indents near Cu substrate; c) indent on CuZn_4 ; d) indent on Cu_5Zn_8 ; e) indent on CuZn ; f) indents on Al_3Ni_2 .

Figure 6-16 shows the representative load-displacement curves of the nanoindentation tests on the different phases, including CuZn_4 , Cu_5Zn_8 , CuZn , Al_3Ni_2 , and Cu , formed at Cu/Zn-Al and Ni-W-P/Zn-Al interfaces. The indentations were conducted with a penetration depth (> 200 nm) to avoid the effects of surface free energy and non-ideal shape of real indenter [6.38, 6.39]. Several burst features occurred in the load-displacement curves for CuZn_4 , Cu_5Zn_8 , and Al_3Ni_2 , characterised as a “pop-in” phenomena, while no “pop-in” events were observed for CuZn and Cu phase. Various materials [6.11, 6.38] have been reported to have a “pop-in” phenomenon, indicating that there is a sudden decrease in the hardness of these materials at that point. The

“pop-in” effect normally results from nucleation and propagation of homogeneous dislocations [6.40, 6.41], formation of cracks [6.42], or phase transformation [6.43]. In addition, it is clear that the softest primary Cu had the largest indentation depth, while the depths for IMCs are relatively small. Among the Cu-Zn IMCs, the hardness sequence from highest to lowest is Cu_5Zn_8 , CuZn , and CuZn_4 .

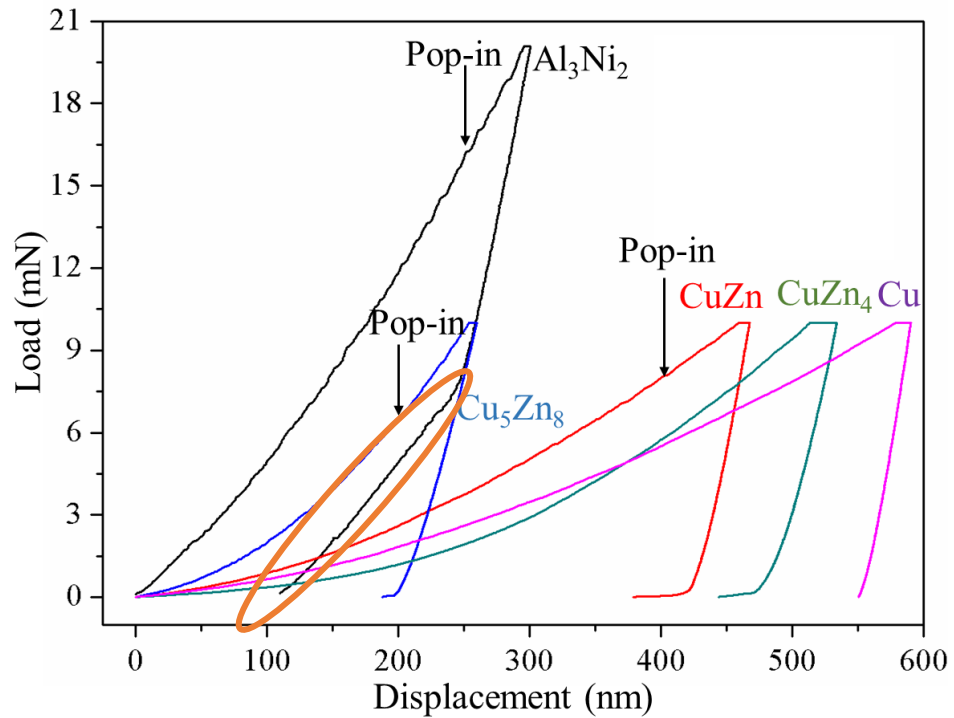


Figure 6-16 Representative load-displacement curves of nanoindentation tests on the constituent phases at the Cu/Zn-Al and Ni-W-P/Zn-Al interfaces after reactions at 450 °C for 30 minutes.

Derived from equation 2-8 and 2-11 based on the displacement curves in figure 6-15, the hardness and elastic moduli of various phases identified along the interfaces of Zn-Al solder interconnects at ambient atmosphere are listed in table 6-3. The elastic moduli and hardness of Cu_5Zn_8 and Al_3Ni_2 were in good agreement with other experimental and simulation works [6.40, 6.42].

Table 6-3 Elastic moduli and hardness of phases in Zn-Al solder interconnects.

IMC types	Elastic moduli (GPa)	Hardness (GPa)	Reference
CuZn_4	68.45 ± 1.43	1.03 ± 0.04	This work
Cu_5Zn_8	142.59 ± 2.26	5.98 ± 0.23	This work
	170 ± 2.2	4.9 ± 0.02	Nanoindentation [6.40]
CuZn	94.71 ± 1.16	1.38 ± 0.16	This work

Cu	80.66 ± 1.32	0.80 ± 0.02	This work
Al_3Ni_2	220.87 ± 18.94	17.67 ± 0.16	This work
	224	-	First-principles [6.42]

6.5 Summary

The interfacial reactions and microstructure evolutions in Zn-Al solder interconnects with and with electroless Ni-W-P coatings during liquid-solid reaction at 450 °C up to 30 minutes were investigated and compared. The elastic moduli and hardness of the interfacial IMCs at the Cu/Zn-Al and Ni-W-P/Zn-Al interfaces after 30 minutes reactions were evaluated. The main findings are summarised as follows:

1. The electroless Ni-W-P coatings obtained in this work were pore-free and compact with different sizes of micro-sized nodular features. The average thickness was approximately 2 μm .
2. At Cu/Zn-5Al interfaces, dendritic $\varepsilon\text{-CuZn}_4$ layer, $\gamma\text{-Cu}_5\text{Zn}_8$ layer and $\beta'\text{-CuZn}$ layer were formed in sequence between Zn-5Al solders and Cu substrates. Some Kirkendall voids were also observed around the CuZn interlayer with increasing reaction durations.
3. At Cu/Zn-5Al interfaces, the growth of CuZn, Cu_5Zn_8 and CuZn_4 at the Cu/Zn-Al interface followed parabolic law with increasing soldering duration. The corresponding growth coefficients are 5.607×10^{-2} , 5.506×10^{-1} and $1.573 \mu\text{m/s}^{1/2}$, respectively.
4. In the Zn-Al solder interconnects with Ni-W-P coatings, the thickness of Al_3Ni_2 layer continued to grow from 0.5 to 2.1 μm with increasing reaction durations from 1 minute to 30 minutes at 450 °C. The shapes of Al_3Ni_2 grains transformed from initial prism-like or plate-like into rod-like and a final faceted scallop-shape.
5. The growth of Al_3Ni_2 layer at Ni-W-P/Zn-Al interconnects is extreme slow with the growth coefficient of $4.90 \times 10^{-2} \mu\text{m/s}^{1/2}$ due to the excellent diffusion barrier property of electroless Ni-W-P coatings.
6. When reacted with Zn-Al solders at 450 °C, Ni-W-P coating can be divided into

two layers, an unreacted Ni-W-P coating and a crystalline interlayer adjacent to Zn-Al solder due to the reactions with solders. The thickness of this resultant interlayer increased from 50 nm after 1 minute reaction to approximately 300 nm after 30 minutes reaction.

7. In nanoindentation tests, “pop-in” event was identified in the load-displacement curves of some IMCs (CuZn_4 , Cu_5Zn_8 , and Al_3Ni_2) after 30 minutes reaction. The elastic moduli of CuZn_4 , Cu_5Zn_8 , CuZn and Al_3Ni_2 were 68.45 ± 1.43 , 142.59 ± 2.26 , 94.71 ± 1.16 , and 220.87 ± 18.94 GPa, respectively. Their corresponding hardness were 1.03 ± 0.04 , 5.98 ± 0.23 , 1.38 ± 0.16 , and 17.67 ± 0.16 GPa.

References

- [6.1] Y. Takaku, L. Felicia, I. Ohnuma, R. Kainuma, and K. Ishida, “Interfacial Reaction between Cu Substrate and Zn-Al Based High Temperature Pb-Free Solders”, *Journal of Electronic Materials*, vol. 37, No. 3, pp. 314-323, 2008.
- [6.2] M. He, Z. Chen, G. Qi, “Mechanical strength of thermally aged Sn-3.5Ag/Ni-P solder joints”, *Metallurgical and Materials Transaction A*, vol. 36, No. 1, pp. 65–75, 2005.
- [6.3] Y. Sohn, J. Yu, S. Kang, D. Shih, T. Lee, “Spalling of intermetallic compounds during the reaction between lead-free solders and electroless Ni-P metallization”, *Journal of Materials Research*, vol. 19, No. 8, pp. 2428–2436, 2004.
- [6.4] F.X. Che, J.H.L. Pang, “Characterization of IMC layer and its effect on thermomechanical fatigue life of Sn-3.8Ag-0.7Cu solder joints”, *Journal of Alloys and Compound*, vol. 541, pp. 6-13, 2012.
- [6.5] W.H. Chen, C.F. Yu, H.C. Cheng, Y.M. Tsai, S.T. Lu, “IMC growth reaction and its effects on solder joints thermal cycling reliability of 3D chip stacking packaging”, *Microelectronic Reliability*, vol. 53 pp. 30-40, 2013.
- [6.6] H.B. Qin, W.Y. Li, W.B. Zhou, X.P. Zhang, Low cycle fatigue performance of ball grid array structure Cu/Sn-3.0Ag-0.5Cu/Cu solder joints, *Microelectronic Reliability*, vol. 54, pp. 2911-2921, 2014.
- [6.7] B. Subrahmanyam, “Elastic moduli of some complicated binary alloy systems”, *Transactions of the Japan Institute of Metals*, vol. 13, pp. 93-95, 1972.
- [6.8] R.J. Fields, S.R. Low III, G.K. Lucey Jr., in: M.J. Cieslak, J.H. Perepezko, S. Kang, M.E. Glicksman (Eds.), *The Metal Science of Joining*, TMS, Warrendale, PA, 1992, p. 165.
- [6.9] X. Deng, N. Chawla, K.K. Chawla, M. Koopman, “Deformation behavior of (Cu, Ag)-Sn intermetallics by nanoindentation”, *Acta Materialia*, vol. 52, 4291-4303, 2004.

- [6.10] L.H. Xu, J.H.L. Pang, “Nanoindentation on SnAgCu lead-free solder joints and analysis”, *Journal of Electronic Materials*, vol. 35, pp. 2107-2115, 2006.
- [6.11] P.F. Yang, Y.S. Lai, S.R. Jian, J. Chen, R.S. Chen, “Nanoindentation identifications of mechanical properties of Cu_6Sn_5 , Cu_3Sn , and Ni_3Sn_4 intermetallic compounds derived by diffusion couples”, *Materials Science and Engineering: A*, vol. 485, No. 1-2, pp. 305-310, 2008.
- [6.12] H.B. Qin, X.P. Zhang, M.B. Zhou, X.P. Li, and Y.-W. Mai, “Geometry effect on mechanical performance and fracture behavior of micro-scale ball grid array structure Cu/Sn-3.0Ag-0.5Cu/Cu solder joints”, *Microelectronics Reliability*, vol. 55, No. 8, pp. 1214-1225, 2015.
- [6.13] J. Bertheau, F. Hodaj, N. Hotellier, J. Charbonnier, “Effect of intermetallic compound thickness on shear strength of 25 mm diameter Cu-pillars”, *Intermetallics*, vol. 51, pp. 37-47, 2014.
- [6.14] J.F. Li, P.A. Agyakwa, and C.M. Johnson, “Kinetics of Ag_3Sn growth in Ag-Sn-Ag system during transient liquid phase soldering process”, *Acta Materialia*, Vol. 58, pp. 3429-3443, 2010.
- [6.15] J.F. Li, P.A. Agyakwa, C.M. Johnson, “Interfacial reaction in Cu/Sn/Cu system during the transient liquid phase soldering process”, *Acta Materialia*, Vol. 59, pp. 1198-1211, 2011.
- [6.16] Y. Zhong, R. An, C. Wang, Z. Zheng, Z. Q. Liu, C. H. Liu, C.F. Li, T.K. Kim, and S. Jin, “Low temperature sintering Cu_6Sn_5 Nanoparticles for superplastic and super-uniform high temperature circuit interconnects”, *Small*, Vol. 11, No. 33, pp. 4097-4103, 2015.
- [6.17] D. Kiener, C. Motz, M. Rester, M. Jenko, G. Dehm, “FIB damage of Cu and possible consequences for miniaturized mechanical tests”, *Materials Science and Engineering: A*, vol. 459, No. 1-2, pp. 262-272, 2007.
- [6.18] G. Xiao, X. Yang, G. Yuan, Z. Li, and X. Shu, “Mechanical properties of intermetallic compounds at the Sn–3.0Ag–0.5Cu/Cu joint interface using nanoindentation”, *Materials and Design*, vol. 88, pp. 520-527, 2015.
- [6.19] M. Kowalski, “Thermodynamic reevaluation of the Cu-Zn system”, *Journal of Phase Equilibria*, vol. 14, No. 3, pp. 432-438, 1993.
- [6.20] P. Nash, “Phase Diagrams of Binary Nickel Alloys”, ASM International, Materials Park, OH, pp. 382-390, 1991.
- [6.21] P. Nash, “Phase Diagrams of Binary Nickel Alloy”, ASM International, Materials Park, OH, pp. 3-11, 1991.
- [6.22] T. Gancarz, J. Pstru s, P. Fima, S. Mosinska, “Effect of Ag addition to Zn–12Al alloy on kinetics of growth of intermediate phases on Cu substrate”, *Journal of Alloys and Compounds*, vol. 582, pp. 313-322, 2014.
- [6.23] K. Suganuma, T. Murata, H. Noguchi, Y. Toyada, “Heat resistance of Sn–9Zn solder/Cu interface with or without coating”, *Journal of Material Research*, vol.15, No.4, pp. 884-891, 2000.
- [6.24] W. Yang, R.W. Messler, and L.E. Felton, “Microstructure evolution of eutectic Sn-Ag solder joints”, *Journal of Electronic Materials*, vol. 23, No. 8, pp. 765-772, 1994.

- [6.25] C.E. Ho, T.T. Kuo, C.C. Wang, and W.H. Wu, "Inhibiting the Growth of Cu₃Sn and Kirkendall Voids in the Cu/Sn-Ag-Cu system by minor Pd alloying", *Electronic Materials Letters*, vol. 8, No. 5, pp. 495-501, 2012.
- [6.26] K. Zeng, R. Stierman, T.C. Chiu, D. Edwards, K. Ano, and K.N. Tu, "Kirkendall void formation in eutectic SnPb solder joints on bare Cu and its effect on joint reliability", *Journal of Applied Physics*, vol. 97, pp. 024508-1-8, 2005.
- [6.27] J. Yu and J.Y. Kim, "Effects of residual S on Kirkendall void formation at Cu/Sn-3.5Ag solder joints", *Acta Materialia*, vol. 56, No. 19, pp. 5514-5523, 2008.
- [6.28] F. Xing, J. Yao, J. Liang, and X. Qiu, "Influence of intermetallic growth on the mechanical properties of Zn-Sn-Cu-Bi/Cu solder joints", *Journal of Alloys and Compounds*, Vol. 649, pp. 1053-1059, 2015.
- [6.29] Y. Takaku, K. Makino, K. Watanabe, I. Ohnuma, R. Kainuma, Y. Yamada, and etc., "Interfacial reaction between Zn-Al-based high-temperature solders and Ni substrate", *Journal of Electronic Materials*, vol. 38, No. 1, pp. 54-60, 2009.
- [6.30] Y.J. Hu, L. Xiong, J.H. Meng, "Electron microscopic study on interfacial characterization of electroless Ni-W-P plating on aluminium alloy", *Applied Surface Science*, vol. 253, pp. 5029-5034, 2007.
- [6.31] Y. Yang, J.N. Balaraju, S.C. Chong, H. Xu, C. Liu, V.V. Silberschmidt, and Z. Chen, "Significantly retarded interfacial reaction between an electroless Ni-W-P metallization and lead-free Sn-3.5Ag solder", *Journal of Alloys and Compounds*, vol. 565, pp. 11-16, 2013.
- [6.32] K.H. Hur, J.H. Jeong, D.N. Lee, "Microstructures and crystallization of electroless Ni-P deposits", *Journal of Material Science*, vol. 25, pp. 2573-2584, 1990.
- [6.33] S.K. Tien, J.G. Duh, and Y.I. Chen, "Structure, thermal stability and mechanical properties of electroless Ni-P-W alloy coatings during cycle test", *Surface and Coatings Technology*, vol. 177-178, pp. 532-536, 2004.
- [6.34] J.W. Jang, P.G. Kim, K.N. Tu, D.R. Frear, and P. Thompson, "Solder reaction-assisted crystallization of electroless Ni-P under bump metallization in low cost flip chip technology", *Journal of Applied Physics*, vol. 85, No. 12, pp. 8456-8463, 1999.
- [6.35] E. Vafaei-Makhsoos, "Electron diffraction study of newly discovered nickel phosphides in partially crystallized amorphous electrodeposited Ni-P thin films", *Journal of Applied Physics*, vol. 51, No. 12, pp. 6366-6376, 1980.
- [6.36] A. Kumar, M. Kumar, and D. Kumar, "Effect of composition on electroless deposited Ni-Co-P alloy thin films as a diffusion barrier for copper metallization", *Applied Surface Science*, vol. 258, No. 20, pp. 7962-7967, 2012.
- [6.37] M. He, Z. Chen, and G.J. Qi, "Solid state interfacial reaction of Sn-37Pb and Sn-3.5Ag solders with Ni-P under bump metallization", *Acta Materialia*, vol. 52, No. 7), pp. 2047-2056, 2004.
- [6.38] A.Z.M.S. Rahman, P.Y. Chia, and A.S.M.A. Haseeb, "Mechanical properties of intermetallic compounds in electrodeposited multi-layered thin film at small

- scale by nanoindentation”, *Material Letters*, vol. 147, pp. 50-53, 2015.
- [6.39] A.C. Fischer-Cripps, *Nanoindentation*, Springer, USA., 2011.
- [6.40] D. Lorenz, A. Zeckzer, U. Hilpert, P. Grau, H. Johnson, and H.S. Leipner, “Poison effect as homogeneous nucleation of dislocations during nanoindentation”, *Physical Review B*, vol. 67, pp. 172101, 2003.
- [6.41] A. Gouldstone, K.J. van Vliet, and S. Suresh, “Nanoindentation: simulation of defect nucleation in a crystal”, *Nature*, vol. 411, pp. 656, 2001.
- [6.42] S.R. Jian and Y.H. Lee, “Nanoindentation-induced interfacial fracture of ZnO thin films deposited on Si (1 1 1) substrates by atomic layer deposition”, *Journal of Alloys and Compounds*, vol. 587, pp. 313-317, 2014.
- [6.43] S.R. Jian, G.J. Chen, and J.Y. Juang, “Nanoindentation-induced phase transformation in (1 1 0)-oriented Si single-crystals”, *Current Opinion in Solid State Materials Science*, vol. 14, No. 3-4, pp. 69-74, 2010.

Chapter 7

Microstructural and Mechanical Characteristics of Au-Ge and BiAgX Solder Joints

In this chapter, electroless Ni-W-P coatings was employed in Au-Ge and BiAgX solder joints with a “sandwich” structure. The shear strength, failure mode, and the potential fracture reasons of these two solder joints were investigated and compared.

7.1 Introduction

As discussed in previous chapters, a lead-free alternative to replace high lead solders (e.g., Pb-5Sn, and Pb-10Sn solders) with a melting temperature range of 305-310 °C has not be found [7.1]. However, due to the strong demands for a drop-in lead-free solder in power electronic applications, the industry field has raised two potential solders of Au-Ge and BiAgX systems for their acceptable melting points. Compared with high lead solders, high temperature lead-free solders possess various disadvantages including a low ductility, poor wettability, and bad reliability, especially at elevated temperature (above 300 °C) [7.2-5]. Moreover, the excessive formations of interfacial IMCs at Cu/solder interfaces can greatly weaken the mechanical strength of the solder joints, which inevitably requires a robust diffusion barrier to retard the interfacial reactions between solders and substrates.

Currently, electroless Ni-P under bump metallisation (UBM) were widely employed in microelectronics as a diffusion barrier. However, when reacted with lead-free solders, conventional Ni-P coatings can produce a columnar-structure Ni_3P layer with enormous nano-voids embedded, resulting in great deterioration in their diffusion barrier property [7.6]. Moreover, electroless Ni-P coatings (thickness: $\sim 5\text{ }\mu\text{m}$) were reported to be completely consumed with Au-Ge solders by the growth of Ni_5Ge_3 and NiGe during aging at 300 °C, leading to a rapid decrease of shear strength [7.7]. Due to

the excellent thermal stability of electroless Ni-W-P coatings, they were employed in Au-Ge and BiAgX solder joints to verify their diffusion barrier property. Presently, limited studies have been reported on the interfacial reactions between electroless Ni-based coatings with Au-Ge and BiAgX solders. Particularly, no works have been reported for electroless Ni-W-P coating. During service, solder joints are generally subjected to mechanical stress and force due to the different coefficients of thermal expansion (CTE) of materials involving in electronic components [7.8]. Poor shear strength can lead to fatigue failures. Shear tests have been widely used to evaluate the mechanical strength of solder joints.

This chapter focused on the interfacial reactions between two high temperature lead-free solders (Au-Ge and BiAgX) and Ni-W-P plated direct bond copper (DBC) substrates. The shear strength of these solder joints were also evaluated and analysed to elaborate the corresponding fracture characteristics.

7.2 Experimental details

7.2.1 Electroless Ni-W-P plating

The 96% aluminium oxide DBC boards (Stellar Industry, Millbury, USA) were used as the substrates for electroless Ni-W-P plating as shown in figure 7-1. The thickness of the Al_2O_3 layer and Cu foil on DBC boards was 0.635 mm and 0.2032 mm, respectively. The area size of the Cu foil was around 60 mm \times 63 mm. The eletroless Ni-W-P plating was carried out in an alkaline bath with a pH value of 8.2 (adjusted with dilute H_2SO_4 and NaOH solution) at 83 ± 2 °C for 10 minutes and 40 minutes to deposit the Ni-W-P coatings with a thickness of approximately 1 μm and 4 μm , respectively. Table 7-1 lists the formulations of this electroless Ni-W-P plating solution. The sources of Ni and W elements were nickel sulphate (NiSO_4) and sodium tungstate (Na_2WO_4), respectively. Sodium hypophosphite (NaH_2PO_2) worked as a reducing agent, while sodium citrate ($\text{Na}_3\text{C}_6\text{H}_5\text{O}_7$) acted as a complexing agent. In addition, sodium lauryl sulphate (SLS, $\text{CH}_3(\text{CH}_2)_{11}\text{OSO}_3\text{Na}$) was added into the bath in a small amount of 0.3 mg/L to eliminate the pinholes and pores in Ni-W-P coatings for a better surface quality.

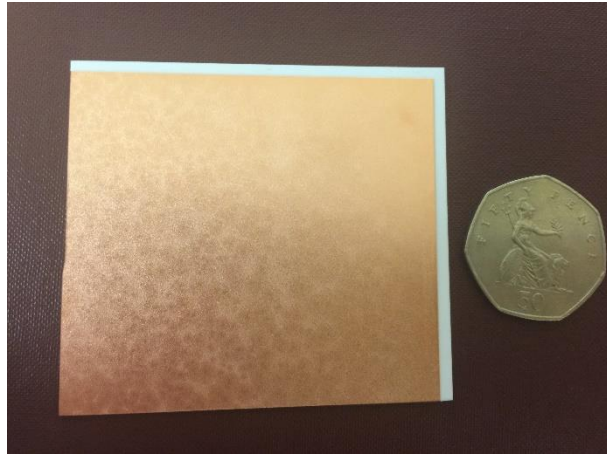


Figure 7-1 Direct bond copper ceramic substrate.

Table 7-1 Composition of the electroless Ni-W-P plating bath.

Chemical reagents	Concentration (g/L)
$\text{NiSO}_4 \cdot 6\text{H}_2\text{O}$	7
$\text{Na}_2\text{WO}_4 \cdot 2\text{H}_2\text{O}$	35
$\text{NaH}_2\text{PO}_2 \cdot \text{H}_2\text{O}$	10
$\text{Na}_3\text{C}_6\text{H}_5\text{O}_7 \cdot 2\text{H}_2\text{O}$	40
$\text{CH}_3(\text{CH}_2)_{11}\text{OSO}_3\text{Na}$	3×10^{-4}

7.2.2 Formation of solder joints

After electroless Ni-W-P plating, sandwich-structure SiC/Au-Ge/Ni-W-P and SiC/BiAgX/Ni-W-P solder joints were prepared by Jinzi Cui for interfacial microstructure analysis and mechanical strength evaluation. As illustrated in figure 7-2, the dies for Au-Ge solder joints were fabricated from a SiC wafer (0.38 mm thickness) with a deposited Ti/Ti:W/Au multi-layer metallisation (Ti content: 10 wt.%). These SiC chips were diced into a square size of 2 mm \times 2 mm. For BiAgX solder joints, the test dies (length \times width \times thickness: 2 mm \times 2 mm \times 0.38 mm) were SiC metallised on their back with a Ti/Ni/Ag multi-layer by e-beam sputtering process. The composition and thickness of these multilayer metallisation are presented in figure 7-2. The different metallisation for Au-Ge and BiAgX solder systems were for decreasing the possibility of involving additional elements.

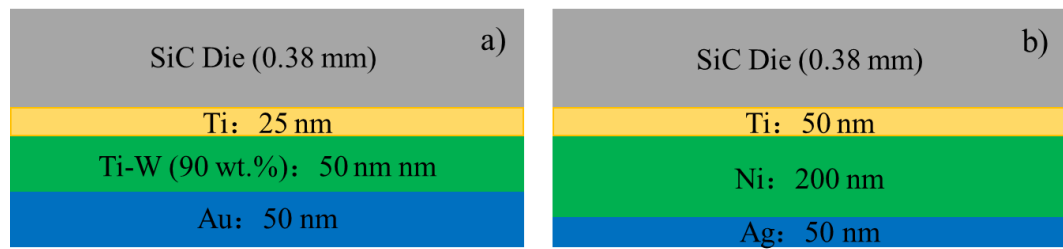


Figure 7-2 The schematic diagrams of SiC dies with the metallisation for: a) Au-Ge solders, b) BiAgX solders.

The Au-Ge solder preforms were from Materion Advanced Materials Group (Buffalo, USA). The Au-Ge solder joints were performed in a SST vacuum furnace with three minutes ramping from room temperature to 385 °C, followed with three minutes dwelling at 385 °C for achieving a good wetting performance.

For BiAgX solder joints, solder pastes were printed on the DBC substrates using a stainless steel stencil (0.127 mm thick). Next, a die placement machine (Palomar Model 3500) located the SiC dies in the required places. Then, these BiAgX solder joints were formed in a PEO 601 furnace at a pure nitrogen atmosphere with a temperature profile as shown in figure 7-3. The joining temperature linearly increased from room temperature to peak temperature (325 °C) for four minutes and then decreases gradually in the furnace chamber.

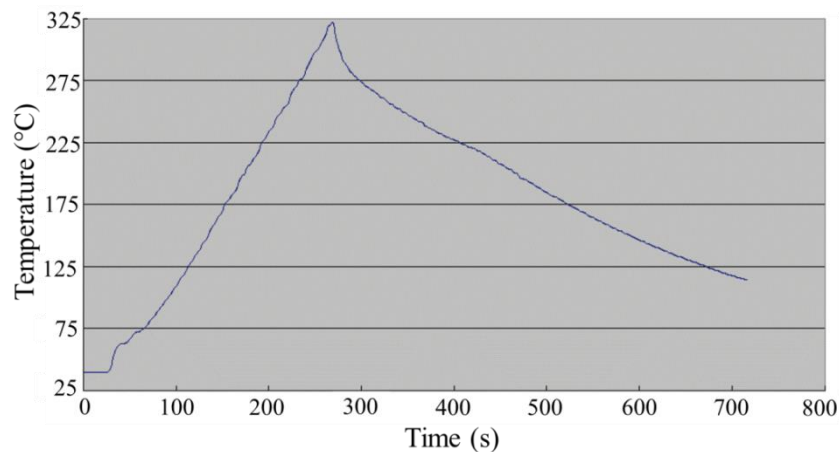


Figure 7-3 Reflow profile of BiAgX solder joints.

7.2.3 Morphological and microstructural observations

The solder joints were cold-mounted, ground and final polished with 1 µm colloidal silica particles for interfacial observations. The interfacial microstructure and IMC morphology in these solder interfaces were observed with a FEG-SEM (Carl Zeiss, Stereoscan 360, Cambridge), using back-scattered electron (BSE) mode. The

composition and diffusion profile at the solder interfaces were characterised by an energy dispersive X-ray (EDX) spectrometer. However, due to the thin thickness ($< 1 \mu\text{m}$) of the interfacial IMCs layer, FEG-SEM technique is not sufficient to clarify the reaction mechanisms between solders and electroless Ni-W-P coatings for the unclear resolutions and inaccurate EDX analysis in high magnifications (above $20000\times$). Therefore, a dual-beam focus ion beam (FIB, FEI Nova 600 Nanolab Dual Beam) was used to fabricate the samples for transmission electron microscopy (TEM, JEOL 2000FX) analysis at a nano-scale. The preparation procedures of TEM samples through FIB machining was illustrated in figure 6-3. Finally, the in-depth material analysis can be conducted at the Ni-W-P/Au-Ge and Ni-W-P/BiAgX solder interfaces.

7.2.4 Shear tests and fracture analysis

The shear strength of solder joints were evaluated through a DAGE PC2400 tester using a 100kg shear module as illustrate in figure 7-4. The shear speed and the shear height was 0.05 mm/s and $25.4 \mu\text{m}$, respectively. For each type of solder joints, eight samples were tested to obtain precise results. This shear tests were conducted with the cooperation of Jinzi Cui. After the shear tests, the fracture surfaces on the SiC die and substrate part were both investigated through FEG-SEM and EDX. Based on these analyses, failure modes can be identified.

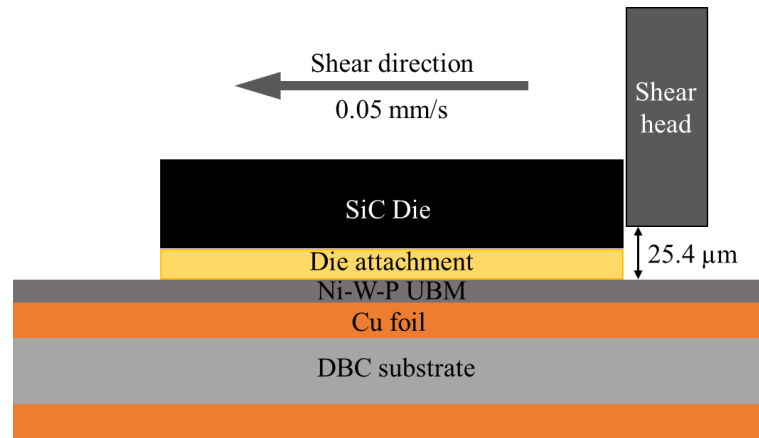


Figure 7-4 Schematic diagram of shear tests.

7.3 Interfacial microstructure and shear strength of as-built Au-Ge solder joints

7.3.1 As-deposited Ni-W-P coatings

The EDX results of as-deposited Ni-W-P coatings are listed in table 7-2. The P content ranged within 6-7 wt.% and the W content was within 15-16 wt.%. Figure 7-5 shows the surface morphology and cross-section of the electroless Ni-W-P coatings. In figure 7-5 a), the surface contains smooth nodules with uneven size range of 1 - 3 μm without any pores. In figure 7-5 b), the thickness of this coating is approximately 3.8 μm . It was closely adhered to the Cu substrate, while no pores or cracking were observed at the Ni-W-P/Cu interface. Overall, this Ni-W-P coating was crack-free, compact and adherent, exhibiting a good morphology quality as a diffusion barrier.

Table 7-2 Composition of as-deposited Ni-W-P coatings through EDX analysis.

Spectrum	Ni	W	P
1	77.8	15.4	6.8
2	76.7	15.9	7.4
3	77.4	15.6	7.0

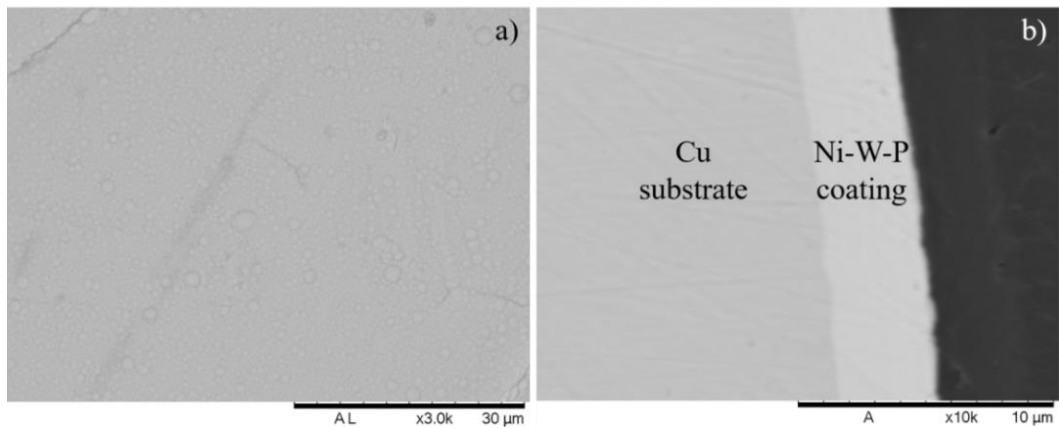


Figure 7-5 Micrographs of the as-deposited Ni-W-P coating: a) surface morphology; b) cross-section morphology.

7.3.2 Interfacial reactions of Au-Ge solder joints

Figure 7-6 shows the cross-section micrograph of the as-built Au-Ge solder joints. In figure 7-6 a), the SiC die horizontally bonds on Cu foil through a thin layer of die attachment. In figure 7-6 b) on enlarged Region b, the thickness of this die attachment is approximately 14 μm , consisting of Au-Ge solder, IMCs and some dispersive Ge-rich phases pointed out by white arrows. Notably, several voids were observed along

boundaries of some Ni-Ge IMC grains and the Ni-W-P coatings, which is likely to induce the separation of Ni-Ge IMCs under shear loads.

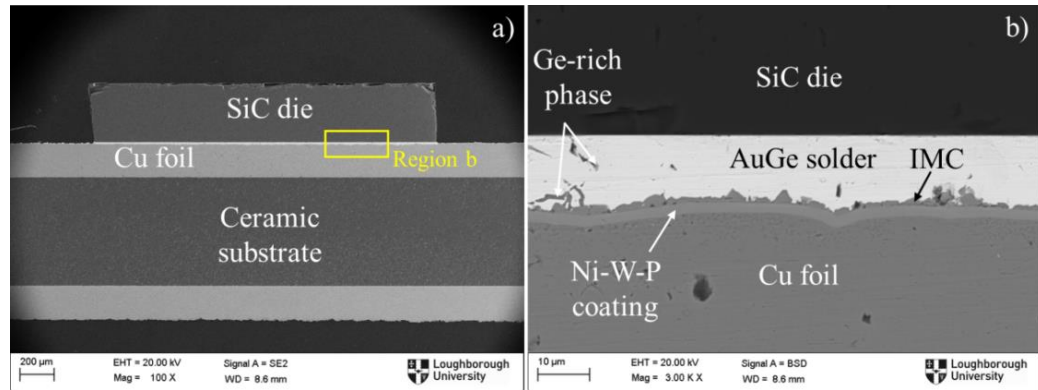


Figure 7-6 Cross-section SEM images of as-built Au-Ge solder joints: a) Overview of entire joints, b) enlarge view of Region b (back-scattered electron mode).

Elemental mapping analysis were conducted on this solder interface and the results are illustrated in figure 7-7. It is clearly observed that nickel (Ni) atoms diffuse out from the Ni-W-P coating to form Ni-Ge IMCs with germanium (Ge) atoms from the Au-Ge solder. The thickness of Ni-Ge IMCs layer was rather thin at approximately 1 μm . According to elemental mapping results, no Cu elements were found within the Au-Ge solder, while Au atoms were also not observed in the Cu substrate. This indicates that Ni-W-P coating is an excellent diffusion barrier to prevent the mutual diffusions and reactions between Cu substrates and Au-Ge solders.

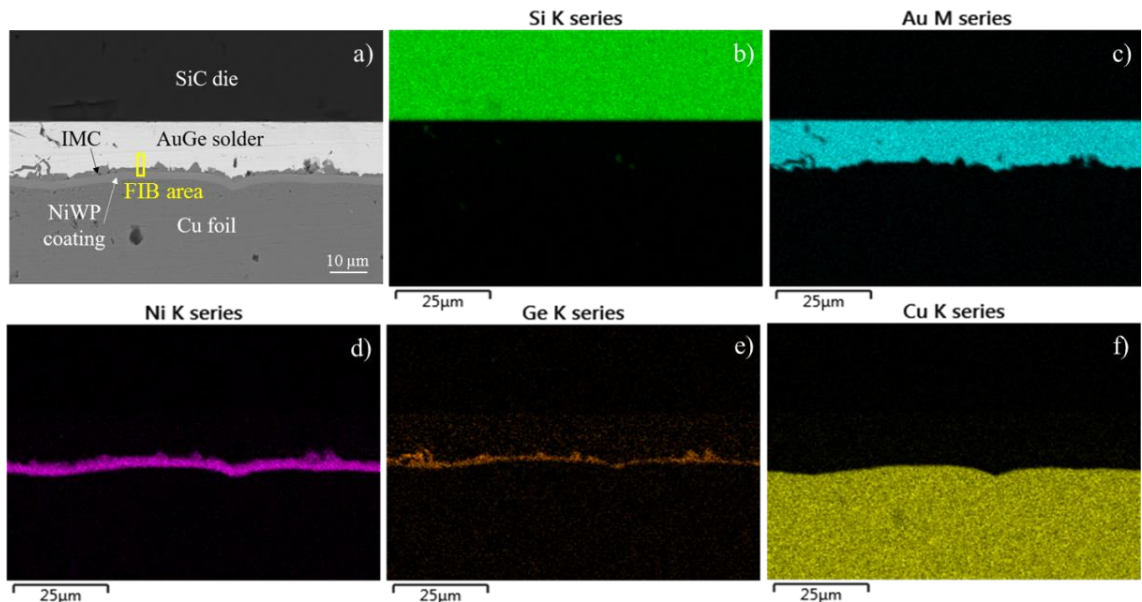


Figure 7-7 EDX element mapping analysis of the Au-Ge solder joints: a) back-scattered SEM image, b) mapping for Si, c) mapping for Au, d) mapping for Ni, e) mapping for Ge, f) mapping for Cu.

Due to the small spot size of FEG-SEM equipment, the accuracy in quantitative composition of the IMC layers from EDX analysis are probably degraded, especially

when the IMC thickness is below 1 μm in Au-Ge solder joints. According to Ni-Ge phase diagram (Figure 7-8), Ni_2Ge , Ni_5Ge_3 and NiGe phases may occur in this Au-Ge solder joints. Lang *et al.* reported that a duplex $\text{Ni}_5\text{Ge}_3/\text{NiGe}$ layer was formed between Au-Ge solder and electroless Ni-P coating [7.7]. To prepare a TEM sample for precise composition results, FIB machining was used to fabricate a thin film (thickness < 100 μm) at the Ni-W-P/Au-Ge solder interface (marked in figure 7-7 a)) for following TEM observations.

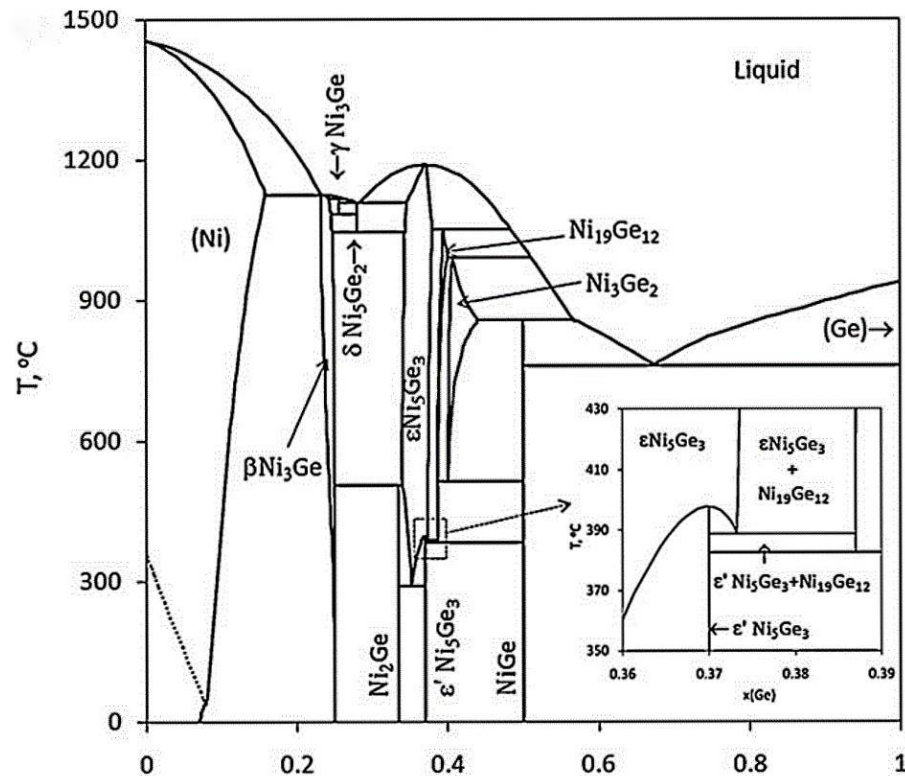


Figure 7-8 Calculated Ni-Ge phase diagram [7.9].

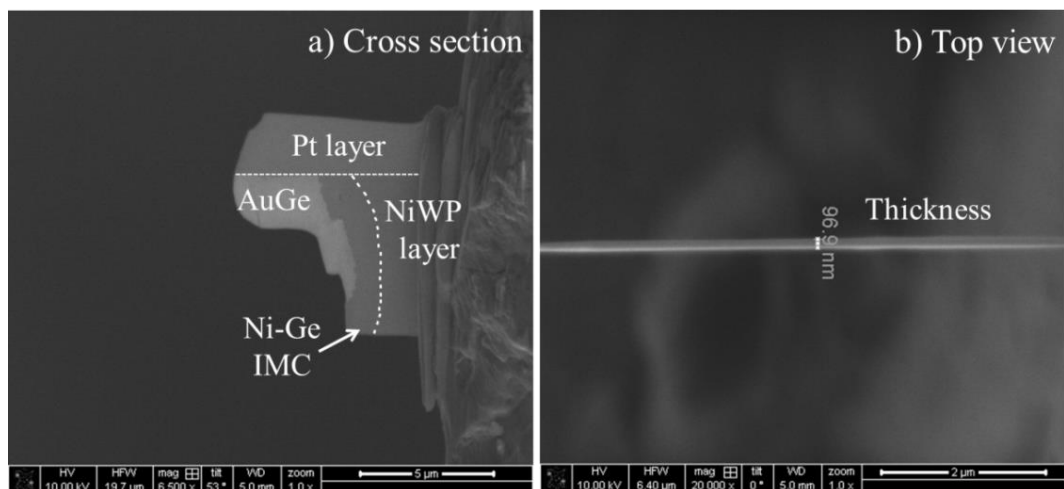


Figure 7-9 Micrographs of prepared FIB sample selected at as-built Ni-W-P/Au-Ge interface from: a) cross-sectional view (tilted at 52°); b) top view (tilted at 7°).

As shown in figure 7-9 a), this TEM sample consists of Au-Ge solder, Ni-Ge IMCs and part of Ni-W-P layer. The top platinum (Pt) layer was for protection of the area of interests during FIB milling. The direction of the FIB milling was from top to bottom side with a beam current of 100 pA during the final thinning to minimise the effect of Ga implantation and contamination of milled materials on the sample surfaces [7.10]. The thickness of the TEM sample was approximately 96.9 nm, ensuring precise and accurate results of selected-area diffraction pattern (SADP), high resolution transmission electron microscopy (HRTEM) and EDX analysis at an nano-scale (over $\times 20000$ magnification).

From the TEM bright-field image in figure 7-10, the IMC layer clearly generates at the Ni-W-P/Au-Ge interfaces in varying morphologies, including dendrite ($\sim 0.5 \mu\text{m}$), scallop ($\sim 0.3 \mu\text{m}$), and granular shape in the smallest size (50 nm approximately). According to the EDX results as listed in table 7-3, although the shapes of IMC are different, they were all identified as Ni_5Ge_3 phase. No NiGe phase was found in this TEM sample, which is different from a previous work on the interfacial reactions between Au-Ge solder and electroless Ni-P coating [7.7]. However, NiGe IMC is still likely to generate in the Au-Ge solder joints because of the small area of selected TEM sample. Some small voids ($<0.4 \mu\text{m}$) were also formed near the IMC/Ni-W-P interface, as shown in figure 7-10. Poor wetting on this area is likely to contribute to these voids.

SADP image on the Ni-W-P coating (Figure 7-10) presents a continuous Debye ring and some individual annuluses, indicating that this Ni-W-P coating has a mixed structure containing amorphous structure and fine polycrystalline FCC-Ni particles. The W and P atoms were dissolved into Ni matrix with a (1 1 1) orientation as discussed in Chapter 4. A similar diffraction pattern has been reported by Torazawa for electroless Ni-8P coating [7.11]. It is observed that some fine crystalline particles (small black dots in figure 7-10) are embedded in the Ni-W-P coating. The grain size of Ni particles are assumed to be under 2 nm as no individual spots replace the continuous rings in the SADP image [7.12]. This Ni-W-P coating was divided into two layers, the unreacted Ni-W-P coating (Spectrum 2 in table 7-3) close to Cu substrate and a reacted layer (Spectrum 3) adjacent to the solder part. The diffusions and reactions between solders and substrates contributed to the formation of this reacted layer. It is interesting to discover that the Ni crystalline particles only scatter within the unreacted Ni-W-P coating but vanish into the resultant layer. This difference in the structure of these two

layers is likely due to the increase of P content from 7.45 wt.% to 11.57 wt.%, leading to an amorphous structure.

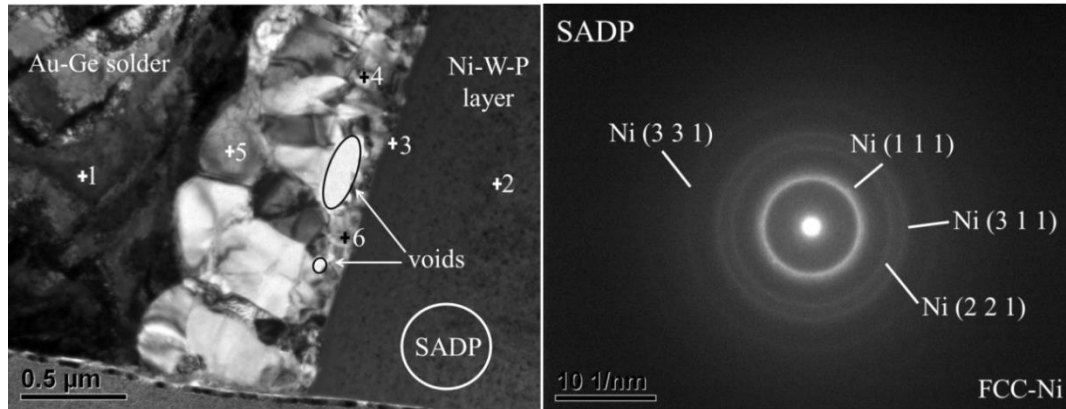


Figure 7-10 TEM bright-field image at the Ni-W-P/Au-Ge interface with SAED pattern.

Table 7-3 Compositions of the spectrums at the Ni-W-P/Au-Ge interface (at.%).

Spectrum	Ni	Ge	Au	W	P
1	1.07	3.96	94.97	-	-
2	74.34	-	-	18.21	7.45
3	64.59	-	-	23.84	11.57
4	59.35	40.65	-	-	-
5	55.63	44.37	-	-	-
6	59.83	40.17	-	-	-

7.3.3 Shear strength and fracture analysis of Au-Ge solder joints

During service time, solder joints are normally subject to shear stress due to the different coefficient of thermal expansions (CTE) of all involving materials in the solder joints. As a result, high shear strength can represent strong reliability of the solder joints. Figure 7-11 lists the shear strength of all tested Au-Ge solder joints, ranging from 120 to 150 MPa. The average shear strength is approximately 138.4 MPa, which is 21 times higher than the strength requirement of die attachments (6.25 MPa) specified in IEC standard Document 60749-19 [7.13]. This indicates robust adhesion strength of the Au-Ge solder joints with electroless Ni-W-P coatings.

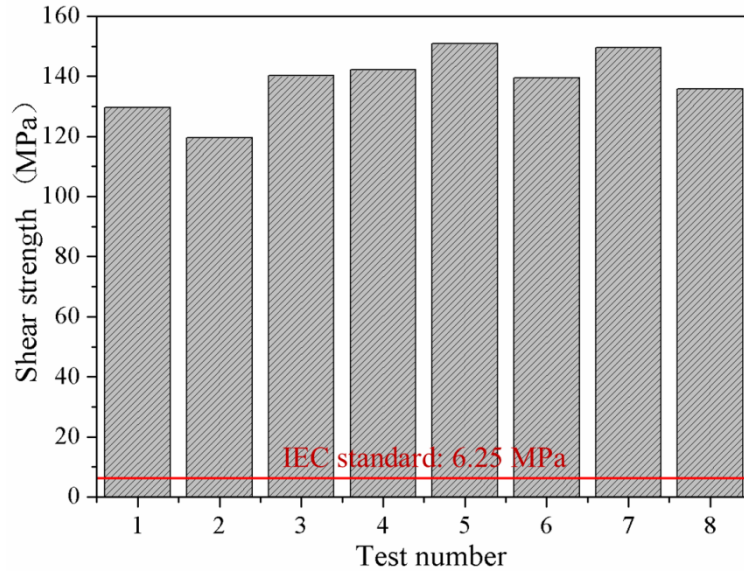


Figure 7-11 Shear strength of as-built Au-Ge solder joints.

After the shear tests, the fracture surfaces of Au-Ge solder joints on DBC substrate and SiC die sides were both investigated to elaborate the fracture characteristics. The failure modes of solder joints can be fall into four types based on the comparative percentage of solders or IMC area: 1) ductile mode (100% solder area remains); 2) quasi-ductile mode (more than 50% solder area remains), 3) quasi-brittle mode (more than 50% IMC area reveals), and 4) brittle mode (100% IMC area reveals) [7.14].

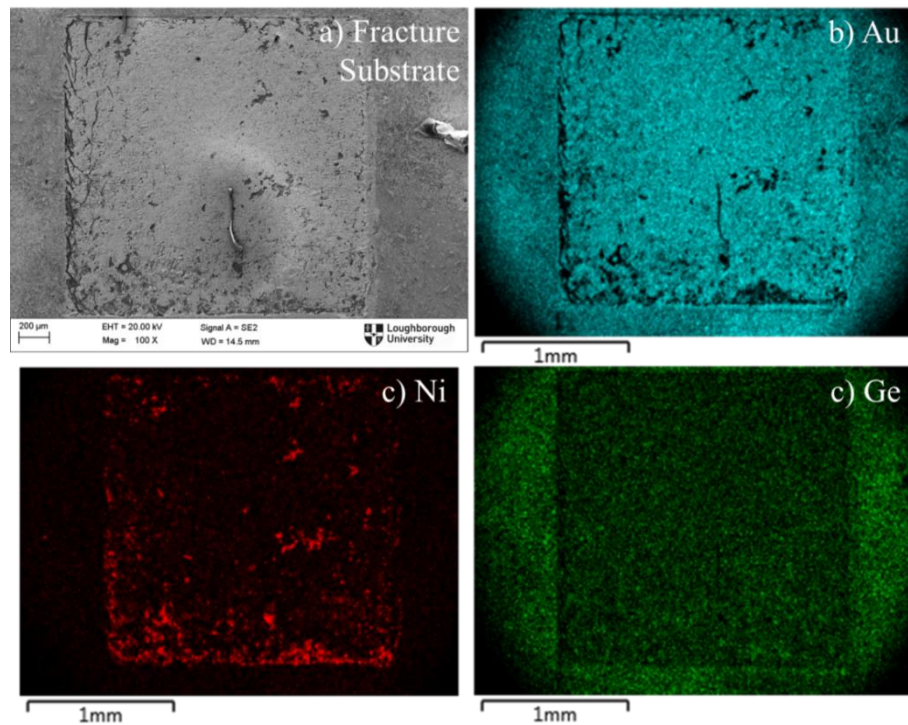


Figure 7-12 SEM and EDX mapping of the fracture surface of Au-Ge solder joints from the DBC substrate side: a) SEM micrograph of overview image; b) mapping for Au; c) mapping for Ni; d) mapping for Ge.

Figure 7-12 shows an overview of the fracture surface and its corresponding elemental mapping results on the substrate side. The fracture surface is mainly consisted of Au-Ge solders, indicating a ductile failure mode. This is attributed to the high adhesion strength between Au-Ge solders and Ni-W-P coatings, making Au-Ge solders the weakest region among the solder joints during shear tests. As a result, the Au-Ge solder joints failed within the Au-Ge solders. Some area of Ni-rich phases were also found in figure 7-12 c). The possible explanations can be the failure at the Ni-Ge phases, the stripping of the electroless Ni-W-P coating or the metallisation on SiC die. Therefore, further investigations on the fracture surface from ceramic substrate side are required to determine the cause.

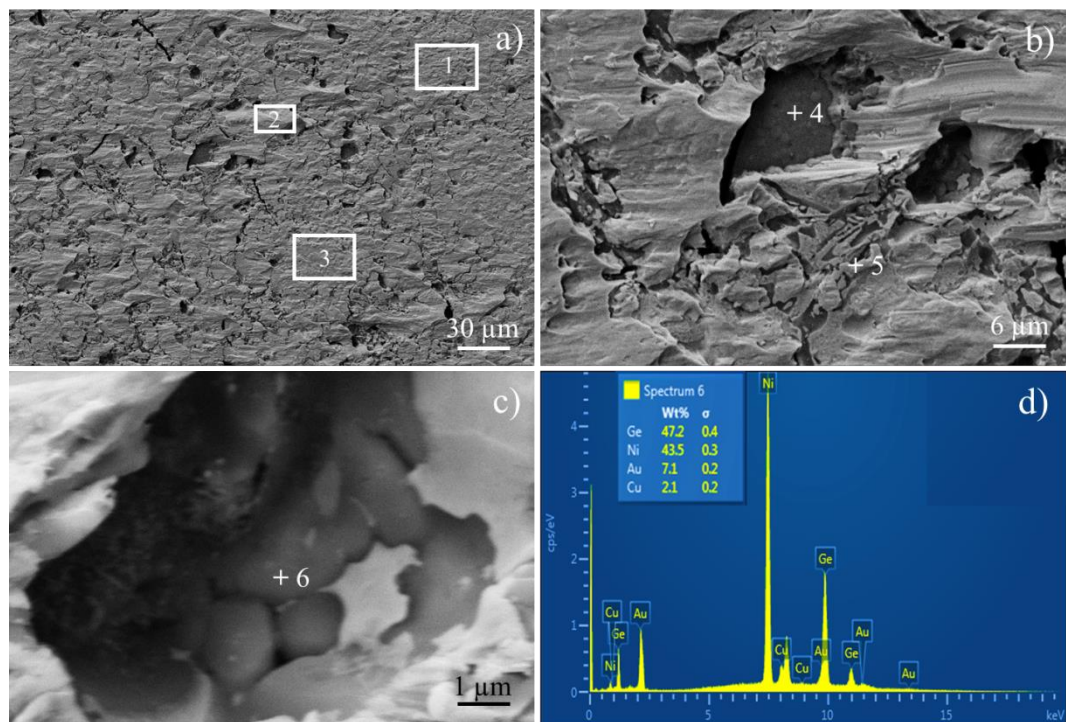


Figure 7-13 Typical fracture surface of the Au-Ge solder joints on substrate side: a) typical fracture surface; b) enlarged view of the dimples; c) NiGe grains; d) EDX spectrum of NiGe in c).

Figure 7-13 displays a typical fracture surface of Au-Ge solder joints from the DBC substrate side with its corresponding elemental results. In figure 7-13 a), the detailed fractographic morphology is slightly rough with some fine dimple features, which can be categorised as a ductile fracture. The compositions of the EDX spectrums in Region 1, 2, and 3 are listed in table 7-4. The materials in these regions are all identified as Au-Ge solder, because it is mainly composed with Au and Ge element (Au content: above 97.8 at.%). From the enlarged images of these dimples in figure 7-13 b) and c), electroless Ni-W-P coating (Spectrum 4: Ni-17.7W-7.6P (at.)) and NiGe

intermetallic (Spectrum 6) can be seen in some dimples. The morphology of NiGe crystalline grains is elliptical and its size is 1 μm approximately. This indicates that NiGe phase indeed existed in some regions of the Au-Ge solder joints, although no NiGe phase was detected at the Ni-W-P/Au-Ge interface in the TEM sample. The formation of the dimples is highly likely due to the low wettability performance of the Au-Ge solders on these area as no flux was applied on the Ni-W-P substrates. As a result, bare Ni-W-P coatings were found due to the unreaction with Au-Ge solders during reflow. Moreover, some voids were formed at the Ni-W-P/Au-Ge interfaces as proven in figure 7-6 b), leading to a poor adhesion strength between partial Ni-Ge IMCs and the Ni-W-P coatings subject to shear stress.

Table 7-4 Composition of the spectrums on the fracture surface at substrate part (at.%).

Spectrum	Au	Ge	Ni	Cu	W	P
1	95.3	2.5	2.2	-	-	-
2	99.4	0.6	-	-	-	-
3	96.4	2.4	1.2	-	-	-
4	-	-	74.7	-	17.7	7.6
5	89.3	5.3	1.2	2.1	-	-
6	2.5	44.6	50.7	2.3	-	-

To elaborate the fracture characteristics of Au-Ge solder joints, the fracture surfaces from the die side were also examined. Generally, the fracture surface is generally smooth and falls into three parts of remaining Au-Ge solder, Ni-Ge intermetallic, and the bare SiC die without its metallisation. The exposed SiC on the fracture surface in figure 7-14 b) indicates that the adhesion strength between Au-Ge solder and the metallisation on SiC chip is excellent. As a result, under the external loads, the Au-Ge solder joints are prone to crack at the weakest parts of solders and the metallisation on SiC die. In figure 7-14 c), Ni-Ge IMC is identified in Spectrum 1 on the fracture surface. However, it is not clear whether it is Ni_2Ge or Ni_5Ge_3 . And, Ge-rich phase was also found according to the composition of Spectrum 2 in figure 7-14, which is consistent with the results in figure 7-6 b). Overall, the failure mode of the Au-Ge

solder joints with electroless Ni-W-P coatings is quasi-ductile since both fracture surfaces from substrate and die sides are mainly covered with Au-Ge solder.

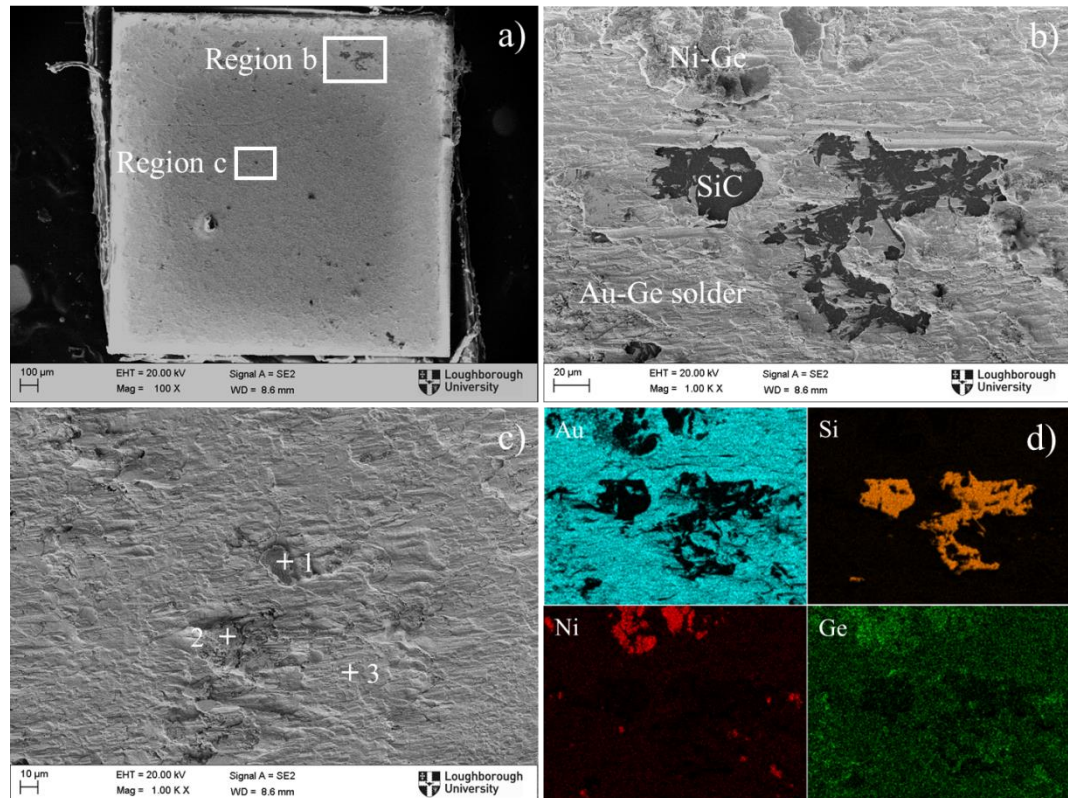


Figure 7-14 SEM images of: a) fracture surface on SiC die; b) enlarge image of Region b; c) enlarge image of Region c; d) Elemental mapping results of Region b.

Table 7-5 Composition of the spectrums on the fracture surface at die side (at.%).

Spectrum	Au	Ge	Ni
1	4.3	31.3	64.4
2	38.0	56.1	5.9
3	97.6	2.4	-

As discussed above, the schematic diagram illustrating the fracture characteristics of the Au-Ge solder joints with electroless Ni-W-P coatings is proposed in figure 7-15. Generally, the solder joints mainly failed within Au-Ge solder matrix due to the lower fracture strength. However, owing to the voids within the Ni-Ge IMCs near the IMC/Ni-W-P interface, partially IMCs are likely to fracture under shear tests as shown in figure 7-13 c). Besides, the bonding strength between SiC die and its metallisation was lower than that of the multi-layer metallisation on SiC die. Therefore, the cracks were likely to be extended into both Ni-Ge IMCs and Ni-W-P UBM on ceramic

substrate and metallisation on SiC die because of the limited thickness of the Au-Ge solder layer ($\sim 14 \mu\text{m}$).

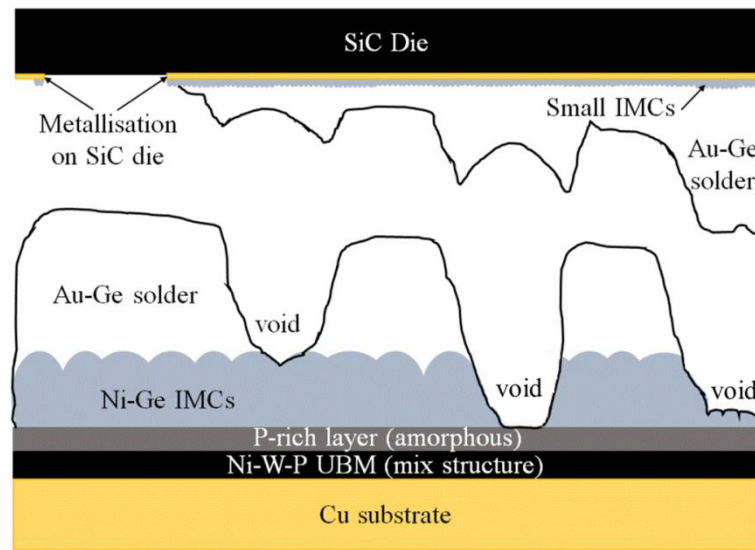


Figure 7-15 Schematic diagram of the fracture mode for as-built SiC/Au-Ge/Ni-W-P solder joints.

7.4 Interfacial microstructure and fracture analysis of as-built BiAgX solder joints

7.4.1 As-deposited Ni-W-P coatings

The EDX results of the electroless Ni-W-P coatings are listed in table 7-6. It is found that the content of P and W ranges within 7-8 wt.% and 15-16 wt.%, respectively.

Table 7-6 Compositions of as-deposited Ni-W-P coatings through EDX analysis.

Spectrum	Ni	W	P
1	76.5	16.0	7.5
2	73.5	16.3	8.2
3	76.6	15.6	7.8

The surface morphology and cross-section microstructure of the Ni-W-P coatings are shown in figure 7-16. In figure 7-16 a), its surface morphology exhibits a large number of individual and agglomerated nodules with an average size of approximately $2 \mu\text{m}$. In the meanwhile, some scattered nodules with a bigger size ($6 \mu\text{m}$ approximately) can be discovered on the surface of Ni-W-P coatings. In cross-section view, this electroless

Ni-W-P coating was adhered closely to the underlying Cu substrate, with a thickness of approximately 1 μm in figure 7-16 b).

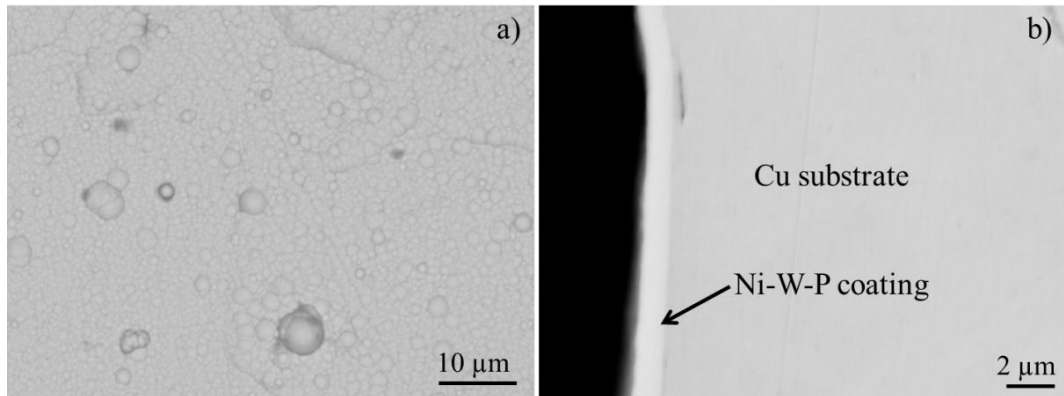


Figure 7-16 Micrographs of as-deposited Ni-W-P coatings: a) surface morphology, b) cross-section morphology.

7.4.2 Interfacial microstructure analysis of BiAgX solder joints

Figure 7-17 shows the cross-section microstructure of as-built BiAgX solder joints. In figure 7-17 a), the SiC die bonded aslant on Cu foil with a gradient of approximately 4 °C. The thickness of entire solder joints ranged from 75 to 125 μm . A single void was observed within the solder joint during the joining process, resulting from the unbalanced melting property of this mixed AgBiX solder paste. As silver additions will not be completely melt at the joining temperature (325 °C), bulky Ag particles is high likely to flow out from the bulky solders and induce the formation of voids.

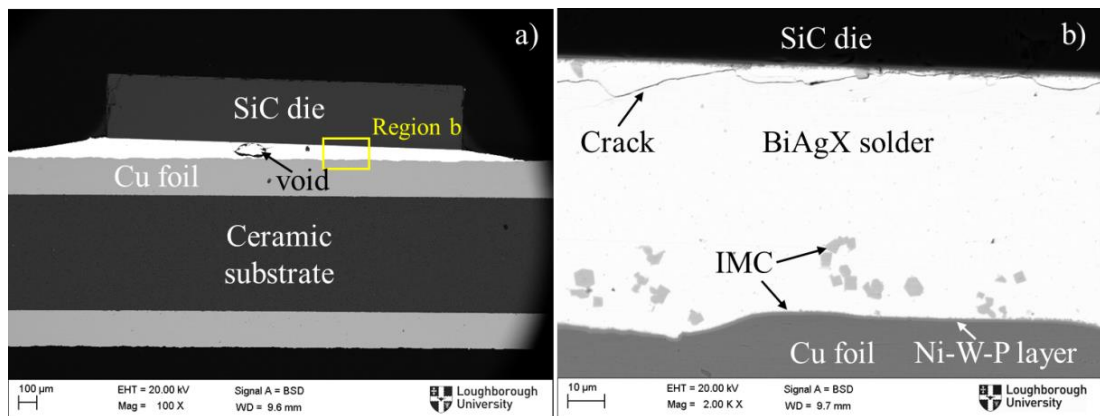


Figure 7-17 Cross-sectional SEM images of as-built BiAgX solder joints: a) Overview microscopy of entire joint, b) enlarge view of region B (back-scattered mode).

When enlarged Region b, a small continuous crack was also found adjacent to the multi-layer metallisation on the SiC die side. However, the causes for this crack were still uncertain. One of the possible reasons is the vast difference in coefficients of thermal expansion (CTE) between SiC die and BiAgX solder. The CTE of BiAgX

solder is estimated to be about $13.3 \times 10^{-6}/^{\circ}\text{C}$, which is 3 times higher than that of SiC ($4.57 \times 10^{-6}/^{\circ}\text{C}$). The other possible reason is the inappropriate processing parameters since BiAgX solder pastes are trial products that lacking of proper joining profiles. According to figure 7-17 b), a number of bulky IMCs (up to 5 μm) were also found in the solder matrix, with their composition detected to be Ag-Sn IMC with a Ag content of approximately 84 at.%.

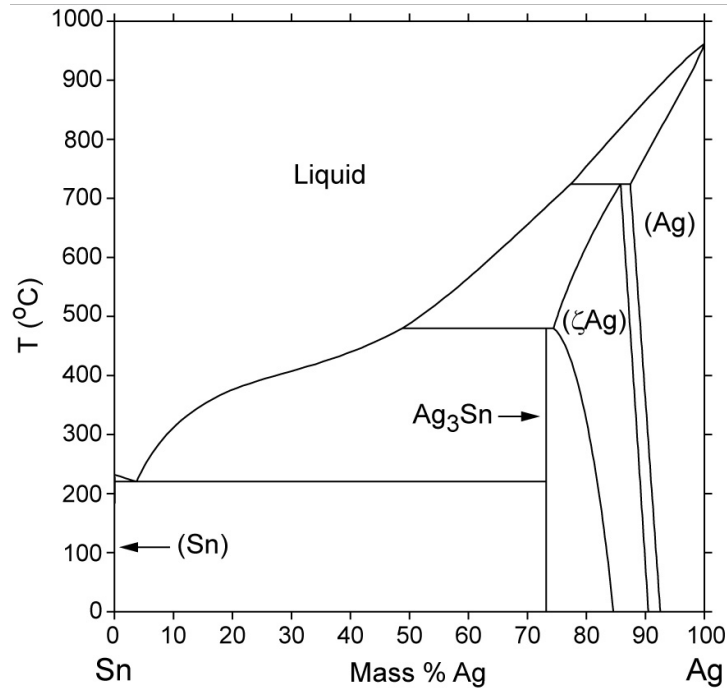


Figure 7-18 Phase diagram of Ag-Sn system [7.15].

However, according to Ag-Sn phase diagram (Figure 7-18 [7.15]) and the reported works on Sn-Ag solders [7.16, 7.17], only needle-structure Ag_3Sn IMCs were formed in a wide size range of 10 - 80 μm . In this work, the Ag-Sn IMC particles have an irregular polygon shape and with a rather smaller size ($< 5 \mu\text{m}$). This is due to the limited contents of Ag and Sn elements in BiAgX solders. In addition, the relative high content of Ag in these Ag-Sn IMC particles (Ag: 84 at.% $>$ 75 at.%) was due to the insufficient Sn amounts in the solder pastes.

From the elemental mapping results of BiAgX solder joints (Figure 7-19), two types of IMCs were found in this solder joint, the Ag_3Sn particles dispersing in solder matrix and the Ni_3Sn_4 formed at Ni-W-P/BiAgX interfaces. Moreover, a mixture of Ni_3Sn_4 and Ag_3Sn particles were also detected at SiC/BiAgX interfaces. The thickness of Ni_3Sn_4 layers at die/solder and substrate/solder interfaces were similar ($\sim 200 \text{ nm}$). Moreover, elemental mapping results indicate that no Cu elements dissolved into the

BiAgX solder and no other elements can be found in Cu substrates. This also proves that electroless Ni-W-P coatings show an excellent ability as a diffusion barrier to prevent the reactions between Cu substrate and BiAgX solder.

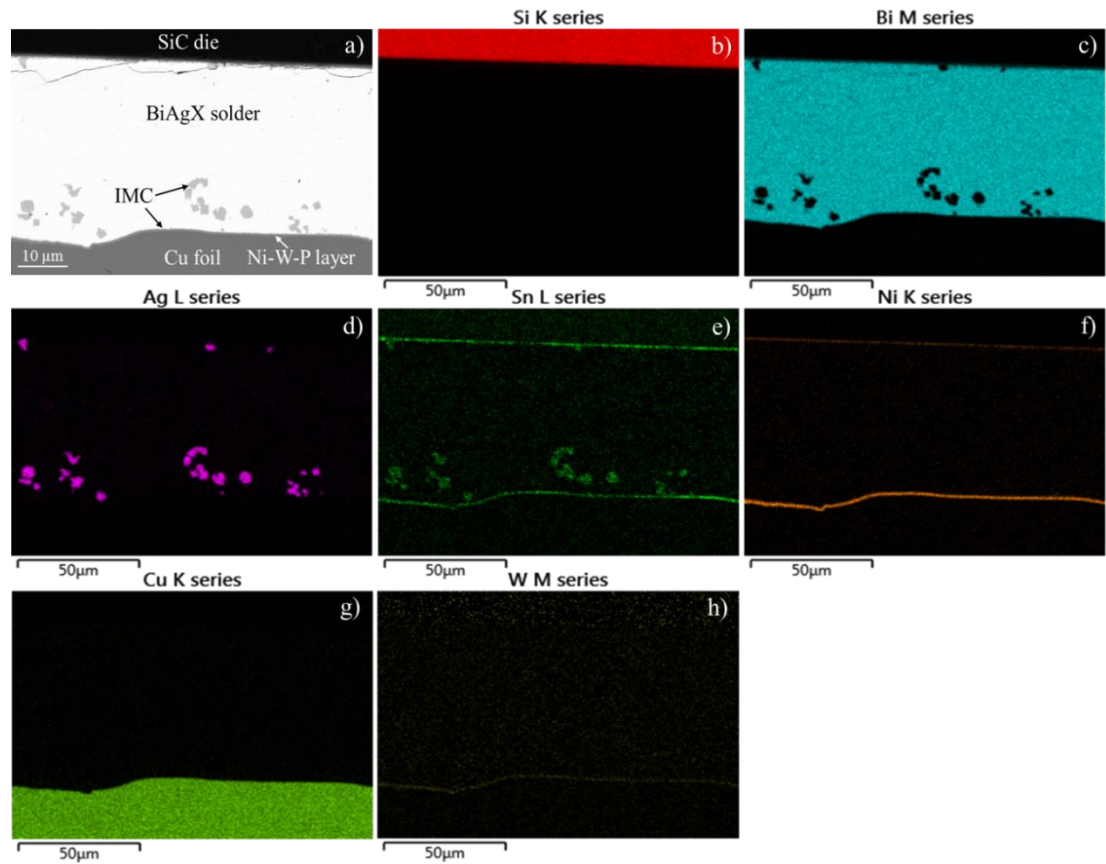


Figure 7-19 EDX element mapping analysis of the BiAgX solder joint: a) SEM-backscattered image; b) mapping for Si; c) mapping for Bi; d) mapping for Ag; e) mapping for Sn; f) mapping for Ni; g) mapping for Cu; h) mapping for W.

As many materials, including Ni, W, P, Bi, Ag, Sn, Ti, and Cu, have been involved in BiAgX solder joints, TEM analysis was thus carried out at the Ni-W-P/BiAgX interface for obtaining accurate elemental results. In figure 7-20, the TEM bright-field image at the Ni-W-P/BiAgX interface shows that BiAgX solder consists of many grains in needle-like, long striped and irregular polygon shapes. Small Ag_3Sn particles are observed in the boundaries and the inside of these solder grains as illustrated in figure 7-20 c). In similar to the formation of bulky Ag_3Sn particles, this phenomenon was due to the unbalanced melting property of mixed AgBiX solder pastes. The diffusions and reactions between solid small Ag particles and trace amount of molten Sn led to the formation of these small solid Ag_3Sn particles in the liquid solders during the joining process. Then, when BiAgX solders started to solidify, the solid Ag_3Sn particles in bigger size (100 - 200 nm) excluded from the solder grains and

aggregated along the grain boundaries of solders. In contrast, the Ag_3Sn particles in small size (< 100 nm) remained in the solder grains in solidification.

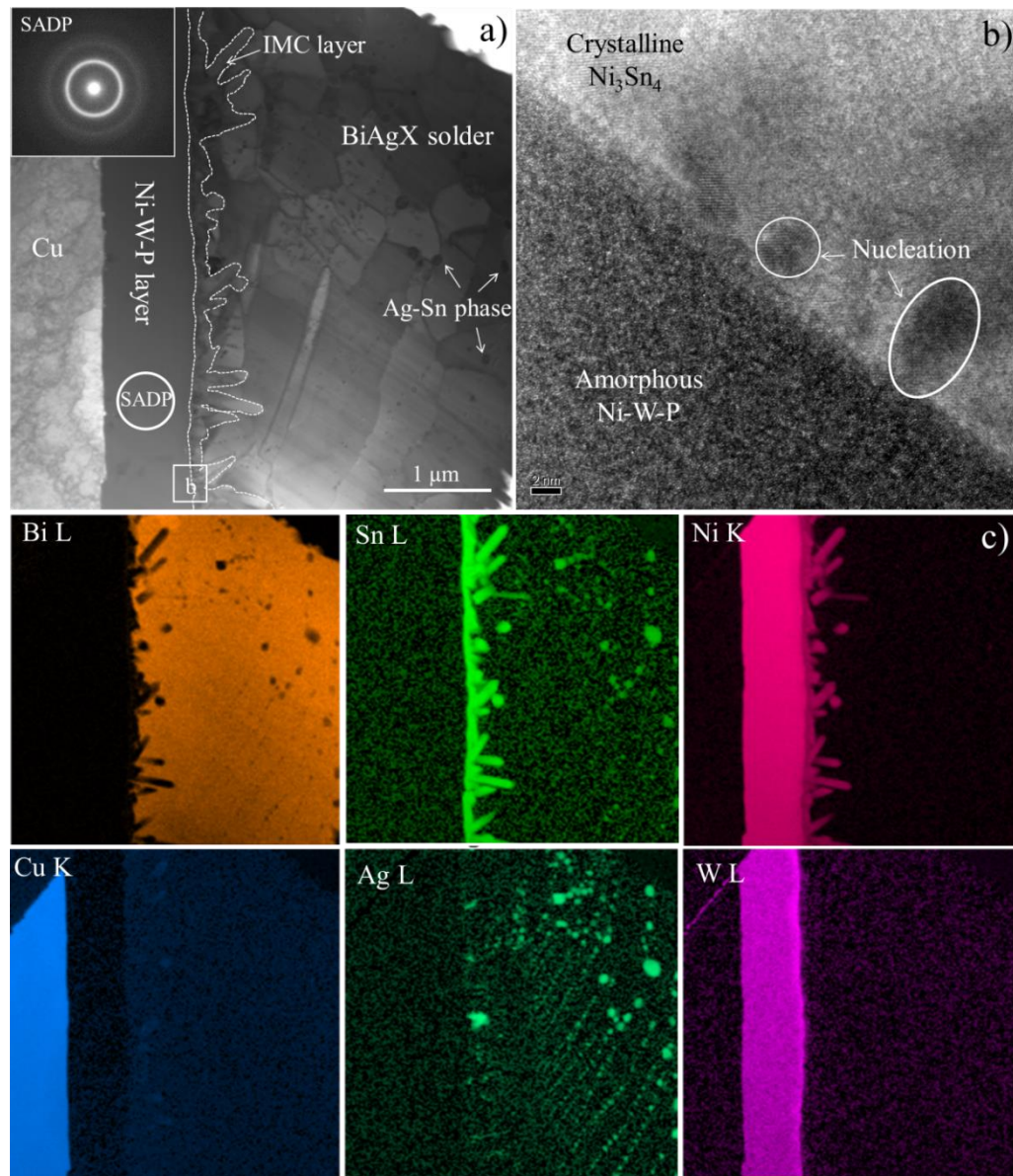


Figure 7-20 TEM results of a) TEM bright-field image at the Ni-W-P/BiAgX solder interconnect with a selected-area diffraction pattern (SADP) taken from Ni-W-P coating; b) high-resolution image of the area highlighted in Region b in figure 7-20 a); c) elemental mapping results of figure 7-20.

The Ni_3Sn_4 layer near the Ni-W-P coating exhibits a columnar-like morphology with a thickness range of 100 nm to 700 nm is shown in figure 7-20 a). Figure 7-20 b) shows a HRTEM image of the interact boundary between the Ni-W-P coating and the crystalline Ni_3Sn_4 grains in local Region b as highlighted in figure 7-20 a). The magnification of this HRTEM image is 56, 000, 000 \times , which is capable to observe the lattices of IMCs and Ni-W-P coating at the interface. The Ni-W-P coating is found to be amorphous for its uniform contrast in the HRTEM figure. This is consistent with the

SADP results on the Ni-W-P coating. The halo patterns in the upper inset image of figure 7-20 a) represent an amorphous structure. In contrast, Ni_3Sn_4 phase exhibited a nanocrystalline structure as demonstrated by the dash lines on behalf of the atomic beams. Notably, the nucleation of Ni_3Sn_4 grains formed at the interact layer between Ni-W-P coating and Ni_3Sn_4 layer can be seen in figure 7-20 b).

7.4.3 Shear strength and fracture analysis of BiAgX solder joints

Figure 7-21 summarises the shear strength of the as-built BiAgX solder joints. The average shear strength is 32.0 MPa approximately, which is still 4 times higher than the requirement of IEC standard (6.25 MPa). But it is clearly smaller than that of Au-Ge solder joints (138.4 MPa). In addition, a work reported that the shear strength of BiAgX solder joints was 61.3 MPa, which is stronger than the average shear strength of the BiAgX joints in this work [7.18]. Various reasons may induce the low mechanical strength, such as a weak BiAgX solder, brittle IMCs, improper joining process, and poor adhesion strength among AgBiX solder joints. Thus, a comprehensive fracture analysis on the fracture surfaces is strongly demanded to provide some advice for future improvements.

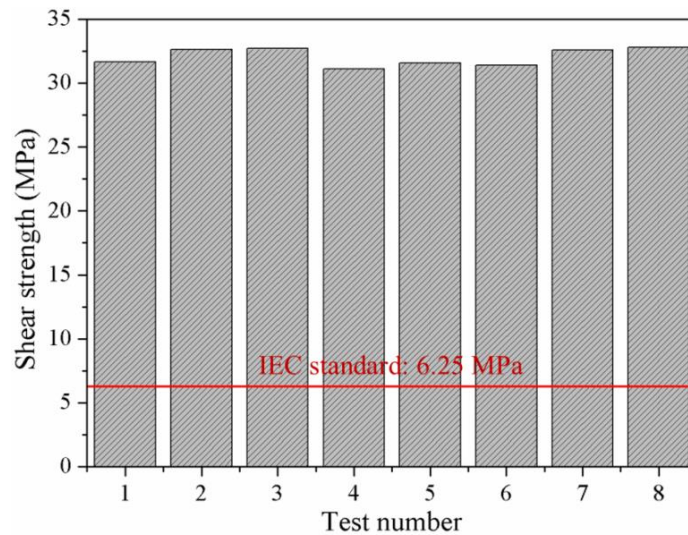


Figure 7-21 Shear strength of BiAgX solder joints.

The fracture surfaces at the sides of DBC substrate and SiC die with their corresponding elemental mapping details are presented in figure 7-22 and figure 7-23, respectively. These solder joints mainly detached from the SiC die side, while the entire die attachment almost remained on the DBC substrate. Only limited solders were separated from this solder matrix during shear tests. This is due to the formation of voids and cracks during joining process, acting as fracture paths for the extension of

fracture at multi-layer metallisation on SiC die. Further investigations on the fracture surface at SiC die side were conducted to elaborate the fracture mechanism of the BiAgX solder joint in figure 7-23.

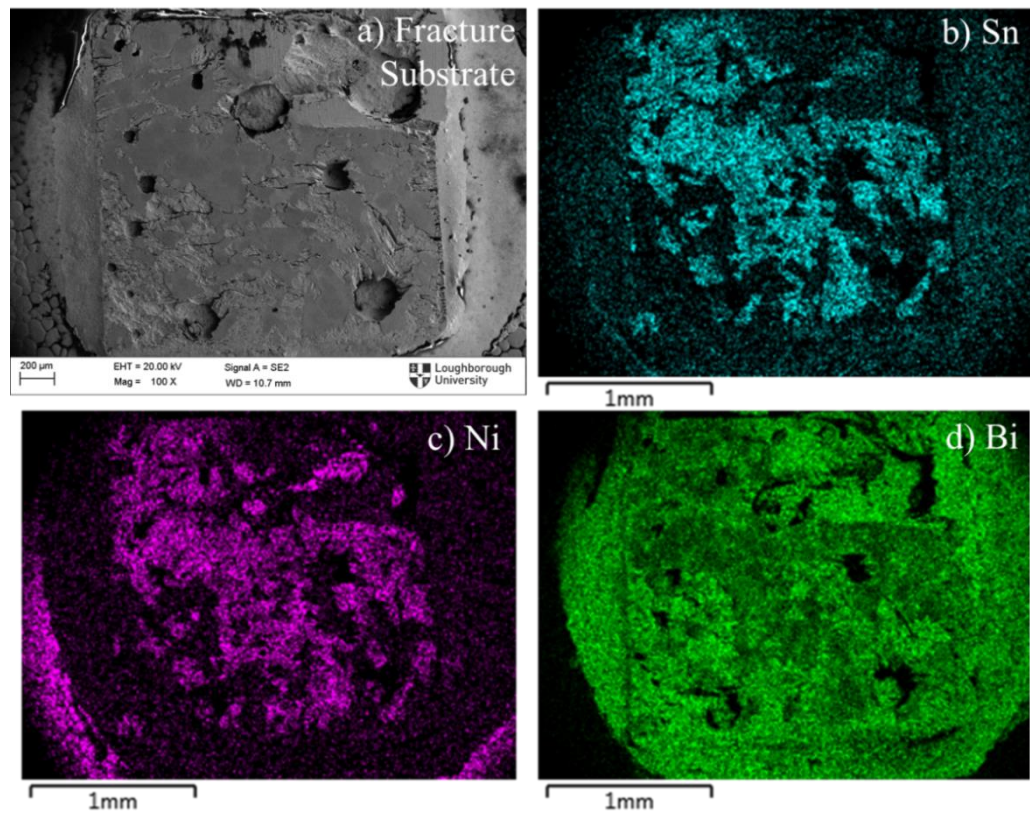


Figure 7-22 SEM and EDX mapping images of the fracture surface on DBC substrate side: a) SEM micrograph; b) mapping for Sn; c) mapping for Ni; d) mapping for Bi.

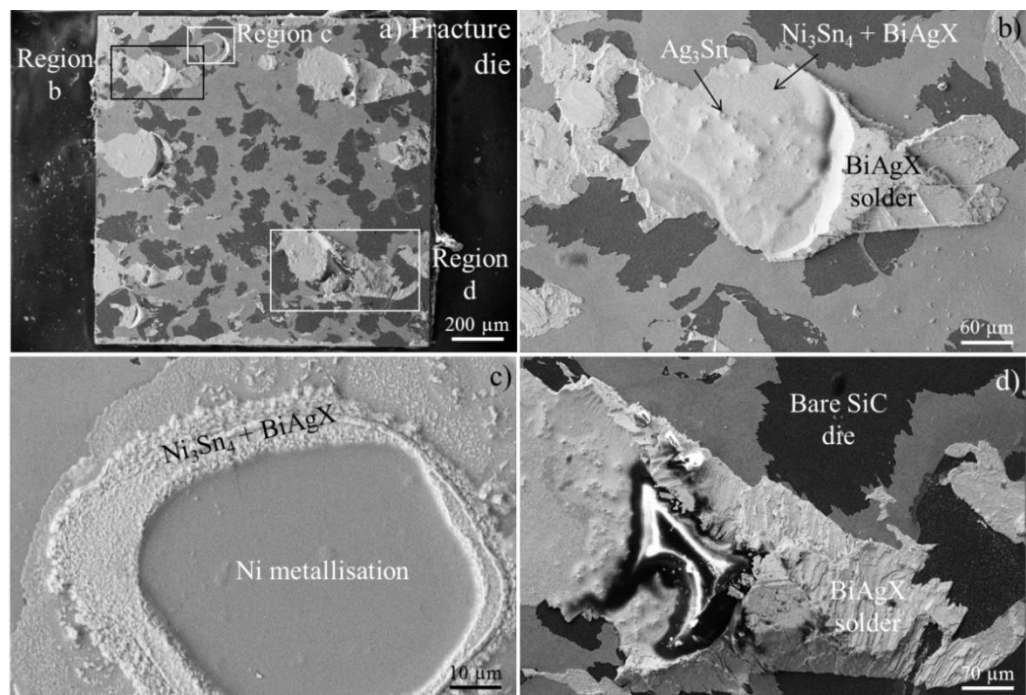


Figure 7-23 The fracture surface of BiAgX solder joints on SiC die side: a) overview image; b) enlarged image of Region b; c) enlarged image of Region c; d) enlarged image of Region d.

It is widely known that solder joints prone to fracture at the weakest part under mechanical loads. As shown in figure 7-23, almost half of the fracture surface is bare SiC die without any metallisation, indicating that the adhesion strength between the multi-layer metallisation and SiC die is rather weak. However, a small amount of BiAgX solders still remained on the fracture surface as indicated in figure 7-23 b), which cannot be simply explained by the adhesion function of Ni_3Sn_4 and Ag_3Sn IMCs as many voids and cracks existed near the multi-layer metallisation (Figure 7-17). Under the mechanical loads, the crack initially formed at the metallisation/SiC interface and then propagated along this interface and extended to some existing voids and cracks within the bulk BiAgX solders, leading to the BiAgX residuals on SiC die.

In addition, bare Ni metallisation and a thin layer of Ni_3Sn_4 and Ag_3Sn grains were aggregately formed around the Ni metallisation as observed in figure 7-23 c); as such, the voids in bulk BiAgX solders prevented the reactions between BiAgX solder and Ni metallisation. However, limited dispersive solders reacted with the Ni metallisation on SiC die to produce the aggregative IMC grains (Ni_3Sn_4 and Ag_3Sn), resulting in the groove formation on the fracture surface from the SiC die side. The cracks also propagated along the boundaries of these grooves.

As discussed above, these defects in the BiAgX solder joints greatly deteriorate its shear strength, especially the poor adhesion between the metallisation and the SiC die is the weakest point within the die attachment due to the bad quality of the metallisation on SiC chip through E-beam sputtering process. In general, the failure mode of the as-built BiAgX solder joints can be summarised in figure 7-24. The BiAgX solder joints typically failed from two regions at the SiC/metallisation interface and within the BiAgX solder adjacent to the metallisation on SiC die. The failure at the SiC/metallisation interface is due to its weak bonding strength, which is attributed to the poor metallisation process on SiC die. As a result, when the BiAgX solder joints were subjected to external loads, cracks initiated at the SiC/metallisation interface and extended to the existing voids and cracks in BiAgX solder (Figure 7-17 b)), leading to a failure of the entire solder joint. During the extension of the cracks, the aggregations of Ni_3Sn_4 and Ag_3Sn particles on Ni metallisation (figure 7-23 c) can also contribute to the significant initiations and propagations of cracks. To achieve higher fracture strength of BiAgX solder joints, both the adhesion strength between multi-layer metallisation and SiC die as well as the joining process of BiAgX solder pastes need to

be improved. In addition, BiAgX solder pastes have not shown an excellent mechanical strength as a die-attach material compared to Au-Ge solders.

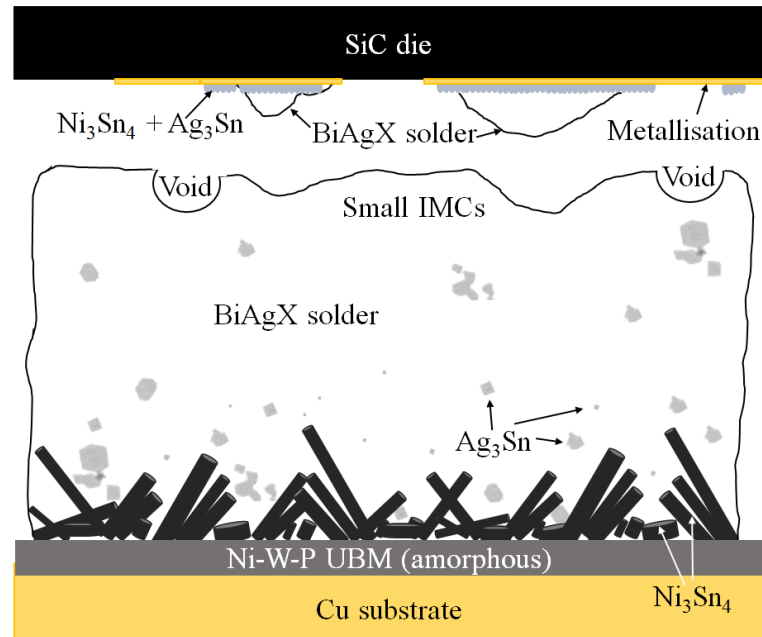


Figure 7-24 Schematic diagram of the failure characteristics of as-built BiAgX solder joints.

7.5 Summary

In this chapter, electroless Ni-W-P coatings were employed in Au-Ge and BiAgX solder systems to form high temperature lead-free solder joints in a sandwich structure. The shear strength and fracture characteristics of these solder joints were investigated and compared. Following conclusions can be made:

1. The composition of the electroless Ni-W-P coatings in Au-Ge and BiAgX die attachments were Ni-16W-7P and Ni-16W-8P, respectively.
2. Due to the thin thickness of the interfacial IMC layers ($< 1 \mu\text{m}$) in the solder joints, the interfacial microstructure at the Ni-W-P/Au-Ge and the Ni-W-P/BiAgX interfaces have been conducted by TEM and FIB techniques.
3. Electroless Ni-W-P coatings showed an excellent property of diffusion barrier to prevent and retard the reactions between Cu substrate and high temperature lead-free solders (Au-Ge and BiAgX solders).
4. After soldering at 385°C , the Ni-W-P coating in Au-Ge solder joints was divided into two layers of one amorphous P-rich layer and another unreacted Ni-W-P

coating with a mixture structure of amorphous compounds and fine crystalline Ni particles. However, the entire Ni-W-P coating in BiAgX solder joints was amorphous due to the low joining temperature at 325 °C

5. In shear tests, Au-Ge solder joints with electroless Ni-W-P coatings generally failed in Au-Ge solders, taking a ductile failure mode. In contrast, BiAgX solder joints mainly fractured at the SiC/metallisation interfaces, which is high likely due to the poor adhesion strength between multi-layer metallisation and SiC die. In addition, the voids and cracks in the bulk BiAgX solders also contributed to this failure.
6. The average shear strength of Au-Ge solder joints was approximately 138.4 MPa, showing a robust adhesion strength. The average shear strength of BiAgX solder joints was approximately 32.0 MPa, which is also 4 times higher than that of IEC standard (6.25 MPa). Compared to Au-Ge solders, BiAgX is not an excellent die-attach material for its relative low shear strength.

References

- [7.1] M. Datta, T. Osaka, and J.W. Schultze, *New Trends in Electrochemistry Technology: Microelectronic Packaging*, CRC Press, USA, 2005.
- [7.2] K. Suganuma, S. J. Kim, and K.S. Kim, “High-temperature lead-free solders: properties and possibilities”, *JOM*, vol. 61, No. 1, pp. 64-71, 2009.
- [7.3] G. Zeng, S. McDonald, and K. Nogita, “Development of high-temperature solders: Review”, *Microelectronics Reliability*, vol. 52, pp. 1306-1322, 2012.
- [7.4] S. Menon, E. George, M. Osterman, and M. Pecht, “High lead solder (over 85%) solder in the electronics industry: RoHS exemptions and alternatives”, *Journal of Materials Science Materials Electronics*, vol. 25, pp. 4021-4030, 2015.
- [7.5] V.R. Manikam, and K.Y. Cheong, “Die attach materials for high temperature applications: A review”, *IEEE Transactions on Components, Packaging and Manufacturing Technology*, vol. 1, No. 4, pp. 457-478, 2011.
- [7.6] M. He, Z. Chen, and G. Qi, “Solid state interfacial reaction of Sn-37Pb and Sn-3.5Ag solders with Ni-P under bump metallization”, *Acta Materialia*, vol. 52, pp. 2047-2056, 2004.
- [7.7] F.Q. Lang, H. Yamaguchi, H. Nakagawa, and H. Sato, “Solid-State Interfacial Reaction between Eutectic Au-Ge Solder and Cu Ni(P) Au Metalized Ceramic Substrate and Its Suppression”, *Journal of Materials Science & Technology*, vol. 31, pp. 445-452, 2015.

- [7.8] M. Abtew and G. Selvaduray, “Lead-free solders in microelectronics”, *Materials Science and Engineering: R*, vol. 27, pp. 95-141, 2000.
- [7.9] Y.Q. Liu, D.J. Ma, Y. Du, “Thermodynamic modelling of the germanium-nickel system”, *Journal of Alloys and Compounds*, vol. 491, pp. 63-71, 2010.
- [7.10] D. Kiener, C. Motz, M. Rester, M. Jenko, and G. Dehm, “FIB damage of Cu and possible consequences for miniaturized mechanical tests”, *Materials Science and Engineering A*, vol. 459, pp. 262-272, 2007.
- [7.11] N. Torazawa, S. Arai, Y. Takase, K. Sasaki, and H. Saka, “Transmission Electron Microscopy of Interfaces in Joints between Pb-free Solders and Electroless Ni-P”, *Materials Transactions*, vol. 44, pp. 1438-1447, 2003.
- [7.12] K.H. Hur, J.H. Jeong, and D.N. Lee, “Microstructures and crystallization of electroless Ni-P deposits”, *Journal of Materials Science*, vol. 25, pp. 2573-2584, 1990.
- [7.13] International Standards, IEC 60749-19, “*Semiconductor devices – Mechanical and climatic test methods – Part 19: Die shear strength*”, 2010.
- [7.14] W.Y. Chen, C.Y. Yu, and J.G. Duh, “Improving the shear strength of Sn-Ag-Cu-Ni/Cu-Zn solder joints via modifying the microstructure and phase stability of Cu-Sn intermetallic compounds”, *Intermetallics*, vol. 54, pp. 181-186, 2014.
- [7.15] I. Ohnuma, M. Miyashita, K. Anzai, X.J. Liu, “Phase equilibria and the related properties of Sn-Ag-Cu based Pb-free solder alloys”, *Journal of Electronic Materials*, vol. 29, No. 10, pp. 1137-1144, 2000.
- [7.16] D. Li, C. Liu, and P.P. Conway, “Characteristics of intermetallics and micromechanical properties during thermal ageing of Sn-Ag-Cu flip-chip solder interconnects”, *Materials Science and Engineering A*, vol. 391, pp. 95-103, 2005.
- [7.17] A.A. El-Daly, H. El-Hosainy, T.A. Elmosalami, and W.M. Desoky, “Microstructural modifications and properties of low-Ag-content Sn-Ag-Cu solder joints induced by Zn alloying”, *Journal of Alloys and Compounds*, vol. 653, pp. 402-410, 2015.
- [7.18] J. Cui, R.W. Johnson, and M.C. Hamilton, “Investigations into the role of different substrate Ni compositions and plating methods on die attach reliability”, in *Proceeding of HiTEN Conference*, Oxford, UK, 2015.

Chapter 8

Conclusions and Future Work

8.1 Main conclusions

This thesis reported a ternary electroless Ni-W-P coating that exhibits excellent thermal stability at elevated temperature (up to 400 °C) and this Ni-W-P coating is able to act as a diffusion barrier for high temperature lead-free solder interconnects (Zn-Al, Au-Ge, and BiAgX solders). Based on the experimental results in previous chapters, the main findings of entire thesis can be drawn in the following sections.

8.1.1 Development of electroless Ni-W-P plating process

In this work, dimethylamine borane (DMAB: $(\text{CH}_3)_2\text{NHBH}_3$) can successfully initiate the deposition reactions on Cu substrates to replace conventional PdCl_2 pre-treatment. This pre-treatment prevents the Ni-W-P plating solution from decomposition at high temperature (below 95 °C) for long plating durations (at least 2 hours), providing better bath stability. The adhesion strength of Ni-W-P coatings resulted from the DMAB pre-treatment was acceptable with the best qualification in tape tests.

Moreover, to obtain a compact Ni-W-P metallisation layer, a sodium lauryl sulphate (SLS: $\text{NaC}_{12}\text{H}_{25}\text{SO}_4$) of 0.3 mg/L concentration can significantly improve the surface quality and certain degree of increase the deposition rate of Ni-W-P deposits without any changes in contents of the ternary Ni-W-P deposits.

A comprehensive investigation was conducted on the critical plating parameters of electroless Ni-W-P coating process for a precise control of the composition of the Ni-W-P deposits. These plating parameters include plating temperature, pH value, and all constituents (NiSO_4 , Na_2WO_4 , NaH_2PO_2 , and $\text{Na}_3\text{C}_6\text{H}_5\text{O}_7$) of the plating bath.

8.1.2 Thermal stability and phase transformation of electroless Ni-W-P coatings

The thermal stability and phase transformation characteristics of obtained amorphous Ni-W-P deposits after annealing at elevated temperature were investigated. The crystallisation of electroless Ni-P and electroplated Ni-W coatings was also studied for comparison.

For Ni-W-P coatings, a small addition of W (5.5 wt.%) can significantly raise the crystallisation temperature of amorphous Ni-P compound from 347 °C to 390 °C. Further addition of W content in Ni-W-P deposits can continue to increase their crystallisation temperature, thus postpone the crystallisation process of amorphous Ni-W-P coatings. Overall, the crystallisation temperature of electroless Ni-W-P coatings with 6-25 wt.% W is in the range of 390 to 416 °C.

From XRD results, the increase of W content in Ni-W-P coatings has been found to significantly retard the crystallisation and formation of equilibrium phases such as Ni₃P and Ni in amorphous Ni-W-P compound. Especially, for Ni-25W-9P coating, its microstructure remained stable along with some metastable phases (Ni₅P₂ and NiP) when heated at 400 °C, in contrast, amorphous Ni-P compound had been fully transferred into a stable Ni₃P phase with no metastable phases under the same condition. In addition, face centered cubic Ni phase was identified in this Ni-P deposit.

Generally, the crystallisation process of Ni-W-P alloy can be divided into two major stages. Firstly, it crystallises into metastable crystalline structures (Ni₅P₂, NiP) at lower temperature due to the elimination of point defect and dislocation in Ni-W-P deposits. Then, a high annealing temperature with prolonged heating duration can lead to thermal migration of the atoms in metastable Ni₅P₂ and NiP phases, and be transformed into stable Ni₃P and Ni crystalline phase.

The thermal stability of electroless Ni-W-P coatings on Cu substrates was also evaluated based on their cross-section microstructure. It was more stable than electroplated Ni-W layer. The electroplated Ni-29W coating showed higher thermal stability than electroless Ni-W-P coating at 500 °C, but became fractured and cracking even at the ambient temperature of 200 °C, which can be very detrimental as a diffusion barrier.

8.1.3 Formation of Zn-Al solder interconnects

In order to apply Ni-W-P UBM as a diffusion barrier, Zn-Al solders were used to form solder interconnects on substrates with and without Ni-W-P coatings. Due to the low wettability of Zn-Al solder, a soldering flux (constituents: LiCl, ZnCl₂, KCL, KF) has been prepared to obtain Zn-Al solder interconnects. In addition, gas dynamic cold spray and self-propagation methods were also tested to form Zn-Al solder interconnects below 250 °C without flux.

In soldering reflow process with a flux, the wettability of Zn-Al solder on Cu and Ni-W-P substrate were significantly improved by effectively removing the oxides during soldering. Without Ni-W-P UBM, dendritic ϵ -CuZn₄ phase and γ -Cu₅Zn₈ layer were formed at the Cu/Zn-Al solder interface, and their thicknesses are 2.57 μ m and 6.69 μ m, respectively. With Ni-W-P coatings, γ -Ni₅Zn₂₁ and Al₃Ni₂ is likely to be formed at the Ni-W-P/Zn-Al interfaces, but the interfacial IMC layer was too thin (< 1 μ m) to be identified by energy dispersive X-ray Detector (EDX) due to the excellent diffusion barrier properties of Ni-W-P coatings.

In the gas dynamic cold spray process, the initial uneven Cu/Zn-Al interface was observed due to the impact of the supersonic Zn-Al particles accelerated by propellant gas. After reflowing, massive voids and cracks can be found within the Zn-Al solder matrix near the Cu/Zn-Al solder interface. In contrast, the Ni-W-P/Zn-Al interface was relatively even since the Ni-W-P coating is much harder to be deformed. After reflowing, a discontinuous layer of Al₃Ni₂ (~ 2 μ m thickness) can be seen at the Ni-W-P/Zn-Al interface. And the whole Zn-Al solder joints with Ni-W-P coatings remain intact.

Self-propagation method using Al/Ni Nanofolds was proven to be viable in forming reliable Zn-Al solder joints for its fluxless low process temperature and less requirements of experimental setup. With the exothermic heat generated from Al/Ni Nanofolds, the Zn-Al solder film fully melted across the entire solder joints and wetting the adjacent substrates during the rapid self-propagation reaction. Then, the Zn-Al solder solidified immediately surround the reacted AlNi layer, which can ensure the mechanical strength and ductility of this solder joint. Metastable interfacial IMC layers were formed in this Zn-Al solder joints due to the wide temperature range of rapid reaction (400-1400 °C). According to TEM observations, various IMCs and phases at

the Si/Zn-Al interface such as Zn, ZnNi, AlNi, and AuZn were formed, while Ni, Zn, ZnNi, AlNi IMCs are likely to be produced at the Nanofoil/Zn-Al interface.

8.1.4 Crystallisation characteristics of Ni-W-P coatings in lead-free solder joints

Thermal stability and crystallisation characteristics of Ni-W-P coatings in Zn-Al, Au-Ge, and BiAgX solder joints were studied. When Ni-W-P UBM soldering with high temperature lead-free solders, it exhibits different crystallisation characteristics in Zn-Al, Au-Ge, and BiAgX solder systems. For BiAgX solder paste, its joining temperature (325 °C) is appreciably below the crystallisation temperature of Ni-W-P UBM (~400 °C). The structure of the Ni-W-P UBM in BiAgX solder joint is generally amorphous according to TEM results without a significant degradation.

When soldering at 385 °C with Au-Ge solders, the Ni-W-P coating became two layers: a P-rich layer adjacent to the Au-Ge solder and an unreacted Ni-W-P layer near the Ni-W-P plated substrates. The latter one slightly crystallised due to self-crystallisation of Ni-W-P coating, exhibiting a mixed structure of amorphous compounds and some fine polycrystalline FCC-Ni particles. However, these Ni crystalline particles only scattered in the unreacted Ni-W-P layer and vanished into the P-rich layer adjacent to the Au-Ge solder. This change in the nanostructure is likely due to the increase of P content from 7.45 wt.% to 11.57 wt.%.

For Ni-W-P/Zn-Al solder interconnects, their reflow temperature was 450 °C and clearly exceeds the crystallisation temperature of Ni-W-P alloys (~400 °C). Similarly, the Ni-W-P coating in Zn-Al solder interconnects was also composed of two layers; an unreacted layer and a reacted Ni-W-P layer near the Zn-Al solder. However, the unreacted Ni-W-P layer has become partially crystallised due to a high soldering temperature, converting into very fine Ni₃P grain particles (< 0.2 nm). The thickness of this layer grew steadily with the increasing soldering durations due to the diffusion and reactions. Unlike the columnar structure of crystalline Ni₃P layer formed in Ni-P UBM containing numerous voids, the crystalline structure of resultant interlayer in these interconnects with Ni-W-P coatings was equiaxed which is free of voids. The unreacted Ni-W-P coating adjacent to the substrate crystallised to certain degree due to spontaneous crystallisation. The diffraction patterns of these unreacted Ni-W-P

coatings after 1 minute and 30 minutes soldering at 450 °C were almost the same, indicating that Ni-W-P coating shows an excellent thermal stability under high soldering temperature.

Generally, the crystallisation process of Ni-W-P UBM in solder joints can be classified into two types, the reaction-assist crystallisation and the spontaneous crystallisation. The rate of reaction-assist crystallisation is much greater than that of spontaneous crystallisation. Based on different lead-free solders of varying joining temperature, the crystallisation characteristics of Ni-W-P UBM were summarised as follows:

1. For the solders with their joining temperature below 400 °C, entire Ni-W-P coatings are generally amorphous, with almost no effect due to soldering.
2. For the solders with joining temperature close to 400 °C, the Ni-W-P coating changed into two layers, an amorphous resultant layer near the solders and an unreacted layer in a mixture structure of amorphous and crystalline phases.
3. For the solders with joining temperature considerably over 400 °C, the Ni-W-P coating became a crystalline resultant layer (Ni_3P) and an unreacted layer with a fine polycrystalline structure. The microstructure of the former one is uniform and free of voids.

8.1.5 Interfacial reactions between electroless Ni-W-P coatings and high temperature lead-free solders

The interfacial reactions between electroless Ni-W-P coatings and three types of high temperature lead-free solders, including Zn-Al, Au-Ge and BiAgX systems, have been investigated.

1. Soldering with Zn-Al solder

Without Ni-W-P coatings, Zn-Al solder directly reacted with Cu substrate to generate enormous Cu-Zn IMCs (thickness: up to 94 μm), including CuZn_4 , Cu_5Zn_8 and CuZn . Initially, inter-diffusion between Zn atoms in Zn-Al solder and Cu produced $\epsilon\text{-CuZn}_4$. This phase can hinder the direct reactions between Zn and Cu. With a continual growth of $\epsilon\text{-CuZn}_4$, Zn atoms in $\epsilon\text{-CuZn}_4$ diffused into Cu substrate and generated $\gamma\text{-Cu}_5\text{Zn}_8$ interlayer between $\epsilon\text{-CuZn}_4$ and Cu substrate. After prolonged reactions, small amount of Zn atoms in $\gamma\text{-Cu}_5\text{Zn}_8$ diffused continuously into Cu substrate, leading to a thin layer

of β' -CuZn. The growth mechanisms of the above Cu-Zn IMCs are all in diffusion-control mode. The growth rate coefficients of ε -CuZn₄, γ -Cu₅Zn₈ and CuZn at 450 °C were estimated as 0.551, 1.573, and $5.607 \times 10^{-2} \mu\text{m/s}^{1/2}$, respectively. Due to the difference in the intrinsic diffusivities between Cu and Zn, some Kirkendall voids were observed at the Cu₅Zn₈/CuZn₄ interface and near the boundaries of CuZn layer. These voids can seriously degrade the reliability of solder joints by providing crack initiations, particularly under external forces.

With Ni-W-P coatings as UBM interlayer, a compact thin layer of Al₃Ni₂ (< 2 μm) was formed at the Ni-W-P/Zn-Al solder interconnects under certain reflow times. In the initial liquid-solid reaction stage (~1 minute) at 450 °C, small Al₃Ni₂ grains (~ 0.5 μm) is formed in prism-like or plate-like shapes. After reacting for 15 minutes, Al₃Ni₂ grains continued to grow into round scallops by merging the adjacent smaller Al₃Ni₂ grains, resulting in a continuous IMC layer. The cross section of these round scallop IMCs ranged from 1 to 2.1 μm . After reacting for 30 minutes, faceted Al₃Ni₂ scallops were finally observed in polygon-like shape with a slight increased size (up to 2.5 μm). Similarly, the growth mechanism of Al₃Ni₂ is diffusion-control process. But its growth rate coefficient is $4.9 \times 10^{-2} \mu\text{m/s}^{1/2}$ at 450 °C, which is 46 time smaller than that of Cu-Zn IMCs. This indicates that Ni-W-P coatings clearly exhibit an excellent diffusion barrier property in preventing and suppressing the interfacial reactions between Cu and Zn.

A nanoindentation technique was utilised to evaluate the elastic moduli and hardness of interfacial IMCs in Zn-Al solder interconnects after 30 minutes reaction. The elastic moduli (hardness) of CuZn₄, Cu₅Zn₈, CuZn and Al₃Ni₂ were estimated to be 68.45 ± 1.43 (1.03 ± 0.04), 142.59 ± 2.26 (5.98 ± 0.23), 94.71 ± 1.16 (1.38 ± 0.16), and 220.87 ± 18.94 (17.67 ± 0.16) GPa, respectively.

2. Soldering with Au-Ge solder

SiC/Au-Ge/Ni-W-P “sandwich” structure solder joints were prepared for interfacial analysis and shear strength testing. The interfacial IMC layer was mainly composed of Ni₅Ge₃ according to TEM observations of interconnect cross-section, however, some NiGe were also found on fracture surfaces through SEM examination. Based on the TEM analysis, the Ni₅Ge₃ grains were formed in different morphologies with varying

sizes, including dendrite ($\sim 0.5 \mu\text{m}$), scallop ($\sim 0.3 \mu\text{m}$), and granular shapes with the smallest size of approximately 50 nm.

The average shear strength of Au-Ge solder joints was approximately 138.4 MPa, proving a robust interfacial adhesion. Post observation of fractures cross sections from shear strength tests showed the failure of the Au-Ge solder joints inside of the solder close to the Ni-W-P/Au-Ge interface, taking a ductile failure mode. The coarse fracture surface near ceramic substrate side consists of some fine dimples, where remaining, Ni-W-P residuals and Ni-Ge IMCs can be found. This can be attributed to the local poor adhesion or insufficient wetting behaviour of Au-Ge solders. In addition, the small voids along the boundaries of the Ni-Ge IMC grains were observed, which may have contributed to the eventual fracture of the joints near the region of Ni-W-P/Au-Ge interface, where IMCs were likely to be fractured due to the formation of the voids during shear tests. Similarly, from die side, fracture also extended into the Au-Ge/Ni/W/Ti interfaces due to the failure of the adhesion of metallisation layers. Therefore, initiating from Au-Ge solder, the cracks was likely to be extended into both Ni-Ge IMCs and Ni-W-P UBM on ceramic substrate and metallisation on SiC die because of the limited thickness of the Au-Ge solder layer (~ 14 microns).

3. *Joining with BiAgX solder*

SiC/BiAgX/Ni-W-P solder joints were fabricated through joining process. In the entire solder joints, a single void was observed during joining due to the unbalanced melting property of the mixed AgBiX solder paste. A small continuous crack was also found near the multi-layer metallisation on the SiC die side. According to TEM analysis, large Ag_3Sn grains (up to $5 \mu\text{m}$) in an irregular polygon shape were observed, with the medium size Ag_3Sn particles ($<1 \mu\text{m}$) being precipitated at the grain boundaries, and smaller Ag_3Sn particles ($<100\text{nm}$) being embedded in the needle-like, long striped and irregular polygon BiAgX solder grains. At Ni-W-P/BiAgX interface, Ni_3Sn_4 of columnar-like with a thickness ranging from 100 - 700 nm was also formed.

The average shear strength of BiAgX solder joints was approximately 32.0 MPa, which was 4 times greater than the required strength of IEC standard (6.25 MPa), but this was much smaller than the strength of Au-Ge solder joints (138.4 MPa). From fractographies analysis, the BiAgX joints mainly failed at the metallisation of SiC die side, and the limited solders remaining on fracture surfaces were due to the voids and

the cracking in solder joints. In addition, the cracking within the solders also contributed to this brittle failure due to the coefficient of thermal expansion (CTE) mismatches.

8.2 Future work

Due to the limit time during this PhD study, some potential future work that are worth of further investigations are summarised as follows.

8.2.1 Electroless deposition of Ni-W-P coatings

1. Though Ni-W-P coatings with various compositions have been achieved by electroless deposition in this work, the deposition process can still be improved, such as reducing the bath temperature in deposition and improving the stability of the bath, in order to adjust the deposition parameters easily.
2. Electroless plating of Ni-W-P UBM on other types of substrate, such as glass and ceramic, is interesting to be carried out, so that the potential applications of electroless Ni-W-P coatings can be expanded. The bath and deposition parameters in electroless Ni-W-P plating on various substrates can also be optimised to obtain the most suitable substrates for Ni-W-P coatings.
3. It has been frequently reported that the content of P is the primary factor that affects the crystalline structure of electroless Ni-W-P and Ni-P coatings. However, the fundamental mechanism behind this relation still remains unclear. Further investigations can significantly facilitate the understandings on electroless Ni-based deposition.

8.2.2 Phase transformation of electroless Ni-W-P coatings

1. The amorphous-crystalline transition of electroless Ni-W-P coatings is one of the most vital factors that deteriorate its efficiency in suppressing the mutual diffusion between solder and substrate. Therefore, the amorphous-crystalline transition temperatures of the Ni-W-P coatings with different W contents need to be studied systematically, thus, the service temperature of the Ni-W-P coatings with various W contents can be recommended. And this can also promote its application in high temperature power electronics.

2. The spontaneous crystallisation mechanism of Ni-W-P coatings at amorphous-crystalline transition temperature should be further investigated. It can provide fundamental insights into the crystallisation of Ni-W-P coatings and their thermal stability. This can provide alternative methods to improve the thermal stability of Ni-W-P coatings at elevated temperature.
3. In this work, it has been found that the crystallisation of Ni-W-P UBM in high temperature solder joints was slightly different from the spontaneous crystallisation of electroless Ni-W-P coatings. The results imply that interfacial reactions can alter the crystallisation behaviours of Ni-W-P UBM after aging. However, this reaction-assisted crystallisation and its comparison with spontaneous crystallisation are still lack of systematic studies. Further works on the mechanism of reaction-assisted crystallisation of Ni-W-P UBM may be carried out, so that the mechanism of deterioration of UBM as a diffusion barrier in solder joints can be revealed.
4. In-situ TEM investigations on the crystallisation of Ni-W-P UBM at elevated temperature can be a powerful tool to provide significant information on the amorphous-crystalline transition of UBM, mutual diffusions between solder and substrate and the mechanism of suppressing the diffusion.

8.2.3 Applications of Ni-W-P UBM with low-cost high temperature solder

1. In this work, it was found that the preparation of Zn-Al solder, a low-cost high temperature solder, was extremely challenging. For instance, the preparation of Zn-Al solder preforms requires significant efforts on minimising the oxidation and improving the yield. Future works should be conducted on improving the joining process and optimising the relevant parameters, so that Zn-Al solder joints can be applicable in hybrid automotive electronics as a low-cost high temperature lead-free solder.
2. Proper flux should be developed for reflowing Zn-Al solder on electroless Ni-W-P coatings to minimise the oxidation of solders and to enhance the wettability of solders on Ni-W-P substrates under elevated temperature.
3. As a new bonding method in electronic assembly, cold spraying should be further optimised in terms of the preparation of Zn-Al powder and the processing parameters. This may provide a new approach to some specific applications.

4. In this work, BiAgX solder joints with electroless Ni-W-P coatings were prepared. But, due to the unbalanced melting properties of BiAgX solder pastes, leading to some defects in solder joints and thus a low shear strength in mechanical tests. Hence, the composition of BiAgX solder should be improved for better reliability. The joining process of BiAgX solder joints should also be optimised, so that the microstructure of this solder matrix and the adhesion strength between the metallisation and SiC die can be improved.
5. Self-propagation was proven to be a potential fluxless interconnection method for preparation Zn-Al solder joints with low wettability. Further study can be conducted on interfacial microstructure, mechanical strength, and failure modes in Zn-Al solder joints with 3D structure by self-propagation.

8.2.4 Interfacial reactions in high temperature lead-free solder joints

1. Though some primary studies on the growth of IMCs at Ni-W-P/Zn-Al interface has been conducted, further works on the growth of IMCs in various high temperature solder joints may be done. Based on this, the efficiency of Ni-W-P UBM as a diffusion barrier in different high temperature solders can be evaluated.
2. The growth of interfacial IMCs at Ni-W-P/Zn-Al interface was investigated at one fixed temperature, 450 °C. The growth of IMCs at different temperatures should be studied, which can help to estimate the performance of Ni-W-P UBM in solder joints at different temperatures.
3. It is generally accepted that the thickness of Ni-W-P coatings is also one of major concerns that may affect the performance of UBM. But a thicker Ni-W-P layer demands more time and resource consumption and can be a reliability problem due to CTE mismatches. Hence, works on the optimal thickness of Ni-W-P UBM in the application with different high temperature solder should also be implemented. It can significantly help its application in high temperature power devices.
4. Because of the amorphous structure of electroless Ni-W-P coatings, the mutual diffusions between solder and substrate in solder/Ni-W-P/substrate structure could be significantly different from that in solder/substrate structure. Future works on the diffusion across solder/Ni-W-P and Ni-W-P UBM should be carried out, so that, the mechanism of suppressing mutual diffusion by Ni-W-P UBM can be revealed.

5. During service, HTE devices are normally operated at high current, elevated temperature and vibration, which may alter the growth behaviour of IMC at solder/Ni-W-P interface. Studies on the growth of IMC in solder joints with Ni-W-P coatings should be carried out to evaluate the performance of UBM under combined loads.

8.2.5 Reliability tests of high temperature lead-free solders joints

1. Reliability tests, such as thermal cycling, aging storage, and concurrent vibration and thermal environment test, can be carried out to investigate the reliability of high temperature solder (i.e. Au-Ge and BiAgX) joints. The usefulness and effectiveness of electroless Ni-W-P coatings as a UBM can be further verified for improving the reliability of the solder joints.
2. With an increasing trend towards miniaturization of electronic packaging, the volume ratio of IMCs in solder joints tends to be higher and even reach 100% ratio. Therefore, the mechanical properties and fracture characteristics of IMCs are of great interests for future researches. The elastic moduli, hardness, creep and crack characteristics of IMCs can be assessed using nanoindentation by varying loading/strain rate, force, and dwelling time. In addition, the fracture strength and failure modes of individual IMCs can be analysed by a combination of nanoindentation and focused ion beam techniques.

Publications

1. L. Liu, L. Zhou, and C. Liu, “Electroless Ni-W-P alloy as a barrier layer between Zn-based high temperature solders and Cu substrates”, in *Proceeding of 64th Electronic Components and Technology Conference (ECTC)*, Orlando, USA, 2014, pp. 1348-1353.
2. L. Liu, M. Mirgizoudi, P. Zhang, L. Zhou, and C. Liu, “Mechanical and interfacial characteristics of Zn-Al solder joints under elevated temperature and vibration conditions”, in *Proceeding of 5th Electronics System-Integration Technology Conference (ESTC)*, Helsinki, Finland, 2014, pp. 1-5.
3. L. Liu, Z. Chen, C. Liu, Y. Wu, and B. An, “Micro-mechanical and fracture characteristics of Cu₆Sn₅ and Cu₃Sn intermetallic compounds under micro-cantilever bending”, *Intermetallics*, vol. 76, pp. 10-17, 2016.
4. G. Chen, L. Liu, V.V. Siberschmidt, Y.C. Chan, C. Liu, and F. Wu, “Retained ratio of reinforcement in SAC305 composite solder joints: effect of reinforcement type, processing and reflow cycle”, *Soldering & Surface Mount Technology*, vol. 28, No. 3, pp. 159-166, 2016.
5. G. Chen, L. Liu, J. Du, V.V. Silberschmidt, Y.C. Chen, C. Liu, and F. Wu, “Thermo-migration behaviour of SAC305 lead free solder reinforced with fullerene nanoparticles”, *Journal of Materials Science*, vol. 51, No. 22, pp. 10077-10091, 2016.
6. L. Liu, S. Li, F. Wu, and C. Liu, “Nanoindentation on Zn-Cu intermetallic compounds at Zn-Al/Cu solder interfaces during soldering”, *Materials Science and Engineering: A*. (In preparation)
7. L. Liu, Z. Zhou, G. Chen, F. Wu, C. Li, and C. Liu, “Interfacial Reactions between molten Zn-Al solders and Ni-W-P substrates during soldering”, *Acta Materialia*. (In preparation)